

**CHEMICAL AND ELECTROCHEMICAL PROPERTIES OF  
Ca(II) AND Mg(II) BASED LIGHTWEIGHT METAL  
ORGANIC FRAMEWORK (LWMOF) MATERIALS**

**A Thesis Submitted to AcSIR for the Degree of  
Doctor of Philosophy  
in  
Chemistry**

**By**

**ARIJIT MALLICK**

**Research Supervisor  
Dr. RAHUL BANERJEE**



**Physical and Materials Chemistry Division  
CSIR-National Chemical Laboratory  
Pune, India**

**February 2015**

---

*Dedicated to  
My Parents*

---

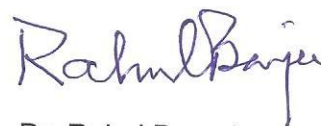
## Certificate

This is to certify that the work incorporated in this Ph.D. thesis entitled Chemical and Electrochemical Properties of Ca(II) and Mg(II) based Lightweight Metal Organic Framework (LWMOF) Materials submitted by Mr. Arijit Mallick to Academy of Scientific and Innovative Research (AcSIR) in fulfillment of the requirements for the award of the Degree of Ph.D. in Chemistry, embodies original research work under my/our supervision/guidance. I/We further certify that this work has not been submitted to any other University or Institution in part or full for the award of any degree or diploma. Research material obtained from other sources has been duly acknowledged in the thesis. Any text, illustration, table etc., used in the thesis from other sources, have been duly cited and acknowledged.



Arijit Mallick

(Student)



Dr. Rahul Banerjee

(Supervisor)

## STATEMENT

I hereby declare that the matter embodied in this thesis entitled “**Chemical and Electrochemical Properties of Ca(II) and Mg(II) based Lightweight Metal Organic Framework (LWMOF) Materials**” is the result of investigations carried out by me in Physical and Materials chemistry Division, National Chemical Laboratory, Pune under the supervision of Dr. Rahul Banerjee.

In keeping with the general practice of reporting scientific observations due acknowledgements have been made wherever the work described is based on the findings of other investigators.

Pune

February, 2015

**Arijit Mallick**

## ACKNOWLEDGEMENT

My most sincere and heartfelt thanks go to my supervisor and mentor, Dr. Rahul Banerjee. I thank him for introducing me to the wonders of scientific research. I thank him for his persistent guidance, encouragement, inspiration and support during every stage of my research work. I warmly thank him for his precious advice, analysis, criticism and discussions on my work. I would like to thank my DAC committee members Dr. C. G. Suresh, Dr. Sreekumar Kurungot and Dr. Ullash K. Kharul for their constructive and innovative suggestion.

I extend my sincere thanks to the Director of CSIR-NCL Dr. Sourav Pal, Dr. Shivram (former Director), Head of Physical and Materials Chemistry Division Dr. Anil Kumar for their kind help and encouragement during the course of this work. Most of the results described in this thesis would not have been obtained without a close collaboration with few laboratories. I would like to acknowledge the assistance of Dr. Vedavati G Puranik for giving us the opportunity to use single crystal instrument. I am also thankful to Dr. David Díaz Díaz, Institut für Organische Chemie, Universität Regensburg, Germany and IQAC-CSIC, Barcelona (Spain) for his valuable scientific discussion and suggestions and Dr. Thomas Hein, School of Engineering and Science, Jacobs University, Germany, for his help in theoretical calculations in few projects. I owe a great deal of appreciation and gratitude to Dr. Sreekumar Kurungot for proton conductivity measurements and studies on MOF and Dr. Asha S. K. for photoluminescence measurement.

I am grateful to CSIR, New Delhi for fellowship support. I thank all the non-teaching staff of CSIR NCL for their assistance on various occasions. I wish to thank all my friendly and cooperative labmates *Tamasda (Tiger)*, *Pradipda (Panchuda)*, *Chandanda (Papa)*, *Subhadeep (Kaka)*, *Tanay (Dr. Kundu)*, *Sharath (Khatarnak)*, *Bishnu (Kaho)*, *Suman (Big short)*, *Bikash (Hacker)*, *Harshitha*, *Divya*, *Mohitosh (Mahi Bhai)*, *Saibal (Khuda)*, *Arjun (Hero)*, *Suwendu (Serious)*, *Subhash (Sahooji)*, *Jayshri (Jayadidi)*, *Gobinda (Dr. G. Bhai)*, *Digambar (Dr. Digs)*, *Manasda*, *Shouvik*, and *Sujitda* for creating a cheerful and enjoyable working atmosphere in the lab. They were extremely supportive as well as helpful during my tenure. I thank project students particularly Kishor, Akhila, Manisha who helped me in various projects.

My stay on this campus has been pleasant with the association of all the research scholars at CSIR NCL. I am thankful to Joyashishda, Krisanuda, Shyamda,

Animeshda, Parthada, Sumantrada, Debasisda, Garaida, Basabda, Binoyda, Analda, Saikatda, Patida, Sajalda, Shymboda, Anupamda, Himadrida, Rajada Ajit shingh, Subha, Munmun, Tanaya, Sampadi, Dossu, Mrinmoy, Achintya, Arpan Manna, Kanak, Susanta, Anjan, Pravat, Himadri, Gouridi, Prithvi, Chandan, Prathit, Amrita, Chinmay, Sekhar, Nagesh, Vishal, Sreekuuan, Vinisha, Pandiraj, Beena, Rajashri, Biplab (Sr.), Manik, Satej, and Sushma.

I would also like to thankful to my all juniors Anup, Soumen (Das), Saibal Bhoumik, Shantanu, Prasenjit, Sanjeev, Jhumur, Prajitha, Dhanya, Atanu, Somen (Dey), Atreyee, Arunava, Shantigopal, Hridesh, Manjur, Kaushik, Subrta, Abhijit, Sandipan, Shibaprasad, Indradeep, Bipul, Dipanjan, Anagh, Basudev, Somsuvra, Anupam, Samik, Sudip, Monalisa, Chayanika, Manik, Gablu, Tapas, Tamal, Manoj, Subhrasis, Bappa, Saikat, Ujjal, Rupa, Piyali, Sumana, Sandeep, Raja, Ramkrishna, Jagadish, Akash, Biplab (Manna), Amrit, Shmal, Sukanta, Sanjay Mondal, Saikat Sarkar, Soumaya, Avishek, wahid and Anand.

I want to thank my table tennis partners, Manoj Sharma, Abhik, Souvik, Santu, Aniruddha, Aryya, Deepak, Deepak kumar, Kundan, Nagraj, kannan, Swagata, Chaitanya, Indrapal, Chakadola, Jitu, Raju, Kaushalendra, P.C., Neghi. Debjoti, Rammy, Sujit, and late Agnimitra for keeping me always active and fit for all works.

I am grateful to my school and college teachers and I expressed my gratitude to Dr. Subrata Ghorui, Dr. Sujit Dolui, Dr. Shamal Roychoudhury, Mr. Milan Kumar Khan and Dr. Arijit Chakraborty for their encouragement in different part of my life.

I thank my brother Amit, Avijit and sister-in-law (Bithi) for their constant support and encouragement. I thank the entire members in my family for their constant care and wishes. Last but not least, I would like to pay high regards to my parents for their sincere encouragement and inspiration throughout my research work and lifting me uphill this phase of life. I owe everything to them. Dedicating this thesis to them is a minor recognition for their invaluable support and encouragement.

**Arijit Mallick**

## PREFACE

Metal organic frameworks (MOFs) are crystalline porous materials consist of array of metal ions, connected with functionalized organic linkers to form 1D chains, 2D layers and 3D frameworks. MOFs can be made with desired functionality with porosity for particular applications. Different metal ions and huge number of functionalized linkers has been used for MOF synthesis under different synthetic conditions, giving rise to unprecedented structural diversity tailored for specific application. Most commonly used linkers are aromatic polycarboxylates, due to the strong binding affinity of metals with the oxygen atoms. Whereas most commonly used metals are the transition metals because of their well define coordination behavior. But lightweight metals i.e. alkali and alkaline-earth metals (s-block elements) are rarely studied in literature. . In my thesis, we will be focused on synthesis and application of Ca(II) and Mg(II) based lightweight MOFs for their application in gas adsorption, proton conduction, chemical sensing and catalysis. Excluding introduction chapter my thesis will be divided into 5 chapters which discuss the details on synthesis of various Ca(II) and Mg(II) based lightweight MOFs, their characterization and applicability in gas adsorption, proton conduction, chemical sensing and catalysis.

Chapter 2 will address the gas adsorption properties of Mg(II) based MOFs. Initially, we will discuss the purpose of synthesizing the Mg based MOFs from very simple ligands like formates and pyridine dicarboxylic acids. The detail synthetic procedures and characterization processes will also be explained. The structure, thermal stability and the gas adsorption properties, especially H<sub>2</sub>, CO<sub>2</sub> and N<sub>2</sub> adsorption properties will be demonstrated. Also Grand Canonical Monte Carlo (GCMC) simulation has been performed to predict the initial positions of the hydrogen molecules in the framework. The positions of the each hydrogen molecules in the framework and their related adsorption energies were optimized using Density Functional Theory (DFT) and ab-initio Hartree-Fock (HF) method. (Adapted from *J. Mater. Chem.*, 2010, **20**, 9073–9080 and *Inorg. Chem.* 2011, **50**, 1392–1401)

In Chapter 3, Proton conductivity of five Ca-based MOFs will be presented, which depends on the amount of water molecules coordinated to the Ca-centres. The effect of the amount of coordinated water molecules on proton conduction value and the activation energy will be discussed. We will also address the role of hydrophilic

and hydrophobic nature of the framework on proton conduction. We will explain the reason behind the high temperature water holding capacity of a MOF and its effect on proton conduction phenomena. (Adapted from *Chem. Commun.*, 2012, **48**, 8829-8831)

In Chapter 4, the design and synthesis of a photochromic and solvatochromic MOF (Mg-NDI) having chromophoric NDI moiety will be discussed. We will briefly explain the chemistry behind the reversible photochromic and solvatochromic behavior of this MOF. The proper experimental characterization for all these properties has also been discussed. We will also demonstrate the visible detection of volatile organic amines in very low concentration using this Mg-NDI MOF in solid state. The mechanism of amine sensing phenomena was supported by DFT calculation and experimental data. (Adapted from *Chem. Sci.*, 2015, **6**, 1420 - 1425,)

In chapter 5, correlation between gelation and crystallization in a Ca(II) based metallo-gel and MOF, will be discussed. This gel have some interesting properties like i) it is very stable in high temperature (~ 150 °C), ii) thixotropic in nature iii) transparent with time iv) porous xerogel formation. All these properties will be elucidated with appropriate experiments. At last both the gel and MOF has been applied as Lewis acid catalyst for hydrosilylation reaction. (Adapted from *J. Mater. Chem.* 2012, **22**, 14951-14963).

Finally chapter 6 will describe the conclusion of the overall work presented in this thesis. The future direction of this thesis also presented in this chapter.

An extended Appendix describes crystallographic informations of all the MOF crystals reported in this thesis.

**Arijit Mallick**



## CONTENTS

Certificate	iii
Statement	iv
Acknowledgement	v
Preface	vii

## CHAPTER 1

<b>Introduction of Lightweight Metal Organic Framework and Its Applications</b>	<b>1-42</b>
1.1 Introduction of porous materials	2
1.2 Synthesis of MOFs	4
1.3 Properties and Applications of MOFs	7
1.4 Gas storage in MOFs	9
1.4.1 H <sub>2</sub> storage in MOFs	9
1.4.2 CO <sub>2</sub> storage in MOFs	13
1.5 Proton transport in MOFs	16
1.6 MOF as chemical sensor	24
1.6.1 Solvatochromic or vapochromic sensor	24
1.6.2 Luminescence based MOF sensors	25
1.6.3 Sensor based on Impedance Spectroscopy	27
1.6.4 Interferometric MOF sensors	27
1.6.5 Surface plasmon resonance based MOF sensors	27
1.6.6 Photochromic MOF sensors	28
1.7 Catalysis in MOFs	28
1.7.1 Metal node based catalysis	29
1.7.2 Organic linker based catalysis	30
1.7.3 Multifunctional catalysis	30
1.8 Introduction to Lightweight Metal-Organic Framework (LWMOFs)	32
1.9 Advantages of Lightweight Metal-Organic Framework (LWMOFs)	33
1.10 Important Applications of Lightweight MOFs (LWMOFs)	37

## CHAPTER 2

<b>Synthesis of Porous Mg(II) based Light Weight Metal-Organic Frameworks (LWMOFs) for Gas Storage</b>	<b>43-74</b>
2.1 Introduction	44
2.2 Result and discussion	46

2.2.1	Structural analysis of $\gamma$ -Mg-formate	46
2.2.2	Structural analysis of Mg-MOF-1 and Mg-MOF-2	50
2.2.3	Thermal properties and X-ray powder diffraction	54
2.2.4	Gas adsorption properties	56
2.2.5	Computational/theoretical results	60
2.3	Conclusion	64
2.4	Experimental procedures	64
2.4.1	Materials	64
2.4.2	Synthesis of $\gamma$ -Mg-formate $\text{Mg}_3(\text{O}_2\text{CH})_6\cdot[\text{NH}(\text{CH}_3)_2]_{0.5}$	64
2.4.3	Synthesis of Mg-MOF-1 $[\text{Mg}(3,5\text{-PDC})(\text{H}_2\text{O})]$	65
2.4.4	Synthesis of Mg-MOF-2 $[\text{Mg}(2,4\text{-PDC})(\text{H}_2\text{O})_3]$	65
2.4.5	General methods for characterization	65
2.4.6	Computational procedures	66
2.4.7	X-ray crystallography	69

### CHAPTER 3

#### **Electrochemical Property of LWMOFs: Correlation between Coordinated Water Content and Proton Transport in Ca-BTC-based Metal-Organic Frameworks 75-96**

3.1	Introduction	76
3.2	Result and discussion	77
3.2.1	Structural analysis of Ca-BTC based MOFs	77
3.2.2	Thermal properties and X-ray powder diffraction analysis	80
3.2.3	Proton conductivity measurements	81
3.3	Conclusion	87
3.4	Experimental procedures	87
3.4.1	Materials	87
3.4.2	Synthesis of all Ca-BTC based MOFs	87
3.4.3	General methods for characterization	89
3.4.4	X-ray crystallography	90

### CHAPTER 4

#### **Solvatochromic and Photochromic Metal-Organic Framework Containing Naphthalenediimide (NDI) based Linker for Solid State Organic Amine Sensing**

97-122

4.1	Introduction	98
4.2	Result and discussion	99
4.2.1	Structural analysis of Mg-NDI	99
4.2.2	FT-IR, Thermal properties and X-ray powder diffraction	101
4.2.3	Solvatochromism in Mg-NDI	102
4.2.4	Photochromism in Mg-NDI	106
4.2.5	Solid state amine sensing in Mg-NDI	107
4.2.6	N <sub>2</sub> Adsorption Analysis	111
4.2.7	Electrochemical measurements	112
4.2.8	DFT calculation for Mg-NDI	114
4.3	Conclusion	114
4.4	Experimental procedures	115
4.4.1	Materials	115
4.4.2	Synthesis of H <sub>4</sub> BINDI and Mg-NDI	115
4.4.3	General methods for characterization	116
4.4.4	X-ray crystallography	116

## CHAPTER 5

### **Ca(II) based Metal-Organic Framework and Metal-Organic Gel for Hydrosilylation Catalysis: Tuning between Gelation and Crystallisation** **123-152**

5.1	Introduction	124
5.2	Result and discussion	125
5.2.1	Synthesis of Ca-5TIA-MOF and Gel	125
5.2.2	Solubility and gelation properties	127
5.2.3	Structural analysis of Ca-5TIA	133
5.2.4	Thermal properties and FT-IR analysis	134
5.2.5	X-ray powder diffraction analysis	135
5.2.6	Morphological characterization	138
5.2.7	Gas adsorption analysis	138
5.2.8	Rheological and SAXS measurements	140
5.2.9	Catalytic performance	142
5.3	Conclusions	145
5.4	Experimental procedures	145
5.4.1	Materials	145
5.4.2	Synthesis of 5-triazole isophthalic acid	145
5.4.3	Synthesis of Ca-5TIA-MOF and Ca-5TIA-Gel	146
5.4.4	General methods for characterization	146
5.4.5	X-ray crystallography	147

## **CHAPTER 6**

### **Conclusion of All Chapters and Future Directives**

**153-156**

6.1 Conclusion

153

6.2 Future direction

155

## **REFERENCES**

**157-179**

About the Author

180

List of Publications

181

## List of Figures, Tables and Schemes

### Figures

1.1	Representation of classification of porous materials based on the pore diameter. The pore diameter scale is in arbitrary unit.	2
1.2	Model representation of 1D, 2D and 3D MOF constructed from organic linkers, metal salt and solvent molecules.	3
1.3	Model representation of three dimensional functionalized MOF.	4
1.4	Scheme of various synthetic approaches and conditions used for the preparation of MOFs.	6
1.5	Various applications of MOFs such as gas storage, separation, catalysis, drug delivery, magnetism, proton conductivity, non linear optics, light harvesting, photoluminescence, explosive sensing, charge carrier mobility etc.	7
1.6	Most Important applications of MOFs discussed in this thesis.	8
1.7	a) Current status of MOFs' hydrogen storage capacity at 77 K versus targets. b) Excess high pressure H <sub>2</sub> uptake capacities at 77 K versus BET surface areas for some highly porous MOFs. Reprinted with permission from [1.10]. Copyright 2012 American Chemical Society.	10
1.8	Comparative high pressure CO <sub>2</sub> uptake properties of literature reported MOFs and activated charcoal Norit RB2. Reprinted with permission from [1.23]. Copyright 2004 American Chemical Society.	14
1.9	Model representation of proton exchange membrane fuel cell (PEMFCs).	17
1.10	a) Vehicle proton hopping mechanism through the network. The arrow indicates the movement of protons. b) Mechanism of Grotthuss proton hopping through the H bonded network of	18
1.11	Inherent Water assisted proton conduction in a) ferrous oxalate dihydrate and b) Mn-dihydroxybenzoquinone MOF {Mn(DHBQ)(H <sub>2</sub> O <sub>2</sub> )}.	20
1.12	Ion assisted proton conduction in a) Zn-oxalate based 2D MOF and b) (NH <sub>4</sub> ) <sub>2</sub> (adp)-[Zn <sub>2</sub> (ox) <sub>3</sub> ]-3H <sub>2</sub> O.	22
1.13	a) Visible spectra and photograph of MOF crystals containing solvents (condensed vapors). A negative vapochromic effect is observed for both hydroxylic and nonhydroxylic vapors (solvents). Reprinted with permission from ref. [1.31]. Copyright: American Chemical Society. b) Illustration of the color changes of Nile Blue@DUT-25 crystals by use of basic or acidic solvents. Reprinted with permission from ref [1.32]. Copyright: Wiley-VCH.	25

1.14	a) MOF powders suspended in organic liquid indicated, under 365 nm irradiation. b) Height-normalized luminescent spectra of guest-containing MOFs upon excitation at 370 nm. Reprinted with permission from ref [1.33]. Copyright: Nature Publishing Group.	26
1.15	a) MOF films deposited on interdigital electrodes. b) MOF pellet pressed between gold disk electrodes. Reprinted with permission from ref [1.35]. Copyright: MDPI AG.	27
1.16	a) NDI chromophore containing Ca-MOF showed reversible photochromism in visible light. b) Methyl viologen cations were loaded MOF showed thermochromic and photochromic properties.	28
1.17	Catalysis in MOFs can be categorized into three types, a) metal node based catalysis, b) organic linker based catalysis and c) multifunctional catalysis.	29
1.18	Example of metal node based catalysis in $\text{Mn}_3[(\text{Mn}_4\text{Cl})_3(\text{BTT})_8(\text{MeOH})_{10}]_2$ . Reprinted with permission from ref [1.42]. Copyright: American Chemical Society	30
1.19	Example of organic linker based catalysis in IRMOF-Pro. Reprinted with permission from ref [1.43]. Copyright: American Chemical Society.	30
1.20	Example of multifunctional catalysis in CMOF-1. Reprinted with permission from ref [1.44]. Copyright: American Chemical	31
1.21	Introduction of lightweight metals and LWMOFs synthesis.	33
1.22	Most important advantages to use lightweight metals for MOF synthesis.	35
1.23	The metal-oxygen bonds in LWMOFs are stronger than other MOFs.	36
1.24	Crystal structure of MIL-100 and MIL-101 showing large pore volume for gas adsorption. Reprinted with permission from ref [1.50]. Copyright: Wiley-VCH.	37
1.25	Generation of open metal sites in Mg-MOF-74 for enhancement of gas storage properties.	38
1.26	Heterogeneous catalysis in MOFs, a) Ca-HFBBA MOF structure, b) hydrogenation reaction kinetics with time. Reprinted with permission from ref [1.52]. Copyright: Wiley-VCH.	39

- 1.27 a) Temperature-dependent fluorescence decay profiles of 1 (squares) and TPE (circles). Heating and cooling cycles are represented as filled and open symbols, respectively. The inset shows PXRD patterns of activated 1 and after heating at 350°C in air. The optical micrographs show fluorescent 1 ( $\lambda_{\text{ex}} = 350$  nm) upon heating at various temperatures in air, b) In situ normalized emission spectra ( $\lambda_{\text{ex}} = 350$  nm) of 1 exposed to various analytes at room temperature and 100 °C. Reprinted with permission from ref [1.54]. Copyright: American Chemical Society. 40
- 1.28 Inclusion study of selected large molecules in a) IRMOF-74-VII and b) IRMOF-74-IX respectively. This process was monitored through the decrease in absorbance at a selected wavelength as a function of contact time. For each measurement, the initial absorbance was normalized to 1.0. (Insets) Illustrations of the inclusion complex for each study Reprinted with permission from ref [1.56]. Copyright: AAAS publishing group. 41
- 2.1 a), b), c) and d) represents the local geometries surrounding the four independent, octahedrally coordinated magnesium centers within  $\gamma$ -Mg-formate. Ball and stick models showing packing diagram for e)  $\alpha$ -Mg-formate f)  $\beta$ -Mg-formate g)  $\gamma$ -Mg-formate. Yellow balls represent the empty space inside the pores. Color code: O (red) C (grey) Mg (green). 47
- 2.2 a) The polyhedral representation of the extended structure of  $\alpha$ -Mg-formate (parallel) viewed down the crystallographic  $b$  axis. b) Trans orientation Mg(4) with respect to the planes formed by Mg(1)–Mg(2)–Mg(1). c) Trans orientation Mg(3) with respect to the planes formed by Mg(1)–Mg(4)–Mg(1)c) in  $\alpha$ -Mg-formate. d) The polyhedral representation of the extended structure of  $\gamma$ -Mg-formate (orthogonal) viewed down the crystallographic  $b$  axis. e) Cis orientation Mg(4) with respect to the planes formed by Mg(1)–Mg(2)–Mg(1). f) Cis orientation Mg(3) with respect to the planes formed by and Mg(1)–Mg(4)–Mg(1) in  $\gamma$ -Mg-formate. 48
- 2.3 Schematic diagram showing structural diversities of Mg-MOFs 51

2.4	a) Polyhedral representation of Mg-MOF-1 [Mg(3,5-PDC)(H <sub>2</sub> O)] showing the coordination environment around Mg. b) Helical connectivity between Mg <sup>+2</sup> ions inside the channels. c) Ball and stick representation of along <i>c</i> axis of Mg-MOF-1 showing the 1D channel with open Mg-metal sites. d) Polyhedral model of Mg-MOF-1 showing 1D channels with coordinated water molecules facing towards the channels. e) Space-fill model of Mg-MOF-1 showing pores along <i>c</i> axis. Color code: Mg (green), N (blue), C (black), O(red).	52
2.5	a) The SBU in the crystal structure of Mg-MOF-2 [Mg(2,4-PDC)(H <sub>2</sub> O) <sub>3</sub> ] showing the coordination environment around Mg. b) Packing diagram of Mg-MOF-2 highlighting the hydrogen bonding network.	53
2.6	a) Thermogravimetric analysis of $\gamma$ -Mg-formate (10 °C/min). b) Thermo gravimetric analysis plot of Mg-MOF-1.	54
2.7	Comparison of PXRD patterns of the as-synthesized MOFs (black) with the simulated pattern from the single-crystal structure (red) for a) $\gamma$ -Mg-formate and b) Mg-MOF-1. VT-PXRD patterns of c) $\gamma$ -Mg-formate and d) Mg-MOF-1 at different temperature which coincides with the patterns simulated from single crystal structures.	55
2.8	Gas adsorption isotherms of $\gamma$ -Mg-formate: a) N <sub>2</sub> at 77 K (blue circles), b) CO <sub>2</sub> (green circles), at 298 K, and c) stick model of $\gamma$ -Mg-formate showing the voids. d) H <sub>2</sub> (red circles) at 77 K. The filled and open shapes represent adsorption and desorption, respectively. P/P <sub>0</sub> , relative is the pressure at saturation vapor pressure of the adsorbate gas.	57
2.9	Selective gas adsorption isotherms of Mg-MOF-1. a) CO <sub>2</sub> (blue, triangles) and N <sub>2</sub> (red, circle) at 298 K, b) H <sub>2</sub> (black, squares) and N <sub>2</sub> (red, circle) at 77 K for Mg-MOF-1; the filled and open shapes represent adsorption and desorption, respectively. P/P <sub>0</sub> , relative pressure at the saturation vapour pressure of the adsorbate gas.	58
2.10	Different positions of hydrogen molecule in (a) $\alpha$ -Mg-formate cluster and (b) $\gamma$ -Mg-formate cluster. Simulated and experimental isotherms for (c) $\alpha$ -Mg-formate and (d) $\gamma$ -Mg-formate.	61
2.11	a) Positions of adsorbed hydrogen molecules in Mg-MOF unit cell from GCMC calculation. Highlighted region was used to as the finite structure for ab-initio quantum chemistry calculation. b) Different adsorption sites of Hydrogen molecules from ab-initio quantum chemical calculations.	63



2.12	ORTEP drawing of the asymmetric unit of $\gamma$ -Mg-formate.	70
2.13	ORTEP drawing of the asymmetric unit of a) Mg-MOF-1 and b) Mg-MOF-2	71
3.1	S Schematic representation highlights the synthetic scheme and water content per metal centre in asymmetric unit of Ca-BTC based MOFs. Color code: Ca-green, O-red, C-black, N-blue, S-yellow and H-redish white. The coordinated waters are highlighted by pink circles.	78
3.2	Packing diagrams showing the 3D arrangement along crystallographic <i>a</i> axis for a) Ca-BTC-H <sub>2</sub> O b) Ca-BTC-DMSO, c) Ca-BTC, d) Ca-BTC-DMF, e) Ca-BTC-DMA. Color code: Ca-green, O-red, C-grey, N-blue, S-yellow and H-redish white. The coordinated waters are highlighted by pink circles.	79
3.3	a) FT-IR spectra patterns of BTC ligand Ca-BTC-H <sub>2</sub> O, Ca-BTC-DMF, Ca-BTC-DMA, Ca-BTC-DMSO and Ca-BTC. b) TGA traces of Ca-BTC-H <sub>2</sub> O, Ca-BTC-DMF, Ca-BTC-DMA and Ca-BTC-DMSO.	80
3.4	a) Water adsorption isotherm for Ca-BTC-H <sub>2</sub> O, Ca-BTC-DMF and Ca-BTC-DMA. b) Variable temperature PXRD peaks of Ca-BTC-H <sub>2</sub> O showing the thermal stability of the materials. c) VTSCXRD of Ca-BTC-H <sub>2</sub> O showing loss of lattice water molecules at 75 °C.	81
3.5	Comparison of PXRD patterns of as synthesised materials with the simulated pattern from the single-crystal structure for a) Ca-BTC-H <sub>2</sub> O, b) Ca-BTC-DMF, c) Ca-BTC-DMA, d) Ca-BTC-DMSO, e) Ca-BTC, f) Ca-BTC-DMSO after water treatment. The red colored patterns symbolized experimental data and black colored patterns symbolized simulated data.	82
3.6	Equivalent circuit model representation of the Nyquist plot.	83
3.7	Proton conductivity of Ca-BTC-H <sub>2</sub> O a) at low temperature and b) at high temperature. Proton conductivity of Ca-BTC-DMF c) at low temperature and d) at high temperature. Proton conductivity of Ca-BTC-DMA e) at low temperature and f) at high temperature.	85
3.8	a) Arrhenius plots of Ca-BTC-H <sub>2</sub> O, Ca-BTC-DMF and Ca-BTC-DMA. The activation energy has been calculated from the slope of the Arrhenius plots. b) The barchart representation of proton conductivity values with respect to different Ca-BTC-MOFs.	86
3.9	Possible scheme of Grotthuss proton hopping mechanism of In and Cd-5TIA.	86

3.10	Ortep Drawing of the assymmetric unit of a) Ca-BTC-H <sub>2</sub> O b) Ca-BTC-DMA, c) Ca-BTC-DMSO, d) Ca-BTC, e) Ca-BTC-DMF. Thermal ellipsoids set to 50% probability level.	93
4.1	Scheme represents the synthesis of Mg-NDI. Color code: Mg-green, O-red, C-black, N-blue and H-redish white.	100
4.2	a) The SBU of Mg-NDI shows coordination geometry of the metal centers and the binding fashion of the ligands. b) The perspective view of 1D channel in Mg-NDI present along <i>c</i> axis. c) Packing diagrams showing the 3D arrangement along crystallographic <i>c</i> axis. d) Solvent accessible void present in Mg-NDI. Color code: Ca-green, O-red, C-grey, N-blue, S-yellow and H-redish white.	101
4.3	a) FT-IR spectra of H <sub>4</sub> BINDI and solvent incorporated Mg-NDI. b) PXRD pattern of water vapor treated Mg-NDI compared with the simulated and as-synthesized pattern of Mg-NDI. c) TGA plots of Mg-NDI and different analyte incorporated MOFs.	102
4.4	a) Schematic representation of Mg-NDI crystals showing different color in different solvents; b) solid state UV-vis spectra; c) solid state photoluminescence of Mg-NDI crystals soaked in different solvents; d) PXRD patterns of solvent@Mg-NDI materials and e) N <sub>2</sub> adsorption isotherm for Mg-NDI.	104
4.5	a) Solid state UV-vis spectra of H <sub>4</sub> BINDI (red), Mg-NDI (black) and aniline@Mg-NDI (brown). b) Band gap value <i>vs.</i> polarity has been plotted, which shows the band gap value increases with increasing polarity.	105
4.6	a) Photograph representing the reversible photochromic behavior of Mg-NDI MOF crystal in sunlight and dark; b) ESR spectra of Mg-NDI crystals before and after irradiation of sunlight; c) PXRD patterns of Mg-NDI crystals before and after irradiation of sunlight; d) solid state UV-vis spectra of H <sub>4</sub> BINDI (red), Mg-NDI (black) and Mg-NDI* (brown).	106
4.7	Optical images representing the color change of Mg-NDI in presence of different amines at different concentrations.	108
4.8	PL quenching spectra of Mg-NDI in presence of different concentration of a) Hydrazine, b) aniline, c) ethylenediamine, d) triethylamine, e) Diethylamine, b) 1,3-propanediamine, c) Ethylamine, d) Methylamine.	109

4.9	a) Photograph representing the selective color change in case of aniline with respect to other aromatic functional molecules; b) Solid state PL spectra of Mg-NDI in different aromatic functional molecules; c) Bar chart representation for quenching efficiency of Mg-NDI in presence of different amines (0.01 M) in EtOH d) bar chart representation for quenching efficiency of Mg-NDI in presence of different analytes (0.01 M in EtOH); (e) Stern-Volmer plot for Mg-NDI with different amines.	110
4.10	N <sub>2</sub> adsorption isotherms for solvent loaded Mg-NDI at 77 K. The filled and unfilled shapes are representing the adsorption and desorption respectively.	111
4.11	The cyclic voltammograms of Mg-NDI in acetonitrile medium and (inset) cyclic voltammogram of ferrocene.	112
4.12	a) HOMO ( $\pi$ ) and LUMO ( $\pi^*$ ) energy levels of Mg-NDI and different amines. The inset shows contour plots of the HOMO and LUMO for Mg-NDI. Energy optimized structures of b) DMF, c) EtOH, d) Aniline and e) Toluene incorporated Mg-NDI has been represented.	113
4.13	Scheme for synthesis of H <sub>4</sub> BINDI.	115
4.14	Ortep Drawing of the asymmetric unit of a) H <sub>4</sub> BINDI b) Mg-NDI. Thermal ellipsoids set to 50% probability level.	118
4.15	Single crystal structure and packing diagram of a) H <sub>4</sub> BINDI showing the $\pi$ - $\pi$ interaction between NDI moieties (3.3 Å) and b) Mg-NDI showing the absence of $\pi$ - $\pi$ interaction between NDI moieties (7.1 Å). The dihedral angle between naphthalene ring and isophthalic acid moiety in c) H <sub>4</sub> BINDI and d) Mg-NDI framework.	119
5.1	Schematic diagram showing the synthesis of Ca-5TIA-MOF and Ca-5TIA-Gel under different conditions. TEM image of Ca-5TIA-Gel (scale bar = 100 nm) and SEM image of Ca-5TIA-MOF (scale bar = 100 $\mu$ m).	126
5.2	a) Digital photograph of the milky solution obtained by mixing 0.1 mmol Ca(OAc) <sub>2</sub> and 0.1 mmol 5TIA in 1 mL DMF upon sonication at RT for 15 min. Gel formation after b) standing at RT or heating at c) 60 °C, d) 90 °C, e) 120 °C in an oil bath for 2 h. f) Gels prepared in DMF, DMSO, DMA and Quinoline at 0.5 M concentration in the gelator system. g) Digital photograph of the Ca-5TIA-Gel made in DMF after 1 day, 3 weeks and 1.5 months; h) digital photograph of the same gels under UV irradiation. i) UV-Vis spectra for 5TIA ligand (black) and Ca-5TIA-Gel (red). j) Time dependent UV-Vis spectra for Ca-5TIA-Gel. k) Fluorescence emission spectra for 5TIA ligand (black) and Ca-5TIA-Gel (red).	131

- 5.3 a) Coordination sites of 5TIA along *c* axis. b) Coordination sites of 5TIA along *a* axis. c) Coordination environment around Ca(II) centre. d) The SBU in the crystal structure of Ca-5TIA-MOF showing the arrangement of 5TIA. e) Packing diagram showing formation of one dimensional pores through *c* axis for Ca-5TIA-MOF. f) Topological simplification of Ca-5TIA-MOF through *c* axis, by joining only Ca(II) centres (orange) with 5TIA ligand (blue). 133
- 5.4 a) TGA traces of Ca-5TIA-Xerogel (black) and Ca-5TIA-MOF (red). b) FTIR spectra patterns of Ca(OAc)<sub>2</sub> (blue), 5TIA ligand (red) Ca-5TIA-Xerogel (yellow) and Ca-5TIA-Gel (green). 135
- 5.5 a) Comparison of PXRD patterns of the Ca-5TIA-Xerogel (green) and Ca-5TIA-MOF (red) with the simulated pattern from the single-crystal structure (black). b) VT-PXRD patterns of the Ca-5TIA-Gel in the temperature range of 25-200 °C. c) Comparison of PXRD patterns of the Ca-5TIA-MOF after catalysis experiment (red) with the simulated pattern from the single-crystal structure of Ca-5TIA-MOF (black). d) Comparison of PXRD patterns of the Ca-5TIA-Xerogel [CaO] (red) and Ca-5TIA-Xerogel [Ca(OH)<sub>2</sub>] (green). 136
- 5.6 SEM images of Ca-5TIA-Gels prepared in 1 mL DMF under different conditions: a) 0.2 mmol Ca(OAc)<sub>2</sub> +0.2 mmol 5TIA sonication at RT for 15 min, then standing at 30 °C → peach coloured gel (scale bar = 50 μm); b) 0.2 mmol Ca(OAc)<sub>2</sub> +0.2 mmol 5TIA sonication at RT for 15 min, then standing at 60 °C inside the oven →peach coloured gel (scale bar = 30μm); c) 0.2 mmol Ca(OAc)<sub>2</sub> +0.2 mmol 5TIA sonication at RT for 15 min, then standing at 90 °C inside the oven → peach coloured gel (scale bar = 5 μm); d) 0.2 mmol Ca(OAc)<sub>2</sub> +0.2 mmol 5TIA sonication at RT for 15 min, then standing at 120 °C inside the oven → bright yellow coloured gel (scale bar = 10 μm); e) 0.1 mmol Ca(OAc)<sub>2</sub> +0.1 mmol 5TIA, sonication at RT for 15 min, then standing at RT → peach coloured gel (scale bar = 2 μm); f-g) 0.1 mmol Ca(OAc)<sub>2</sub> + 0.1 mmol 5TIA, sonication at RT for 15 min, then heating at 120 °C in an oil bath for 2 h (scale bars = 5 and 2 μm, respectively); h) 0.1 mmol Ca(OAc)<sub>2</sub> +0.1 mmol 5TIA, sonication at RT for 15 min, then heating at 120 °C in an oil bath for 20 h → yellow coloured gel (scale bar = 2 μm); i) 0.1 mmol Ca(OAc)<sub>2</sub> + 0.1 mmol 5TIA, sonication at RT for 15 min, then standing at 4 °C (scale bar = 100 μm); j-k) 0.1 mmol Ca(OAc)<sub>2</sub> + 0.075 mmol 5TIA, sonication at RT for 15 min, then heating at 120 °C in an oil bath for 3 h → bright yellow coloured gel (scale bars = 20 and 1 μm, respectively); l) 0.1 mmol Ca(OAc)<sub>2</sub> + 0.075 mmol 5TIA, sonication at RT for 15 min, then heating at 60 °C in an oil bath for 2.5 h → bright peach coloured gel (scale bar = 5 μm). 137

5.7	CO <sub>2</sub> adsorption isotherms below 1.0 bar for Ca-5TIA-Xerogel (blue) and Ca-5TIA-MOF (red) at 298 K. Filled and open circles represent adsorption and desorption data, respectively.	139
5.8	Rheology studies: a) A plot of the solid modulus ( $G'$ ) and loss modulus ( $G''$ ) as a function of frequency ( $\omega$ ) for Ca-5TIA-Gel; b) A plot of the solid modulus ( $G'$ ) and loss modulus ( $G''$ ) as a function of frequency ( $\omega$ ) at final holding time (720 minutes) and after preshere with strain ( $\gamma$ ) of 1% and frequency ( $\omega$ ) from 0.1 to 100 rad·s <sup>-1</sup> using Couette geometry for Ca-5TIA-Gel. c) plot of the solid modulus ( $G'$ ) as a function of frequency ( $\omega$ ) with ageing time at RT using Couette geometry for Ca-5TIA-Gel. d) Plot of the loss modulus ( $G''$ ) as a function of frequency ( $\omega$ ) with ageing time at RT using Couette geometry for Ca-5TIA-Gel.	140
5.9	a) SAXS plot of $q$ (Å <sup>-1</sup> ) as a function of scattering intensity (a.u) with varying time. b) SAXS plot of time (hours) as a function of correlation length (right-red) and Invariant (left-black) plots for Ca-5TIA-Gel at 60 °C.	142
5.10	Kinetic profile for the hydrosilylation of benzaldehyde catalyzed by Ca-5TIA-MOF (red), Ca-5TIA-Xerogel (blue) and Ca-5TIA-Gel (green) (catalyst loading = 10 mol%).	143
5.11	ORTEP drawing of the asymmetric unit of Ca-5TIA-MOF.	148
6.1	Scheme for synthesis of electron conducting MOFs using a photochromic MOF.	151

## Table

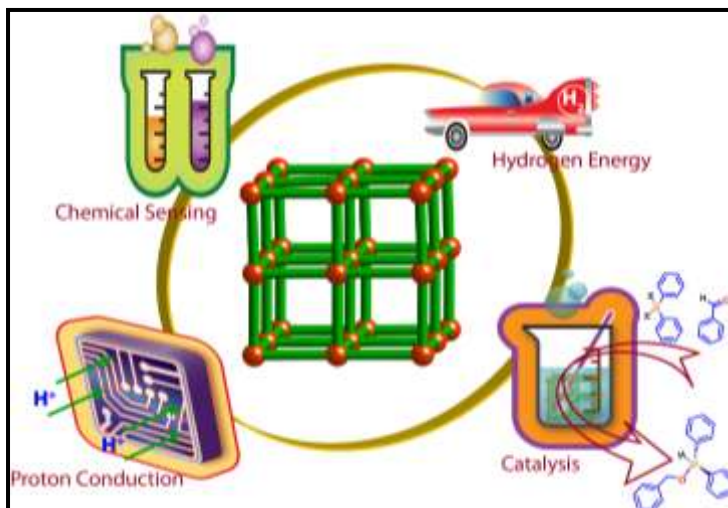
1.1	Low pressure H <sub>2</sub> adsorption in Metal-Organic Frameworks at 77 K temperature and 1 atm pressure.	12
1.2	Low pressure CO <sub>2</sub> adsorption capacities for Metal-Organic Frameworks at 273 and 298 K temperature and 1 atm pressure.	15
1.3	Proton-conducting MOFs under hydrous condition reported in literature.	23
1.4	Literature reported examples of MOF based catalysts and summary of active functionalities involved in these MOFs as catalytic centers.	31
1.5	Top 10 abundance elements present in earth crust.	34
1.6	Human body elemental abundance.	34
1.7	Properties of lightweight Metal Cations.	36
1.8	Average bond distance variation in lightweight metal carboxylate networks.	37

2.1	Spatial position of H <sub>2</sub> molecules from ab-initio quantum chemistry calculations.	63
2.2	Crystal data and structure refinement for Mg-MOFs.	72
3.1	Crystal data and structure refinement for Ca-BTC-MOFs.	95
4.1	Crystal data and structure refinement for H <sub>4</sub> BINDI and Mg-NDI.	121
5.1	Gelation ability in various solvents for the system [Ca(OAc) <sub>2</sub> (0.1 mmol) + 5TIA (0.1 mmol)]	128
5.2	Controlling of gelation and crystallisation by addition of water for the system [Ca(OAc) <sub>2</sub> (0.2 mmol) + 5TIA (0.2 mmol) + 2mL DMF]	129
5.3	Gelation ability of the system [Ca-salt (0.1 mmol) + 5TIA (0.1 mmol)] in DMF (1.0 mL) using different metal counteranions.	130
5.4	Crystal data and structure refinement for Ca-5TIA-MOF:	150

## CHAPTER 1

# Introduction of lightweight metal organic framework and its applications

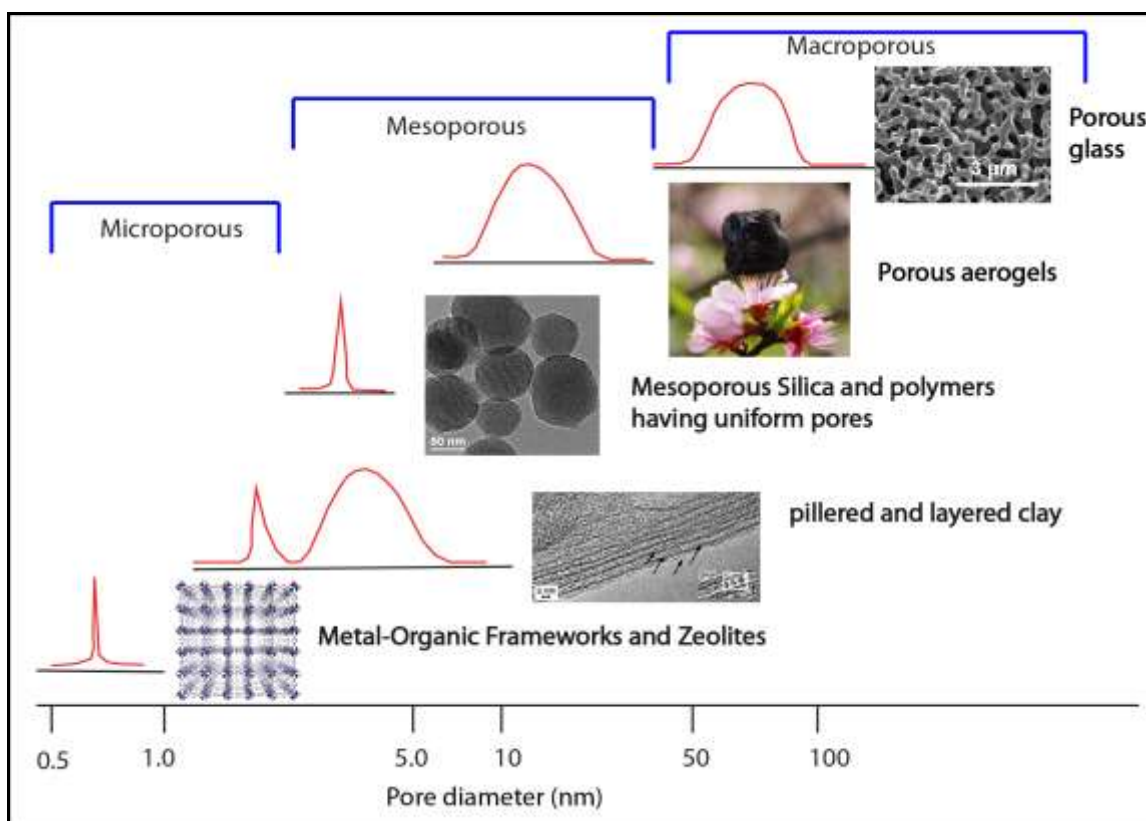
**Abstract:** Metal organic frameworks (MOFs) are crystalline porous materials consist of array of metal ions, connected with functionalized organic linkers to form 1D chains, 2D layers and 3D frameworks. MOFs can be made with desired functionality with porosity for particular applications. Different metal ions and huge number of



functionalized linkers has been used for MOF synthesis under different synthetic conditions, giving rise to unprecedented structural diversity tailored for specific application. Most commonly used linkers are aromatic polycarboxylates, due to the strong binding affinity of metals with the oxygen atoms. Whereas most commonly used metals are the transition metals because of their well define coordination behavior. But lightweight metals i.e. alkali and alkaline-earth metals (s-block elements) are rarely studied in literature. In this thesis, design and synthesis of Ca(II) and Mg(II) based lightweight MOFs for their application in gas adsorption, proton conduction, chemical sensing and catalysis have been focused. Excluding introduction chapter the thesis is divided into 5 chapters which discuss the details on synthesis of various Ca(II) and Mg(II) based lightweight MOFs, their characterization and applicability in gas adsorption, proton conduction, chemical sensing and catalysis.

## 1.1 Introduction of porous materials:

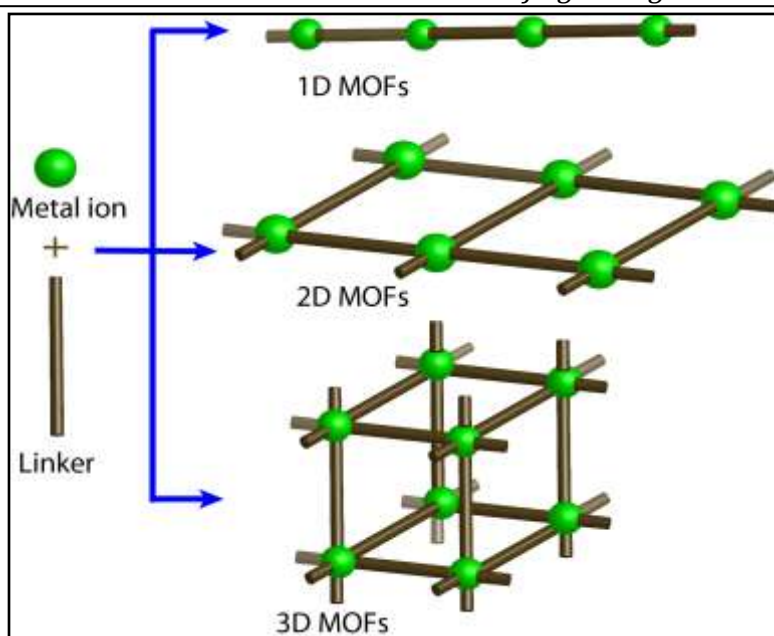
A porous solid can be defined as a solid material that contains cavities, channels or interstices for particular applications. Porous materials are widely used in various applications, ranging from catalysis, gas storage, energy storage, chemical sensing and electronics owing to their high surface area, tuneable pore size, adjustable framework and surface properties.[1.1] The surface area of these porous materials can be reach up to several thousand square meter per gram depending on the materials.[1.2] According to the definition accepted by IUPAC, the porous materials can be classified in three classes based on their pore diameters ( $\phi$ ): a) Microporous materials,  $\phi < 2.0$  nm (zeolites and metal organic frameworks); b) mesoporous materials,  $2.0 \text{ nm} < \phi < 50$  nm (silica and alumina); and c) macroporous materials  $\phi > 50$  nm (porous glass and foams) (**Figure 1.1**).



**Figure 1.1:** Representation of classification of porous materials based on the pore diameter. The pore diameter scale is in arbitrary unit.



In this thesis, mainly microporous materials and their applications have been discussed. Before 1970 researchers extensively used porous carbon for gas storage, separation, purification of water, solvent removal, etc. But porous carbon doesn't have high surface area, uniform pore size and crystallinity, which limits



**Figure 1.2:** Model representation of 1D, 2D and 3D MOF constructed from organic linkers, metal salt and solvent molecules.

its application in large scale. Then researchers discover zeolites as inorganic porous materials having crystallinity, uniform porosity for aforementioned applications. Zeolites also have some limitation like pore tuneability, chemical stability. In 1998 researchers have come up with an organic-inorganic hybrid porous materials i.e. metal-organic frameworks (MOFs) having better opportunity.

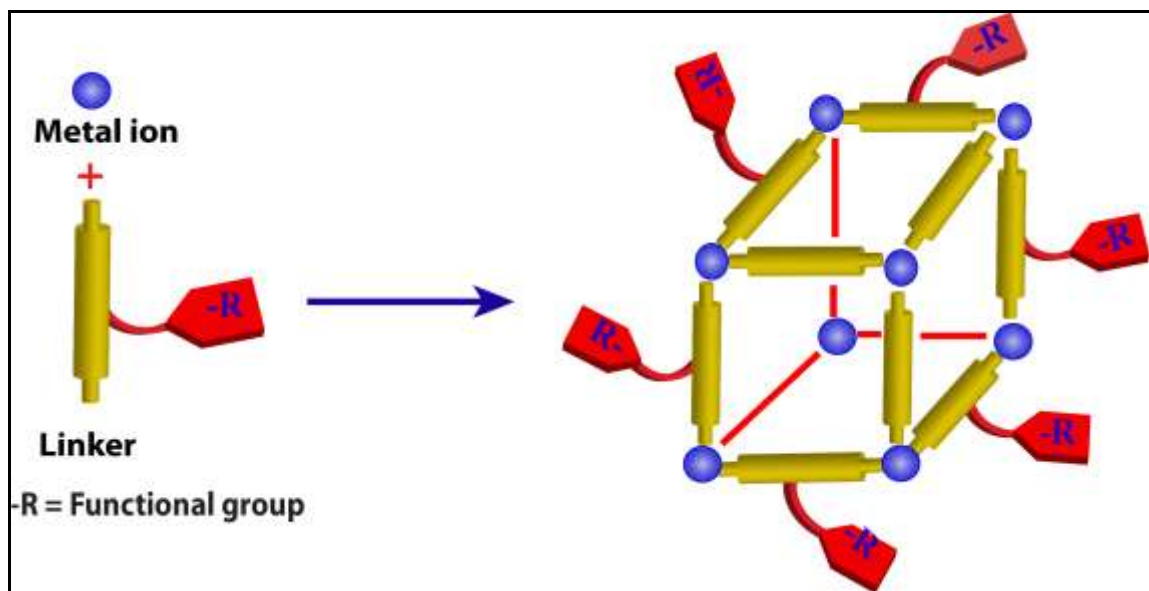
Metal organic frameworks (MOFs), are highly crystalline porous materials, mainly constructed by coordination bonds between metal ions or clusters and organic linkers to form 1D chains, 2D layers and 3D frameworks (**Figure 1.2**), have emerged as most promising candidate for sorbent applications. [1.3] MOFs have much higher surface area for gas adsorption than zeolites, carbon and porous polymer materials. One of the greatest advantages of MOF materials is its crystallinity. The high resolution single crystal structures can provide accurate pore size/dimension of the MOF channel. This in turn, provides better insight into the structural parameters that facilitates rational design of MOF architectures (**Figure 1.3**). On the other hand, by changing the different organic linkers the porosity of MOFs can be tuned according to the requirement. In addition, various reaction sites of the organic linkers inside MOF channels facilitate post-synthetic

modification and pore fictionalization, a unique advantage, which is beyond the scope of organic or inorganic adsorbent materials.

The uniform porosity and thermal stability of MOF materials have been utilized for important applications that include gas adsorption and storage, gas separation, magnetism, chemical sensing, drug delivery etc. [1.3] However, in recent years, focus has been shifted to other interesting applications such as proton conduction, lithium ion battery, charge carrier motion, oxygen reduction catalysis, light harvesting etc. [1.4] These applications are highly important for renewable energy research involving MOF materials. In the next part of this chapter has been focus on a brief overview of synthesis, structural and different applications of MOFs.

### 1.2 Synthesis of MOFs:

The metal-organic frameworks (MOFs) has been synthesized using almost all type of metal ions, starting from s-block metals, transition metals and lanthanides metals with organic linkers. The organic linkers are mainly polydentate ligands and most commonly used ligands are aromatic polycarboxylates. Including carboxylates, other functionality



**Figure 1.3:** Model representation of three dimensional functionalized MOF.

such as -OH, -NH<sub>2</sub>, -SH, -N<sub>3</sub>, -CN, -H<sub>2</sub>PO<sub>4</sub>, -SO<sub>3</sub>H has also been used extensively for MOFs synthesis. Heterocyclic compounds like imidazole, triazole, tetrazole, pyrazine, pyridine and their derivatives are also used as linkers for MOFs synthesis. MOFs are

principally synthesized using different liquid phase methods, where metal salts and organic linkers are dissolved in solvents and then at a particular temperature and pressure MOF materials are started crystallized from the mixture. Solvent is the most important factor of a particular reaction which determines the thermodynamic control as well as activation energy of the system and also enhance the crystallinity at higher extent.

### **1.2.1 Solvothermal Synthesis of MOFs:**

The most common method for MOF synthesis is the solvothermal method. In this method metal salts and organic linkers first dissolve in suitable solvent in a glass vial having teflon cap. The cap should be sealed tightly to make the container a close system. 60 - 100 °C temperature and 10 – 100 h time is required for this solvothermal reaction condition. [1.5]

### **1.2.2 Hydrothermal Synthesis of MOFs:**

Hydrothermal synthesis method is only used for high temperature reaction condition. Here metal salts and organic linkers are dissolving in high boiling solvents like DMF, DEF, DMA, DMSO, NMP, NMF, etc. in Teflon made container. The container then placed in a stainless still autoclave to avoid accident. In this reaction condition temperature should be maintained 100 – 200 C for 3 – 5 days to get better quality single crystal of MOFs. [1.5]

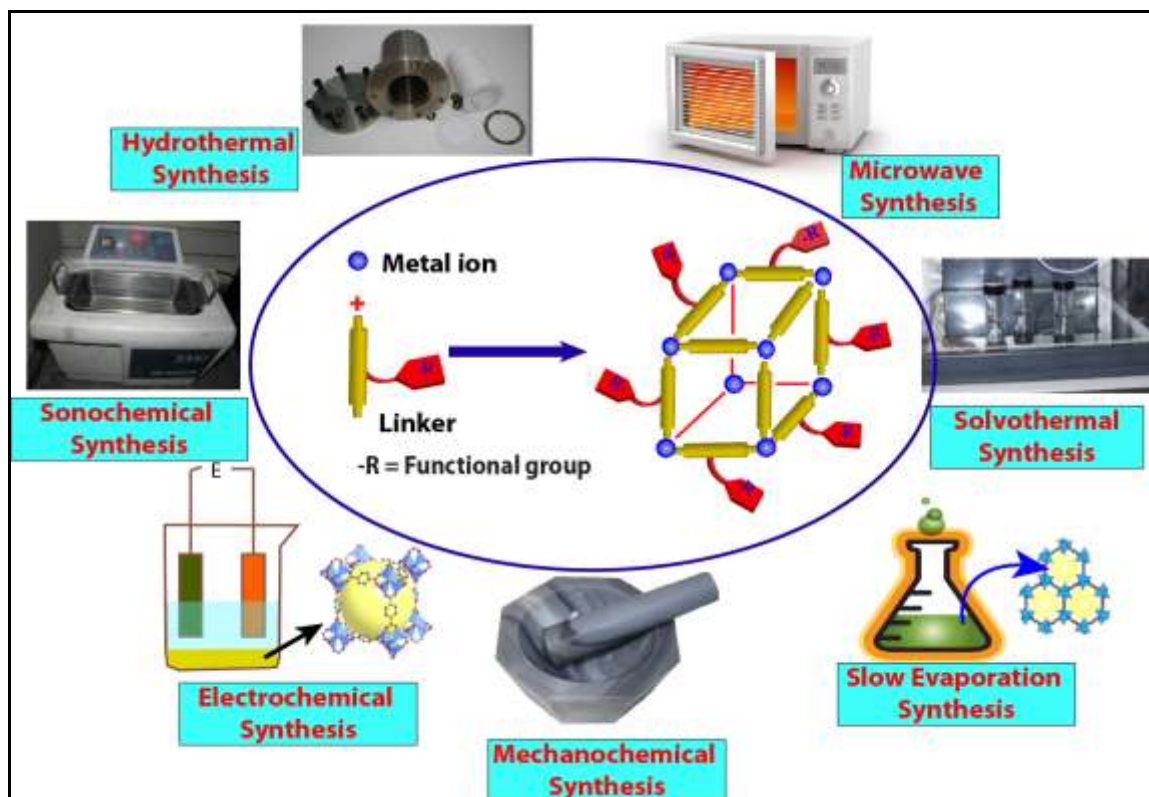
### **1.2.3 Room Temperature Synthesis of MOFs:**

There are several reports on synthesis of MOFs in room temperature. In general three types of method has been used for room temperature MOF synthesis i) slow evaporation method, ii) layering method and iii) slow diffusion method.

i) *Slow evaporation method:* Here, mixture of metal and ligands are dissolved in a low boiling solvents in a container (vials or conical flask) and then the solvent is allowed to evaporate slowly. Time required for crystallization is 3- 20 days (**Figure 1.4**).

ii) *Layering method:* In this method two different density solvents are used for MOF synthesis. The metal salt and ligand are dissolved in two solvents and then the lower density solution should be carefully layered on top of high density solution (e.g. methanol solution can be layered on aqueous solution). The single crystals grow on the junction of the layers.

iii) *Slow diffusion method*: This method also required two different solvents. The metal and ligand are dissolved in a solvent and kept in a saturated vapor of another low boiling solvent. The solvent vapor slowly diffuses into the mixture solution and start crystallization.



**Figure 1.4:** Scheme of various synthetic approaches and conditions used for the preparation of MOFs.

#### 1.2.4 Microwave Synthesis of MOFs:

Microwave synthesis method is important for industrial bulk scale production of MOFs. In this process MOFs can be synthesized within few minutes in gram scale. Here metal salt and ligand dissolved in solvent and then reaction happens in presence of microwave irradiation. Most of the cases microcrystalline MOF materials has been synthesized in this method and getting big single crystal is difficult here (**Figure 1.4**) [1.5].

#### 1.2.5 Mechanochemical Synthesis:

Mechanical force can induce many physical phenomena (mechano-physics) as well as chemical reactions in presence of solvents or without solvents [1.6f]. In mechanochemical synthesis, the mechanical breakage of intramolecular bonds followed

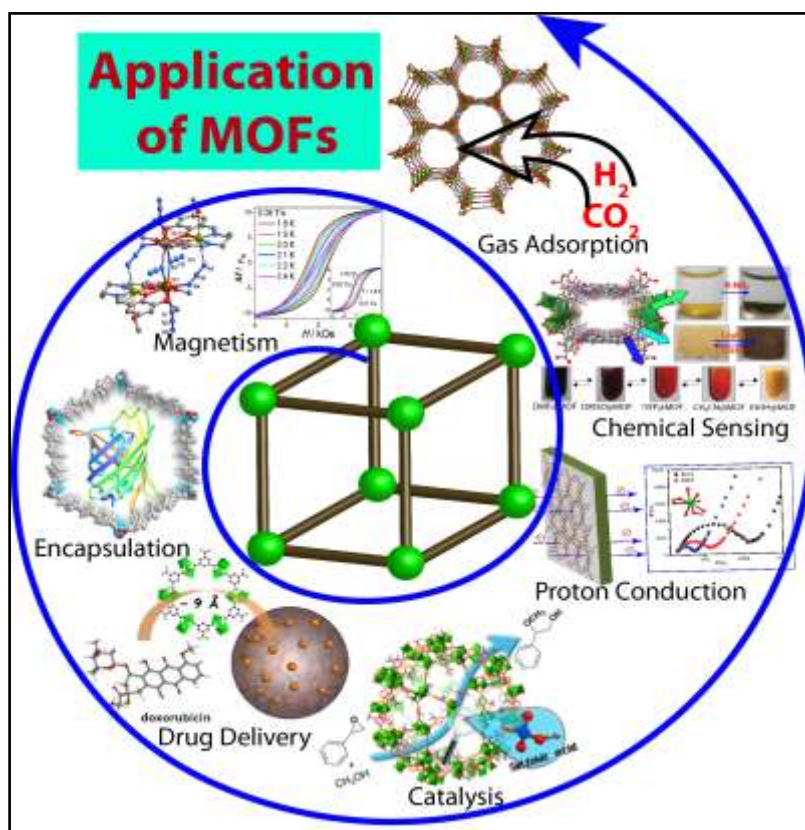
by a chemical transformation takes place. Treatment of the starting materials for 2–10 min in a steel reactor containing a steel ball or mortar and pestle leads to a highly crystalline and single-phase product of MOFs with guest molecules in the pores (**Figure 1.4**). These can be removed by thermal activation to yield the guest-free porous compound.

### 1.2.6 Electrochemical Synthesis:

The electrochemical synthesis of MOFs was followed in order to prohibit the entry of anions like nitrate, perchlorate or halides during the syntheses, which are of concern to large-scale production processes (**Figure 1.4**) [1.6g]. The large scale synthesis of MOFs using metal precursors and linkers can be achieved following electrochemical synthesis. The highly crystalline and pure products are anticipated during this synthetic procedure.

### 1.3 Properties and Applications of MOFs:

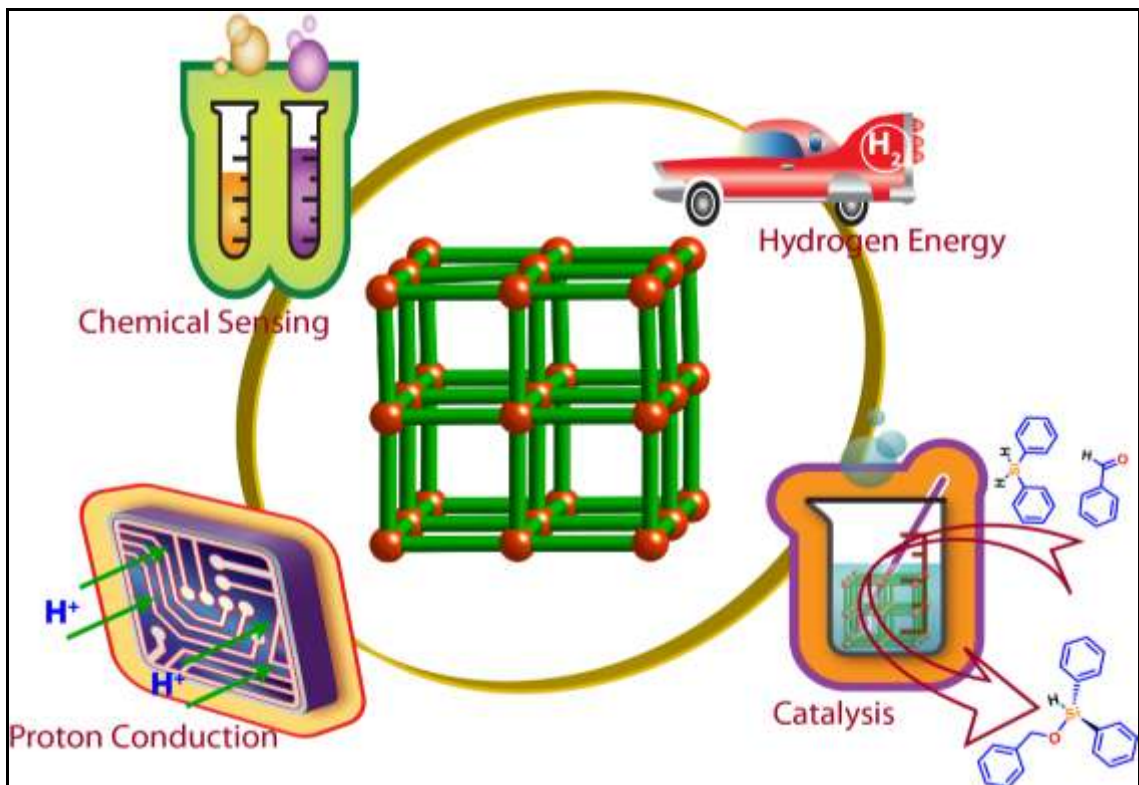
Porous materials find their applications in gas storage, gas/vapor adsorption and separation, shape/size-selective catalysis, drug delivery, etc. [1.3]



**Figure 1.5:** Various applications of MOFs such as gas storage, separation, catalysis, drug delivery, magnetism, proton conductivity, non linear optics, light harvesting, photoluminescence, explosive sensing, charge carrier mobility etc.

In order to take advantage of the properties of both organic and inorganic porous materials, porous MOFs, can be generated that are both stable and ordered and possess

high surface areas. These materials have attracted a great deal of attention in the past decade due to its fascinating applications in gas storage, gas/vapor separation, size/shape/enantio-selective catalysis, luminescent and fluorescent materials, and drug delivery, etc (**Figure 1.5**) [1.7]. Since, MOFs have following structural attractiveness; these materials have been successfully utilized for various applications:



**Figure 1.6:** Most Important applications of MOFs discussed in this thesis.

- i) Structural diversity due to possibility of synthesis of various MOFs by combining a range of metal centers and organic linkers. The ability to tune the framework architectures and properties in MOFs via the ligand and the metal ion provides a significant advantage over the zeolites because essentially an infinite number of variations are possible with predictable structures.
- ii) Easy synthesis and scale up following various strategies like room temperature synthesis, electrochemical synthesis, etc is possible.
- iii) High porosity, tunable pore sizes, easy incorporation of functional groups is possible in MOFs. The dimensions and topology of channels can be tuned through

organic synthesis by modifying the molecular structure of the organic ligand that bridges the metal ions.

- iv) The surface properties of channels can be altered by appending different organic substituent's onto the organic ligand without changing the architecture of the framework.
- v) The prospect of predictable alteration of organic units to provide tailored materials for given applications.

Due to aforementioned reasons MOFs over other materials finds several applications as they possesses structural integrity. Although, MOFs have been successfully synthesized by various ways and potentially applied for several applications, here few important applications have been discussed. In this thesis four important applications of LWMOFs are focused: i) gas storage, ii) proton transport, iii) chemical sensing and vi) catalysis (**Figure 1.6**).

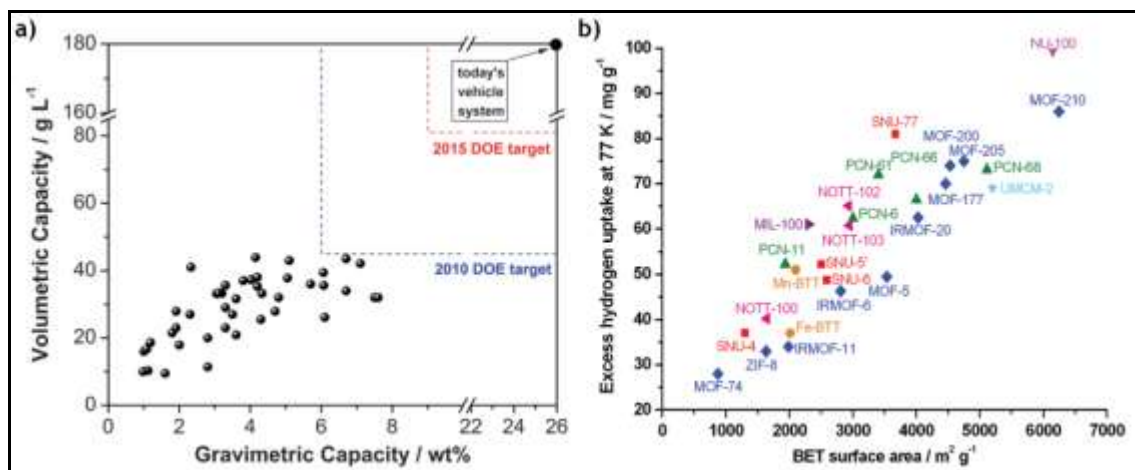
#### **1.4 Gas storage in MOFs:**

In last two decades, researchers paid much attention to find out excellent gas storage materials. Gas storage has huge importance in energy and fuel application. For storage of fuel gases such as hydrogen, ethylene, acetylene and methane under practical conditions need highly porous and stable material. MOFs are one of the excellent candidates due to their high porosity, crystallinity, tunable pore sizes and easy incorporation of functional groups in MOF. Other toxic and environmental hazardous gases like CO<sub>2</sub>, SO<sub>2</sub>, CO, NO<sub>2</sub> and NH<sub>3</sub> can also be captured and separated using porous MOFs. In this thesis, the storage of H<sub>2</sub> and CO<sub>2</sub> adsorption of Ca(II) and Mg(II) based LWMOFs studied extensively. So, H<sub>2</sub> and CO<sub>2</sub> storage application of MOFs has been briefly discussed here.

##### **1.4.1 H<sub>2</sub> storage in MOFs:**

Storage of H<sub>2</sub> is highly important due to its application of H<sub>2</sub> as a fuel for mobile or portable fuel-cell applications. But storage of H<sub>2</sub> is also a great challenge due to its very small volumetric density, 0.0899 kg/m<sup>3</sup> at STP, storing hydrogen at ambient temperature and pressure is very difficult [1.8]. Even in the liquid state, the volumetric density of hydrogen 70.8 kg/m<sup>3</sup> is very low compare to gasoline. As a result, serious difficulties need to be faced during the H<sub>2</sub> filling at lower temperature (20.27 K). From the last decades, MOFs have been used for the H<sub>2</sub> storage materials due to its permanent porosity

and high surface area [1.9]. MOF-storage for  $H_2$  works fully reversibly, avoids complicated heat treatments and recharging proceeds within seconds or minutes [1.10]. This is clearly an advantage over, e.g., metal hydrides, clathrates as storage materials. This makes,  $H_2$  storage, the most important and attractive application of MOFs. The comparative uptake of  $H_2$  by an empty tank without any porous materials and MOF filled container, thereby showing how important these MOFs are, for the world of today. The availability of high resolution crystal structures of MOFs allows direct observation and comparison of pore size and geometry, which is almost impossible in other porous materials. Potential reaction sites on the organic ligands in MOFs renders post-synthetic modifications possible, leading to the introduction of additional active sites for stronger  $H_2$  binding. The first study of hydrogen adsorption was reported in 2003 for MOF-5 which shows high BET surface area ( $3800 \text{ m}^2\text{g}^{-1}$ ) and 7.1 wt%  $H_2$  uptake at 40 bar and 77 K [1.11a]. After that, more than 300 MOFs have been tested till now for their  $H_2$  uptake capacity. The highest  $H_2$  uptake in NOTT-112 reaches up to 10 wt% at 77 bar and 77 K [1.11b]. On the other hand, NU-100 and MOF-210 [1.11c and d] have exhibited hydrogen adsorption as high as 7.9 to 9.0 wt% at 56 bar for both MOFs and 15 wt% at 80 bar for MOF-210. In general, the functionality of organic linkers has little influence on hydrogen adsorption, whereas increasing the pore volume and surface area of MOFs



**Figure 1.7:** a) Current status of MOFs' hydrogen storage capacity at 77 K versus targets. b) Excess high pressure  $H_2$  uptake capacities at 77 K versus BET surface areas for some highly porous MOFs. [Reprinted with permission from [1.10]. Copyright: American Chemical Society]



markedly enhances the gravimetric hydrogen uptake at 77 K under high pressure [1.8]. However, for volumetric hydrogen capture, adsorption enthalpy of hydrogen ( $Q_{st}$ ) plays the role rather than surface area. In this condition, unsaturated open metal sites are the effective tool to enhance the hydrogen uptake capacity in MOF architecture. There are some strategies to improve  $H_2$  storage in MOFs, such as: i) increase in pore size, pore volume and surface area; ii) generation of open metal sites; iii) incorporation of functional groups; iv) interpenetration or catenation; v) doping of metal nanoparticles and alkali metals in MOFs.

i) *Increase in pore size, pore volume and surface area:*  $H_2$  storage capacity of MOFs depends on its pore size as well as surface area. It has been observed that there is a linear relationship between BET surface area and  $H_2$  storage capacity i.e. with increasing surface area the  $H_2$  storage capacity should increase. But this phenomena only applicable for high pressure gas adsorption. In literature, the IRMOFs shows similar trends of storage properties.

ii) *Generation of open metal sites:* The porous MOFs having solvent coordinated metal centers can be used for generation of open metal sites. At first the coordinated solvents were exchanged by low boiling solvents like MeOH or EtOH and then these coordinated solvents removed by activation. Due to the unsatisfied coordination, the metal centers able to form a strong Vander-Waals interaction which leads to improve in  $H_2$  storage capacity. MOF-74 (Mg, Co, Ni, Zn) and HKUST-1 are the best examples which show efficient  $H_2$  uptake due to open metal sites.

iii) *Incorporation of functional groups:* The organic linkers in MOFs play an important role in  $H_2$  storage capacity. Experimentally and theoretically it has been proved that  $H_2$  adsorption depends on the numbers of aromatic rings present in the framework. Also the functional groups like  $-F$ ,  $-OH$ ,  $-COOH$ ,  $-NH_2$ , etc. have some affinity towards the adsorb  $H_2$ . Hence MOFs synthesized using the aforementioned functionalized linkers will have greater opportunity for  $H_2$  adsorption. The best example on this line are IRMOF-2, IRMOF-3 and IRMOF-18 having functionality  $-Br$ ,  $-NH_2$  and  $-CH_3$  groups respectively show improvement in  $H_2$  adsorption.

**Table 1.1:** Low pressure H<sub>2</sub> adsorption in Metal-Organic Frameworks at 77 K temperature and 1 atm pressure.

Name of MOFs	H <sub>2</sub> uptake (wt%)	Name of MOFs	H <sub>2</sub> uptake (wt%)
PCN-12 <sup>[1.19a]</sup>	3.05	MOC-2 <sup>[1.17h]</sup>	2.17
UTSA-20 <sup>[1.19b]</sup>	2.80	UMCM-150 <sup>[1.17i]</sup>	2.10
PCN-14 <sup>[1.19c]</sup>	2.70	Ni\DOBDC <sup>[1.17j]</sup>	2.10
NOTT-103 <sup>[1.19d]</sup>	2.56	Zn <sub>2</sub> (BDC)(TMBDC)(DABCO) <sup>[1.17k]</sup>	2.10
PCN-11 <sup>[1.19e]</sup>	2.55	Ni <sub>3</sub> (BTC) <sub>2</sub> (3-PIC) <sub>6</sub> (PD) <sub>3</sub> <sup>[1.18a]</sup>	2.10
HKUST-1 <sup>[1.7]</sup>	2.54	(In <sub>3</sub> O)(OH)(ADC) <sub>2</sub> (IN) <sub>2</sub> · 4.67H <sub>2</sub> O <sup>[1.19k]</sup>	2.08
Cu <sub>2</sub> (tptc) <sup>[1.19f]</sup>	2.52	Zn <sub>2</sub> (BDC) <sub>2</sub> (DABCO) <sup>[1.17k]</sup>	2.00
NOTT-100 <sup>[1.19d]</sup>	2.52	Mg\DOBDC <sup>[1.17j]</sup>	1.98
NOTT-140 <sup>[1.19g]</sup>	2.50	PCN-6 <sup>[1.18b]</sup>	1.90
MOF-505 <sup>[1.19h]</sup>	2.48	NOTT-116 <sup>[1.18c]</sup>	1.90
NOTT-101 <sup>[1.19d]</sup>	2.46	CPM-6 <sup>[1.18d]</sup>	1.88
NOTT-105 <sup>[1.19d]</sup>	2.46	PCN-68 <sup>[1.17c]</sup>	1.87
Cu <sub>4</sub> Cl(btt) <sub>3,8</sub> <sup>[1.19i]</sup>	2.42	Cd-ANIC-1 <sup>[1.18n]</sup>	1.84
Cu <sub>6</sub> O(tzi) <sub>3</sub> (NO <sub>3</sub> ) <sup>[1.19j]</sup>	2.40	Co\DOBDC <sup>[1.17j]</sup>	1.81
PCN-12 <sup>[1.19a]</sup>	2.40	IRMOF-3 <sup>[1.18e]</sup>	1.80
PCN-10 <sup>[1.19e]</sup>	2.34	PCN-66 <sup>[1.17c]</sup>	1.79
(In <sub>3</sub> O)(OH)(ADC) <sub>2</sub> (NH <sub>2</sub> IN) <sub>2</sub> · 2.67H <sub>2</sub> O <sup>[1.19k]</sup>	2.31	Zn <sub>2</sub> (C <sub>2</sub> O <sub>4</sub> )(C <sub>2</sub> N <sub>4</sub> H <sub>3</sub> ) <sub>2</sub> · (H <sub>2</sub> O) <sub>0.5</sub> <sup>[1.18f]</sup>	1.70
NU-100 <sup>[1.17a]</sup>	2.29	Co-ANIC-1 <sup>[1.18n]</sup>	1.64
NOTT-112 <sup>[1.17b]</sup>	2.30	[Co <sub>4</sub> (OH) <sub>2</sub> (p-CDC) <sub>3</sub> DMF <sub>2</sub> ] <sub>n</sub> <sup>[1.18g]</sup>	1.61
NOTT-109 <sup>[1.19d]</sup>	2.28	ZTF-1 <sup>[1.18h]</sup>	1.60
PCN-61 <sup>[1.17c]</sup>	2.25	CUK-1 <sup>[1.18i]</sup>	1.60
Mn-BTT <sup>[1.17d]</sup>	2.25	H <sub>3</sub> [(Cu <sub>4</sub> Cl) <sub>3</sub> -(BTTri) <sub>8</sub> ] <sup>[1.18j]</sup>	1.58
Cu <sub>2</sub> (qptc) <sup>[1.17e]</sup>	2.24	Zn\DOBDC <sup>[1.17j]</sup>	1.54
NOTT-106 <sup>[1.19d]</sup>	2.24	Bio-MOF-11 <sup>[1.18k]</sup>	1.50
NOTT-107 <sup>[1.19d]</sup>	2.21	ZIF-11 <sup>[1.18l]</sup>	1.37
[Zn <sub>2</sub> (1)(DMF) <sub>2</sub> ] <sub>n</sub> (DMF) <sub>m</sub> [MOF(4)] <sup>[1.17f]</sup>	2.20	MOF-5 <sup>[1.18m]</sup>	1.32
NOTT-102 <sup>[1.19d]</sup>	2.19	ZIF-8 <sup>[1.18l]</sup>	1.30
[Zn <sub>3</sub> (OH)(p-CDC) <sub>2.5</sub> (DEF) <sub>4</sub> ] <sup>[1.17g]</sup>	2.10	MOF-177 <sup>[1.18m]</sup>	1.25

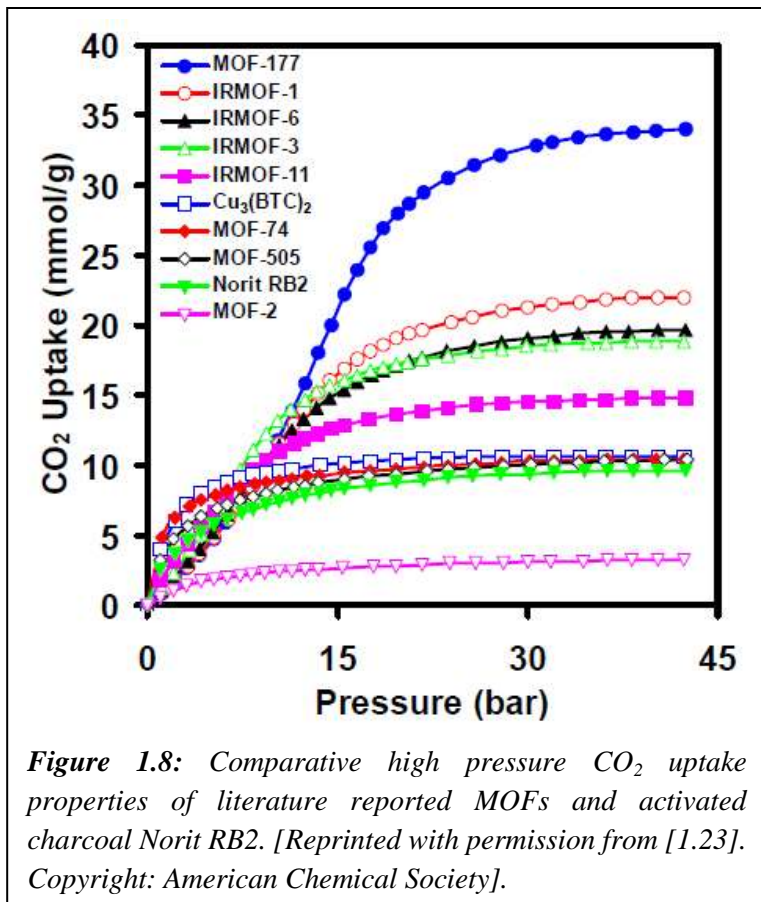
iv) *Interpenetration or catenation*: The ongoing studies on the H<sub>2</sub> uptake in MOFs have confirmed that smaller pores actually take up H<sub>2</sub> more effectively than very large ones [1.12]. Ideally, pore sizes ranging from 4 to 5 Å, which are comparable to the kinetic diameter of H<sub>2</sub> (~2.8 Å) seems to be ultimate for H<sub>2</sub> adsorption in porous MOFs [1.13]. Pores of this size allow the dihydrogen molecule to interact with multiple portions of the framework rather than just one SBU or organic linker, increasing the interaction energy between the framework and H<sub>2</sub> [1.14]. This increased interaction between adsorbing gas molecules and framework ingredients like SBU, linkers, etc. results into the improvement in isosteric heat (Q<sub>st</sub>) of H<sub>2</sub> adsorption giving high uptake at low pressure.

v) *Doping of metal nanoparticles and alkali metals in MOFs*: The doping of metal nanoparticles into the MOF matrix has been studied extensively for its various applications in catalysis, drug delivery and gas adsorption [1.15]. The phenomenon of H<sub>2</sub> adsorption in metal doped MOFs is also known as hydrogen spillover effect [1.16]. This hydrogen spillover effect has been known for a long time in the hydrogenation catalysts. It is defined as the dissociative chemisorptions of hydrogen on the metal and the subsequent migration of atomic hydrogen onto the surface of the support such as alumina, carbon, etc [1.16a]. The support can be considered as the primary receptor for atomic hydrogen. It has been suggested that hydrogen spillover will play a much larger role in terms of H<sub>2</sub> storage at ambient temperatures, which is the preferred temperature for practical applications. These materials are getting attentions of researches due to the probable applications of these materials for H<sub>2</sub> storage at ambient conditions.

#### **1.4.2 CO<sub>2</sub> storage in MOFs:**

The tremendous growth in global population and industrialization results in huge increase in energy consumption. All most 85% of global energy produced from burning of readily available natural fossil fuels which releases huge amount of CO<sub>2</sub> in atmosphere. Over the last half century the concentration of CO<sub>2</sub> in atmosphere changes from 310 ppm to over 390 ppm, which is highest steep ever in human history. The increasing level of atmospheric CO<sub>2</sub> is one of the greatest environmental concerns [1.20]. CO<sub>2</sub> is one of the major components of greenhouse gases which cause global warming. Also the excess amount of CO<sub>2</sub> can easily dissolve in sea water and converted to carbonic acid. So pH of

sea water drops down and make harm to aquatic lives. In these regards, despite of the sequestration pathway, carbon capture systems (CCS) must capture the CO<sub>2</sub> from flue gas in an efficient and reversible fashion. Although utilization of alkanolamines and aqueous ammonia-based liquids for CO<sub>2</sub> capture is well settled on the industrial and domestic levels, the difficulties due to regeneration of these CCS brings the limitations



for their usages [1.21]. Also, solid porous adsorbent materials like zeolites, porous alumina, porous silica and activated charcoals or carbons has been used for selective capture of CO<sub>2</sub> from flue gases, but their amorphous structures, with limited stability in environmental conditions restricts their uses on industrial scale [1.22]. From an applications point of view, their extraordinary surface areas, finely tunable pore surface properties and potential scalability to industrial scale have made MOF materials an attractive target for CO<sub>2</sub> capture systems (**Figure 1.8**) [1.23]. Highly crystalline structures with predictable topologies, tunable pore sizes, and functionalizable pores with functional groups incorporated *via* linkers or post-synthetic modification makes MOFs as eligible materials for highly efficient CO<sub>2</sub> capture systems.

The high CO<sub>2</sub> uptake in interpenetrated MOFs than that of its non-interpenetrated analogues has been achieved [1.24a]. Since, it has been observed that MOFs possessing open metal sites enhances the performance by providing a mechanism for the separation of polar/non polar gas pairs such as CO<sub>2</sub>/CH<sub>4</sub>; synthesis of MOFs having open metal sites

**Table 1.2:** Low pressure CO<sub>2</sub> adsorption capacities for Metal-Organic Frameworks at 273 and 298 K temperature and 1 atm pressure.

Name of MOF	CO <sub>2</sub> uptake (mmol/g)		Name of MOF	CO <sub>2</sub> uptake (mmol/g)	
	273K	298K		273K	298K
Mg\DOBDc <sup>[1.16j]</sup>	NA	8.08	MOF-505 <sup>[1.18h]</sup>	NA	3.27
Co\DOBDc <sup>[1.16j]</sup>	NA	7.11	H <sub>3</sub> [(Cu <sub>4</sub> Cl) <sub>3</sub> - (BTTri) <sub>8</sub> ] <sup>[1.17j]</sup>	NA	3.25
Ni\DOBDc <sup>[1.16j]</sup>	NA	5.80	(In <sub>3</sub> O)(OH)(ADC) <sub>2</sub> ( NH <sub>2</sub> IN) <sub>2</sub> . 2.67 H <sub>2</sub> O <sup>[1.18k]</sup>	NA	3.21
Zn\DOBDc <sup>[1.16j]</sup>	NA	5.51	CPM-6 <sup>[1.17d]</sup>	4.76	2.90
UTSA-20 <sup>[1.18b]</sup>	NA	5.01	TMA@ Bio-MOF- 1 <sup>[1.25f]</sup>	4.5	NA
HKUST-1 <sup>[1.9c]</sup>	NA	4.72	TEA@ Bio-MOF- 1 <sup>[1.25f]</sup>	4.2	NA
Zn + 4,4' bipy + (BTA-TBA) <sup>[1.25a]</sup>	NA	4.10	TBA@ Bio-MOF- 1 <sup>[1.25f]</sup>	3.5	NA
Bio-MOF-11 <sup>[1.17k]</sup>	6.0	4.01	UMCM-150 <sup>[1.16i]</sup>	NA	2.80
[Zn <sub>2</sub> (1)(DMF) <sub>2</sub> ] <sub>n</sub> (DM F) <sub>m</sub> [MOF(4)] <sup>[1.25b]</sup>	5.80	NA	Zn <sub>2</sub> (BDC) <sub>2</sub> (DABCO) <sup>[1.16k]</sup>	NA	2.71
[Zn <sub>3</sub> (OH)(p- CDC) <sub>2.5</sub> ] <sub>n</sub> <sup>[1.25c]</sup>	NA	4.00	CPM-5 <sup>[1.17d]</sup>	3.62	2.43
Cd-ANIC-1 <sup>[1.17n]</sup>	4.72	3.84	ZIF-78 <sup>[1.25g]</sup>	3.348	2.23
ZTF-1 <sup>[1.17h]</sup>	5.35	3.79	ZIF-96 <sup>[1.25h]</sup>	NA	2.16
Zn <sub>2</sub> (C <sub>2</sub> O <sub>4</sub> )(C <sub>2</sub> N <sub>4</sub> H <sub>3</sub> ) <sub>2</sub> .( H <sub>2</sub> O) <sub>0.5</sub> <sup>[1.17f]</sup>	4.30	3.78	IRMOF-3 <sup>[1.17e]</sup>	NA	2.14
Co-ANIC-1 <sup>[1.17n]</sup>	4.22	3.48	(In <sub>3</sub> O)(OH)(ADC) <sub>2</sub> (I N) <sub>2</sub> . 4.67 H <sub>2</sub> O <sup>[1.18k]</sup>	NA	2.08
CUK-1 <sup>[1.17i]</sup>	NA	3.48	MOF-177 <sup>[1.17m]</sup>	NA	1.72
YO-MOF <sup>[1.25d]</sup>	NA	3.39	ZIF-69 <sup>[1.25g]</sup>	3.03	1.69
SNU-M10 <sup>[1.25e]</sup>	NA	3.30	MOF-5 <sup>[1.17m]</sup>	NA	0.92

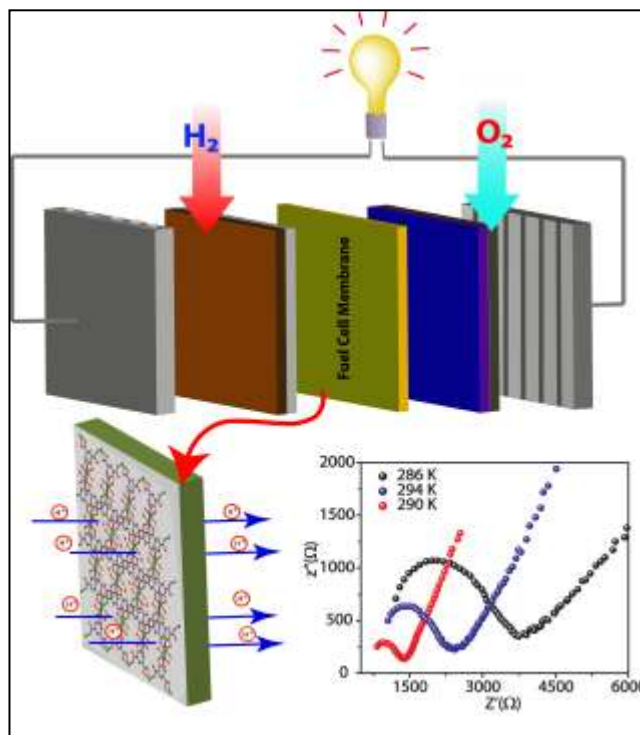
has been reported vastly in the literature [1.24b,c]. For example, in HKUST-1 high CO<sub>2</sub> uptake has been achieved as a result of open metal sites [1.24d]; whereas in the case of Mg-MOF-74, as a result of open metal Mg-sites high CO<sub>2</sub> uptake and separation of CO<sub>2</sub> from flue gases has been achieved [1.24e]. The selective adsorption mechanism may occur due to the coordination of CO<sub>2</sub> to the metal center in an end-on fashion, i.e. O=C=O...Metal centre. The MOFs having free functional groups, i.e. surface functionalized frameworks enhances the capacity and selectivity of MOFs for CO<sub>2</sub> adsorption by grafting a functional group with a high affinity for CO<sub>2</sub> (e.g. amine, arylamine, alkylamine, hydroxyl groups, etc.). These functional groups enhance the selective interaction between CO<sub>2</sub> and the functionalized molecule as well as the constriction in the pore space of functionalized framework compared to the parent non-functionalized material. The high CO<sub>2</sub> uptake observed in Bio-MOF-11 and ZTF-1 are the examples of high CO<sub>2</sub> uptake in functionalized MOFs [1.17h,k,n]. The utilization of porous materials with highly electronegative functionalities like -F, -CF<sub>3</sub> etc. having optimal adsorption thermodynamics and kinetics for CO<sub>2</sub> separation at room temperature has been successfully achieved [1.24f].

As discussed earlier, although materials with high CO<sub>2</sub> uptake capacities are important for various applications, the necessity of another kind of porous substances which can selectively adsorb CO<sub>2</sub> from mixture of gases are very important for industrial applications. The preferential uptake of CO<sub>2</sub> from mixture of gases like N<sub>2</sub>, CO, H<sub>2</sub>, CH<sub>4</sub>, etc. is desired to separate the harmful gases from others in order to avoid the environmental issues. In these regards, MOFs with open metal sites, functional groups are mostly used as these MOFs adsorb the CO<sub>2</sub> very strongly over other gases due to high affinity. The successful utilization of several MOFs like SIFSIX-2-Cu, SIFSIX-2-Cu-I, SIFSIX-3-Zn, Mg-dobdc, IRMOFs, ZIFs, etc. having functional groups or open metal sites is successfully achieved [1.24]. The higher separation factor desired in porous materials has been successfully acquired in Mg-MOF-74, due to CO<sub>2</sub> adsorption over large temperature range as shown in [1.24e].

### 1.5 Proton transport in MOFs:

The extensive use of fossil fuel as an energy source for rapidly growing industry and population shows a big question mark on availability of this natural source in near future

[1.26]. Hence, there are growing pressures to progress from a fossil fuel based economy to an alternative renewable energy economy [1.27]. Fuel cell technology is one of the promising alternatives of fossil fuel technology. In the hydrogen fuel cells,  $H_2$  has been as the source of proton. The basic setup of fuel cell consist a negative side anode which withdraw electron from hydrogen to produce proton (**Figure 1.9**). These electrons then flow through the external circuit to reach cathode by producing direct current. On the other hand, the protons generated in



**Figure 1.9:** Model representation of proton exchange membrane fuel cell (PEMFCs).

anode pass through a proton conducting membrane to reach cathode. On cathode, protons react with supplied oxygen to produced heat and water. Thus the chemical energy of  $H_2$  converted to electrical energy. The heart of fuel cell is the proton conduction process. Till date most explored proton conducting materials are polymers like nafion and polybenzamidazole. These polymer membranes have high proton conducting performance, but they have some disadvantages such as i) only work in presence of moisture (water), ii) efficiency goes down at high temperature ( $> 80\text{ }^\circ\text{C}$ ), iii) high cost to use in large scale for any technology. In these circumstances researchers are giving huge attention to develop some cheap and efficient alternative proton conducting materials. Last few years, researchers have explore some proton conducting materials in addition with polymers like oxo acids, metal oxides or hydroxides, inorganic- organic hybrid materials, etc. Porous solids such as mesoporous silica, organic porous solids, metal-organic frameworks (MOFs) have also been used as possible proton conducting materials. Now days the modern electronic devices like laptop, and cellular phones required fuel cells which have higher proton conductivity ( $> 0.1\text{ S/cm}$ ) and operating

temperature range 25 to 300 °C. Porous solids like MOF could be most promising materials to fulfill these requirements.

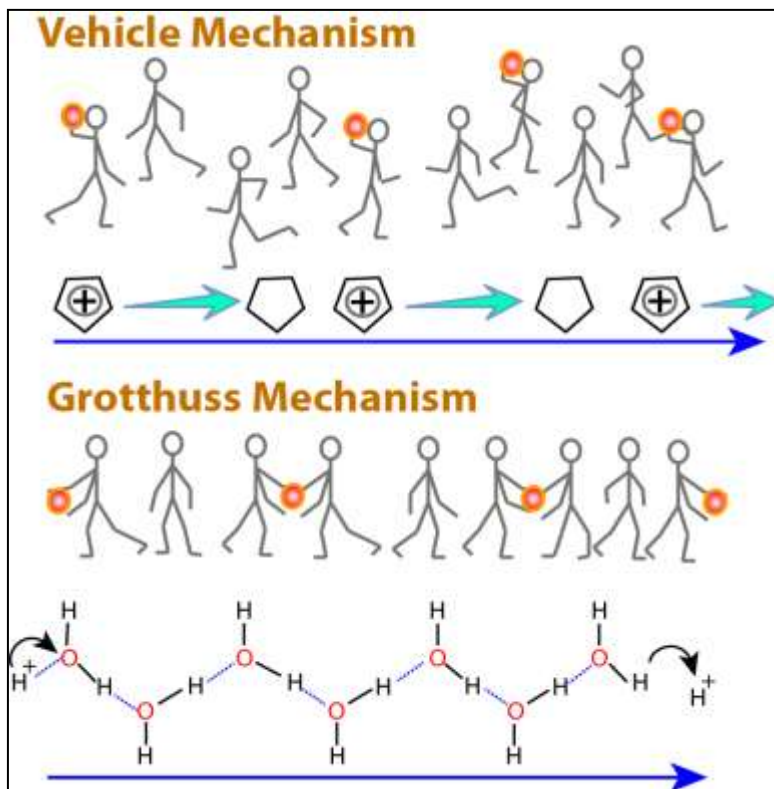
During last few years metal-organic frameworks (MOFs), have been utilized as efficient proton conductors due to their permanent porosity, thermal stability which could be exploited for the development of proton-conducting membranes. Generally, two types of proton conductivity mechanisms have been

sought in MOFs (1) Grotthuss mechanism (2) Vehicle mechanism (**Figure 1.10**) [1.28, 3.8].

In Grotthuss mechanism proton transport occurs through the hydrogen bonded H<sub>2</sub>O molecule chain along the MOF channels. The overall mechanism performs well under hydrous condition as well as at lower temperature (< 80 °C). On the other hand, vehicle mechanism occurs by the movement of guest molecules (imidazole, triazole etc.) through the MOF architecture to conduct protons (**Figure 1.10**). Based on the above discussion the proton conductivity in MOFs is divided mainly in two ways (a) water mediated (hydrous) proton conductivity [1.29] (b) Anhydrous proton conductivity [1.30].

### 1.5.1 Challenges of proton conductivity in MOFs:

There are some challenges and opportunity in designing MOFs as proton conducting materials which are discussed here.



**Figure 1.10:** a) Vehicle proton hopping mechanism through the network. The arrow indicates the movement of protons. b) Mechanism of Grotthuss proton hopping through the H bonded network of water.



- i) In general MOFs are unstable in humidified condition. In presence of water MOF framework get deconstructed to form metal oxides or hydroxides. However, few selected metal clusters linked by carboxylate moieties [e.g.  $\text{Cr}_3\text{O}(\text{COO})_6\text{F}/\text{OH}$ ,  $\text{Zr}_6\text{O}_4(\text{OH})_4(\text{COO})_6$ ] proved to be effective in tolerating water even at higher temperatures.
- ii) The inherent porosity inside MOF framework can provide fuel cell crossover problem in PEMFCs. This problem can be minimized by filling up these pores with water or proton conducting molecules. Otherwise incorporation of proton conducting functional groups inside pore walls can also help to overcome this problem.
- iii) MOFs are highly crystalline or microcrystalline powder which creates grain boundary problem during palate making. Due to the presence of grain boundary the materials show lower proton conduction performances. This problem can be minimized by using MOF-polymer composite membranes where polymer will be act as binding agent to reduced grain boundary.

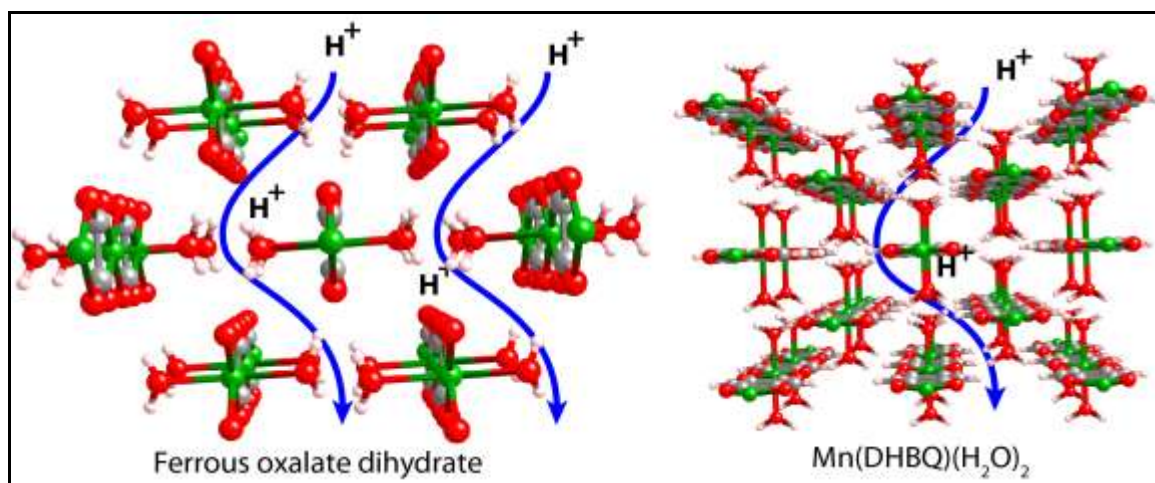
### **1.5.2 Water assisted proton conductivity in MOF:**

Humidified condition is required for hydrous proton conduction process in case MOF based materials. The incoming water molecules, as well as trapped water (solvent of crystallization) form a water channel inside the MOF pores. The proton produced from water by electrical potential stimuli. These protons conduct through the hydrogen bonded water channels at low activation energy ( $< 0.4$  eV) and low temperature (below  $100$  °C). This is the typical characteristics of Grotthouss proton conduction mechanism pathway. Proton conduction in MOFs in humidified condition can be categorised in two primary sections based on the framework nature, conduction pathway and proton carrier molecules. a) Inherent water assisted proton conduction and b) Framework ion induced proton conduction.

#### **1.5.2.1 Inherent Water assisted proton conduction:**

The inherent water assisted proton conduction happens due to the presence of water molecules inside the MOF pores. Two types of water can be present inside the MOF pores, a) water molecules coordinated to the metal centre of the MOF moieties or b) water molecules trapped inside the pore of MOF structure. Bothe the cases proton

conduction phenomena enhances in humidified conditions. Proton conducting ability have been investigated on 1-dimensional chain systems based MOFs with oxalate bridging moieties [1.29c]. The first system examined was ferrous oxalate dihydrate which consists of octahedral  $\text{Fe}^{2+}$  metal centres linked with bidentate oxalate ligands and axially coordinated water molecules to form one-dimensional (1D) chain polymer (**Figure 1.11**). The proton conductivity showed by this material is  $1.3 \times 10^{-3} \text{ Scm}^{-1}$  at 25 °C under 98% RH with activation energy of 0.37 eV. Lewis acidic ferrous ion ( $\text{Fe}^{2+}$ ) have tendency to subtract proton from coordinated water molecules. Hence, periodic arrangement of coordinated water molecules have been built inside the structure to facilitate the pathway for proton hopping under hydrous environment that could be the possible reason for high proton conduction. Similar kind of study also been performed on 2,5-dihydroxy- 1,4-benzoquinone (Dhbq) [structurally modified from oxalate] based coordination polymers [1.29h and i] with various divalent metal centre (Co, Mg, Mn, Ni and Zn) (**Figure 1.11**) . However, the proton conductivity of these materials are low [ $4 \times 10^{-5} \text{ Scm}^{-1}$ ] in hydrous condition. Both ferrous oxalate and Dhbq based MOF do not show proton conductivity in



**Figure 1.11:** Inherent Water assisted proton conduction in a) ferrous oxalate dihydrate and b) Mn-dihydroxybenzoquinone MOF  $\{\text{Mn}(\text{DHBQ})(\text{H}_2\text{O})_2\}$ .

absence of coordinated water molecules which indicate that the coordinated water molecules play an important role for high proton conduction at humidified condition.

Proton conductivity studies also have been investigated on MOFs where water molecules are trapped inside the void spaces of MOF architecture. A phosphonate-based

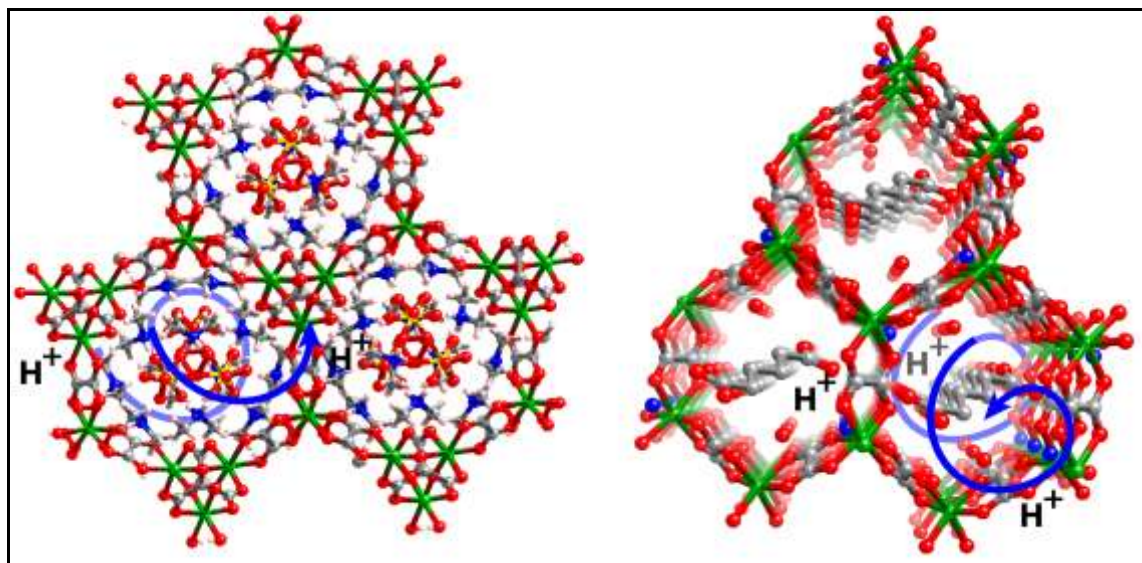
two dimensional coordination polymer has been reported [1.29b] for hydrous proton conduction. The MOF ( $Zn_3Btp/PCMOF3$ ) has been synthesized from the 1,3,5 benzenetriphosphonate with  $Zn(NO_3)_2$  under hydrothermal condition. The framework has been assembled in 2D layer fashion where each layer is stacked through alternating sets of zinc metal centres layers. Water molecules reside in order fashion among the layers and create strong hydrogen bonded network which promotes the proton conduction pathway. PCMOF3 showcased decent proton conductivity value  $3.5 \times 10^{-5} \text{ Scm}^{-1}$  at 25 °C and 98% RH. However, under anhydrous condition the conductivity is extremely low which indicates that PCMOF3 is highly humidity-dependent proton conducting material. Along the same line, another report in 2012, where a phosphonate based MOF (PCMOF3) can perform better proton conduction than previous analogue (PCMOF2). The structure of PCMOF2 [trisodium salt of 2,4,6-trihydroxy-1,3,5-benzenetrisulfonate (L1)] contains pores lined with sulfonate oxygen atoms and exhibit poor proton conducting efficiency. In order to improve the proton conductivity in PCMOF2 structure, replacement of the (L1) linkers with 1,3,5 benzenetriphosphonate (L2) linkers by keeping the hybrid nature of both PCMOF2 and PCMOF3 [1.29j]. The resulting material named as PCMOF2<sup>1/2</sup> has very high proton conductivity  $2.1 \times 10^{-2} \text{ Scm}^{-1}$  at 90% RH and 85 °C. The PCMOF2<sup>1/2</sup> also showed highly humidity dependent proton conductivity. At 50% RH, the conductivity of PCMOF2<sup>1/2</sup> decreases to  $2.4 \times 10^{-5} \text{ Scm}^{-1}$ . The activation energy ( $E_a$ ) measured 0.21 eV, is indicative of Grotthuss hopping mechanism for high proton conduction.

Similar kind of water channel resides in close proximity inside the MOF void space has been examined for hydrous proton conduction. A series of MOF isomers,  $[Zn(l-LCl)(Cl)](H_2O)_2$  (**1**),  $[Zn(l-LBr)(Br)](H_2O)_2$  (**2**)  $[Zn(d-LCl)(Cl)](H_2O)_2$  (**3**), and  $[Zn(d-LBr)(Br)](H_2O)_2$  (**4**) with unprecedented *unh* topology was reported [1.30k]. All these MOFs contain helical water chains inside the structure, have explored for proton conduction. **1** and **3** have continuous water chains which promotes proton conduction ( $4.45 \times 10^{-5}$  and  $4.42 \times 10^{-5} \text{ Scm}^{-1}$  respectively at ambient temperature under 98% RH) through the channels. On the other hand, **2** and **4** do not show any conductivity due to absence of discrete water assembly inside the cavity, confirmed by VT-SCXRD experiments. Sometimes two different solvents occupied the void spaces of MOF

architectures also play the role for hydrous proton conduction. A report of a three dimensional MOF [ $\{(Zn_{0.25})_8(O)\}Zn_6(L)_{12}(H_2O)_{29}(DMF)_{69}(NO_3)_2\}_n$ ] has been synthesized from 1,3 bis (4carboxy phenyl) imidazolium and  $Zn_8O$  clusters [1.30i]. The inner cavities of this framework are occupied by the large numbers of DMF and water molecules. The imidazolium groups of the organic linkers aligned in the channels and interact with DMF and water to facilitate the hydrous proton conductivity. The proton conductivity increases with an increase of humidity and reaches  $2.3 \times 10^{-3} \text{ Scm}^{-1}$ .

### 1.5.1.2 Ion assisted proton conduction:

There are several MOFs reported where metal coordination creates anionic framework. Hence, to neutralize the anionic framework various cationic molecules [ $NH_4^+$ ,  $(CH_3)_2NH_2^+$ ,  $(C_2H_5)_2NH_2^+$  etc.] gets trapped inside the framework. It has been observed that, cation trapped MOFs could be used as proton transfer sites and can initiate the conduction process under hydrous condition. Such kind of cationic MOFs also have been examined for proton conduction. There is a report in 2009, [1.29e] where zinc oxalate based framework  $(NH_4)_2(adp)-[Zn_2(ox)_3] \cdot 3H_2O$ , consist ammonium cations, water molecules and adipic acids (adp) inside the interlayer spaces of 2D network (**Figure**



**Figure 1.12:** Ion assisted proton conduction in a) Zn-oxalate based 2D MOF and b)  $(NH_4)_2(adp)-[Zn_2(ox)_3] \cdot 3H_2O$ .

1.12). The proton conductivity of this MOF was found to be  $8 \times 10^{-3} \text{ Scm}^{-1}$  at  $25^\circ \text{C}$  under 98% RH, which is comparable to the proton conductivity of nafion. The higher

proton conductivity at hydrous condition is due to the extended hydrogen-bonded network that is generated from the strong hydrogen bonding between ammonium cations, adipic acids and water molecules inside the 2D architecture. The proton conductivity of similar kind oxalate-bridged bimetallic complexes  $\text{NH}(\text{proI})_3 \{ [\text{M}^{\text{II}}\text{Cr}^{\text{III}}(\text{ox})_3] \}$  ( $\text{M}^{\text{II}} = \text{Mn}^{\text{II}}, \text{Fe}^{\text{II}}, \text{Co}^{\text{II}}$ ) also have been examined, [1.29n] where the hydrophilic tri(3-hydroxy propyl) ammonium  $[\text{NH}(\text{proI})_3^+]$  cations inside the crystal structure promote hydrous proton conductivity. They reveal lower proton conductivity ( $\sim 1 \times 10^{-4} \text{ Scm}^{-1}$ ) and show performance only under the humidified condition only. The proton conductivities of the complexes significantly decrease to  $4.4 \times 10^{-10} \text{ Scm}^{-1}$  under 40% RH. Proton conduction of related bimetallic oxalate-based MOFs  $[\text{N}(\text{R})_3(\text{CH}_2\text{COOH})][\text{FeCr}(\text{ox})_3]$  also have been investigated [1.29q] replacing  $\text{NH}(\text{proI})_3$  cations by  $\text{N}(\text{R})_3(\text{CH}_2\text{COOH})$  cations where  $\text{R} = \text{Me}$  (methyl),  $\text{Et}$  (ethyl) or  $\text{Bu}$  (n-butyl). Since, the cationic component consist

**Table 1.3:** Proton-conducting MOFs under hydrous condition reported in literature.

SL.No	MOFs and CPs	Proton conductivity ( $\text{Scm}^{-1}$ )	Ea (eV)	Conditions	Reference
1	$(\text{NH}_4)_2(\text{adp})[\text{Zn}_2(\text{ox})_3] \cdot 3\text{H}_2\text{O}$	$8 \times 10^{-3}$	0.63	25 °C and 98% RH	1.29e
2	1D Ferrous Oxalate Dihydrate	$1.3 \times 10^{-3}$	0.37	25 °C and 98% RH	1.29c
3	$(\text{NH}_4)_4[\text{MnCr}_2(\text{ox})_6]_3 \cdot 4\text{H}_2\text{O}$	$1.1 \times 10^{-3}$	0.23	25 °C and 98% RH	1.29o
4	Cucurbit[6]uril (CB[6])	$1.1 \times 10^{-3}$	0.39	25 °C and 98% RH	1.29d
6	$\{\beta\text{-PCMOF2}(\text{Tz})_{0.45}\}$	$5 \times 10^{-4}$	0.51	150 °C	1.29b
7	$\text{Mg}_2(\text{dobdc})_3 \cdot 0.35\text{LiO}i\text{Pr}_3 \cdot 0.25\text{LiBF}_4 \cdot \text{EC}3 \cdot \text{DEC}$	$3.1 \times 10^{-4}$	0.14	27 °C	1.29p
8	$\{\text{NH}(\text{proI})_3\}[\text{MII}(\text{ox})_3]$ (MII) = MnII, FeII, CoII	$1 \times 10^{-4}$		25 °C and 75% RH	1.29n
9	$(\text{H}_3\text{C}_2)_2(\text{dtoa}) \text{Cu}$	$1 \times 10^{-4}$		25 °C and 80% RH	1.29i
11	$[\text{Zn}(\text{l-L}_\text{Cl})(\text{Cl})](\text{H}_2\text{O})_2$	$4.45 \times 10^{-5}$	0.34	28 °C and 98% RH	1.29l
12	PCMOF-3	$3.5 \times 10^{-5}$	0.17	25 °C and 98% RH	1.29b
13	$[\text{M IL-53}(\text{Fe})-(\text{COOH})_2]$	$2.0 \times 10^{-6}$	0.21	25 °C and 98% RH	1.29a

carboxyl group that will be fruitful for proton carrier under hydrous condition. The hydrophilicity of the cationic ion was tuned by the  $\text{NR}_3$  residue. Generally, hydrophilicity

decreases with increasing the size of the R group of the residue:  $[\text{NMe}_3(\text{CH}_2\text{COOH})]^+ > [\text{NEt}_3(\text{CH}_2\text{COOH})]^+ > [\text{NBu}_3(\text{CH}_2\text{COOH})]^+$ . The hydrophilicity of  $[\text{N}(\text{Me})_3(\text{CH}_2\text{COOH})][\text{FeCr}(\text{ox})_3]$  is very high compare to others which is reflected in high water vapour adsorption as well as high proton conductivity of  $\sim 10^{-4} \text{ Scm}^{-1}$  under 65% relative humidity (RH).

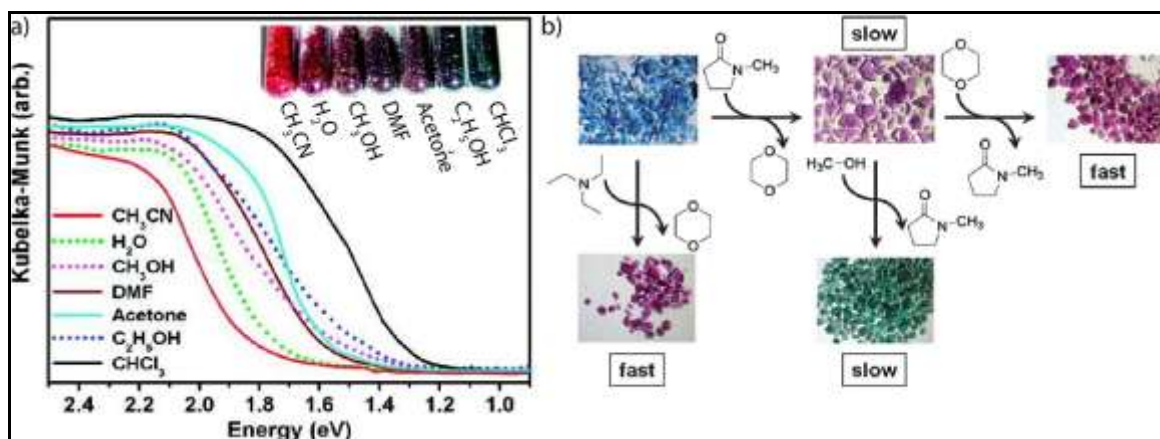
### 1.6 MOF as chemical sensor:

Conversion of chemical information of a molecule into detectable and analyzable signals is defined as chemical sensing. A huge range of sensor materials, starting from very small molecules to large polymeric materials, have been used for chemical sensing. The sensor materials generally interact or react with analyte molecules and produce some response in terms of mechanical, photophysical or electrical signals. Chemo sensors are essential for range of applications including chemical threat detection, medical diagnostics, food quality control, occupational safety, environmental monitoring and industrial process management. MOFs can be applied as an important candidate for sensor materials due to its tunable properties and structure [1.31]. For device application needs thig thermally and chemically stable materials. MOFs are advantageous on this respect, because it has high thermal stability ( $> 350 \text{ }^\circ\text{C}$ ) and some of the MOFs are chemically stable also. MOFs can be easily designed according to the desire properties for particular applications. Since MOFs have uniform and definite pore size, it can allow size selective sensing. Depending on the techniques or mechanism of sensing process the chemo sensors can be classified as-

#### 1.6.1 Solvatochromic or vapochromic sensor:

This is the simplest process of detection, where the detection can be recognize by visible color change of the sensor materials. Solvatochromism happens due to the large shift in the absorption spectra of the materials in presence of different polarity of solvents. The difference in polarity of the solvent, changes the dipole moment of the excited electronic state of the chromophoric component of the material. If the excited state features a larger dipole moment than the ground state, it is preferentially stabilized by polar solvents, and bathochromic shifts (red shifts) are observed with increasing solvent polarity. Conversely, if the ground state has the larger dipole moment, hypsochromic shifts (blue shifts) occur with increasing solvent polarity. For a chromophore containing MOF,

sorption of vapor is the equivalent of solvating a molecular absorber, and vapo-chromic trends should match solvatochromic ones. As an example, Lu et al. synthesized a copper MOF containing the ligand 3,6-di(pyridin-4-yl)-1,2,4,5-tetrazine (dptz), which shows solvatochromic behavior when immersed in solvents ranging in polarity from water to chloroform (**Figure 1.13a**) [1.32]. Overall, the material shows a negative solvatochromic effect with the absorption band blue-shifting with increasing solvent polarity.



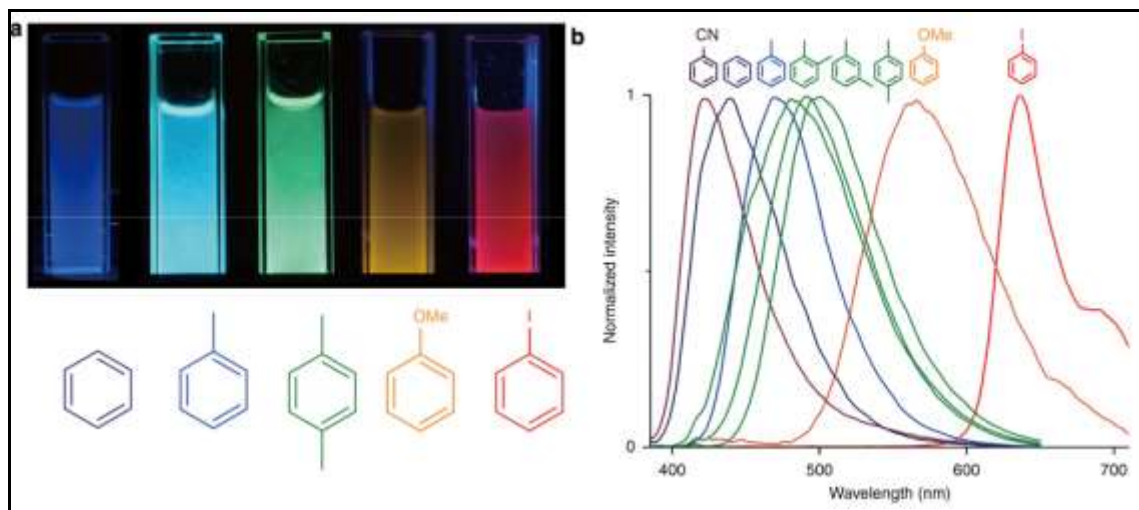
**Figure 1.13:** a) Visible spectra and photograph of MOF crystals containing solvents (condensed vapors). A negative vapo-chromic effect is observed for both hydroxylic and nonhydroxylic vapors (solvents). Reprinted with permission from ref. [1.31]. Copyright: American Chemical Society. b) Illustration of the color changes of Nile Blue@DUT-25 crystals by use of basic or acidic solvents. Reprinted with permission from ref [1.32]. Copyright: Wiley-VCH.

Two distinct groupings were observed, one for hydroxylic and one for nonhydroxylic solvents, when the measured band gaps were plotted versus solvent polarity. An appropriate example of Vapo-chromic MOFs reported by Lee and coworkers, where Co(II) nodes coordinated to 1,2,4,5-tetra(2H-tetrazole-5-yl)-benzene (TTB) (**Figure 1.13b**) [1.33]. This red colored MOF can sense chloride ions derived from chlorine-containing vapors or gases. Interestingly, when the MOF was exposed to chlorine-containing gases, including HCl, SOCl<sub>2</sub>, (COCl)<sub>2</sub>, and COCl<sub>2</sub> (phosgene), its color changes from red to blue.

### 1.6.2 Luminescence based MOF sensors:

The most widely used MOF sensors are based on the photo luminescence properties. Luminescence properties can be studied using fluorescence spectroscopy, which is very well explored technique. In MOF based materials, the analytes come contact with

fluorescence centers present in pores and interact or react to produce signals in terms of enhancement or quenching of the fluorescence intensity and also by shifting of emission maxima. Luminescent MOFs are also works in three ways such as i) luminescent organic linker based MOFs, ii) luminescent metal based MOFs and iii) MOFs incorporated with luminescent guest. Among these three types linker based MOFs are most effective, because analytes can easily interact with linkers present on the MOF pores rather than core metal centers. The appropriate example will be The chemosensory material,  $Zn_2(bdc)_2(dpNDI)$  ( $bdc = 1,4\text{-benzenedicarboxylate}$ ;  $dpNDI = N,N\text{-di}(4\text{-pyridyl})\text{-}1,4,5,8\text{-naphthalenediimide}$ ) reported by Kitagawa and coworkers [1.34]. NDI is well known to generate exciplex emission when interacting with aromatic molecules in solution, and these phenomena are transferred to the MOF structure. Different pure aromatic substituents are soaked in  $Zn_2(bdc)_2(dpNDI)$  MOF. The analytes include benzonitrile, toluene, benzene, anisole, iodobenzene, and xylenes. In all cases it was observed that a new broad absorption peak popped up between 420 and 500 nm, indicating a ground-state charge transfer (CT) interaction between NDI and the guest (**Figure 1.14**). The exceptional behavior observed



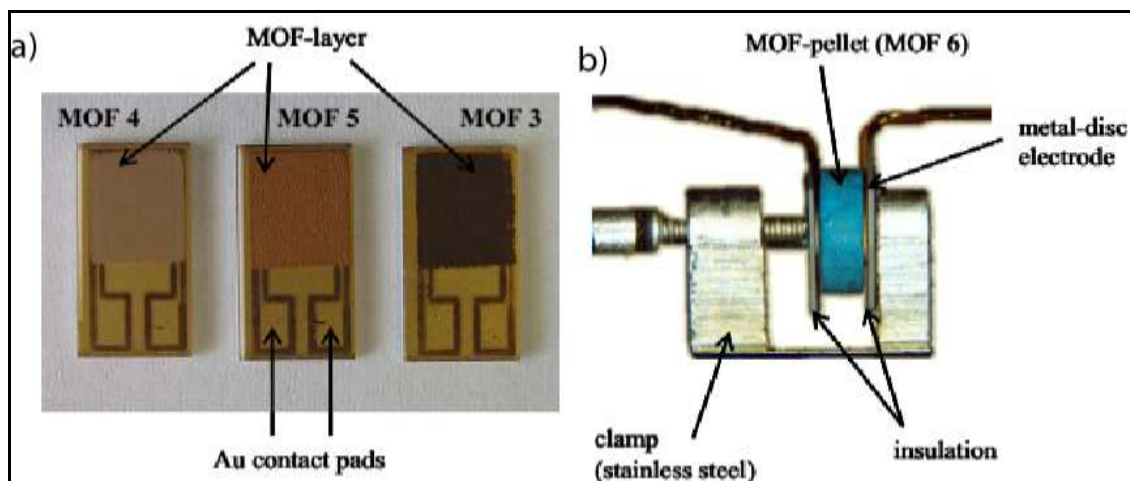
**Figure 1.14:** a) MOF powders suspended in organic liquid indicated, under 365 nm irradiation. b) Height-normalized luminescent spectra of guest-containing MOFs upon excitation at 370 nm. Reprinted with permission from ref [1.33]. Copyright: Nature Publishing Group.

for benzonitrile. Each analyte also exhibited exciplex emission, but at different wavelengths. The emission systematically shifted to longer wavelength with increasing electron-donating capability of the analyte.



### 1.6.3 Sensor based on Impedance Spectroscopy:

Electrochemical sensors are also important for quantitative and high performance sensing. The electrochemical signals produced in presence of analytes can be measured by impedance spectroscopy. MOF based electrochemical sensors generally works due to the conduction of electrons, protons or ions through the MOF pores. The analyte



**Figure 1.15:** a) MOF films deposited on interdigital electrodes. b) MOF pellet pressed between gold disk electrodes. Reprinted with permission from ref [1.35]. Copyright: MDPI AG.

concentration can be measured from the change in the conductivity values. Mainly gases like CO<sub>2</sub>, NO, O<sub>2</sub>, H<sub>2</sub> and etc can be quantitatively sensed using this type of MOF sensors (Figure 1.15) [1.35].

### 1.6.4 Interferometric MOF sensors:

Other optical methods that have been used for sensing differ from luminescence and solvatochromic measurements in that they do not involve absorption or emission of light by the MOF. Instead, they measure the MOF refractive index (RI), a bulk property (i.e., composite, volume-weighted property of vacuum (RI = 1), empty framework, and adsorbed guest) that changes depending on the amount and RI of the guest.

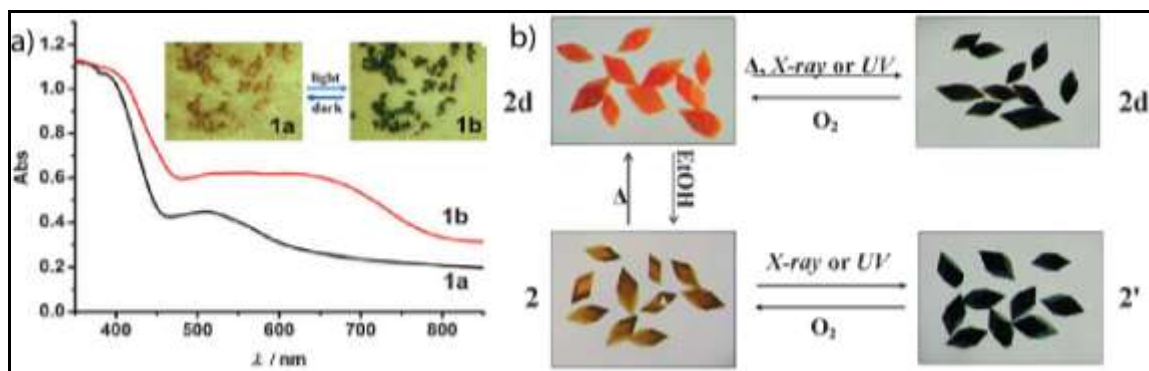
### 1.6.5 Surface plasmon resonance based MOF sensors:

Like interferometry, surface plasmon resonance spectroscopy indirectly detects analytes by measuring changes in MOF RI. When small silver, gold, or copper nanoparticles are irradiated with white light, the conduction band electrons oscillate coherently, a phenomenon known as localized surface Plasmon resonance (LSPR) [1.36]. The

frequency of this resonance depends on the RI of the medium surrounding the particles, and changes in this RI can be detected as shifts in the visible extinction spectrum via LSPR spectroscopy. Kreno and co-workers exploited this RI sensitivity to sense sorption of guests inside of a MOF grown on the surface of plasmonic nanoparticles.

### 1.6.6 Photochromic MOF sensors:

Other than molecules MOF can also applied for sensing of different electromagnetic waves like X-ray, Uv light, visible light, etc. In this thesis we also describe the some photochromic properties of MOFs. In literature very few light sensing MOFs are reported. Zuo and coworkers reported [1.37] a reversible photochromic MOF using Ca(II) as metal source and NDI based organic linker as chromophoric unit. These materials (as synthesized) are yellow in color and by shining with sunlight it converts to dark green crystals. The green crystals again go back to original state after keeping it into dark for 2 days (**Figure 1.16a**). Gong and coworkers reported [1.38] a photochromic and thermochromic MOF using Cd(II) and triphenyltricarboxylic acid (TTCA). Methyl viologen cations were loaded into the MOF to get the photochromic material. The as synthesized



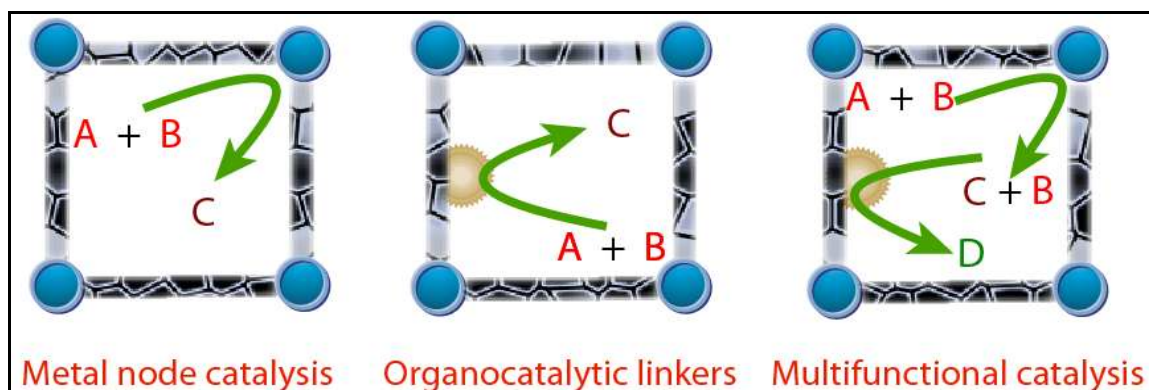
**Figure 1.16:** a) NDI chromophore containing Ca-MOF showed reversible photochromism in visible light. b) Methyl viologen cations were loaded MOF showed thermochromic and photochromic properties. Copyright: Royal Society of Chemistry.

orange colored material converted into dark on shining with X-ray or UV light. The dark crystals go back to original state in presence of oxygen gas (**Figure 1.16b**).

### 1.7 Catalysis in MOFs:

MOFs can be used as porous heterogeneous catalyst for lots of organic reactions. In industrial applications zeolites are used as porous heterogeneous catalyst. But MOFs are

more advantageous over Zeolites in terms of chemical stability, tunable porosity and design functionality according to desired catalytic property. Also MOF catalyst are cheap, green and have high recycle numbers. The high surface areas, uniform pore size and high density of active sites within the open structures of MOFs offer their use in catalysis [1.39]. The first MOF based catalysis was reported by Fujita and coworkers in 1994. A 2D MOF synthesized from  $\text{Cd}^{2+}$  and 4,4'-bipyridine, was used for shape and size selective clathration of aromatic guests[1.40]. In 2000 Kim and coworkers first reported [1.41] asymmetric

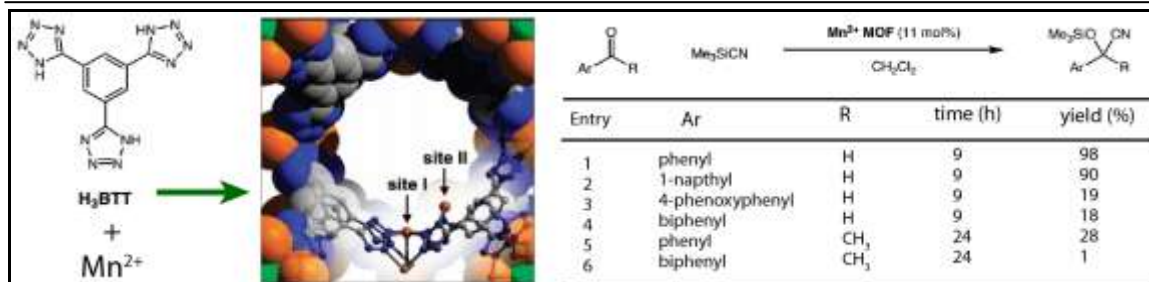


**Figure 1.17:** Catalysis in MOFs can be categorized into three types, a) metal node based catalysis, b) organic linker based catalysis and c) multifunctional catalysis.

catalysis in MOF. Zn(II) based homochiral 3D MOF was synthesized using a chiral linker in which  $\text{Ru}(\text{bpy})_3^{2+}$  complex was incorporated to make the material catalytically active. This MOF showed high catalytic performance for transesterification reaction with  $\sim 8$  ee(%) at room temperature. Since MOFs are well known as inorganic-organic hybrid materials, both organic linker and metal centers can take part in catalysis. Based on the position of the catalytic inside the framework, it can be categorized into three types, i) metal node based catalysis, ii) organic linker based catalysis, iii) multifunctional catalysis (**Figure 1.17**).

### 1.7.1 Metal node based catalysis:

There are some reports where the metal centers in MOF perform the catalysis. The unsaturated metal centers acts as the Lewis acid centers and hence if coordinations can be created in MOF, it will act as catalyst. Long and coworkers have shown Lewis acid catalyzed cyanosilylation of aromatic ketones and aldehydes in presence of Mn based

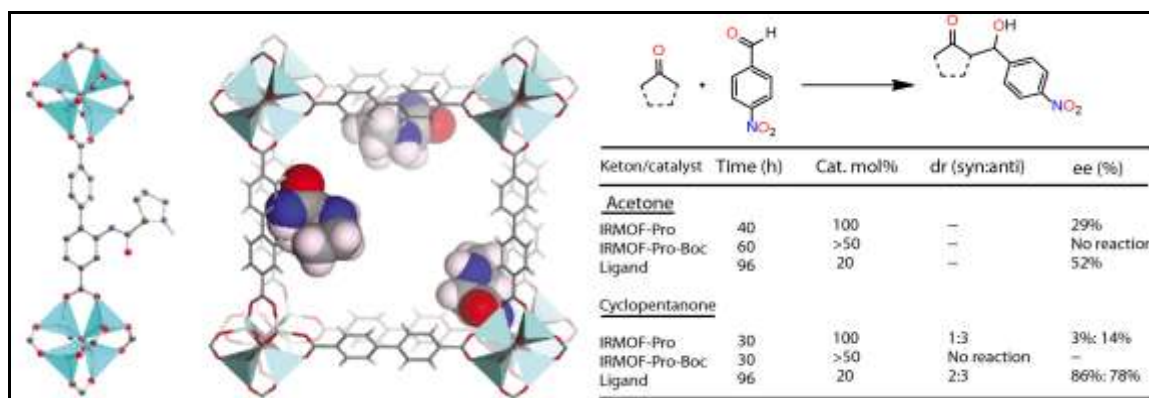


**Figure 1.18:** Example of metal node based catalysis in  $Mn_3[(Mn_4Cl)_3(BTT)_8(MeOH)_{10}]_2$ . Reprinted with permission from ref [1.42]. Copyright: American Chemical Society.

MOF ( $Mn_3[(Mn_4Cl)_3(BTT)_8(MeOH)_{10}]_2$ ) [1.42]. There was unsatisfied coordination of  $Mn^{2+}$  which acts as catalytic centers. The yield was nearly 90% and also showed size selectivity due to the 10 Å MOF pore diameter (**Figure 1.18**).

### 1.7.2 Organic linker based catalysis:

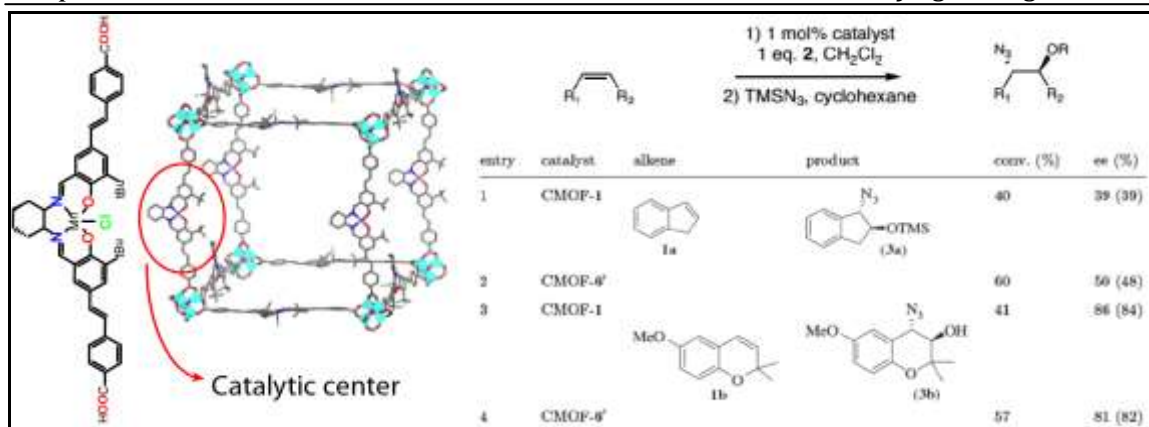
MOFs can be designed using catalytically active organic linkers. Mostly the organic linkers are more exposed to the pore walls than metal centers, which makes the reactant accessible to the catalyst. Telfer and coworkers [1.43] have made proline functionalized linker for synthesis of Zn based MOF. Proline is well known for organic catalytic reactions. Here the IRMOF-Pro has been demonstrated catalytic activity towards asymmetric aldol reactions (**Figure 1.19**).



**Figure 1.19:** Example of organic linker based catalysis in IRMOF-Pro. Reprinted with permission from ref [1.43]. Copyright: American Chemical Society.

### 1.7.3 Multifunctional catalysis:

When metal and ligand both can show catalytic activity inside a MOF, it can be possible to perform sequential catalysis reaction in one pot. Lin and coworkers reported



**Figure 1.20:** Example of multifunctional catalysis in CMOF-1. Reprinted with permission from ref [1.44]. Copyright: American Chemical Society.

**Table 1.4** Literature reported examples of MOF based catalysts and summary of active functionalities involved in these MOFs as catalytic centers.

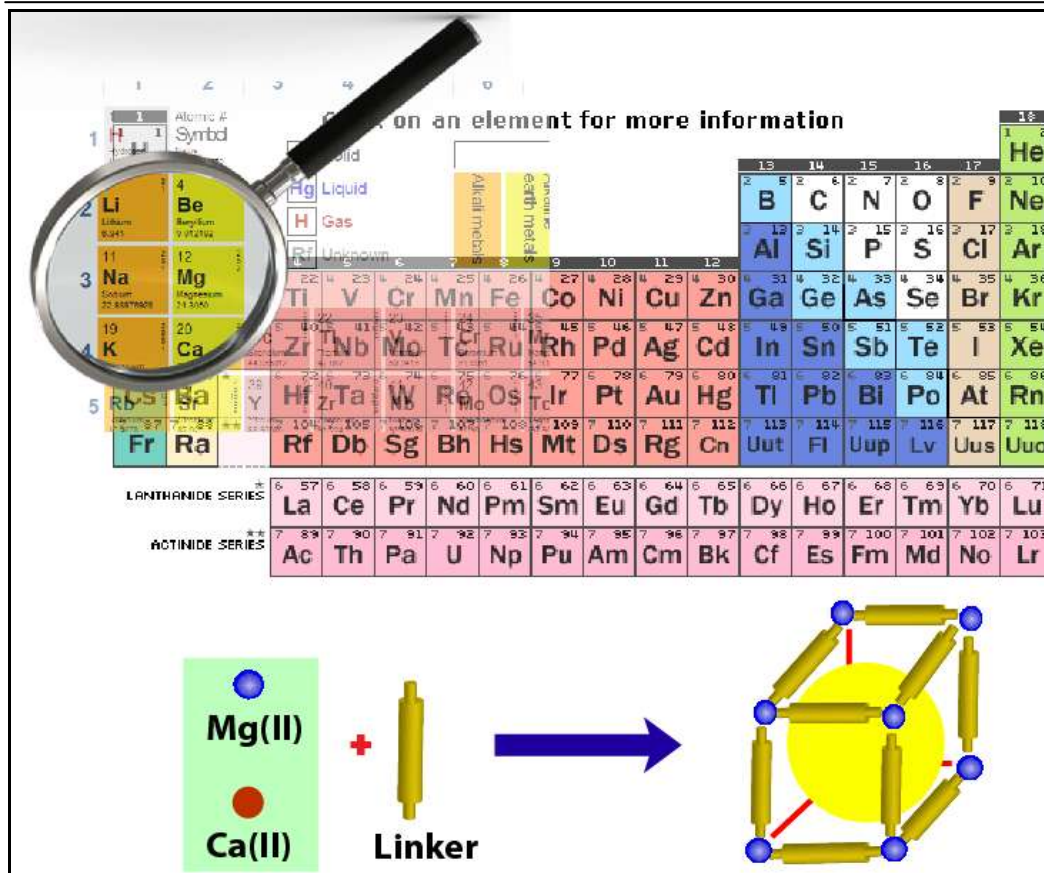
MOF Metal	MOF Linker	Active Centre	Catalytic Reaction
Cu	4,4'-bipyridine	Metal	Allylic oxidation <sup>[1.46a]</sup>
Zn	1,4-benzene dicarboxylic acid (IRMOF-1)	Metal	Cycloaddition of CO <sub>2</sub> and epoxides <sup>[1.46d]</sup>
Cu	1,2,4,5-benzenetetracarboxylic acid, 2,2'-bipyridine	Metal	Oxidation of olefinz <sup>[1.46b]</sup>
Zn	1,4-benzene dicarboxylic acid, 2-amino terephthalic acid	Linker and Metal	Cycloaddition of CO <sub>2</sub> and epoxides <sup>[1.46c]</sup>
Zn	2-aminoterephthalic acid (IRMOF-3)	Linker	Knoevenagel reaction <sup>[1.46d]</sup>
Cr	1,4-benzene dicarboxylic acid, ethylenediamine (ED-MIL-101)	Coordinated ethylene-diamine	Knoevenagel reaction <sup>[1.46e]</sup>
Zn	2-methyl imidazole (ZIF-8)	Incorporated Au/Ag/Pd/Pt nanoparticles	Nitro reduction, CO oxidation, Suzuki coupling <sup>[1.45]</sup>
Cu	Imidazole [Cu(im) <sub>2</sub> ]	Metal	Oxidation of activated alkanes, 1,3-dipolar cycloaddition <sup>[1.46f]</sup>
Zn	Porphyrin [ZnPO-MOF]	Zn(II) - porphyrin sites	Acyl transfer between N-acetylimidazole and pyridylcarbinols <sup>[1.46g]</sup>
Co	Benzimidazole (Co-ZIF-9)	Metal and coordinated N-atoms	Photocatalysis and water splitting <sup>[1.46h]</sup>

multifunctional MOF (CMOF-1) [1.44], which was used as catalyst for sequential reaction of epoxidation-epoxide opening reaction. Mn(salen) linkers catalyze the asymmetric epoxidation of alkenes and Zn SBUs catalyze the stereo and regioselective epoxide opening (**Figure 1.20**).

MOFs can also be used as catalytic supports, whereby the MOF is used as a carrier for an active site e.g. MOF-5 [1.45]. The porous MOFs and ZIFs with considerable stability have been successfully utilized as a catalytic support in many catalytic reactions such as use in the epoxidation of propylene with molecular oxygen by incorporating Ag into MOF-5, H<sub>2</sub>O<sub>2</sub> synthesis from the elements utilizing Pt on MOF-5, the synthesis of methanol from synthesis gas utilizing Cu on MOF-5, and also in the hydrogenation of cyclooctene by incorporating Pd onto MOF-5 [1.46a]. The Au and Ag nanoparticle incorporated ZIFs and MOFs have been effectively utilized as catalyst for nitro reduction reaction to produce commercially important amines and other reagents [1.46b]. The various as synthesized or post-synthetically modified MOFs have been used for the synthesis of various commercially important chemicals, to catalyze organic transformation reactions (e.g. Suzuki, Sonogashira, Heck, etc.), various oxidation and reduction reactions, tandem and cascade reactions [1.46c-e].

### **1.8 Introduction to Lightweight Metal-Organic Framework (LWMOFs):**

Most commonly used metals for MOF synthesis are the transition metals and lanthanides because of their well define coordination behavior. But lightweight metals i.e. Li, Na, Ca, Mg, Al, K, etc are rarely used for MOF synthesis in literature. Metal-organic frameworks made of such lightweight metals are well known as lightweight metal-organic frameworks (LWMOFs) (Figure 1.5). Since, inside the MOF structure the organic linkers are constructed from C, H, N, O, S and B, which are light elements and only the heaviest parts are the metal centers. So by using the lightweight metals LWMOFs can be synthesized. All the chapters in this thesis mainly focused on the synthesis of Ca(II) and Mg(II) based LWMOFs followed by deeply investigate their chemical as well as electrochemical properties and their applications in important areas based on their properties.



**Figure 1.21:** Introduction of lightweight metals and LWMOFs synthesis.

### 1.9 Advantages of Lightweight Metal-Organic Framework (LWMOFs):

As previously discussed that transition metals and lanthanides are widely used for MOF synthesis, but lightweight metal containing MOFs are less explored. The lightweight metals have high charge density, which results in high affinity to bind to the ligands with unpredicted geometry. Also these metals have tendency to bind with polar solvents and form low dimensional structures rather than three dimensional (3D) MOF structures. Even then, there are lots of advantages of lightweight metals, if 3D MOFs can be synthesized by overcoming these limitations. Since in this thesis mainly Ca(II) and Mg(II) based LWMOFs have been discussed, here the advantages of Ca and Mg metals are focused.

- i) *High abundance in earth crust:* The lightweight metals especially Ca and Mg are one of those most abundant elements present in the upper shell of the earth's crust (**Table 1.5**) [1.47]. Hence the materials produced from these elements will be

**Table 1.5:** Top 10 abundance elements present in earth crust.

Element	Abundance percent by weight	Abundance parts per million by weight
Oxygen	46.1%	461,000
Silicon	28.2%	282,000
Aluminum	8.23%	82,300
Iron	5.63%	56,300
Calcium	4.15%	41,500
Sodium	2.36%	23,600
Magnesium	2.33%	23,300
Potassium	2.09%	20,900
Titanium	0.565%	5,650
Hydrogen	0.14%	1,400

**Table 1.6:** Human body elemental abundance.

Serial	Element	Proportion (by mass)
1	Oxygen	65%
2	Carbon	18%
3	Hydrogen	10%
4	Nitrogen	3%
5	Calcium	1.5%
6	Phosphorus	1.2%
7	Potassium	0.2%
8	Sulfur	0.2%
9	Chlorine	0.2%
10	Sodium	0.1%
12	Magnesium	0.05%
13	Iron	< 0.05%
14	Cobalt	< 0.05%
15	Copper	< 0.05%
16	Zinc	< 0.05%
17	Iodine	< 0.05%
18	Selenium	< 0.01%



very low cost materials (**Figure 1.22**).

ii) *Nontoxic for biological system*: All lightweight metals have high importance in

biological system.

Calcium and Magnesium

are the 5<sup>th</sup> and 12<sup>th</sup> highly

abundant element in

human body (Table 1.6)

[1.47]. Calcium is

essential for

living organisms, in

particular

in cell physiology, where

movement of the calcium

ion  $\text{Ca}^{2+}$  into and out of

the cytoplasm functions

as a signal for many

cellular processes. As a

major material used in

mineralization

of bone, teeth and shells,

calcium is the most

abundant metal by mass

in many animals. In human biology, magnesium is the eleventh-most-abundant element

by mass in the human body. Its ions are essential to all living cells, where they play a

major role in manipulating important biological polyphosphate compounds like ATP,

DNA, and RNA. Hundreds of enzymes, thus, require magnesium ions to function (**Figure**

**1.22**) [1.48].

iii) *Environmental nonhazardous*: The lightweight metals are nontoxic as well as

environmentally nonhazardous. So, environmental friendly MOFs can be easily

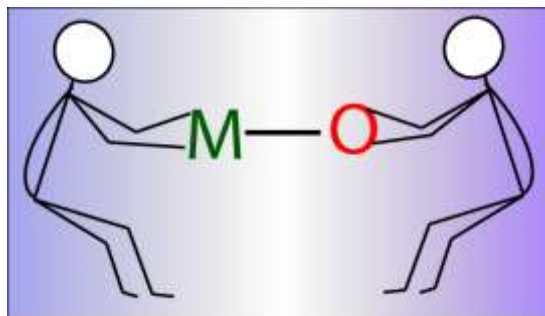
synthesized by designing such nontoxic organic linkers (**Figure 1.22**).



**Figure 1.22:** Most important advantages to use lightweight metals for MOF synthesis.

iv) *Low mass density storage materials:* MOFs are well known for gas storage application and for this low density materials are advantageous over others. Especially for vehicular engine (high speed cars or aircraft) needs very lightweight materials for fuel (hydrogen gas) storage gadgets (**Figure 1.22**) [1.49].

v) *Stable ionic bond formation:* As compare to transition metals the lightweight metals have high charge density (Table 1.7). So, lightweight metals forms strong ionic bonds rather than covalent bonds. The ionic bonds are far strong than covalent bonds and hence LWMOFs are more stable than other MOFs (**Table 1.8**) [1.48].



**Figure 1.23:** The metal-oxygen bonds in LWMOFs are stronger than other MOFs.

**Table 1.7:** Properties of lightweight Metal Cations.

Metals	Atomic radius (Å)	Ionic radius (Å)	Ionization energy (KJ/mol)	Electronegativity (Pauling)
Li	1.52	0.76	520.1	1.0
Na	1.86	1.02	495.7	0.9
K	2.27	1.38	418.6	0.8
Rb	2.48	1.52	402.9	0.8
Cs	2.65	1.67	375.6	0.7
Be	1.12	0.31	1757	1.5
Mg	1.60	0.72	1450	1.2
Ca	1.97	1.00	1145	1.0
Sr	2.15	1.18	1064	1.0
Ba	2.22	1.35	965	0.9

**Table 1.8:** Average bond distance variation in lightweight metal carboxylate networks\*

Metal–O <sub>carboxylate</sub>	Distance (Å)	Metal–O <sub>carboxylate</sub>	Distance (Å)
Li–O	1.976 (0.09)	Be–O	1.636 (0.005)
Na–O	2.431 (0.004)	Mg–O	2.066 (0.02)
K–O	2.802 (0.006)	Ca–O	2.428 (0.006)
Rb–O	2.997 (0.016)	Sr–O	2.622 (0.006)
Cs–O	3.185 (0.015)	Ba–O	2.816 (0.005)

\*Cambridge Crystallography Database (CSD).

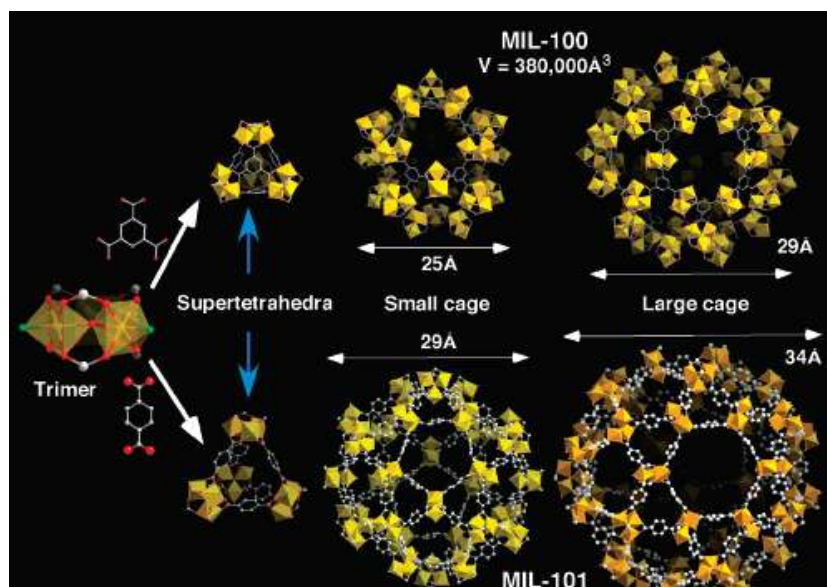
### 1.10: Important Applications of Lightweight MOFs (LWMOFs):

Based on the aforementioned advantages the LWMOFs has been used for several applications like i) gas storage and separation, ii) heterogeneous catalysis, iii) chemical sensing, iv) proton or ion conduction, v) drug delivery, vi) encapsulation of active molecules, etc.

**i) Gas storage and separation:** The most important application of porous LWMOFs is the gas storage. The

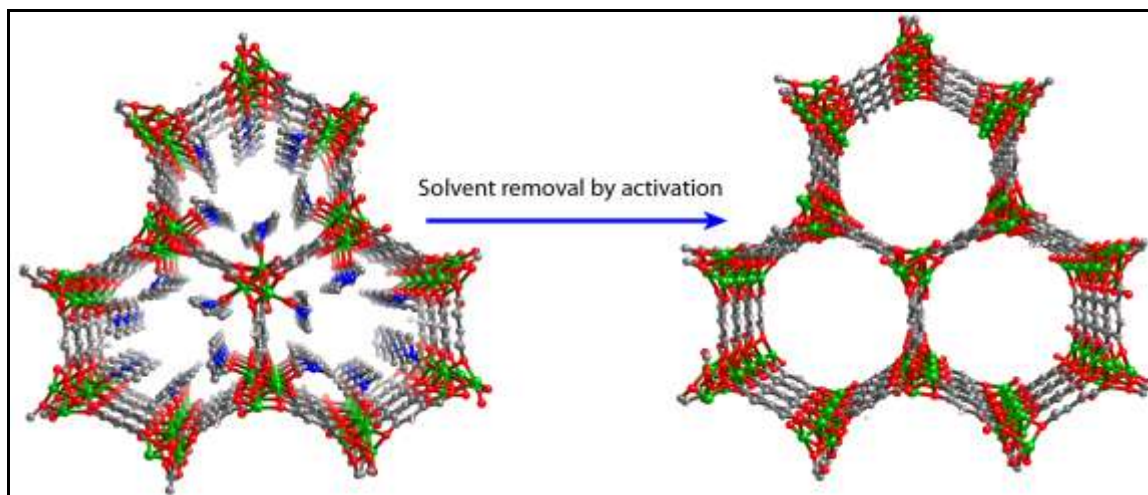
commonly used metals for MOF synthesis are transition metals and lanthanides. Because of their well define coordination geometry, highly porous MOFs can be easily synthesized. Due to the high mass density of these

metals, the gravimetric gas adsorption is less. So researchers started using main group metals for MOF synthesis. The main group metals like Na, K, Mg, Ca, Al, etc have low mass density, which results



**Figure 1.24:** Crystal structure of MIL-100 and MIL-101 showing large pore volume for gas adsorption. Reprinted with permission from ref [1.50]. Copyright: Wiley-VCH.

in formation of very low density MOF materials or LWMOFs. The gravimetric gas uptake is higher in case of LWMOFs. Férey and coworkers [1.50] synthesized Al-MIL-53, Al-MIL-100 and Al-MIL-101 which have been applied for H<sub>2</sub> storage application. Al-MIL-53 was synthesized using 1,4-benzene dicarboxylic acid and Al(NO<sub>3</sub>)<sub>3</sub>, have 1D channels with large free diameters of about 8.5 Å and a large BET surface area of 1100 m<sup>2</sup>g<sup>-1</sup>. The compound exhibited a maximal hydrogen storage capacity of 3.8 wt% at 77 K and 16 bar. Al-MIL-100 and Al-MIL-101 was synthesized from carboxylate moieties (BTC for MIL-100 and BDC for MIL-101). These MILs have two types of pores, smaller pore has 12 pentagonal pores and larger pores have 12 pentagonal and 4 hexagonal faces. The accessible diameters of the cages were 25 and 29 Å for MIL-100 and 29 and 34 Å for MIL-101. The MIL-100, which was previously out-gassed at 493 K, had a Langmuir surface area of 2700 m<sup>2</sup>g<sup>-1</sup> and a maximum hydrogen uptake of 3.28 wt% at 77 K and 26.5 bar. The MIL-101b, obtained after removal of all guests from the pores, have very high Langmuir surface area 5500 m<sup>2</sup>g<sup>-1</sup>. The maximum hydrogen adsorption capacity of MIL-101b reached 6.1 wt% at 80 bar and 77 K. The high adsorption capacity of MIL-101b was attributed to its high adsorption heat (9.3 to 10.0 kJ mol<sup>-1</sup> at low coverage), which was larger than that of MIL-100 (5.6 to 6.3 kJ mol<sup>-1</sup> at low coverage).

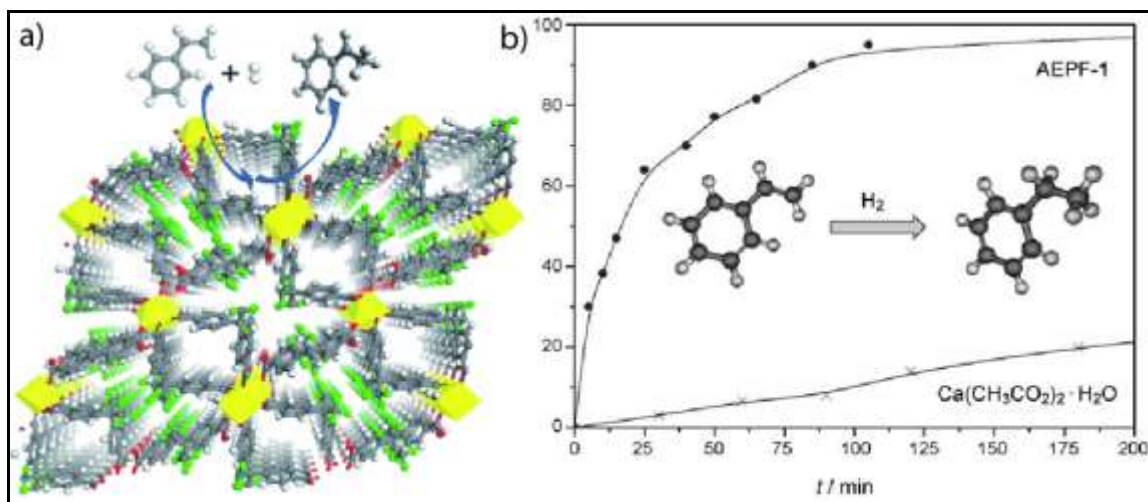


**Figure 1.25:** Generation of open metal sites in Mg-MOF-74 for enhancement of gas storage properties.

Since the lightweight metals have tendency to coordinate with solvent along with the ligand, the framework have opportunity to produce open metal sites inside the MOFs. The open metal sites are advantageous for high gas storage and separation. Especially polar gases like CO<sub>2</sub>, CO, NO

etc have high affinity towards open metal sites. Yaghi and co-workers [1.51] showed that, Mg-MOF-74 (**Figure 1.25**), with open magnesium sites, rivals competitive materials in CO<sub>2</sub> capture, with 8.9 wt. % dynamic capacity, and undergoes facile CO<sub>2</sub> release at significantly lower temperature, 80 °C. Also Ahn and coworkers reported the adsorption isotherms of Mg-MOF-74 for CO<sub>2</sub>, which showed high adsorption capacity (350 mg g<sup>-1</sup> at 298 K) and high isosteric heats of adsorption for CO<sub>2</sub> (42 to 22 kJ mol<sup>-1</sup>). The breakthrough experiment confirmed excellent selectivity to CO<sub>2</sub> over N<sub>2</sub> at ambient conditions (saturation capacity of *ca.* 179 mg g<sup>-1</sup>).

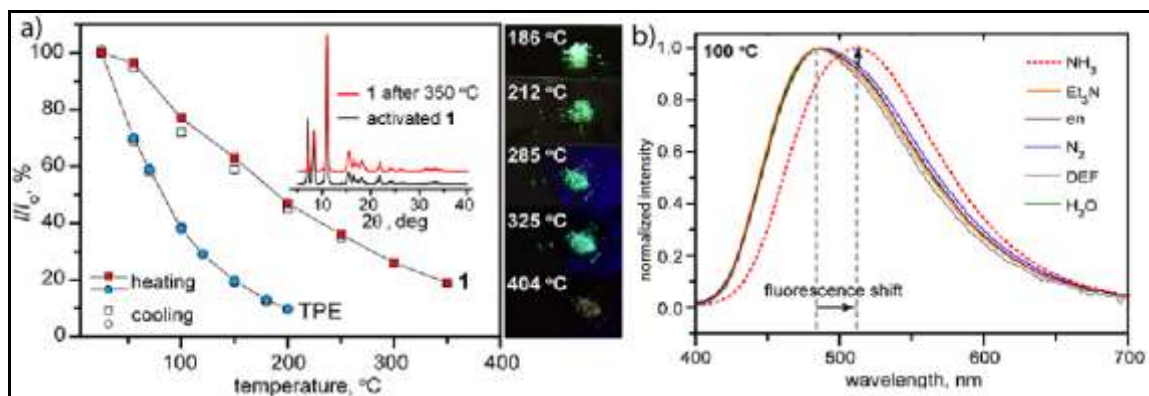
**ii) Heterogeneous catalysis:** Lightweight metals especially alkaline earth metal complexes are Lewis acid in character. So these complexes have been used for hydrogenation (hydrophosphination, hydrosilylation, hydroamination) and polymerization reactions as homogeneous catalyst. The heterogeneous catalysis is possible in porous LWMOFs using the Lewis acid centers in the frameworks. Gutiérrez-Puebla and co-workers [1.52] reported a LWMOF based on cheap, abundant calcium, with the bent ligand, 4,4'-hexafluoroisopropylidenebisbenzoic acid. This LWMOF serves as a highly efficient heterogeneous catalyst for the hydrogenation of styrene to form ethyl benzene under mild conditions (**Figure 1.26**). Complete hydrogenation occurs after 2 h at 373 K without formation of byproduct.



**Figure 1.26:** Heterogeneous catalysis in MOFs, a) Ca-HFBBA MOF structure, b) hydrogenation reaction kinetics with time. Reprinted with permission from ref [1.52]. Copyright: Wiley-VCH.

**iii) Chemical sensing:** The lightweight metals don't have d orbital electrons which is advantageous for synthesis of desired fluorescent MOFs. The transition metals generally

quench the luminescence properties of organic linkers due to the presence of paramagnetic d electrons. Dinca and coworkers [1.53] reported an Mg based fluorescent MOF, which was applied for sensing of harmful gas (ammonia). The linker, 2,5-dihydroxybenzene-1,4-dicarboxylate was fluorescent and the MOF, synthesized from this had a emission maxima at 487 nm. This MOF exhibits selective turn on sensing in presence of trace amount ammonia vapor (**Figure 1.27**). The emission maxima of the MOF were shifted to 511 nm in presence of analyte. In high temperature the sensing performance was also intact in that case (**Figure 1.27**). Recently, N. C. Jeong and coworkers reported a metal–organic framework (CDMOF-2) [1.54], where structure containing six units of  $\gamma$ -cyclodextrin linked together in cube-like fashion by rubidium ions ( $\text{Rb}^+$ ).  $\text{CO}_2$  can be detected selectively from the atmosphere by electrochemical impedance spectroscopy. The as-synthesized CDMOF-2 which exhibits high proton conductivity in pore-filling methanolic media, displays a  $\sim 550$ -fold decrease in its ionic conductivity on binding  $\text{CO}_2$ . This fundamental property has been exploited to create a sensor capable of measuring  $\text{CO}_2$  concentrations quantitatively even in the presence of ambient oxygen.

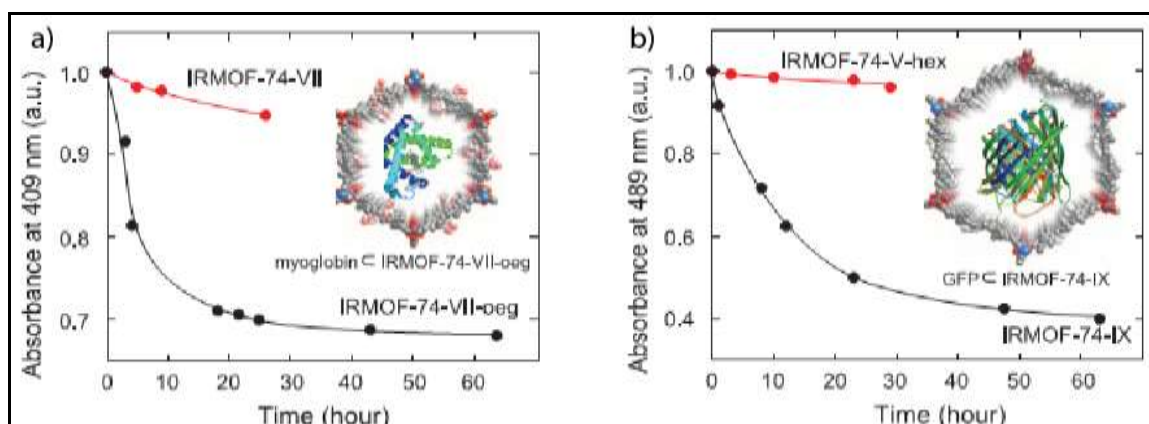


**Figure 1.27:** a) Temperature-dependent fluorescence decay profiles of 1 (squares) and TPE (circles). Heating and cooling cycles are represented as filled and open symbols, respectively. The inset shows PXRD patterns of activated 1 and after heating at 350°C in air. The optical micrographs show fluorescent 1 ( $\lambda_{\text{ex}} = 350 \text{ nm}$ ) upon heating at various temperatures in air, b) In situ normalized emission spectra ( $\lambda_{\text{ex}} = 350 \text{ nm}$ ) of 1 exposed to various analytes at room temperature and 100 °C. Reprinted with permission from ref [1.54]. Copyright: American Chemical Society.

**v) Drug delivery:** As the lightweight metals are biocompatible (discussed earlier), the LWMOF can be used for challenging application like drug delivery in biological system.

Ferey and coworkers [1.55] used stable MOFs like MIL-100, MIL-101 for loading of ibuprofen inside the large pores. MIL-100 could uptake 0.35 g of ibuprofen/g of dehydrated MIL-100, whereas MIL-101 could uptake 1.4 g of ibuprofen/g of dehydrated MIL-101.

**vi) Encapsulation of active molecules:** Large pore LWMOFs are applicable for encapsulation of active molecules like portions, enzymes and etc. Yaghi and coworkers [1.56] have synthesized a series of isorecticular MOF-74 structures having large pore size  $\sim 98$  Å. These IRMOF-74 materials have been used for encapsulation of active biomolecules like proteins and enzymes. The IRMOF-74-VII, having pore diameter  $\sim 34$  Å, has been used for myoglobin encapsulation. Also IRMOF-74-IX, having pore diameter  $\sim 45$  Å, has been applied for inclusion of green fluorescent protein (GFP) inside the MOF pores (Figure 1.27).



**Figure 1.28:** Inclusion study of selected large molecules in a) IRMOF-74-VII and b) IRMOF-74-IX respectively. This process was monitored through the decrease in absorbance at a selected wavelength as a function of contact time. For each measurement, the initial absorbance was normalized to 1.0. (Insets) Illustrations of the inclusion complex for each study Reprinted with permission from ref [1.56]. Copyright: AAAS publishing group.

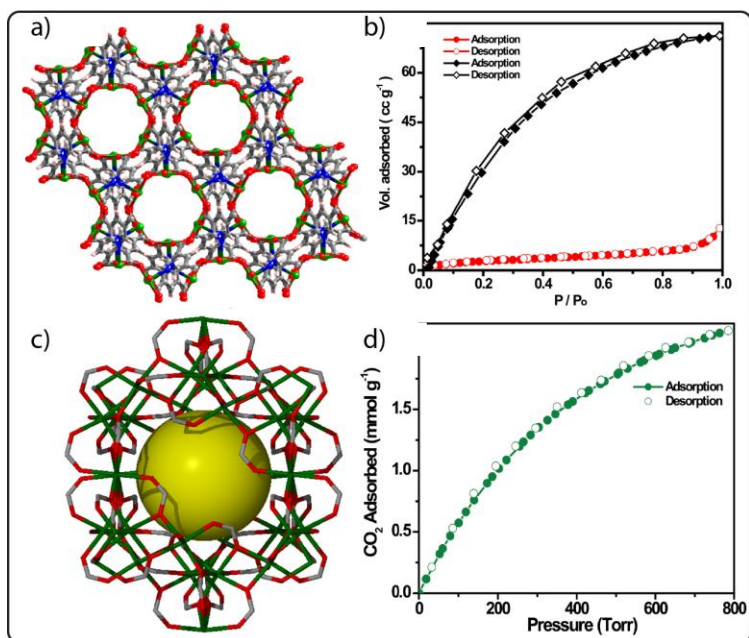




## CHAPTER 2

### Synthesis of Porous Mg(II) based Light Weight Metal-Organic Frameworks (LWMOFs) for Gas Storage

**Abstract:** In this chapter two new 3D Mg(II) based lightweight MOFs, synthesized using Mg(II) salts and very simple ligands, formate anion and 3,5 pyridinedicarboxylic acid has been presented. These MOFs are porous and show interesting  $H_2$ ,  $CO_2$  and  $N_2$  adsorption properties. Also Grand



Canonical Monte Carlo (GCMC) simulation has been performed to predict the initial positions of the hydrogen molecules in the framework. The positions of the each hydrogen molecules in the framework and their related adsorption energies were optimized using Density Functional Theory (DFT) and ab-initio Hartree-Fock (HF) method.

## 2.1 Introduction:

Metal-organic frameworks (MOFs) [2.1] are the important class of porous solids that have potential application in gas storage [2.2], separation [2.3], magnetism [2.4], heterogeneous catalysis [2.5], multiferroics [2.6], drug delivery [2.7], chemical sensing [2.8], etc. Among all this gas storage and separation is the most promising application in such porous network materials. The gases like CO<sub>2</sub>, CO, NO<sub>2</sub>, SO<sub>2</sub>, NH<sub>3</sub>, H<sub>2</sub>S, Br<sub>2</sub>, Cl<sub>2</sub>, etc which, are very harmful for biological system as well as environment, should be captured and separated. It is also important to store some gases like H<sub>2</sub>, CH<sub>4</sub>, C<sub>2</sub>H<sub>4</sub>, C<sub>2</sub>H<sub>2</sub>, C<sub>4</sub>H<sub>10</sub>, etc, which are useful for energy and fuel applications. Last two decades researchers emphasizing on H<sub>2</sub> storage in MOFs because it has a curtail role in fuel cell engine vehicles. Hydrogen storage materials for fuel cells became an important research topic due to the increasing demand of clean and efficient alternatives for fossil fuels [2.9]. MOFs in this regard have attracted great deal of attention because of their fascinating topologies [2.10] and potential applications such as hydrogen storage [2.2] and CO<sub>2</sub> sequestration [2.11]. In comparison to other materials such as inorganic zeolites [2.12], metal hydrides [2.13] and carbon-based porous materials [2.14], MOFs exhibit promising hydrogen storage capacities, owing to their low framework density, high specific surface area, and tunable surface structures on which hydrogen molecules can be adsorbed. MOFs formed by light main group metals such as Mg<sup>2+</sup> and Al<sup>3+</sup> may play an important role in this endeavor [2.15]. However, most studies in the literature have focused on MOFs assembled from d- or f-block elements (e.g. cobalt, nickel, zinc and copper). MOFs based on main-group metals, in particular, light main group metals are very rare [2.16]. Divalent magnesium has a number of similarities to the transition metal ions, typically used to make MOFs, in that it prefers octahedral coordination, has a comparable ionic radius (72 pm for Mg<sup>2+</sup> compared to 74 pm for Zn<sup>2+</sup> and 73 pm for Cu<sup>2+</sup>) and similar hydration energy. However, only a handful of magnesium containing MOFs were reported presumably due to the difficulty in synthesizing three dimensional porous structures with a high hydrogen storage capacity [2.17].

In order to build MOF based materials with high gas storage capacity it is essential to have a molecular level understanding of interactions. As a result several researchers' attempted ab-initio quantum mechanical study on the finite structure of the

MOFs [2.18]. The storage capacity of different types of gases at different temperatures is strongly dependent upon the interactions between the MOF framework and gas molecules. It is expected that finding the adsorption sites in the framework and their energies will also produce valuable information about the amount of the intake of gas molecules. Therefore first principle quantum chemistry calculations are useful to scan the adsorption sites and their respective adsorption energies to predict the adsorption capacity and further tuning the chemistry of the framework [2.19].

In this chapter we presented the synthesis and structural studies of new three dimensional magnesium formate polymorph namely  $\gamma$ -[Mg<sub>3</sub>(O<sub>2</sub>CH)<sub>6</sub>] synthesized via in situ formate anion generation method and adding 1,3-benzene-ditetrazole as structure directing agent (SDA) and a porous chiral 3D Mg-MOF-1 synthesized from 3,5-pyridine di-carboxylic acid (C<sub>7</sub>H<sub>5</sub>NO<sub>4</sub>, H<sub>2</sub> 3,5-PDC) and Mg<sup>2+</sup> metal ion as a metal centre in DMF media. Crystal structure of this new  $\gamma$  polymorph of magnesium formate was completely different from other reported magnesium formates ( $\alpha$  and  $\beta$  polymorph) [2.20]. The occurrence of polymorphism [2.21] was likely for a particular compound that can be synthesized or crystallized under different experimental conditions. Chiral 3D Mg-MOFs are rare as there are only four chiral Mg-MOFs reported in the CSD that poses a 3-dimensional architecture [2.22]. The MOF synthesized can be formulated as [Mg(3,5-PDC)(H<sub>2</sub>O)] (Mg-MOF-1) (3,5-PDC = 3,5-pyridine dicarboxylate) and display an interesting 3D chiral architecture containing parallel hexagonal channels. We also report crystal structure of one zero-dimensional (0D) analogue of Mg-MOF-1, namely Mg-MOF-2 synthesized from 2,4-pyridine di-carboxylic acid (C<sub>7</sub>H<sub>5</sub>NO<sub>4</sub>, H<sub>2</sub> 2,4-PDC) and Mg<sup>2+</sup>. The structure of  $\gamma$ -[Mg<sub>3</sub>(O<sub>2</sub>CH)<sub>6</sub>], Mg-MOF-1 and -2 has been determined by single crystal X-ray diffraction (XRD) and further identified by IR spectroscopy (FTIR) and powder X-ray diffraction (PXRD). We measured the thermal stability of these MOFs by thermogravimetric analysis (TGA) and its ability to adsorb and release carbon dioxide (CO<sub>2</sub>) and hydrogen (H<sub>2</sub>) gas. In addition, in-situ variable temperature PXRD has been carried out on *these* MOFs to analyze their stability and crystallinity at high temperature and dehydration-rehydration cycle. We have used Grand Canonical Monte Carlo (GCMC) simulation [2.23] to predict the initial positions of the hydrogen molecules in the framework and Density Functional Theory (DFT) method to optimize the positions of

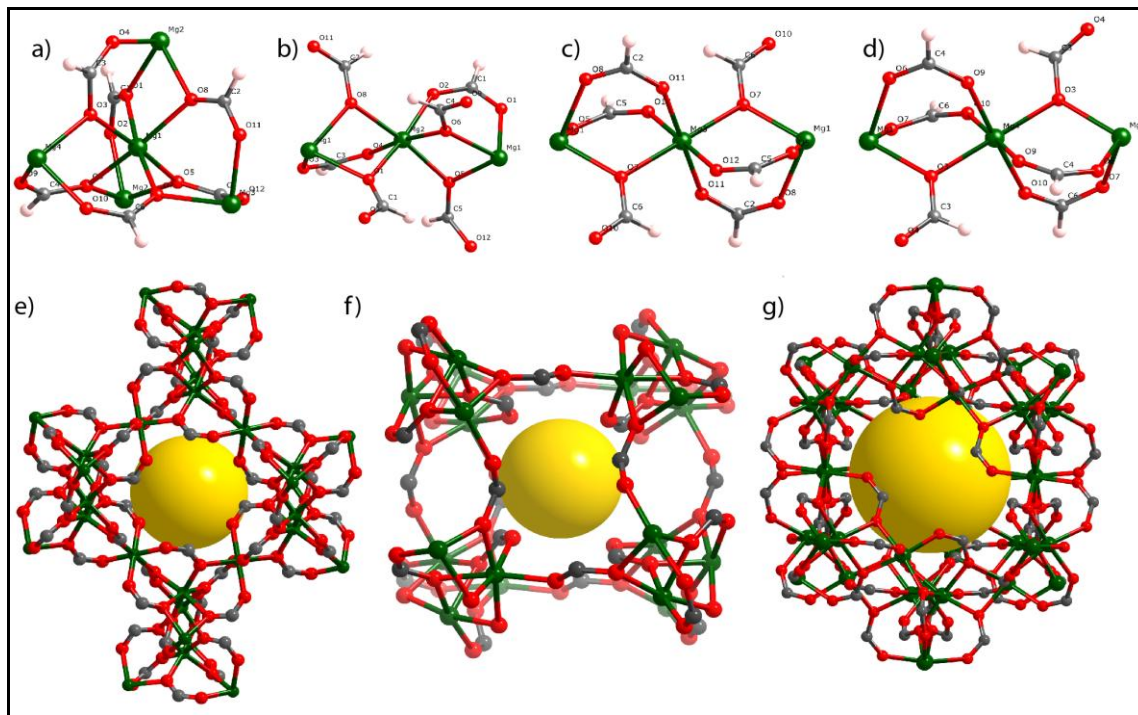
the each hydrogen molecules in the framework and their related adsorption energies. Also ab-initio Hartree-Fock (HF) method has applied to optimize the positions of the each hydrogen molecules in the framework and their related adsorption energies.

## 2.2 Result and discussion:

### 2.2.1 Structural analysis of $\gamma$ -Mg-formate $Mg_3(O_2CH)_6\cdot[NH(CH_3)_2]_{0.5}$ :

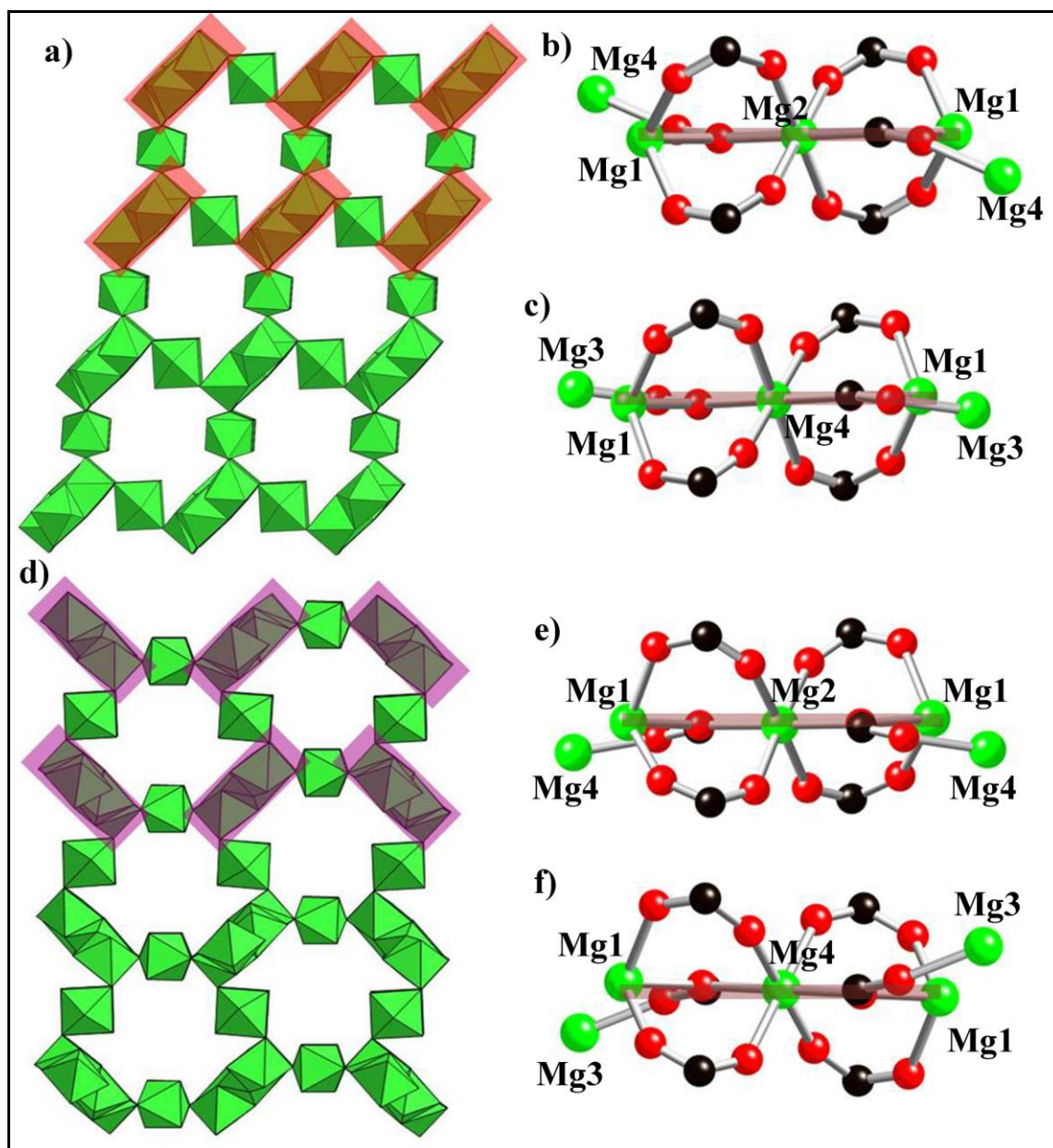
In most of the literature on Mg-formates,  $Mg^{2+}$  centers were surrounded by formate groups as well as coordinated water molecules [2.24]. Till date, there were only three anhydrous Mg-formates reported in the literature where  $Mg^{2+}$  centers were coordinated only with formate anions. Powell and coworker [2.20a] first reported the solvothermal synthesis of two un-solvated Mg-formates ( $\alpha$  form and  $\beta$  form) of which only nonporous  $\beta$ -[Mg(O<sub>2</sub>CH)<sub>2</sub>] form was structurally determined. Later Rood *et al.* reported the structural characterization and gas adsorption study of  $\alpha$ -Mg-formate [Mg<sub>3</sub>(O<sub>2</sub>CH)<sub>6</sub>·HCO<sub>2</sub>H]. [2.20b] Recently there has been a report of a third anhydrous phase Mg(HCOO)<sub>2</sub>(HCOOH)·(CH<sub>3</sub>)<sub>2</sub>NH [2.24]. Formic acid had been the source of formate anion in all these three cases. Mg(NO<sub>3</sub>)<sub>2</sub>·6H<sub>2</sub>O was the source of metal for the  $\alpha$  and  $\beta$  form, whereas anhydrous Mg(HCOO)<sub>2</sub>(HCOOH)·(CH<sub>3</sub>)<sub>2</sub>NH could be prepared from Mg(NO<sub>3</sub>)<sub>2</sub>·6H<sub>2</sub>O, Mg(CO<sub>2</sub>CH<sub>3</sub>)<sub>2</sub>·4H<sub>2</sub>O and Mg(ClO<sub>4</sub>)<sub>2</sub>·6H<sub>2</sub>O. We introduced a different synthetic route of generating formate anion in situ by addition of nitric acid (HNO<sub>3</sub>) into the reaction media that contains *N,N'*-dimethylformamide (DMF) as a solvent [2.25]. We anticipated that reaction between nitric acid and DMF at high temperature and pressure inside a teflon-lined stainless steel autoclave may create formate anion, which upon reaction with  $Mg^{2+}$  might result into Mg-formate. All our attempts to synthesize a new Mg-formate polymorph resulted into the production of mixtures of  $\gamma$ -Mg-formate (major product) and previously reported anhydrous Mg(HCOO)<sub>2</sub>(HCOOH)·(CH<sub>3</sub>)<sub>2</sub>NH (minor product). Our attempt of using diverse structure directing agents (like tetra-butyl ammonium salts) to synthesize phase pure  $\gamma$ -Mg-formate also resulted in the precipitation of either the aforementioned mixtures or unreacted starting material. However, after several attempts we discovered that solvothermal reaction (in teflon-lined stainless steel autoclave at 125 to 150 °C) of Mg(CO<sub>2</sub>CH<sub>3</sub>)<sub>2</sub>·4H<sub>2</sub>O with nitric acid (HNO<sub>3</sub>) in a DMF solution in the presence of 1,3-

benzene-ditetrazole in 3:2:1 mol ratio for 72 h afforded a colorless homogeneous microcrystalline  $\gamma$ -Mg-formate as phase pure form with a dodecahedron morphology. So far we were unable to understand the role of 1,3-benzene-ditetrazole



**Figure 2.1:** a), b), c) and d) represents the local geometries surrounding the four independent, octahedrally coordinated magnesium centers within  $\gamma$ -Mg-formate. Ball and stick models showing packing diagram for e)  $\alpha$ -Mg-formate f)  $\beta$ -Mg-formate g)  $\gamma$ -Mg-formate. Yellow balls represent the empty space inside the pores. Color code: O (red) C (grey) Mg( green).

during the synthesis and crystallization of  $\gamma$ -Mg-formate as we were unable to find its existence in the resulting crystal structure. We anticipate that it might be acting as a structure directing agent. The as-synthesized compound was stable in most organic solvents and was characterized and formulated by single-crystal X-ray diffraction (XRD) studies as  $\text{Mg}_3(\text{O}_2\text{CH})_6 \supset [\text{NH}(\text{CH}_3)_2]_{0.5}$ . The same result was obtained when we used either  $\text{Mg}(\text{ClO}_4)_2 \cdot 6\text{H}_2\text{O}$  or  $\text{Mg}(\text{NO}_3)_2 \cdot 6\text{H}_2\text{O}$ , with no significant differences for phase purity (less than 50% yield), as confirmed by the PXRD patterns (**Figure 2.7a**). The  $\gamma$ -Mg-formate crystallizes in space group *Pbcn* and structural determination by x-ray single crystal diffraction reveals a three dimensional network of  $\text{Mg}^{2+}$  linked by formate anions. The asymmetric unit of Mg-formate consists of four crystallographically independent  $\text{Mg}^{2+}$  ions, each of which was octahedrally coordinated by six different formate anions.



**Figure 2.2:** a) The polyhedral representation of the extended structure of  $\alpha$ -Mg-formate (parallel) viewed down the crystallographic  $b$  axis. b) Trans orientation Mg(4) with respect to the planes formed by Mg(1)–Mg(2)–Mg(1). c) Trans orientation Mg(3) with respect to the planes formed by Mg(1)–Mg(4)–Mg(1) in  $\alpha$ -Mg-formate. d) The polyhedral representation of the extended structure of  $\gamma$ -Mg-formate (orthogonal) viewed down the crystallographic  $b$  axis. e) Cis orientation Mg(4) with respect to the planes formed by Mg(1)–Mg(2)–Mg(1). f) Cis orientation Mg(3) with respect to the planes formed by and Mg(1)–Mg(4)–Mg(1) in  $\gamma$ -Mg-formate.

All formate anions pose similar binding mode to the metal center with one oxygen of a particular formate anion binds to one metal center ( $\mu^1$  oxygen) and other oxygen binds to two metal centers ( $\mu^2$  oxygen). So each formate anion binds with three  $\text{Mg}^{2+}$  and each

Mg<sup>2+</sup> binds with six formate anions and hence the chemical formula could be derived as Mg<sub>3</sub>(O<sub>2</sub>CH)<sub>6</sub> with 1:2 Mg<sup>2+</sup> and ligand ratio (**Figure 2.1a,b,c,d**). This  $\eta^2 \mu^3$  type binding motif was also seen in  $\alpha$ - and  $\beta$ -Mg-formates.  $\gamma$  Mg-formate has interesting structural similarity with its  $\alpha$ - polymorph as it contains similar coordination environments for the metal centers. Mg(1) center was connected with the six  $\mu^2$  oxygen, Mg(2) center was connected with four  $\mu^2$  oxygen and two  $\mu^1$  oxygen, whereas Mg(3) and Mg(4) centers were connected with four  $\mu^1$  oxygen and two  $\mu^2$  oxygen. Although Mg(3) and Mg(4) centers have similar connectivity but they have different coordination environments. The Mg(3) was connected to Mg(1) through two formate bridges and one  $\mu^2$  oxygen (O7), and here the bridging dihedral angles ( $\tau$ ) were 21.29° (Mg3–O11–O8–Mg1) and 27.00° (Mg3–O1–O5–Mg1) (**Figure 2.1c**). Mg(4) was also connected with Mg(1) through two formate bridges and one  $\mu^2$  oxygen (O3), but the dihedral bridging angles ( $\tau$ ) were 21.90° (Mg4–O10–O7–Mg1) and 14.18° (Mg4–O9–O6–Mg1). The Mg–O( $\mu^1$ ) bond distance ranges from 2.012(2) to 2.053(3) Å and the Mg–O( $\mu^2$ ) bond distance ranges from 2.063(2) Å to 2.132(2) Å. Mg(1) and Mg(2) were linked through edge-shared MgO<sub>6</sub> octahedra and form one dimensional chain along crystallographic *a*-axis. That chains were connected to each other through vertex-sharing octahedra of Mg(3) and Mg(4) and thus it forms a three dimensional network. The network contains one dimensional channel along crystallographic *a*-axis. Here the channels were filled by the disordered dimethylamine molecules. The void space was calculated using *PLATON* [2.39] suggesting 5.1% void volume to the total crystal volume; however, this would be increased to 24.7% after removal of the disordered solvent molecules. The pore diameter of the channel was 3.6 Å (the channel size was measured by considering the van der Waals radii of the constituting atoms).

As mentioned previously there were three other anhydrous Mg-formates ( $\alpha$ -Mg-formate,  $\beta$ -Mg-formate, Mg(HCOO)<sub>3</sub>⊃(CH<sub>3</sub>)<sub>2</sub>NH) reported in literature. In case of  $\alpha$ ,  $\beta$  and  $\gamma$ -Mg-formate (reported in this chapter),  $\mu^1$  and  $\mu^2$  oxygen were binding with Mg<sup>2+</sup> centers (**Figure 2.1e,f,g**). Whereas anhydrous Mg(HCOO)<sub>2</sub>(HCOOH)⊃(CH<sub>3</sub>)<sub>2</sub>NH has only  $\mu^1$  oxygen binding metal centers. The  $\alpha$ -Mg-formate crystallizes in monoclinic space group (*P2<sub>1</sub>/n*) and  $\beta$ ,  $\gamma$ -Mg-formate crystallizes in orthorhombic space group (*Pca2<sub>1</sub>* and

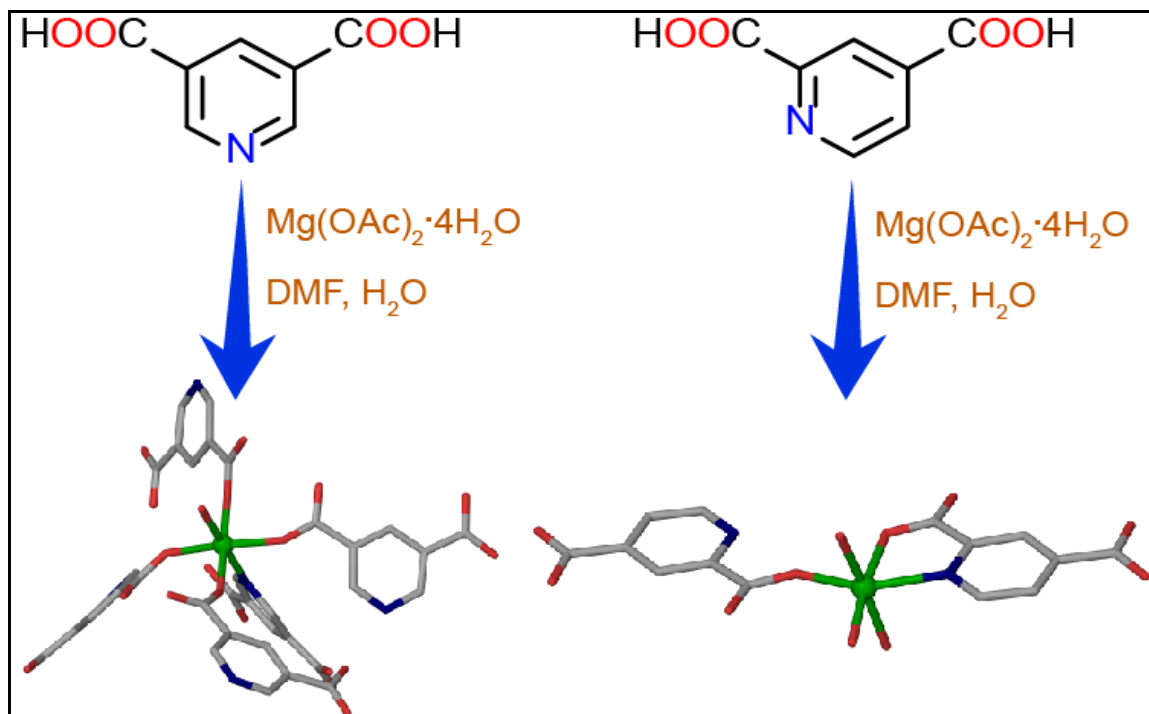
*Pbcn*). All the Mg-formates contain octahedral  $\text{Mg}^{2+}$  centers. In case of  $\alpha$ -Mg-formate and  $\gamma$ -Mg-formate, the edge share  $\text{MgO}_6$  octahedra form one dimensional chain and the chains were also connected through vertex share octahedra to form three dimensional frame works. Whereas, in  $\beta$ -Mg-formate the one dimensional chains, formed by edge share octahedra, were connected through formate anions ( $\text{HCO}_2^-$ ) not through vertex share octahedra. In  $\alpha$ -Mg-formate Mg(3) and Mg(4) were in transoid orientation with respect to the planes formed by Mg(1)–Mg(2)–Mg(1) (**Figure 2.2b**) and Mg(1)–Mg(4)–Mg(1) (**Figure 2.2c**); whereas in  $\gamma$ -Mg-formate those Mg atoms were arranged in cisoid orientation (**Figure 2.2e** and **Figure 2.2f**). As a result, the edge shared  $\text{MgO}_6$  octahedra in  $\alpha$ -Mg-formate were arranged parallel (**Figure 2.2a**) while in  $\gamma$ -Mg-formate they were arranged in an orthogonal manner (**Figure 2.2d**). The  $\mu^1$  and  $\mu^2$  Mg–O bond distances in all three  $\alpha$ ,  $\beta$  and  $\gamma$ -Mg-formate range from 2.01 Å to 2.05 Å and 2.06 Å to 2.13 Å respectively.

### 2.2.2 Structural analysis of Mg-MOF-1 and Mg-MOF-2:

As 3,5-pyridine dicarboxylic acid was sparingly soluble in water at moderate temperature we used the solvent DMF in which it was readily soluble. 2,4-pyridine dicarboxylic acid, was soluble in water and we used the same for the synthesis. Also the reaction of it with  $\text{Mg}(\text{CO}_2\text{CH}_3)_2 \cdot 4\text{H}_2\text{O}$  at room temperature results into the formation of microcrystalline precipitate of Mg-MOF-1 and -2. So we used the hydrothermal condition (teflon-lined stainless steel autoclave at 125 to 150 °C) for synthesis which results into the formation of single crystals suitable for X-ray diffraction. Before solvothermal reactions, stirring of the heterogeneous solutions for a period of time was helpful for a high purity of both compounds, which was confirmed by their PXRD patterns. As expected, IR spectra of Mg-MOF-1 and -2 were very similar. For the IR spectra, the broad bands centered at ca.  $3401\text{ cm}^{-1}$  and  $3435\text{ cm}^{-1}$  indicates the O–H stretching of water for Mg-MOF-1 and -2. Notably, in the IR spectra of Mg-MOF-1, the presence of characteristic absorption bands of carboxyl, which appears at  $1687\text{ cm}^{-1}$  for the coordinated ligand, reveals its complete/partial deprotonation in the crystal lattice. In the IR spectra of Mg-MOF-2, the presence of characteristic absorption bands of carboxyl, which appears at  $1662\text{ cm}^{-1}$  and  $1699\text{ cm}^{-1}$  for the coordinated and free carboxylic acid ligand, reveals its presence in the crystal lattice. Mg-MOF-1 crystallizes in hexagonal chiral space group  $P6_122$ , and

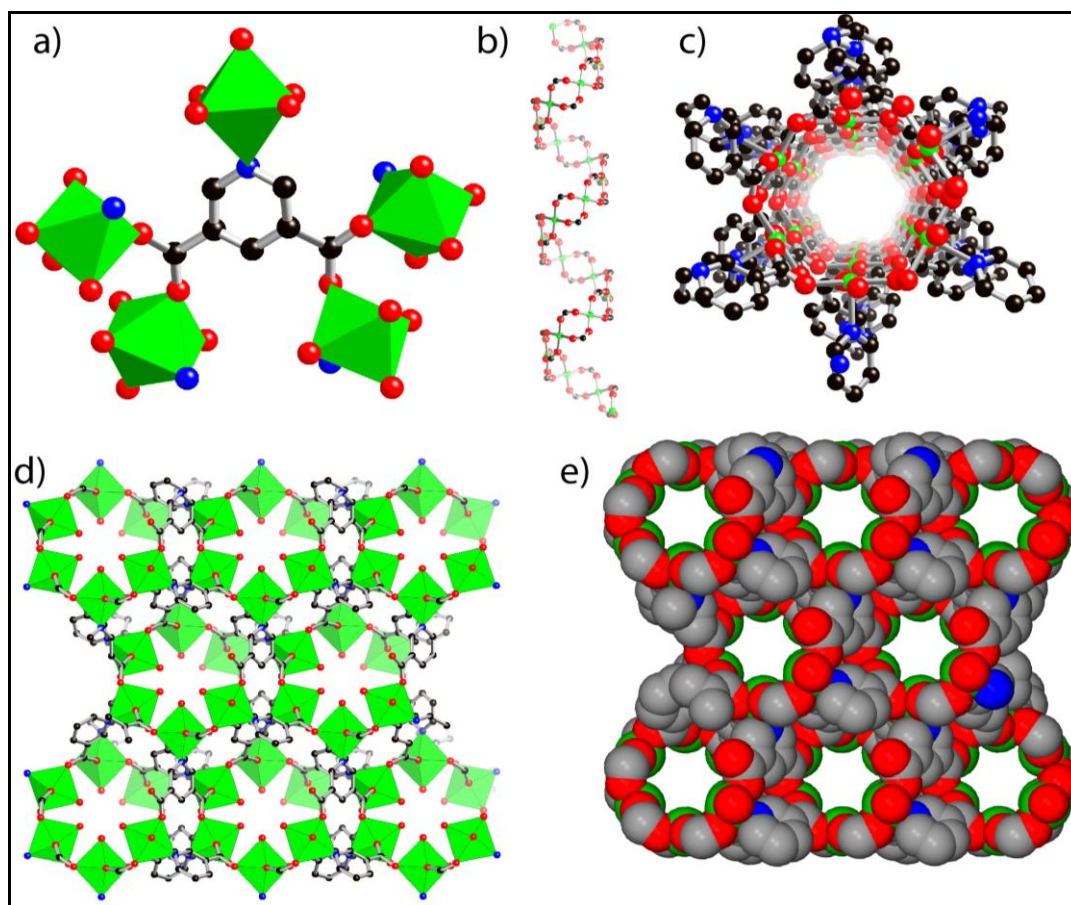


structural determination by x-ray single crystal diffraction reveals a 3D network of  $\text{Mg}^{2+}$  linked by 3,5-PDC (**Figure 2.3**). The asymmetric unit of Mg-MOF-1 consists of one crystallographically independent  $\text{Mg}^{2+}$  ion, five 3,5-pyridine dicarboxylate (3,5-PDC) and one coordinated  $\text{H}_2\text{O}$  molecule. In the framework each  $\text{Mg}^{2+}$  was surrounded by one nitrogen atom (from the pyridine  $-\text{N}$  functionality) and five oxygen atoms (O1, O2, O3, O1A and O2A) from four  $\mu_2\text{-CO}_2^-$  groups of 3,5-PDC ligands and one coordinated



**Figure 2.3:** Schematic diagram showing structural diversities of Mg-MOFs.

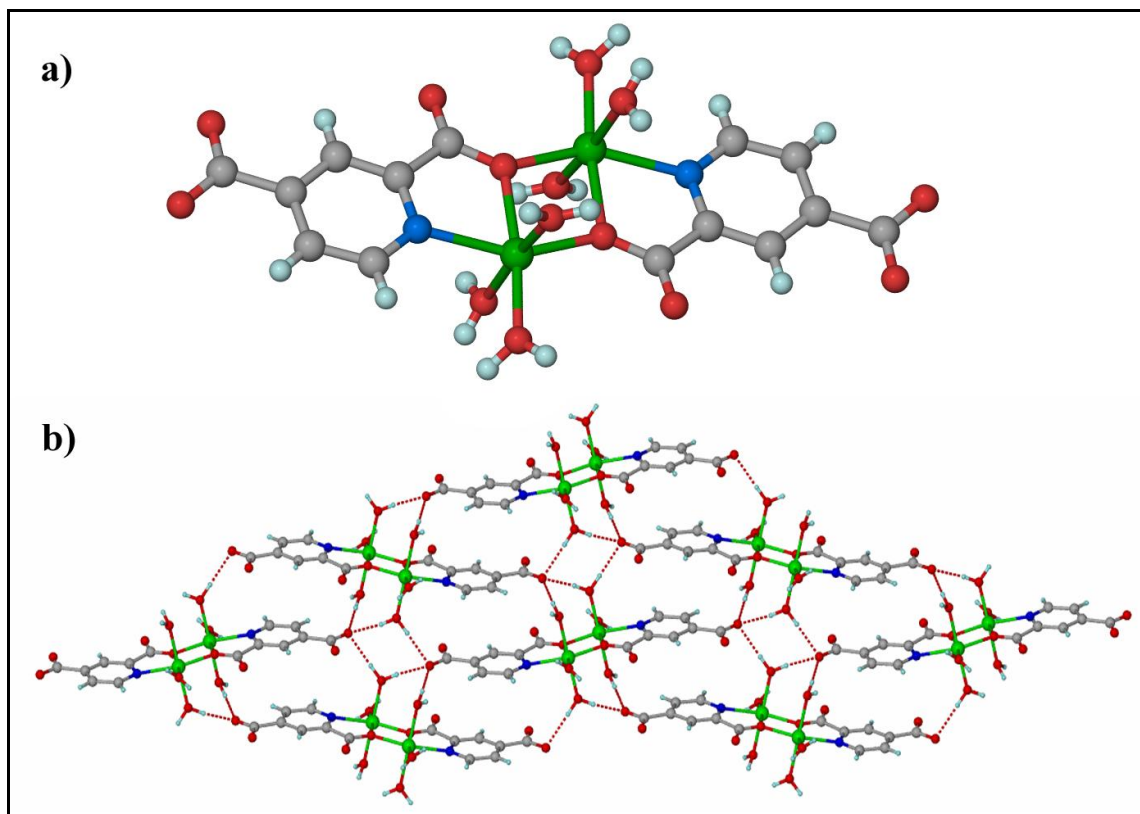
water molecule giving an octahedral coordination environment. In the crystal structure, each pentadentate 3,5-PDC ligand was coordinated with five different  $\text{Mg}^{2+}$  ions with  $\text{Mg}-\text{O}$  bond distance ranges from 2.024(3) to 2.092(3) Å.  $\text{Mg}-\text{O}_{\text{water}}$  bond distance was 2.078(2) Å and the  $\text{Mg}-\text{N}_{3,5\text{-PDC}}$  bond distance was 2.254(3) Å. The Mg-MOF-1 contains hexagonal 1D channel along crystallographic  $c$  axis. Figure 2.4b shows the helical connectivity between  $\text{Mg}^{2+}$  ions inside these channels with a 4.56 (2) Å distance between adjacent  $\text{Mg}^{2+}$  ions. The void space was calculated using *PLATON* [2.39] suggesting a 11.9% void volume to the total crystal volume; however, this would be increased to 38.7% after removal of the coordinated water molecules. The pore diameter of the channel was 4.0 Å (the channel size was measured by considering the Van der



**Figure 2.4:** a) Polyhedral representation of Mg-MOF-1 [Mg(3,5-PDC)(H<sub>2</sub>O)] showing the coordination environment around Mg. b) Helical connectivity between Mg<sup>2+</sup> ions inside the channels. c) Ball and stick representation of along c axis of Mg-MOF-1 showing the 1D channel with open Mg-metal sites. d) Polyhedral model of Mg-MOF-1 showing 1D channels with coordinated water molecules facing towards the channels. e) Space-fill model of Mg-MOF-1 showing pores along c axis. Color code: Mg (green), N (blue), C (black), O (red).

Walls radii of the constituting atoms). Topologically, each 3,5-PDC ligand provides five donor sites and connects five Mg<sup>2+</sup> ions, so each 3,5-PDC and Mg<sup>2+</sup> ion can be defined as a five-connected node at a ratio of 1:1, which generated a new chiral hexagonal network (**Figure 2.4d,e**). The hexagonal network was notably interesting as they hold helical channels and along the channel H<sub>2</sub>O molecules coordinated to the Mg<sup>2+</sup> and were facing towards the channel (**Figure 2.4d**). A chiral hexagonal Mg-MOF has been synthesized from an achiral organic building unit for the first time. There were four chiral Mg-MOFs reported in the CSD, but none of them obtain a hexagonal orientation. Thus, this was a new example of a magnesium based metal-organic framework adopting a neutral non-interpenetrated chiral topological network.

The structural detail of its 0D analogue Mg-MOF-2 [Mg(2,4-PDC)(H<sub>2</sub>O)<sub>3</sub>] has been discussed to show how subtle variation in the ligand architecture changes the resulting structure from 0D to 3D. Changing the ligand from 3,5-pyridine dicarboxylic acid to 2,4-pyridine dicarboxylic acid affords compound Mg-MOF-2 which crystallizes in the orthorhombic *Pbca* space group. The asymmetric unit of Mg-MOF-2 consists of one



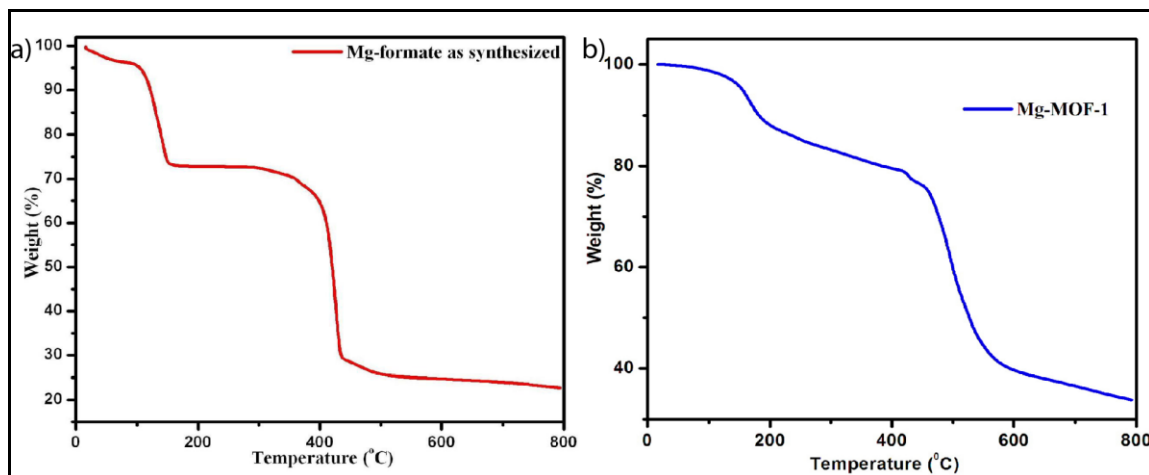
**Figure 2.5:** a) The SBU in the crystal structure of Mg-MOF-2 [Mg(2,4-PDC)(H<sub>2</sub>O)<sub>3</sub>] showing the coordination environment around Mg. b) Packing diagram of Mg-MOF-2 highlighting the hydrogen bonding network.

crystallographically independent Mg<sup>2+</sup> ion, one 2,4-pyridine dicarboxylate (2,4-PDC) and three coordinated H<sub>2</sub>O molecules. Structural determination reveals that each Mg<sup>2+</sup> was chelated to symmetry related 2,4-PDC ligand centers through the pyridine nitrogen (N1) and carboxylate functionality adjacent to pyridine nitrogen. Each Mg<sup>2+</sup> ion was coordinated to three water molecules (O5, O6 and O7) and fulfills the octahedral geometry. Mg–O bond distances were in the range of 2.014(1) to 2.099(1) Å, and the Mg–N1 bond distance was 2.2199(4) Å, slightly higher than that of Mg-MOF-1. The

coordinated water molecules and non-coordinated carboxylate oxygens of 2,4-PDC were involved in O–H...O hydrogen bonding<sup>25</sup> [D, 2.665(2) Å; *d*, 1.801(3) Å;  $\theta$ , 172.1°], forming a 3D supramolecular network (**Figure 2.5**).

### 2.2.3 Thermal properties and X-ray powder diffraction analysis:

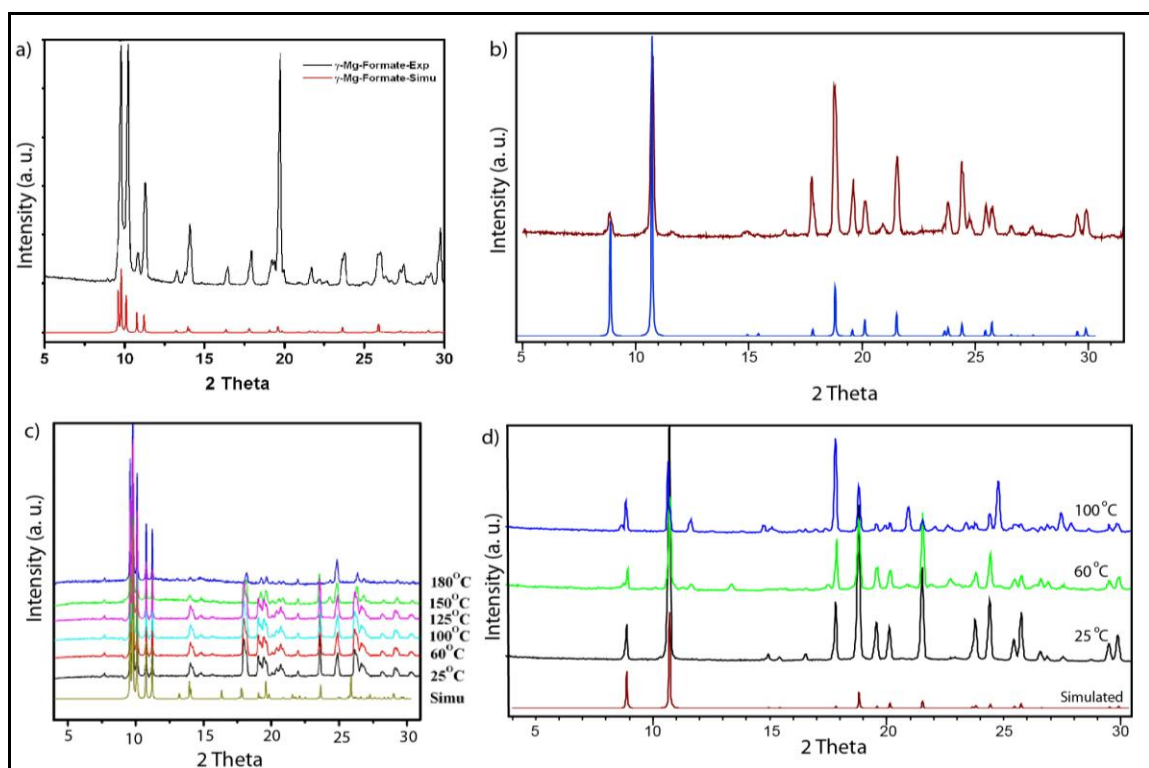
We have synthesized  $\alpha$ - and  $\gamma$ -Mg-formates in bulk for in situ variable temperature PXRD analysis. In order to confirm the phase purity of the bulk materials, powder X-ray diffraction (PXRD) experiments were carried out on those compounds. The PXRD of experimental and computer-simulated pattern of  $\gamma$ -Mg-formate was shown in the figure 2.7a. All major peaks of experimental powder X-ray patterns (PXRD) matches quite well that of simulated XRPD, indicating their reasonable crystalline phase purity. Thermal gravimetric analysis (TGA) performed on as-synthesized  $\gamma$ -Mg-formate revealed this compound high thermal stability (**Figure 2.6a**). The TGA trace for  $\gamma$ -Mg-formate showed a gradual weight-loss step of 27% (108–155 °C), corresponding to the escape of all



**Figure 2.6:** a) Thermogravimetric analysis of  $\gamma$ -Mg-formate (10 °C/min). b) Thermo gravimetric analysis plot of Mg-MOF-1.

solvent molecules trapped in the pores [ $2(\text{CH}_3)_2\text{NH}$ ; calc. 27%] followed by a plateau (155–370 °C) indicating its high thermal stability in the absence of guest molecules (**Figure 2.6a**). We note that the dimethylamine molecules in Mg-formate were released without damaging the frameworks, as evidenced by the coincidence of the powder x-ray diffraction (PXRD) patterns of  $\gamma$ -Mg-formate powder sample heated to and held at 120 °C, in  $\text{N}_2$  atmosphere with the PXRD patterns simulated from single crystal structures. Such high thermal and architectural stability of  $\gamma$ -Mg-formate was also verified from its

in situ VTPXRD patterns at different temperature which coincides with the patterns simulated from single crystal structures. In situ VTPXRD of  $\alpha$ -Mg-formate and  $\gamma$ -Mg-formate (**Figure 2.7c**) indicate the retention of crystallinity of these samples at high temperature. It also reveals the fact that there were no possibilities of phase changes at higher temperature for these samples. We were unable to perform a VTPXRD experiment on  $\beta$ -Mg-formate as all our attempts to synthesize it in phase pure bulk failed resulting in the production of a mixture of  $\beta$ -Mg-formate and anhydrous  $\text{Mg}(\text{HCOO})_2(\text{HCOOH})\cdot(\text{CH}_3)_2\text{NH}$ .



**Figure 2.7:** Comparison of PXRD patterns of the as-synthesized MOFs (black) with the simulated pattern from the single-crystal structure (red) for a)  $\gamma$ -Mg-formate and b) Mg-MOF-1. VT-PXRD patterns of c)  $\gamma$ -Mg-formate and d) Mg-MOF-1 at different temperature which coincides with the patterns simulated from single crystal structures.

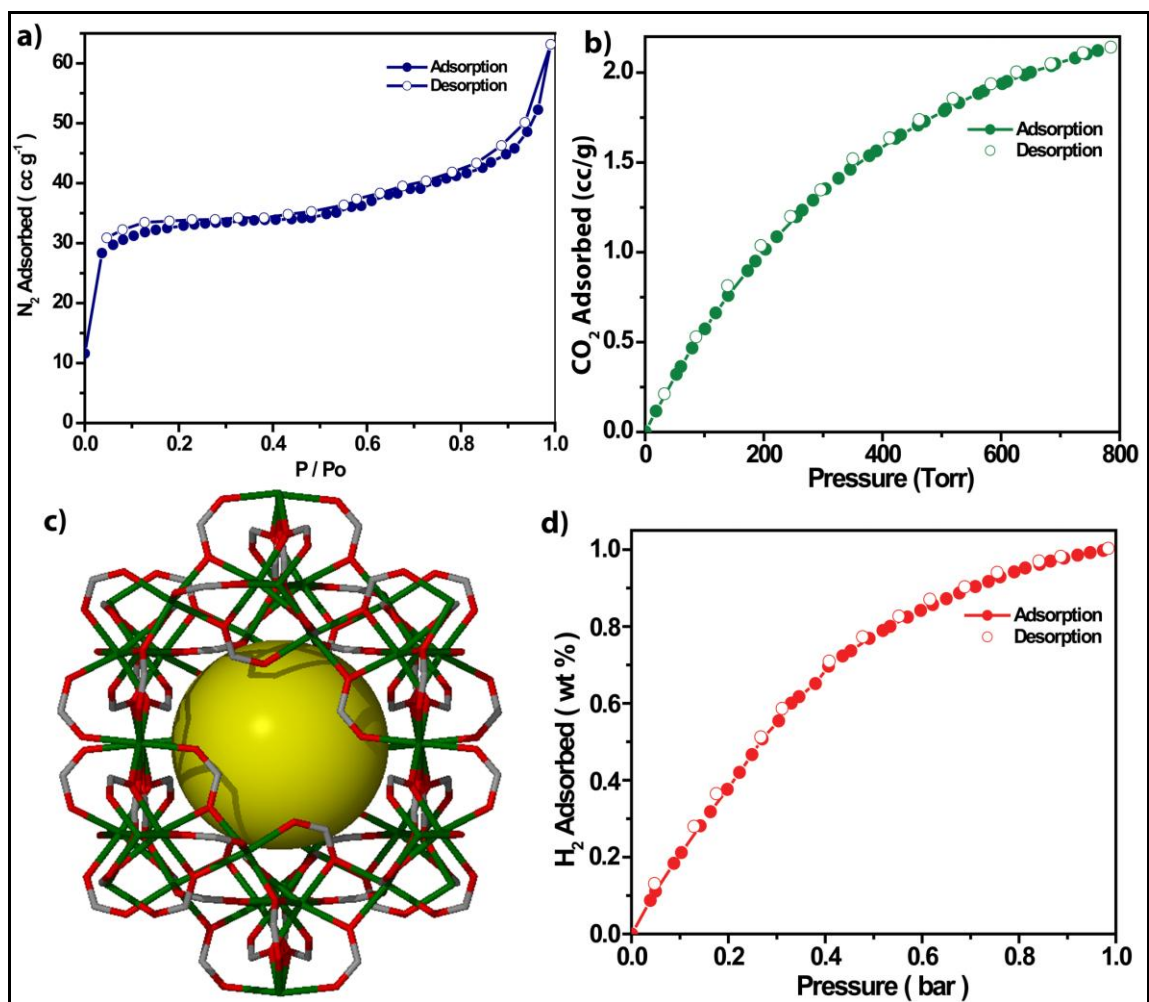
All major peaks of experimental powder X-ray patterns (PXRD) of compound Mg-MOF-1 matches quite well that of simulated XRPD, indicating their reasonable crystalline phase purity. Thermal gravimetric analysis (TGA) performed on as-synthesized Mg-MOF-1 revealed this compound remarkable thermal stability (**Figure 2.6b**). The TGA trace for Mg-MOF-1 showed a gradual weight-loss step of 10.3% (100–

150 °C), corresponding to the escape of all water molecules trapped in the pores [1 H<sub>2</sub>O; calc. 10.9%], followed by a plateau (120–450 °C) indicating its high thermal stability in the absence of guest molecules. We note that the water molecules in Mg-MOF-1 were released without damaging the frameworks, as evidenced by the coincidence of the powder x-ray diffraction (PXRD) patterns of Mg-MOF-1 sample heated to and held at 120 °C, in N<sub>2</sub> atmosphere with the PXRD patterns simulated from single crystal structures. Such high thermal and architectural stability of Mg-MOF-1 was also verified from its in situ VT-PXRD patterns at different temperature (**Figure 2.7d**) which coincides with the patterns simulated from single crystal structures.

#### 2.2.4 Gas adsorption properties:

We focused to examine the porosity of  $\gamma$ -Mg-formate and prepared it at the gram scale to allow detailed investigation of the aforementioned property. An important structural feature of this  $\gamma$ -Mg-formate was that they possess pores (3.6 Å in diameter) (**Figure 2.8c**). Recently researchers envisaged that MOFs containing open Mg metal sites (Mg-MOF-74) rivals competitive materials in CO<sub>2</sub> capture, with 8.9 wt.% dynamic capacity, and undergoes facile CO<sub>2</sub> release at 80 °C [2.26]. The dimethylamine molecules inside the pore in as-synthesized  $\gamma$ -Mg-formate could be more readily removed by solvent-exchange. The thermogravimetric behavior of  $\gamma$ -Mg-formate was significantly simplified after they were immersed in organic solvents, such as chloroform. To remove the guest species from the frameworks and prepare the evacuated forms of  $\gamma$ -Mg-formate for gas-adsorption analysis, the as-synthesized  $\gamma$ -Mg-formate sample were immersed in chloroform at ambient temperature for 48 h, and evacuated at ambient temperature for 24 h, then at an elevated temperature (120 °C) for 6 h. MOF sample thus obtained was optimally evacuated, as evident from the long plateau (108–370 °C) in the TGA traces.

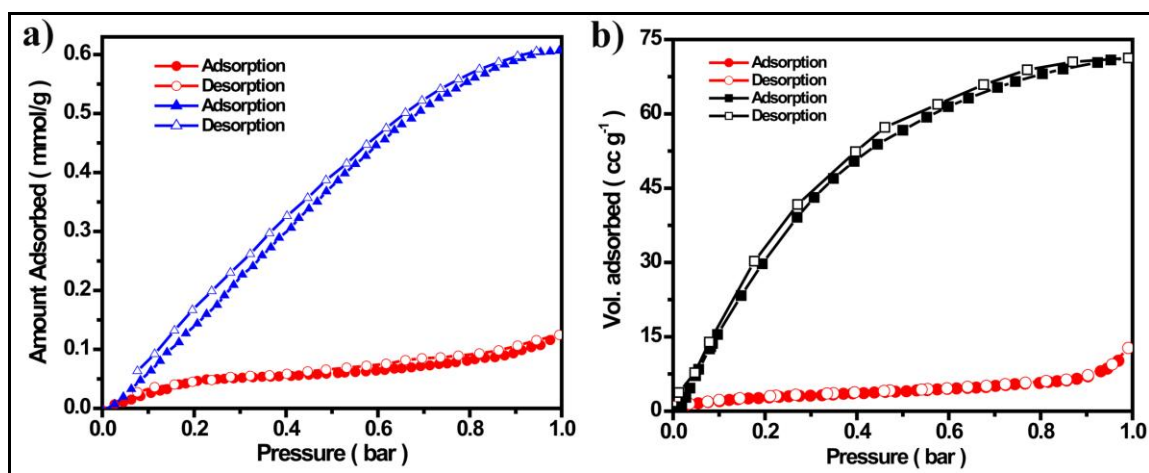
The architectural rigidity and consequently the permanent porosity of evacuated  $\gamma$ -Mg-formate were unequivocally proven by gas-adsorption analysis. The nitrogen (N<sub>2</sub>), hydrogen (H<sub>2</sub>) and carbon-dioxide (CO<sub>2</sub>) gas-adsorption experiments were carried out on  $\gamma$ -Mg-formate (**Figure 2.8b,c**). These isotherms exhibit typical physisorption behavior, with a steep initial increase at low pressures and saturation at higher pressures.  $\gamma$ -Mg-formate adsorbs less nitrogen (38 cc g<sup>-1</sup>) than the  $\alpha$ -Mg-formate (88 cc g<sup>-1</sup>) reported by



**Figure 2.8:** Gas adsorption isotherms of  $\gamma$ -Mg-formate: a)  $N_2$  at 77 K (blue circles), b)  $CO_2$  (green circles), at 298 K, and c) stick model of  $\gamma$ -Mg-formate showing the voids. d)  $H_2$  (red circles) at 77 K. The filled and open shapes represent adsorption and desorption, respectively.  $P/P_0$ , relative is the pressure at saturation vapor pressure of the adsorbate gas.

Rood *et al.* [2.20b] As a result the specific surface area of  $\gamma$ -Mg-formate (BET,  $120 \text{ m}^2 \text{ g}^{-1}$ ) was lower than the  $\alpha$ - polymorph (BET,  $150 \text{ m}^2 \text{ g}^{-1}$ ). However, initial hydrogen uptake of  $\gamma$ -Mg-formate reached almost 1.0 wt% when the adsorbate pressure approached 760 torr at 77 K (**Figure 2.8d**). This was higher than the hydrogen uptake of  $\alpha$ -Mg-formate (0.6 wt%) reported by Rood *et al* [2.20b] under similar conditions. It was noteworthy that low pressure hydrogen uptake of newly found  $\gamma$ -Mg-formate compared well with the reported hydrogen uptake of  $\alpha$ -Mg-formate at pressure higher than 760 torr [2.20b]. The maximum excess hydrogen uptake of the  $\alpha$ -Mg-formate at 77 K was about 1.1 wt% with no hysteresis between adsorption and desorption. Although this  $H_2$  adsorption was

somewhat moderate, they compare well with the value of 0.7 wt% obtained for the highest capacity zeolite ZSM-5 and some of Mg-MOFs reported in the literature [2.27]. Recently researchers have shown that MOFs can hold large amounts of carbon dioxide and have demonstrated that MOFs can capture CO<sub>2</sub> selectively from CO and CH<sub>4</sub>. Figure 2.8b shows the CO<sub>2</sub> adsorption isotherms for  $\gamma$ -Mg-formate, which shows a moderate affinity and capacity for CO<sub>2</sub> (3.4 Å kinetic diameter) at 298 K. The CO<sub>2</sub> uptake of  $\gamma$ -Mg-formate at 298 K (2.01 mmol g<sup>-1</sup>) (Figure 2.8b) was higher than the  $\alpha$ - polymorph (1.69 mmol gm<sup>-1</sup>). Although this CO<sub>2</sub> uptake was somewhat modest, but it compared well with the CO<sub>2</sub> uptake of several Mg-MOFs and ZIFs reported in the literature.



**Figure 2.9:** Selective gas adsorption isotherms of Mg-MOF-1. a) CO<sub>2</sub> (blue, triangles) and N<sub>2</sub> (red, circle) at 298 K, b) H<sub>2</sub> (black, squares) and N<sub>2</sub> (red, circle) at 77 K for Mg-MOF-1; the filled and open shapes represent adsorption and desorption, respectively.  $P/P_0$ , relative pressure at the saturation vapour pressure of the adsorbate gas.

We focused to examine the chemical stability and porosity of Mg-MOF-1 and prepared it at the gram scale to allow detailed investigation of the aforementioned properties. An important structural feature of this Mg-MOF-1 was that they possess pores (4.0 Å in diameter) containing open Mg metal sites. Recently researchers envisaged that MOFs containing open Mg metal sites (Mg-MOF-74) rivals competitive materials in CO<sub>2</sub> capture, with 8.9 wt.% dynamic capacity, and undergoes facile CO<sub>2</sub> release at 80 °C [2.26a]. The H<sub>2</sub>O molecules coordinated in as-synthesized Mg-MOF-1 could be more readily removed by solvent-exchange. The thermogravimetric behavior of Mg-MOF-1 was significantly simplified after they were immersed in organic solvents, such as methanol. To remove the guest species from the frameworks and prepare the evacuated



forms of Mg-MOF-1 for gas-sorption analysis, the as-synthesized Mg-MOF-1 sample were immersed in methanol at ambient temperature for 48 h, and evacuated at ambient temperature for 5 h, then at an elevated temperature (100 °C) for 2 h. MOF samples thus obtained were optimally evacuated, as evidenced by their well maintained PXRD patterns and the long plateau (25–350 °C) in their TGA traces.

The architectural rigidity and consequently the permanent porosity of evacuated Mg-MOF-1 were unequivocally proven by gas-sorption analysis. Mg-MOF-1 was nonporous to nitrogen because its aperture size (4.0 Å) was almost equivalent to the kinetic diameter of nitrogen (3.6 Å); however, it was able to take up hydrogen (H<sub>2</sub>) and carbon-dioxide (CO<sub>2</sub>). Mg-MOF-1 showed reversible hydrogen sorption behavior (*Figure 2.9b*). The initial hydrogen uptake of Mg-MOF-1 reached almost 0.8 wt% in when the adsorbate pressure approached 1 atm. Although the H<sub>2</sub> adsorptions were somewhat moderate, they compare well with the value of 0.7 wt% obtained for the highest capacity zeolite ZSM-5 and some of Mg-MOFs reported in the literature [2.27]. As shown in figure 2.9a, the framework exhibits a typical reversible CO<sub>2</sub> (3.4 Å) uptake profile at 298 K. The modest CO<sub>2</sub> uptake at 760 torr was 14 cm<sup>3</sup> gm<sup>-1</sup>. Activated Mg-MOF-1 exhibits very interesting selective adsorption of H<sub>2</sub> and CO<sub>2</sub> over N<sub>2</sub>. The gas uptake of Mg-MOF-1 for H<sub>2</sub>, CO<sub>2</sub> and N<sub>2</sub> was 75.0, 14.0 and 2.0 cm<sup>3</sup> g<sup>-1</sup> and at  $P/P_0$  of about 0.9, respectively, underlying the potential of Mg-MOF-1 for selective separation of H<sub>2</sub> and CO<sub>2</sub> over N<sub>2</sub> (*Figure 2.9*). Such preferential H<sub>2</sub> and CO<sub>2</sub> uptake over nitrogen might be attributed to size-exclusive effect in which the hexagonal channels were accessible to hydrogen and oxygen, but not to nitrogen because of their differential kinetic diameters of 2.8, 3.46 and 3.64 Å, respectively. Such higher storage capacity was practically important for porous MOFs to be efficiently utilized for the H<sub>2</sub>/N<sub>2</sub> and CO<sub>2</sub>/N<sub>2</sub> separation

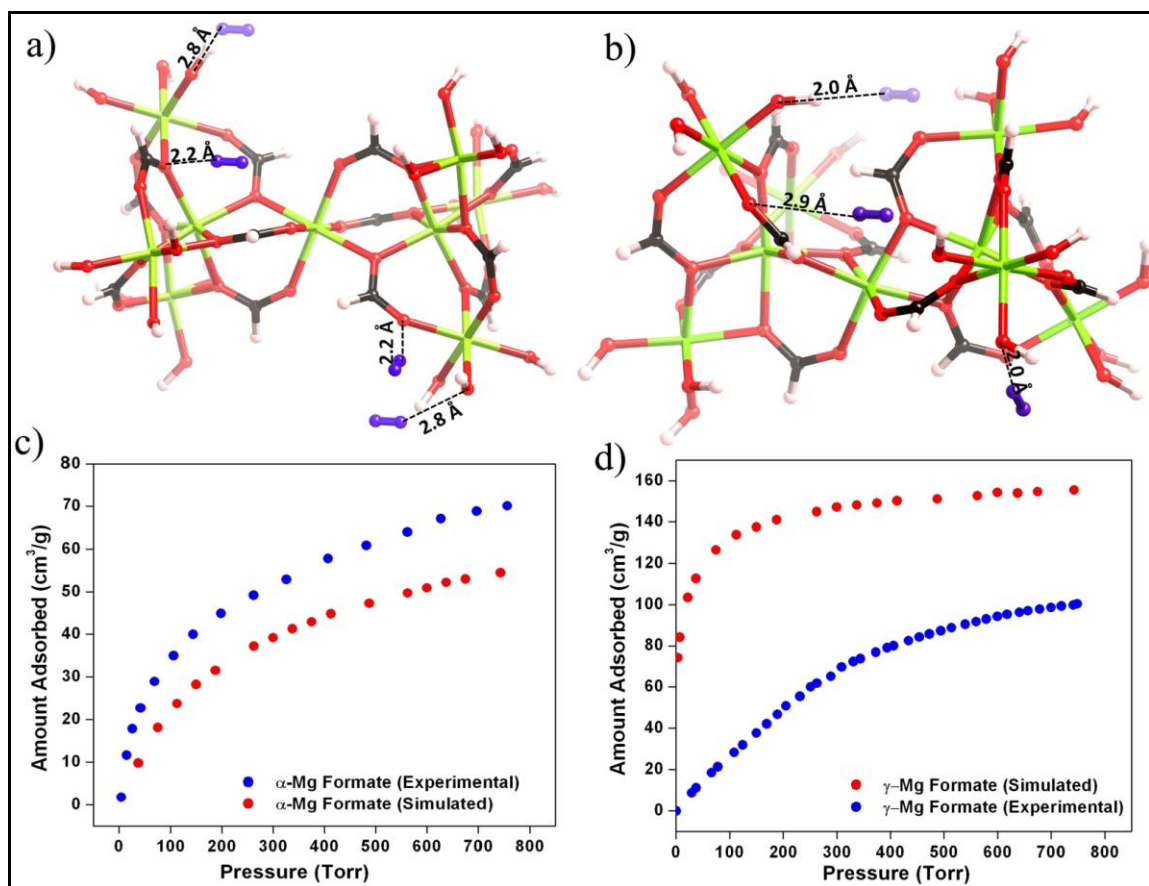
Recently Yaghi and co-workers proved that MOFs could show exceptional resistance to hydrolysis [2.28]. The chemical stability of Mg-MOF-1 was examined by suspending samples in boiling benzene, and methanol, conditions that reflect extreme operational parameters of typical industrial chemical processes. MOF samples were immersed in the desired solvent for 1–7 days at ambient temperature, 50 °C, and at the boiling point of each medium. During this process, samples were periodically observed under an optical

microscope and found to be insoluble under each of these conditions. PXRD patterns collected for each sample at designated intervals showed that the solid samples of Mg-MOF-1 maintained their full crystallinity. A plausible explanation of this chemical stability could be due to the hydrophilic pores in Mg-MOF-1 was likely to repel benzene and MeOH molecules preventing the attack of MgO<sub>5</sub>N units and dissolution of the framework.

### **2.2.5 Computational/theoretical results:**

#### **2.2.5.1 Quantum chemical calculations for $\gamma$ -Mg-formate:**

Portion of the 111 supercell of both  $\alpha$  and  $\gamma$ -Mg-formate, which have been used for all ab-initio quantum chemical calculation as cluster model (**Figure 2.3**). It was clearly visible from the crystal structure of these two  $\alpha$  and  $\gamma$ -Mg-formate (**Figure 2.1**) that there were highly electronegative oxygen atoms (from formate ligand), which were exposed to the pore surface. These particular surface areas have been scanned for adsorption energies and adsorption sites. We have calculated adsorption energies for each position for each hydrogen and compared the lowest energy positions at each surface sites. The adsorption energies we get were the local energy minima from every complete optimization cycle. Comparison of the adsorption energies often suggested similar adsorption energies and sites due to the choice of initial position of hydrogen molecules. The corresponding position of the hydrogen molecule with lowest adsorption energy can be obtained from the coordinate of the optimized geometry, which was depicted in figure 2.1. It was clearly visible from the figure 2.1 that the hydrogen molecules were oriented towards oxygen i.e. to the pore surface. This showed that oxygen atoms have pronounced affinity to bind to the free hydrogen molecules. The lowest energy adsorption sites of hydrogen molecules with respect to the oxygen atoms of formate anion were represented in figure 2.10. The cluster for quantum chemical calculations was extracted from the supercells of these two formates. Therefore some oxygen carbon bonds were cleaved and hydrogen atoms saturated the dangling bonds. So the chemistry of those oxygen atoms changed and we had two types of oxygen atoms in the cluster, first one was the original formate oxygen from the supercell and the second one was hydroxyl oxygen which we have generated while making the



**Figure 2.10:** Different positions of hydrogen molecule in (a)  $\alpha$ -Mg-formate cluster and (b)  $\gamma$ -Mg-formate cluster. Simulated and experimental isotherms for (c)  $\alpha$ -Mg-formate and (d)  $\gamma$ -Mg-formate.

cluster (**Figure 2.10a,b**). We had found from this quantum chemical calculation that hydroxyl oxygen (binding energy is  $\sim -5.9$  KJ/mol for  $\alpha$ -formate and  $\sim -5.5$  KJ/mol for  $\gamma$ -formate) has a higher affinity to attract hydrogen than the formate oxygen ( $\sim -2.6$  KJ/mol for both of them). But it was also evident that if we do not replace the formate oxygen with hydroxyl oxygen, hydrogen molecule would interact with formate oxygen but with lesser interaction energy than that of hydroxyl oxygen.

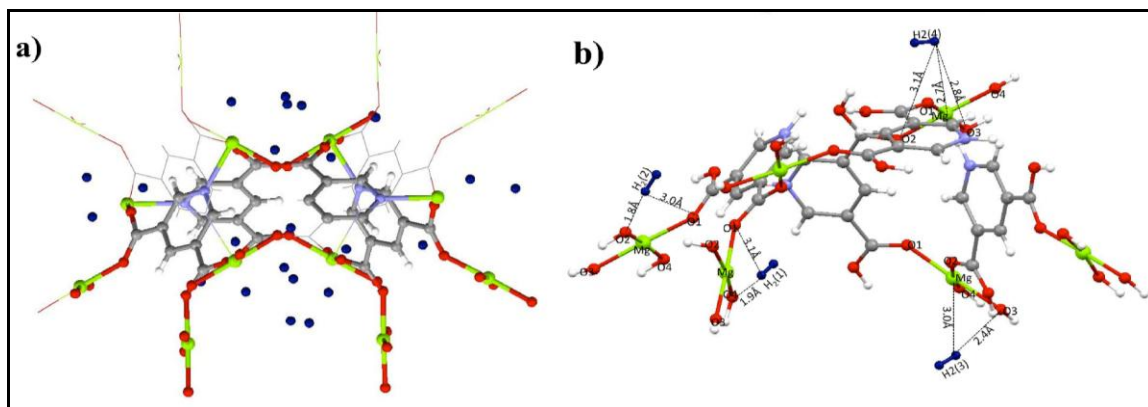
Figure 2.10c and 2.10d shows the comparison between experimental and simulated single component H<sub>2</sub> adsorption isotherm of  $\alpha$ -Mg-formate and  $\gamma$ -Mg-formate at low pressure region. The excess amount adsorbed,  $N_{\text{ex}}$ , was defined as  $N_{\text{ex}} = N_{\text{total}} - \rho v$ , where  $\rho$  was the density of the bulk gas phase and  $v$  was the pore volume (calculated from the x-ray crystallographic structure). Data for H<sub>2</sub> adsorption isotherm in  $\alpha$ -Mg-formate has been taken from the literature [2.20a]. Calculated adsorption isotherms for

pure H<sub>2</sub> were obtained by GCMC simulations. The GCMC simulations predict the measured and available experimental results with acceptable accuracy. The calculated loading of hydrogen in  $\alpha$ -Mg-formate was 54.38 cc/g and in case of  $\gamma$ -Mg-formate the value was 155.34 cc/g at 760 torr. pressure. The difference between experimental and simulated isotherms can be attributed to the contraction of pores after removal of the solvent [2.29]. These pore contractions of the  $\gamma$ -Mg-formate giving rise to lesser amount of loading with respect to the theoretically predicted isotherm which has been calculated from the original crystal structure (ignoring the solvent molecules). In addition, the empirical force fields used may not be accurate enough to describe such discrepancy, particularly in case of  $\alpha$ -Mg-formate.

### 2.2.5.2 Quantum chemical calculations for Mg-MOF-1:

In table 1, we have summarized the results of adsorption energies and the positions of adsorption sites of 4 Hydrogen molecules out of 18, which possess higher adsorption energies than others. After optimization some of the final configurations result in the same adsorption sites of hydrogen molecules in framework. This suggested that there were some positions, which have much higher interaction strength than others. Hydrogen at position 1 (**Table 2.1**) shows the highest adsorption energy, which was -36.17 KJ/mol at 0 K. We have found that 2 initial structures among 18 showed the same site of hydrogen adsorption with the same energy. This confirmed that the adsorption position near to the Mg atoms (metal centers) inside the pore have high affinity to adsorb hydrogen and results in strong interaction. Hydrogen at position 2 shows much lower adsorption energy (40% lower) than position 1. Position 3 and 4 has even lower energies and the adsorption sites were representing positions with weak interactions. In figure 2.11b we have depicted all the 4 positions and their relative distance from the nearer atoms mainly the magnesium and oxygen to elucidate the spatial positions of the adsorption sites of the each hydrogen molecules. It was evident from the table 2.1 and the figure 2.11 that H<sub>2</sub> at positions 1 and 2 has some spatial differences with positions 3 and 4. It was important to note that at positions 1 and 2, H<sub>2</sub> molecules were closer to one oxygen atom, which was bonded to magnesium. In these two positions hydrogen molecules were approaching in a tilted fashion towards the Magnesium atom. However hydrogen at position 4 was almost parallel to the Mg-O plane. Therefore we can infer that

hydrogen at position 1 and 2 get induced by the electronegative oxygen atom (which was at a distance of 1.9 Å) and become stabilized



**Figure 2.11:** a) Positions of adsorbed hydrogen molecules in Mg-MOF unit cell from GCMC calculation. Highlighted region was used as the finite structure for ab-initio quantum chemistry calculation. b) Different adsorption sites of Hydrogen molecules from ab-initio quantum chemical calculations.

due to induced electrostatic interaction. This was confirmed by checking the separation of charge on each hydrogen atoms of the hydrogen molecules. Hydrogen molecules at position 1 have the highest adsorption energy and consequently the highest charge separation (**Table 2.1**). However position 3 and 4 has no significant charge separation. This was also cleared from the bond length between hydrogen atoms of hydrogen molecules at position 1 and 2, which was longer than H<sub>2</sub> at position 3 and 4. The spatial arrangement of H<sub>2</sub>(1) and H<sub>2</sub>(2) was almost same (**Table 2.1**). But the adsorption energy of H<sub>2</sub>(1) was higher than H<sub>2</sub>(2). H<sub>2</sub>(1) was inside the pore of the finite structure and get stabilized by the environment. H<sub>2</sub>(2) was situated in another pore, which was not considered in this finite calculation and therefore showed much lower binding energy.

**Table 2.1:** Spatial position of H<sub>2</sub> molecules from ab-initio quantum chemistry calculations.

Position of H <sub>2</sub>	Binding energy of H <sub>2</sub> at that position (KJ/mol)	H-H bond (Å)	Distance between H <sub>2</sub> and Mg (Å)	Distance between H <sub>2</sub> and O <sub>1</sub> (Å)	Distance between H <sub>2</sub> and O <sub>2</sub> (Å)	Distance between H <sub>2</sub> and O <sub>3</sub> (Å)	Distance between H <sub>2</sub> and O <sub>4</sub> (Å)	Partial charge (e) of H(1) atom of H <sub>2</sub> molecule	Partial charge (e) of H(2) atom of H <sub>2</sub> molecule
H <sub>2</sub> (1)	-36.17	0.767	3.5	3.1	5.4	4.8	1.9	0.293	-0.365
H <sub>2</sub> (2)	-21.92	0.766	3.4	3.0	1.8	4.7	5.3	0.154	-0.226
H <sub>2</sub> (3)	-18.49	0.734	3.0	4.6	3.6	2.4	3.9	0.026	-0.052
H <sub>2</sub> (4)	-16.80	0.733	2.7	3.9	3.1	2.8	3.8	0.080	-0.086

Similarly differences in adsorption energies between H<sub>2</sub>(3) and H<sub>2</sub>(4) can also be explained. Actually the positions 1 and 2 were equivalent and so as were the positions 3 and 4. The reported adsorption energies were binding enthalpies (not binding free energies) because the thermal contributions were ignored.

### 2.3 Conclusions:

A new three dimensional magnesium formate polymorph namely  $\gamma$ -[Mg<sub>3</sub>(O<sub>2</sub>CH)<sub>6</sub>] has been synthesized via in situ formate anion generation method and structurally characterized. Crystal structure of this new  $\gamma$  polymorph of magnesium formate was completely different from other reported magnesium formates ( $\alpha$  and  $\beta$  polymorph). The  $\gamma$ -Mg-formate has one-dimensional channels along the  $a$ -axis, and shows reversible hydrogen (~1.0 wt% at 77 K, 760 torr) and CO<sub>2</sub> uptake (2.1 mmol g<sup>-1</sup> at 298 K, 760 torr). Quantum chemical calculation predicted the adsorption energies, which was in the range of physisorption and explained the low intake of hydrogen gas in this system.  $\gamma$ -Mg-formate outperformed the  $\alpha$  and  $\beta$  polymorph with respect to CO<sub>2</sub> and H<sub>2</sub> uptake. Also, two new Mg containing metal organic framework materials have been synthesized and structurally characterized. One of which (Mg-MOF-1) adopts the chiral hexagonal topology while the other one (Mg-MOF-2) exhibits a 0D network. The Mg-MOF-1 has one dimensional, hexagonal channel along  $c$  axis and it showed reversible hydrogen (~0.8 wt% at 77 K, 760 torr) and CO<sub>2</sub> uptake (14 cc g<sup>-1</sup> at 298 K, 760 torr).

### 2.4 Experimental procedures:

#### 2.4.1 Materials:

All reagents and solvents for synthesis and analysis were commercially available and used as received.

#### 2.4.2 Synthesis of $\gamma$ -Mg-formate Mg<sub>3</sub>(O<sub>2</sub>CH)<sub>6</sub>⊃[NH(CH<sub>3</sub>)<sub>2</sub>]<sub>0.5</sub>:

Solvothermal reaction of Mg(CO<sub>2</sub>CH<sub>3</sub>)<sub>2</sub>·4H<sub>2</sub>O (0.214 g, 1 mmol) with 1,3-benzene-ditrazole (0.214 g, 1 mmol) in a 25 mL Teflon-lined stainless steel autoclave in 5 ml DMF and 0.2 ml HNO<sub>3</sub> (3.6 M) mixture at 150 °C for 60 h produces colorless crystals of Mg<sub>3</sub>(O<sub>2</sub>CH)<sub>6</sub>⊃[NH(CH<sub>3</sub>)<sub>2</sub>]<sub>0.5</sub> in 61% yield. Crystals were collected by filtration and dried in air (10 min). [Yield: 61%, 0.130 g depending on Mg(CO<sub>2</sub>CH<sub>3</sub>)<sub>2</sub>·4H<sub>2</sub>O]. **FT-IR** : (KBr

4000-400  $\text{cm}^{-1}$ ): 3302(br), 2906(w), 1683(w), 1598(s), 1404(m), 1375(m), 1364(m), 841(w), 761(w), 694(w), 574(w). Elemental Analysis calc: C (23.20%), H (0.82%), N (1.93%); Found C (21.20%), H (0.72%), N (2.03%).

#### 2.4.3 Synthesis of Mg-MOF-1 [ $\text{Mg}(3,5\text{-PDC})(\text{H}_2\text{O})$ ]:

Solvothermal reaction of  $\text{Mg}(\text{CO}_2\text{CH}_3)_2 \cdot 4\text{H}_2\text{O}$  (0.020 g, 0.08 mmol) with 3,5-pyridine dicarboxylic acid (0.023 g, 0.14 mmol) in a 15 mL vial in DMF and  $\text{CH}_3\text{CN}$  mixture (1:1) 2 mL at 120 °C for 3 days produced colorless crystals of Mg-MOF-1 in 40% yield. Crystals were collected by filtration and dried in air (10 min). **FT-IR** : (KBr 4000-400  $\text{cm}^{-1}$ ): 3401(br), 1637(s), 1385(s), 1281(w), 1127(w), 1031(w), 927(w), 814(w), 773(m), 724(m).

#### 2.4.4 Synthesis of Mg-MOF-2 [ $\text{Mg}(2,4\text{-PDC})(\text{H}_2\text{O})_3$ ]:

A mixture of  $\text{Mg}(\text{CO}_2\text{CH}_3)_2 \cdot 4\text{H}_2\text{O}$  (0.214 g, 1mmol) with 2,4- pyridine dicarboxylic acid (0.167 g, 1 mmol) was added to 5 mL water in a teflon-lined stainless steel autoclave. The mixture was heated at 150 °C for 72 h. Colorless hexagonal crystals were collected by filtration (73% yield) and washed with water and acetone and dried in air. **FT-IR** : (KBr 4000-400 $\text{cm}^{-1}$ ): 3435(br), 3082 (s) 1699(s), 1662(s), 1560(s), 1485(s), 1403(s), 1365(s), 1017(s), 778(s), 701(s).

#### 2.4.5 General methods for characterization:

**Powder X-Ray diffraction (PXRD).** The PXRD patterns were collected on a Phillips PANalytical diffractometer on a Cu  $\text{K}\alpha$  radiation ( $\lambda = 1.5406 \text{ \AA}$ ), with a scan speed of 2°  $\text{min}^{-1}$ . The tube voltage and amperage were set at 40 kV and 50 mA respectively. Each sample was scanned between 5 and 50°  $2\theta$  with a step size of 0.02°. The instrument was previously calibrated using a silicon standard.

**Thermogravimetric analysis (TGA).** TGA was performed on a SDT Q600 TG-DTA analyzer instrument. Approximately 5 mg of the sample was added to a platinum crucible and heated from 25 to 800 °C under  $\text{N}_2$  atmosphere at a heating rate of 10 °C  $\text{min}^{-1}$ .

**IR spectroscopy.** The Fourier transform (FT) infrared spectra of the MOFs were taken on a *PERKIN ELMER FT-IR SPECTRUM* (Nicolet) spectrometer. KBr samples (2 mg in

20 mg of KBr) were prepared and 10 scans were collected at  $4\text{ cm}^{-1}$  resolution for each sample. The spectra were measured over the range of  $4000\text{-}400\text{ cm}^{-1}$

**Gas adsorption.** Hydrogen adsorption-desorption experiments were conducted at 77 K using Quantachrome Quadrasorb automatic volumetric instrument. Ultrapure  $\text{H}_2$  (99.95%) was purified further by using calcium aluminosilicate adsorbents to remove trace amounts of water and other impurities before introduction into the system. For measurements at 77 K, a standard low-temperature liquid nitrogen Dewar vessel was used.  $\text{CO}_2$  adsorption-desorption measurements were done at room temperature (298 K). Before gas adsorption measurements, the sample was activated at room temperature (for 24 hrs) and  $120\text{ }^\circ\text{C}$  (for 6 hrs) under ultrahigh vacuum ( $10^{-8}$  mbar) overnight. About 75 mg of samples were loaded for gas adsorption, and the weight of each sample was recorded before and after out-gassing to confirm complete removal of all guest molecules.

#### **2.4.6 Computational procedures:**

**Initial structure generation.** Selection of initial positions of hydrogen molecules in the framework was the most important step for calculating the probable binding sites and the corresponding binding energy. Proper scanning of pore surface was important to get the adsorption site with the lowest binding energy. It was difficult to create homogeneously distributed initial positions of hydrogen molecules in the framework due to the 3D structure of the MOF. Even if we find homogeneously distributed positions, executing calculations for all the initial structures leads to large number of optimization calculations. Therefore, we choose the initial structure from the output of our classical grand canonical Monte Carlo simulation, which we have performed for calculating adsorption isotherms.

The conventional GCMC simulation technique was used to compute adsorption isotherms. The input for the simulation consists of models (structures) for the adsorbent and the adsorbate as well as force fields which describe the interactions between them. MOFs were crystalline therefore model for the adsorbent in the atomistic representation of the framework was taken from its crystallographic coordinates. Here, for Mg-MOFs we have used the original crystal structure ignoring the solvent molecule residing in the



pore. In all the simulations, the framework was treated as rigid (a valid assumption for many MOFs at low temperature), although models for flexible MOFs have been proposed recently. We have calculated the theoretical hydrogen adsorption isotherm for  $\gamma$ -Mg-formate and  $\alpha$ -Mg-formate formate. In order to avoid boundary or finite size effects and to allow simulations that were valid for the extended crystal lattice, periodic boundary conditions has been used, [2.23] resulting in simulations that take place in an infinite, perfect structure. To model adsorbate/adsorbate and adsorbate/framework interactions, Van der Waals interactions (normally modelled by Lennard-Jones potentials) have been taken into account. Lennard-Jones (LJ) parameters for the individual atoms and for H<sub>2</sub> molecule UFF [2.30] potential parameters has been considered. LJ potential parameters for cross interactions were computed from Lorentz–Berthelot combining rules. The cutoff radii for both the MOFs were set to be 4.8 Å. For GCMC calculations the volume (V), the temperature (T) and the chemical potential ( $\mu$ ) were kept fixed and under these conditions, the average number of H<sub>2</sub> molecules adsorbed was computed. Each step in the Monte Carlo routine consisted of the insertion of a new molecule, deletion of an existing molecule, or translation of an existing molecule. A total of 5 million steps were used, the first half for equilibration and the second half to calculate the ensemble averages. A configuration was defined as an attempted translation, rotation, creation or deletion of a H<sub>2</sub> molecule. The probability of attempting creation or deletion of a molecule was set to 0.3 an equation of state for hydrogen [2.31] was used to obtain the relationship between the bulk pressure and fugacity. We have converted the total adsorption obtained from simulation to excess adsorption to compare with the experiments. The details of the conversion calculations can be found in the literature. Along with the adsorption isotherm the positions (coordinates) of the adsorbed hydrogen molecules in the pores of both of all Mg-MOFs were obtained. Finite structures (shown in figure 2.11) of the frameworks have been generated with different positions of hydrogen molecules. These initial structures were further optimized by ab-initio quantum chemical calculations.

**Calculation of adsorption energy and site.** Finite structure obtained from the periodic structure possesses artificial dangling bonds. We have saturated those bonds with H atoms. For geometry optimization Gaussian 09 software suite [2.32] has been used. The

ModRedundant option has been employed to perform the selective optimization of H atoms which have been attached to the clusters to saturate the dangling bonds at the B3LYP [2.33]/6-31G level of theory to get the energy,  $E_{(\text{BAREMOF})}$  of the finite structure. Hydrogen molecule on the finite structure was inserted at the same positions that we obtained from GCMC simulation. Then we have optimized the positions of hydrogen molecules of each initial structure containing finite formate clusters ( $\alpha$ -formate and  $\gamma$ -formate both) and one hydrogen molecule using density functional theory (DFT) with 6-31G basis set. The energies we calculated from these calculations were for adsorbate-adsorbent complex,  $E_{(\text{BAREMOF}+\text{H}_2)}$ . We have determined the binding energy of hydrogen using the following equation, where  $E_{(\text{H}_2)}$  was the energy of  $\text{H}_2$  molecule obtained from DFT calculation with the same basis set.

$$E_{\text{ads}} = E_{(\text{BAREMOF}+\text{H}_2)} - (E_{(\text{BAREMOF})} + E_{(\text{H}_2)})$$

Adsorption energies after optimization of all initial configurations for each type of MOFs were compared. The lowest adsorption energies refer to the positions of the hydrogen molecules in the pores and reported in the paper.

**Calculation of adsorption energy and site using:** Finite structure extracted from periodic structure possesses artificial dangling bonds. We have saturated those bonds with H atoms. For geometry optimization we have used the Gaussian 09 software suite [2.32]. The ModRedundant option was employed to perform the selective optimization of the moieties associated with saturating the dangling bonds on the clusters at the HF/6-31G level of theory to get HF energy,  $E_{(\text{BAREMOF})}$  of the finite structure. We inserted hydrogen molecule on the finite structure at the same positions that we got from GCMC simulation. Then we optimized the positions of hydrogen molecules of these inputs containing finite Mg-MOF and one hydrogen molecule using ab-initio HF with 6-31G basis set to get HF energy of the adsorbate-adsorbent complex,  $E_{(\text{MOF}+\text{H}_2)}$ . We determined the binding energy of hydrogen adsorption using the following equation, where  $E_{(\text{H}_2)}$  was the HF energy of  $\text{H}_2$  molecules with the same basis set.

$$E_{\text{ads}} = E_{(\text{BAREMOF}+\text{H}_2)} - (E_{(\text{BAREMOF})} + E_{(\text{H}_2)})$$

Adsorption energies after optimization of all 18 initial configurations compared and we have reported four best energies.

### 2.4.7 X-ray crystallography:

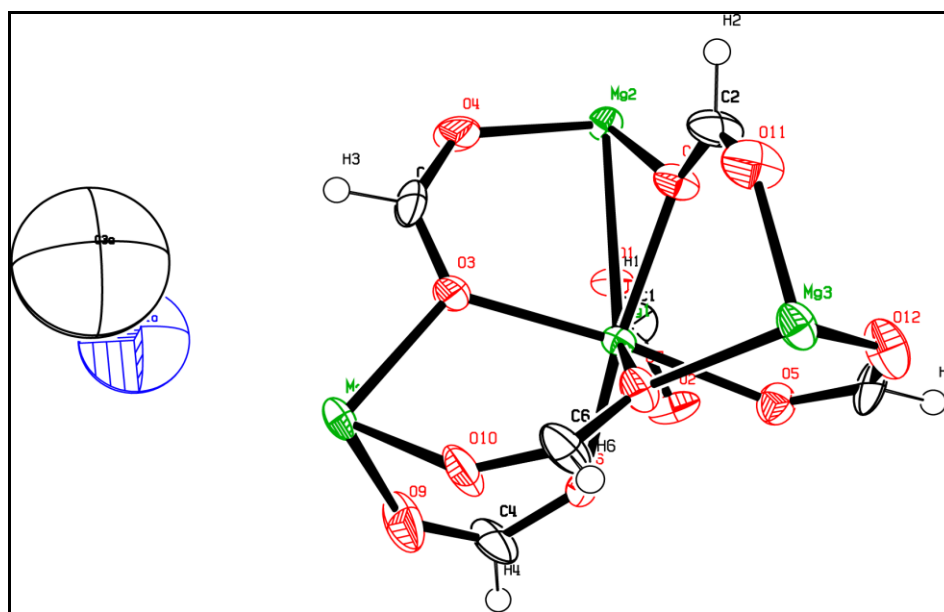
#### 2.6.7.1 General data collection and refinement procedures:

All single crystal data were collected on a Bruker SMART APEX three circle diffractometer equipped with a CCD area detector (Bruker Systems Inc., 1999a) [2.34] and operated at 1500 W power (50 kV, 30 mA) to generate Mo K $\alpha$  radiation ( $\lambda=0.71073$  Å). The incident X-ray beam was focused and mono-chromated using Bruker Excalibur Gobel mirror optics. Crystals of the Mg-MOFs reported in the paper were mounted on nylon CryoLoops (Hampton Research) with Paratone-N (Hampton Research). Data were integrated using Bruker SAINT software [2.35]. Data were subsequently corrected for absorption by the program SADABS [2.36]. Space group determinations and tests for merohedral twinning were carried out using *XPREP* [2.37]. All cases, the highest possible space group was chosen. All structures were solved by direct methods and refined using the *SHELXTL 97* software suite [2.38]. Atoms were located from iterative examination of difference F-maps following least squares refinements of the earlier models. Hydrogen atoms were placed in calculated positions and included as riding atoms with isotropic displacement parameters 1.2-1.5 times  $U_{eq}$  of the attached C atoms. Data were collected at 298(2) K for all the Mg-MOFs reported in this chapter. All structures were examined using the *Adsym* subroutine of PLATON [2.39] to assure that no additional symmetry could be applied to the models. All ellipsoids in ORTEP diagrams were displayed at the 50% probability level unless noted otherwise. ESI contains a detailed data collection strategy and crystallographic data for the two Mg-MOFs reported in this chapter. Crystallographic data (excluding structure factors) for the structures reported in this chapter have been deposited with the CCDC as deposition No. CCDC 772894, 772895 & 791926 for Mg-MOF-1, Mg-MOF-2 and  $\gamma$ -Mg-formate respectively. Copies of the data can be obtained, free of charge, on application to the CCDC, 12 Union Road, Cambridge CB2 1EZ UK [fax: + 44 (1223) 336 033; e-mail: [deposit@ccdc.cam.ac.uk](mailto:deposit@ccdc.cam.ac.uk)].

#### 2.6.7.2 Experimental and refinement details for $\gamma$ -Mg-formate:

A colorless crystal ( $0.20 \times 0.16 \times 0.12$  mm<sup>3</sup>) of  $\gamma$ -Mg-formate was placed in a 0.7 mm diameter CryoLoops (Hampton Research) with Paratone-N (Hampton Research). The loop

was mounted on a SMART APEX three circle diffractometer. A total of 2830 reflections were collected of which 1417 were unique and 1000 of these were greater than  $2\sigma(I)$ . The range of  $\theta$  was from 2.47 to 25.97°. All non-hydrogen atoms were refined anisotropically.  $\gamma$ -Mg-formate contains six formate anion and three metal atom in the asymmetric unit. It should be noted that other supporting characterization data were consistent with the crystal structure. Final full matrix least-squares refinement on  $F^2$  converged to  $R_1 = 0.0687$  ( $F > 2\sigma F$ ) and  $wR_2 = 0.1257$  (all data) with GOF = 0.937 (Table-2.2).



**Figure 2.12:** ORTEP drawing of the asymmetric unit of  $\gamma$ -Mg-formate.

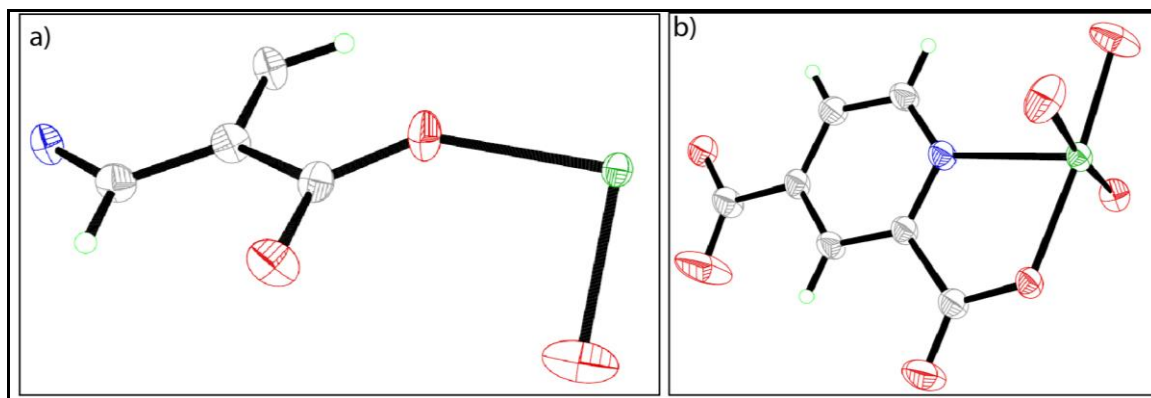
### 2.6.7.3 Experimental and refinement details for Mg-MOF-1:

A colorless prismatic crystal ( $0.20 \times 0.16 \times 0.12 \text{ mm}^3$ ) of Mg-MOF-1 was placed in 0.7 mm diameter nylon CryoLoops (Hampton Research) with Paraton-N (Hampton Research). The loop was mounted on a SMART APEX three circle diffractometer. A total of 16416 reflections were collected of which 6231 were unique and 1000 of these were greater than  $2\sigma(I)$ . The range of  $\theta$  was from 2.47 to 25.97°. All non-hydrogen atoms were refined anisotropically. Mg-MOF-1 contain one 3,5-pyridine dicarboxylic acid and one metal atom in the asymmetric unit. It should be noted that other supporting characterization data were consistent with the crystal structure. Final full matrix least-

squares refinement on  $F^2$  converged to  $R_1 = 0.0752$  ( $F > 2\sigma F$ ) and  $wR_2 = 0.2331$  (all data) with GOF = 1.237 (**Table-2.2**).

#### 2.6.7.4 Experimental and refinement details for Mg-MOF-2:

A colorless prismatic crystal ( $0.14 \times 0.12 \times 0.09$  mm<sup>3</sup>) of Mg-MOF-2 was placed in a 0.7 mm diameter nylon CryoLoops (Hampton Research) with Paraton-N (Hampton Research). The loop was mounted on a SMART APEX three circle diffractometer. A total of 10533 reflections were collected of which 6236 were unique and 4944 of these were greater than  $2\sigma(I)$ . The range of  $\theta$  was from 1.38 to 28.09°. All non-hydrogen atoms were refined anisotropically. Mg-MOF-1 contains two 2,4-pyridine dicarboxylic acid and three water molecule in the asymmetric unit. It should be noted that other supporting characterization data were consistent with the crystal structure. Final full matrix least-squares refinement on  $F^2$  converged to  $R_1 = 0.0607$  ( $F > 2\sigma F$ ) and  $wR_2 = 0.1505$  (all data) with GOF = 0.816 (**Table-2.2**).



**Figure 2.13:** ORTEP drawing of the asymmetric unit of a) Mg-MOF-1 and b) Mg-MOF-2.

**Table 2.2.** Crystal data and structure refinement for Mg-MOFs.

	<b>Mg-MOF-1</b>	<b>Mg-MOF-2</b>	<b><math>\gamma</math>-Mg-formate</b>
Empirical formula	C7 H3 Mg N O5	C14 H18 Mg2 N2 O14	C <sub>14</sub> H <sub>12</sub> Mg <sub>6</sub> N O <sub>24</sub>
Formula weight	205.41	486.92	724.11
Temperature	293(2) K	298(2) K	293(2)K
Wavelength	0.71073 Å	0.71073 Å	0.71073Å
Crystal system	Hexagonal	Orthorhombic	Orthorhombic
Space group	<i>P</i> 6 <sub>1</sub> 22	<i>P</i> bca	<i>P</i> bcn
Unit cell dimensions	$a = 11.4858(17) \text{ \AA}$ $b = 11.4858(17) \text{ \AA}$ $c = 14.756(3) \text{ \AA}$ $\alpha = 90^\circ$ $\beta = 90^\circ$ $\gamma = 120.00^\circ$	$a = 7.9273(18) \text{ \AA}$ $b = 12.057(3) \text{ \AA}$ $c = 20.301(4) \text{ \AA}$ $\alpha = 90.00^\circ$ $\beta = 90.00^\circ$ $\gamma = 90.00^\circ$	$a = 9.9638(18)\text{\AA}$ $b = 18.450(3)\text{\AA}$ $c = 18.082(3)\text{\AA}$ $\alpha = 90.00^\circ$ $\beta = 90.00^\circ$ $\gamma = 90.00^\circ$
Volume	1685.9(5)	1940.4(8)	3324.1(10) Å <sup>3</sup>
Z	6	4	4
Density (calculated)	1.214	1.667	1.447 Mg/m <sup>3</sup>
Absorption coefficient	0.153	0.205	0.236
F(000)	624	1008	1468
Crystal size	0.20 × 0.16 × 0.12 mm <sup>3</sup>	0.20 × 0.16 × 0.12 mm <sup>3</sup>	0.20×0.16×0.12 mm <sup>3</sup>
Theta range for data collection	2.47 - 25.97	2.57- 27.98	2.47- 25.97
Index ranges	-13 ≤ h ≤ 13, -13 ≤ k ≤ 13, -17 ≤ l ≤ 17	-10 ≤ h ≤ 10, -16 ≤ k ≤ 15, -25 ≤ l ≤ 26	-11 ≤ h ≤ 11, -21 ≤ k ≤ 21, -21 ≤ l ≤ 21
Reflections collected	16416	2340	2830
Independent reflections	6231	2199	1417
Completeness to theta = 26.02°	100 %	96.3 %	100 %
Absorption correction	Semi-empirical from equivalents	Semi-empirical from equivalents	Semi-empirical from equivalents
Refinement method	Full-matrix least-squares on F <sup>2</sup>	Full-matrix least-squares on F <sup>2</sup>	Full-matrix least-squares on F <sup>2</sup>
Data / restraints / parameters	6231 / 0 / 68	2340 / 0 / 145	2830 / 0 / 198
Goodness-of-fit on F <sup>2</sup>	1.237	0.816	0.937
Final R indices [I > 2σ(I)]	$R_1 = 0.0752$ , $wR_2 = 0.2331$	$R_1 = 0.0461$ , $wR_2 = 0.1299$	$R_1 = 0.0687$ , $wR_2 = 0.1257$
R indices (all data)	$R_1 = 0.0757$ , $wR_2 = 0.2337$	$R_1 = 0.0483$ , $wR_2 = 0.1324$	$R_1 = 0.1337$ , $wR_2 = 0.1567$
Largest diff. peak and hole	0.215 and -0.556 e.Å <sup>-3</sup>	0.085 and -0.342 e.Å <sup>-3</sup>	0.900 and -0.400e.Å <sup>-3</sup>

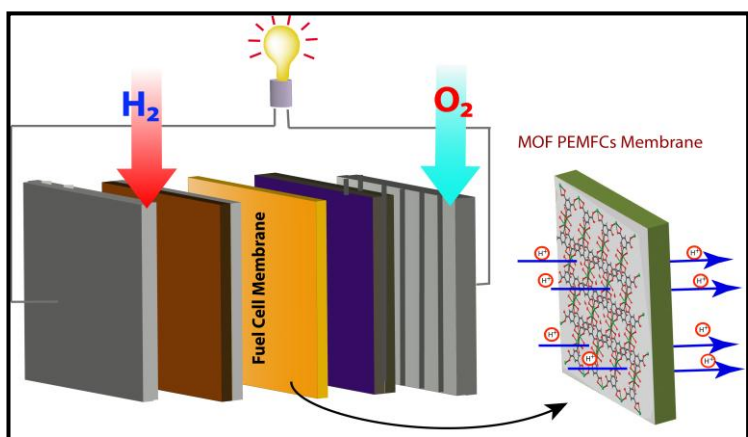
**NOTE:** The results of this chapter have already been published in *J. Mater. Chem.*, **2010**, **20**, **9073–9080**, with the title: “*Selective CO<sub>2</sub> and H<sub>2</sub> Adsorption in a Chiral Magnesium based Metal Organic Framework (Mg-MOF) with Open Metal Sites*” and *Inorg. Chem.* **2011**, **50(4)**, **1392–1401**, with the title: “*Structure and Gas Sorption Behavior of a New Three Dimensional Porous Magnesium Formate*” This publication was the result of a collaboration between the group of Dr. Rahul Banerjee with his students Arijit Mallick, Subhadeep Saha and Pradip Pachfule and the group of Dr. Sudip Roy from the Physical/Materials Chemistry Division at CSIR-National Chemical Laboratory in Pune, India.

Major works were contributed by Arijit Mallick with the help of the instrumental facilities of CSIR National Chemical Laboratory. Subhadeep Saha was involved in theoretical calculation of the materials. Pradip Pachfule helped in gas adsorption measurement.

## CHAPTER 3

### Electrochemical Property of LWMOFs: Correlation between Coordinated Water Content and Proton Transport in Ca-BTC-based Metal-Organic Frameworks

**Abstract:** In this chapter Proton conductivity of five Ca-based MOFs which depends on the amount of water molecules coordinated to the Ca-centres has been presented. These Ca-BTC based MOFs possess distinct



difference in their proton conducting ability. Ca-BTC-H<sub>2</sub>O, which has the highest amount of water content per Ca unit (1.00/Ca unit), shows high conductivity  $1.2 \times 10^{-4} \text{ Scm}^{-1}$  and exhibit low activation energy of 0.18 eV. It also shows proton conductivity at high temperature (72 °C). Ca-BTC-DMF and Ca-BTC-DMA have water content per Ca unit as 0.66 and 0.50 respectively, and show lower proton conductivity ( $4.8 \times 10^{-5} \text{ Scm}^{-1}$  and  $2.0 \times 10^{-5} \text{ Scm}^{-1}$ ) as well as higher activation energy (0.32 and 0.40 eV). Ca-BTC-DMSO and Ca-BTC does not show any proton conductivity due to structural instability at humidified condition and zero water content/Ca unit respectively.



### 3.1 Introduction:

Electrochemical properties of a material can be defined as the properties shown by materials when it has been placed in between electrodes. The electrochemical property is one of the important phenomena of materials due to its possible application in next generation energy storage system. Conduction of protons is also an important electrochemical property of materials. Proton conducting porous solids has recently picked up researchers attention due to its beneficial application in solid state electrochemical devices like fuel cells [3.1]. In fuel cells these proton conducting materials has been used as membrane through which protons travel from cathode to anode and complete the cell circuit. In general nafion has been used as proton conducting membrane in fuel cells, which have very high commercial value. Also nafion has the technical problem like, decrease proton conduction performance at higher temperature ( $> 80\text{ }^{\circ}\text{C}$ ) due to dehydration [3.2]. As an alternative, researchers suggested the use of Metal-Organic Frameworks (MOFs) as proton conductors because of high chemical and thermal stability and diverse topological architecture with tunable functionality [3.3].

In general, proton conduction in MOFs has been classified in two categories: water assisted proton-conducting MOFs operating below  $100\text{ }^{\circ}\text{C}$  and anhydrous proton conductors operating above  $100\text{ }^{\circ}\text{C}$ . There are several attempts like incorporation of water channel, doping of organic molecules (imidazole, triazole etc.) inside the pores of MOFs have been implemented to get higher proton conductivity. However, it is clearly visible that applications of MOFs as proton conductors have not been explored as broadly as gas storage properties [3.4]. Extensive amount of research is still necessary to explore the potential of MOFs as promising proton conducting materials for fuel cell application. Although transition metal based MOFs (e.g. cobalt, nickel, zinc and copper) have been widely investigated, [3.5] the coordination chemistry of MOFs based on main-group metals, (like  $\text{Li}^+$ ,  $\text{Ca}^{2+}$ ,  $\text{Mg}^{2+}$  or  $\text{Al}^{3+}$ ), especially Ca-based MOFs are rarely explored and the properties are not studied widely [3.6].

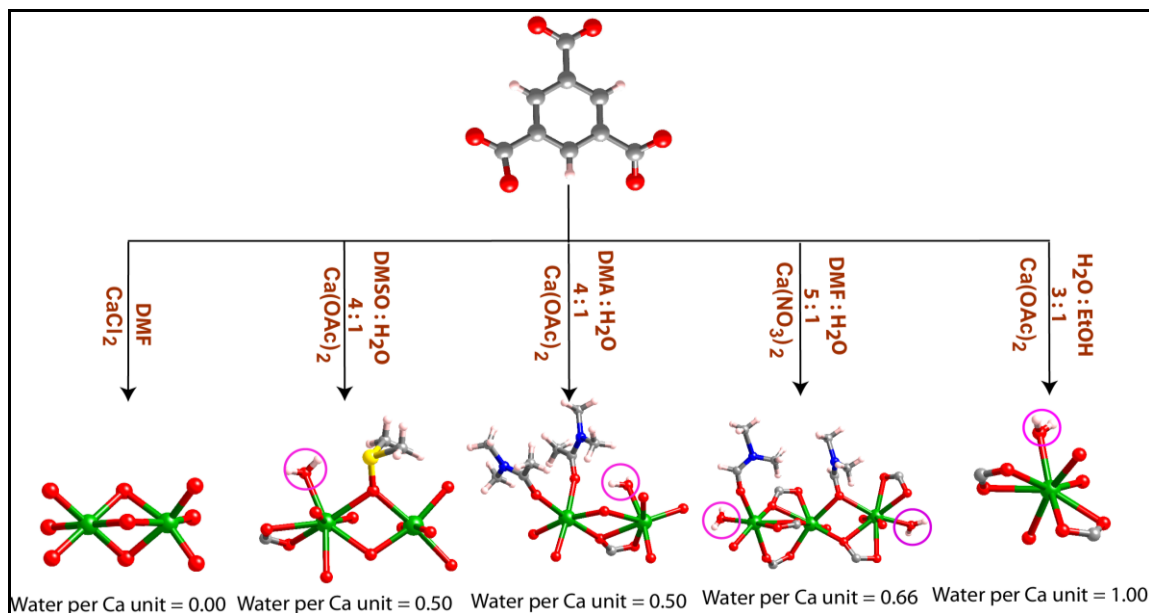
In these regards, herein, in this chapter, synthesis of a series of Ca-based MOFs prepared using 1,3,5-benzenetricarboxylic acid (BTC) as linker in different solvents ( $\text{H}_2\text{O}$ , DMF, DMA, DMSO) has been presented. These Ca-based MOFs have different

amount of water content per Ca unit (Ca-BTC-H<sub>2</sub>O: 1.00, Ca-BTC-DMF: 0.66, Ca-BTC-DMA: 0.50, Ca-BTC: 0.00). It has been observed that water molecules coordinated to the metal play an important role for proton conduction due to the polarization effect. As a result, Ca(II) as a metal center has been preferred for its higher polarizing ability compare to other metals, which should increase the proton conduction ability of the MOF by increasing the acidity of coordinated water molecules. These Ca-BTC based MOFs possess distinct difference in their proton conducting ability, as the water content per Ca-BTC unit is different. Ca-BTC-H<sub>2</sub>O, which has the highest amount of water content per Ca unit (1.00/Ca unit), shows high conductivity  $1.2 \times 10^{-4} \text{ Scm}^{-1}$  and exhibit low activation energy of 0.18 eV. It also shows proton conductivity at high temperature (72 °C). Ca-BTC-DMF and Ca-BTC-DMA have water content per Ca unit as 0.66 and 0.50 respectively, and show lower proton conductivity ( $4.8 \times 10^{-5} \text{ Scm}^{-1}$  and  $2.0 \times 10^{-5} \text{ Scm}^{-1}$ ) as well as higher activation energy (0.32 and 0.40 eV). Ca-BTC-DMSO and Ca-BTC does not show any proton conductivity due to structural instability at humidified condition and zero water content/Ca unit, respectively.

### 3.2 Result and discussion:

#### 3.2.1 Structural analysis of Ca-BTC based MOFs:

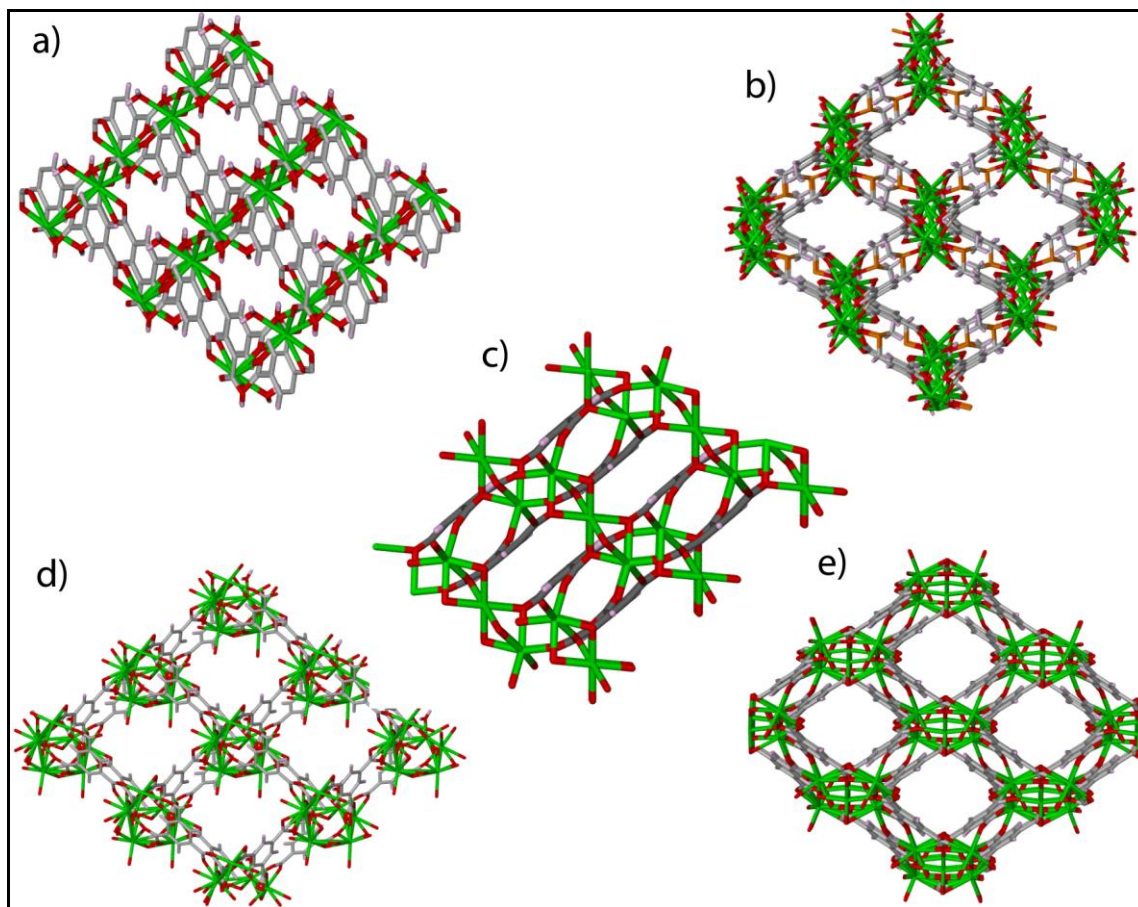
Since, the calcium is one of the most abundant metal present in earth, Ca(II) has been used here as metal centre for MOF synthesis. As a result, these MOFs will be commercially cheap and also environmental friendly. In this work, we have used 1,3,5-benzenetricarboxylic acid (BTC) as linker due to its *C*<sub>3</sub> symmetry which favour to 3D framework formation and easy crystallization. In addition to the previously reported two MOFs synthesized using BTC and Ca(II), herein, we report three more structures using similar precursors (**Figure 3.1**). Ca-BTC-H<sub>2</sub>O [3.6a] has been synthesized by using a 1:1 (0.2 mmol) mixture of BTC and Ca(OAc)<sub>2</sub> in H<sub>2</sub>O-Ethanol mix-solvent (3:1) at 90 °C for 24 h. The Ca-BTC-DMF [3.6b] has been synthesized by mixing Ca(NO<sub>3</sub>)<sub>2</sub>·4H<sub>2</sub>O, (0.3 mmol) and BTC (0.1 mmol) in mix-solvent (5.0 mL DMF and 1mL H<sub>2</sub>O) at 85 °C for 48 h. Ca-BTC-DMA has been synthesized by mixing Ca(OAc)<sub>2</sub> (0.1 mmol) and BTC (0.3 mmol) in DMA- H<sub>2</sub>O (4:1) mix-solvent at 85 °C for 24 h. The synthesis of Ca-BTC-DMSO is similar to Ca-BTC-DMA, where DMSO has been used in place of DMA. Ca-



**Figure 3.1:** Schematic representation highlights the synthetic scheme and water content per metal centre in asymmetric unit of Ca-BTC based MOFs. **Color code:** Ca-green, O-red, C-black, N-blue, S-yellow and H-redish white. The coordinated waters are highlighted by pink circles.

BTC has been synthesized using  $\text{CaCl}_2$  (0.1 mmol), BTC (0.3 mmol) and 2.5 mL in dry DMF at 85 °C for 24 h. During synthesis of Ca-BTC-MOFs (apart from Ca-BTC- $\text{H}_2\text{O}$  and Ca-BTC) the amount of  $\text{H}_2\text{O}$  should be added very carefully because addition of excess  $\text{H}_2\text{O}$  will lead to form Ca-BTC- $\text{H}_2\text{O}$  only.

Crystal structure of Ca-BTC- $\text{H}_2\text{O}$  and Ca-BTC-DMF were reported earlier [3.6a,b]. Ca-BTC- $\text{H}_2\text{O}$  contains 1D channel along crystallographic  $a$  axis containing one dimensional array of lattice  $\text{H}_2\text{O}$  molecules strongly hydrogen bonded [ $\text{O}-\text{H}\cdots\text{O}$ ,  $D=2.762(6)$  Å,  $d = 1.937(5)$  Å,  $\theta = 159.1^\circ(3)$ ] to the coordinated  $\text{H}_2\text{O}$  and oxygen atoms of carboxylate groups [3.7]. Ca-BTC-DMF contains edge shared  $\text{CaO}_8$  and  $\text{CaO}_7$  polyhedrons connected through BTC ligand to form a 3D framework. Ca-BTC-DMF contains three lattice  $\text{H}_2\text{O}$  molecules, discretely hydrogen bonded to the coordinated  $\text{H}_2\text{O}$ , carboxylate oxygen atom and to other lattice  $\text{H}_2\text{O}$  molecules. Ca-BTC-DMA (space group  $C2/c$ ) contains 1D channel along the crystallographic  $c$  axis and the coordinated DMA solvents and  $\text{H}_2\text{O}$  molecules are facing towards the channel. Ca-BTC-DMSO ( $C2/c$ ) does not contain any lattice  $\text{H}_2\text{O}$ , but only one  $\text{H}_2\text{O}$  coordinated to the Ca2 center (**Figure 3.2**)



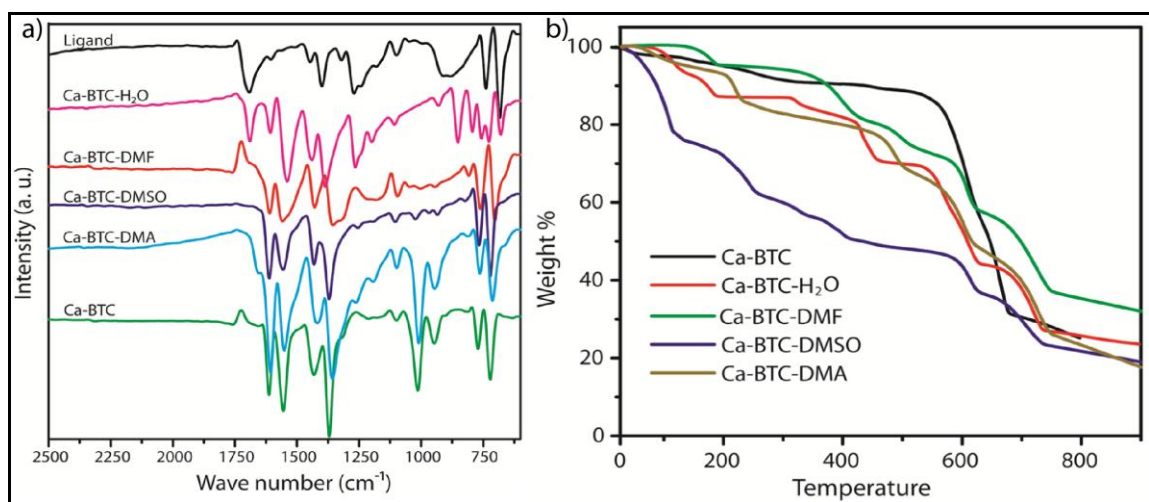
**Figure 3.2:** Packing diagrams showing the 3D arrangement along crystallographic *a* axis for a) *Ca-BTC-H<sub>2</sub>O* b) *Ca-BTC-DMSO*, c) *Ca-BTC*, d) *Ca-BTC-DMF*, e) *Ca-BTC-DMA*. **Color code:** Ca-green, O-red, C-grey, N-blue, S-yellow and H-redish white. The coordinated waters are highlighted by pink circles.

It is noteworthy that, in all four Ca-BTC based MOFs; water content per Ca-center varies systematically as 0, 0.5, 0.66 and 1 unit. As, in *Ca-BTC-H<sub>2</sub>O* each Ca-center is coordinated to single water molecules, the water content per Ca center is 1.0. In *Ca-BTC-DMF*, each three Ca-centers contain two H<sub>2</sub>O and two DMF molecules; hence calculated water content per Ca unit is 0.66. Whereas, in *Ca-BTC-DMA* and *Ca-BTC-DMSO* MOFs, the calculated water content per Ca unit is 0.50. In order to complete the series, we attempted to synthesize one Ca-BTC MOF isomer without any coordinated or lattice H<sub>2</sub>O, but despite of several efforts we could not isolate any anhydrous Ca-BTC MOF. A possible reason could be strong hygroscopic nature of Ca metal. On the other hand, we could successfully synthesize anhydrous Ca-BTC by using CaCl<sub>2</sub> as a precursor in dry DMF. Unlike *Ca-BTC-DMF*, *DMA* and *DMSO*, does not contain any lattice as

well as coordinated H<sub>2</sub>O molecules.

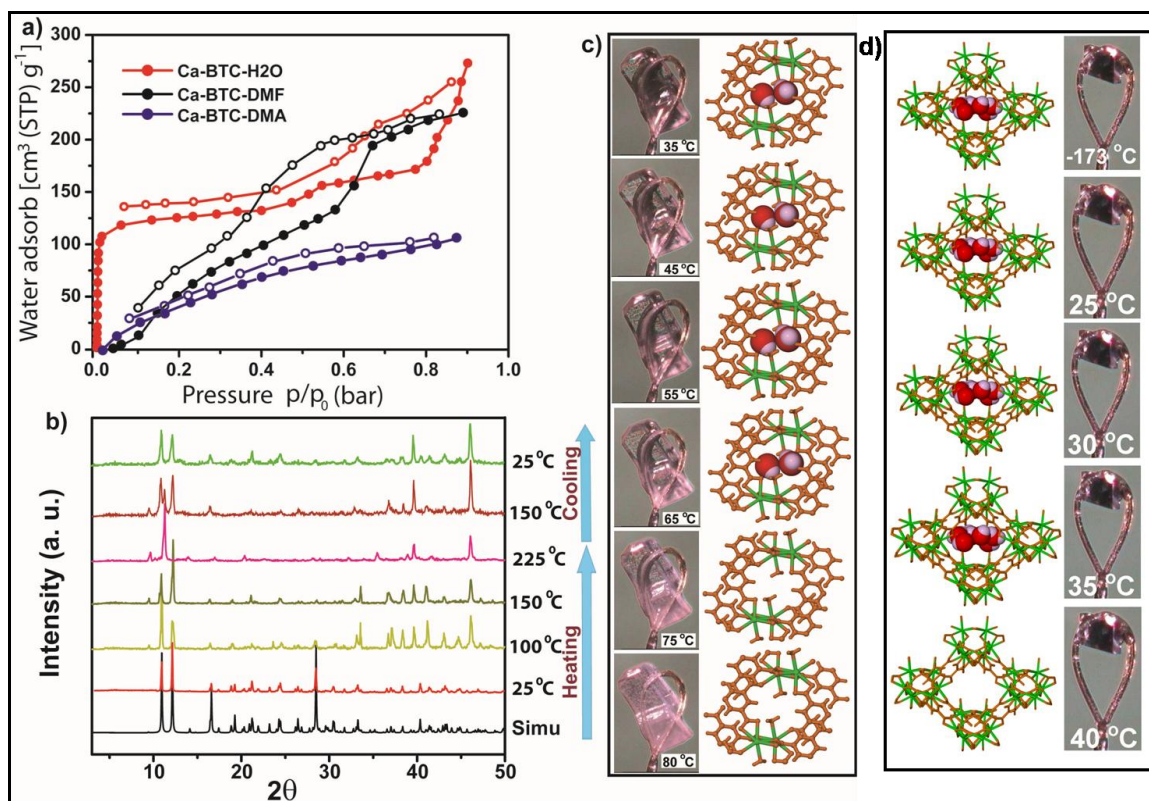
### 3.2.2 Thermal properties and X-ray powder diffraction analysis:

TGA techniques of Ca-BTC-H<sub>2</sub>O, Ca-BTC-DMF and Ca-BTC-DMA under N<sub>2</sub> atmosphere show almost similar stepwise weight loss, first (6–15 wt%) around 30–200 °C due to ready removal of both coordinated and lattice solvent molecules, followed by sharp weight loss (20–30 wt%) at 350–440 °C, probably due to the decomposition of the framework (**Figure 3.3**). Since, the Ca-BTC doesn't have any coordinated or lattice solvent inside the framework; it shows framework decomposition at 550 °C. Except Ca-BTC-DMSO, all four Ca-BTC-MOFs are thermally stable and show similar decomposition behaviors at high temperature. Ca-BTC-DMSO shows a gradual weight loss up to 250 °C due to removal of solvent molecules and simultaneously framework decomposition. TGA traces of Ca-BTC-H<sub>2</sub>O and Ca-BTC-DMF show that the lattice H<sub>2</sub>O molecules leave at 75 °C and 40 °C, respectively; without degradation of the framework.



**Figure 3.3:** a) FT-IR spectra patterns of BTC ligand Ca-BTC-H<sub>2</sub>O, Ca-BTC-DMF, Ca-BTC-DMA, Ca-BTC-DMSO and Ca-BTC. b) TGA traces of Ca-BTC-H<sub>2</sub>O, Ca-BTC-DMF, Ca-BTC-DMA and Ca-BTC-DMSO.

Variable-temperature single crystal data of Ca-BTC-H<sub>2</sub>O collected at different temperature [e.g. 25, 33, 43, 53, 65, 75, 80, and 90 °C] reveals that 75 °C is the optimum temperature at which we could achieve a stable and solvent-free framework of Ca-BTC-H<sub>2</sub>O with reasonably good structural parameters [ $R_1 = 4.1\%$ ,  $wR_2 = 10.72\%$ , GOF = 1.079] (**Figure 3.4c**). In case of Ca-BTC-DMF, the VTSCXRD collected at different



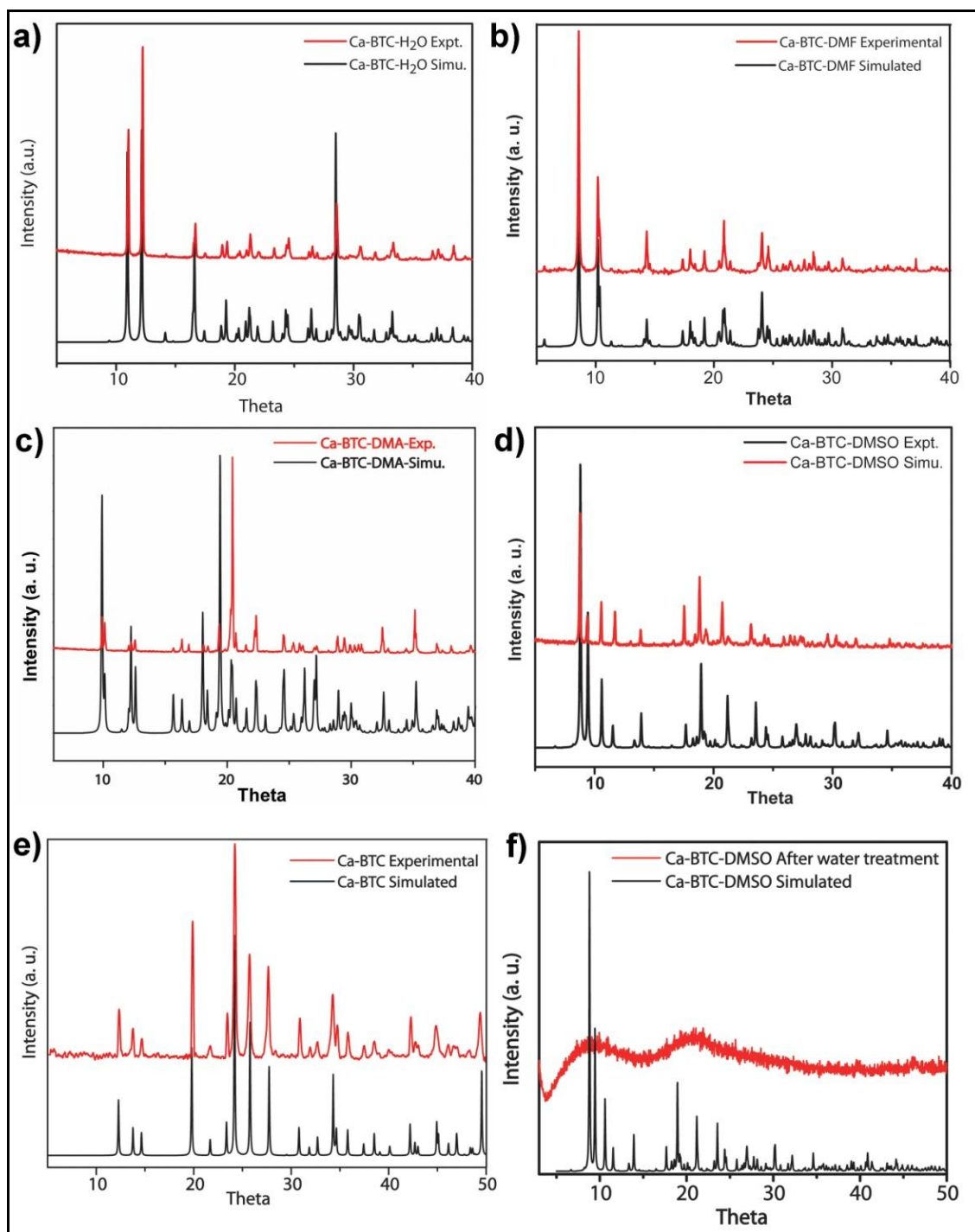
**Figure 3.4:** a) Water adsorption isotherm for Ca-BTC-H<sub>2</sub>O, Ca-BTC-DMF and Ca-BTC-DMA. b) Variable temperature PXRD peaks of Ca-BTC-H<sub>2</sub>O showing the thermal stability of the materials. c) VTSCXRD of Ca-BTC-H<sub>2</sub>O showing loss of lattice water molecules at 75 °C.

temperature [e.g. -173, 25, 30, 35, and 40 °C] reveals that similar stable solvent free framework could be achieved at 40 °C [ $R_1 = 5.2\%$ ,  $wR_2 = 19.72\%$ ,  $GOF = 1.435$ ] (**Figure 3.4d**). The framework stability of Ca-BTC-H<sub>2</sub>O has also been proved by variable temperature PXRD (VTPXRD). It has been observed that the framework is stable upto 150 °C with reversible phase change after 150 °C (**Figure 3.4b**). All major peaks of experimental and simulated PXRDs of Ca-BTC-MOFs match well indicating their reasonable crystalline phase purity (**Figure 3.4 and 3.5**).

### 3.2.3 Proton conductivity measurements:

#### 3.2.3.1 Methods and plots:

Proton conductivity was measured by a quasi-two-probe method, with a Solatron 1287 Electrochemical Interface with 1255B frequency response analyzer. As synthesized samples of Ca-BTC-MOFs were pelletized under hydraulic pellet pressure with 0.5 mm and 0.6 mm thickness and 6.5 mm diameter under humidified condition for 24 hours and



**Figure 3.5:** Comparison of PXRD patterns of as synthesised materials with the simulated pattern from the single-crystal structure for a) Ca-BTC-H<sub>2</sub>O, b) Ca-BTC-DMF, c) Ca-BTC-DMA, d) Ca-BTC-DMSO, e) Ca-BTC, f) Ca-BTC-DMSO after water treatment. The red colored patterns symbolized experimental data and black colored patterns symbolized simulated data.

then subjected to analysis for proton conduction. The resistances were calculated from the semicircle of the Nyquist plots. The activation energy values were obtained from the

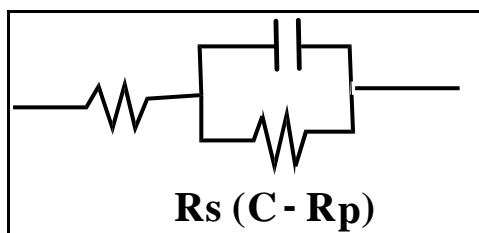
slope by least square fitting of the straight line. If the data points are  $(x_1, y_1)$ ,  $(x_2, y_2)$ , ...,  $(x_n, y_n)$ ; where  $x$  is the independent variable and  $y$  is the dependent variable. The fitting curve  $f(x)$  has the deviation (error)  $d$  from each data point, i.e.  $d_1 = y_1 - f(x_1)$ ,  $d_2 = y_2 - f(x_2)$ , ...,  $d_n = y_n - f(x_n)$ . According to the method of least squares, the best fitting curve has the properties:

$$\Pi = d_1^2 + d_2^2 + \dots + d_n^2 = \sum_{i=1}^n d_i^2 = \sum_{i=1}^n [y_i - f(x_i)]^2 = \text{a minimum}$$

**N.B.** From the semicircle we got the resistance **R** (Ohm).

Further, from diameter **r** (mm) and thickness **A** (mm); proton conductivity ( $\sigma$ ) value can be calculated by the following equation,

$$\sigma = A / (R \times \pi r^2) \text{ Scm}^{-1}$$



**Figure 3.6:** Equivalent circuit model representation of the Nyquist plot.

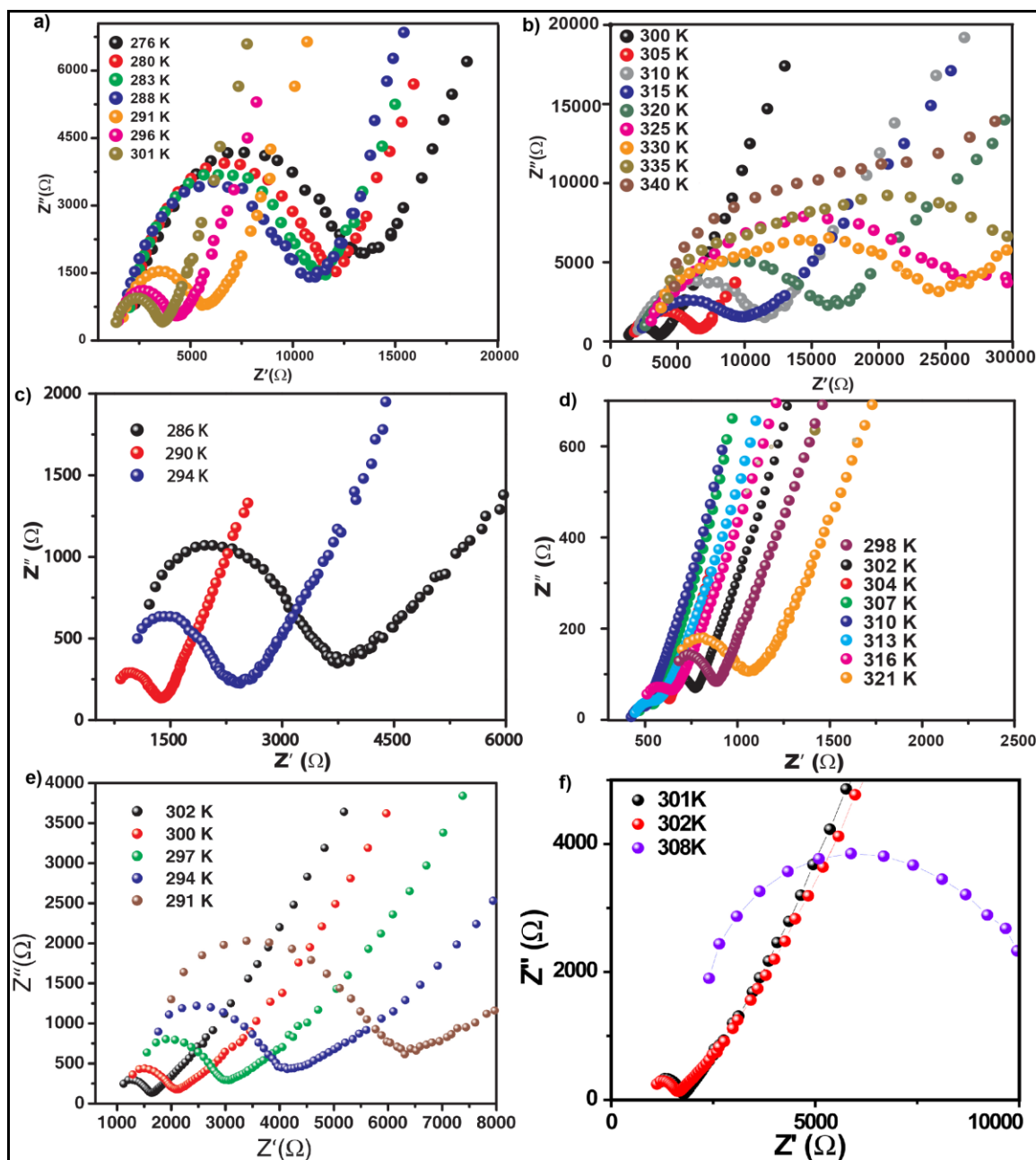
For high-temperature proton conductivity measurements, the pellets were inserted within a humidification chamber, which was encircled with a controlled heating coil attached with an automated temperature controller. The heat flow within the temperature controller was controlled by a dimerstat accordingly. The temperature of the chamber was measured by an infrared temperature sensor attachment, having a sensing accuracy of  $\pm 0.5$  °C. For low-temperature proton conductivity measurements, the pellets were inserted within a humidification chamber, which was encircled with a water circulation coil attached with a chiller integrated with an automated temperature controller. The heat flow within the chamber was controlled by the chiller, accordingly. The temperature of the chamber was measured by an infrared temperature sensor attachment, having a sensing accuracy of  $\pm 0.5$  °C.



### 3.2.3.2 Proton conductivity measurements of Ca-BTC-MOFs:

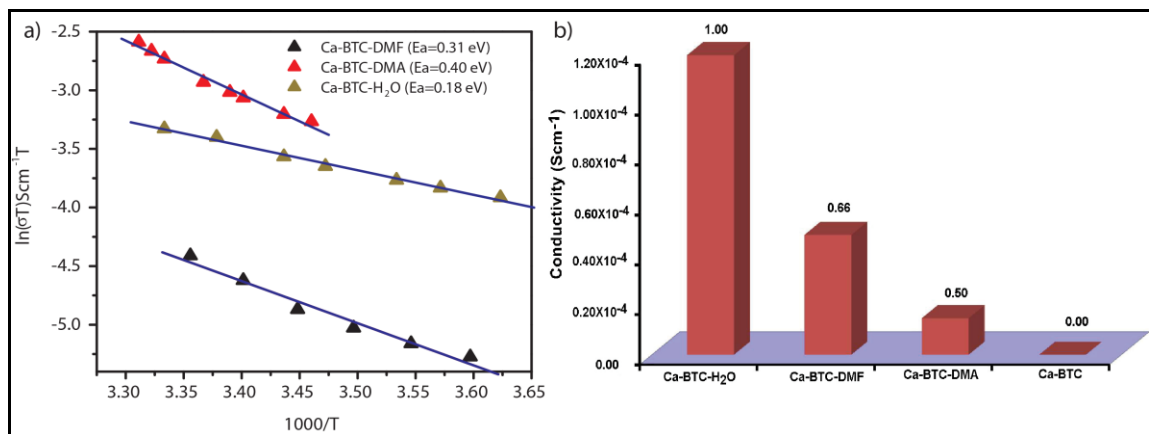
The proton conductivities in all the Ca-BTC-MOFs have been observed only after humidification for 24 h, which eventually confirms the role of water as proton carrier and grain boundary remover. In case of Ca-BTC-H<sub>2</sub>O, Ca-BTC-DMF and Ca-BTC-DMA, the water molecules are absorbed within the crystals by strong hydrogen bonding with the carboxylate bound metal centers, coordinated and non-coordinated solvent molecules, which facilitate the proton conduction. The observed proton conductivity values for the Ca-BTC-H<sub>2</sub>O, Ca-BTC-DMF and Ca-BTC-DMA are  $1.2 \times 10^{-4} \text{ Scm}^{-1}$ ,  $4.08 \times 10^{-5} \text{ Scm}^{-1}$  and  $1.46 \times 10^{-5} \text{ Scm}^{-1}$  at 25 °C and 98% relative humidity (RH), respectively (**Figure 3.7**). However, Ca-BTC and Ca-BTC-DMSO doesn't show any proton conductivity at the same condition due to structural instability and lack of coordinated H<sub>2</sub>O molecules. There is a clear tendency that higher proton conductivity is observed in MOFs, where more water content per Ca unit is present. Ca-BTC-H<sub>2</sub>O shows highest proton conductivity because water content per Ca unit is 1.00. Whereas, Ca-BTC-DMF, Ca-BTC-DMA and Ca-BTC show gradually low to nil proton conductivity due to the steady decrease of water content per Ca unit. The activation energy values calculated for Ca-BTC-H<sub>2</sub>O, Ca-BTC-DMF and Ca-BTC-DMA are 0.18 eV, 0.31 eV and 0.40 eV, respectively (Grotthuss proton hopping mechanism), [1.28, 3.8] and accordance with the aforementioned trend (**Figure 3.8**).

We have also performed the temperature dependent proton conductivity for all these Ca-MOFs. Ca-BTC-H<sub>2</sub>O shows proton conductivity at wide range of temperature from 10 °C ( $1.2 \times 10^{-5} \text{ Scm}^{-1}$ ) to 72 °C ( $3.2 \times 10^{-5} \text{ Scm}^{-1}$ ), while Ca-BTC-DMF and Ca-BTC-DMA showed proton conductivity of  $8.4 \times 10^{-6} \text{ Scm}^{-1}$  (40 °C) and  $9.4 \times 10^{-6} \text{ Scm}^{-1}$  (35 °C), respectively (**Figure 3.7**). Noticeably, Ca-BTC-H<sub>2</sub>O shows proton conductivity at much higher temperature (72 °C), than Ca-BTC-DMF (40 °C) and Ca-BTC-DMA (35 °C). Proton conduction in MOF at higher temperature (more than 72 °C and 98% RH) is a rare phenomenon. There are only few reports which demonstrates MOFs containing lattice H<sub>2</sub>O molecules can conduct proton at high temperature (MIL-53(Fe)-(COOH)<sub>2</sub> :  $6.5 \times 10^{-6} \text{ Scm}^{-1}$  at 72 °C).<sup>3c</sup> These MOFs exhibit lower proton conductivity than Ca-BTC-H<sub>2</sub>O at 72 °C ( $3.2 \times 10^{-5} \text{ Scm}^{-1}$ ). The plausible reason behind the proton conductivity at higher temperature is the strong and continuous hydrogen bonding between coordinated



**Figure 3.7:** Proton conductivity of Ca-BTC- $H_2O$ : a) at low temperature, and b) at high temperature. Proton conductivity of Ca-BTC-DMF: c) at low temperature and d) at high temperature. Proton conductivity of Ca-BTC-DMA: e) at low temperature and f) at high temperature.

and lattice  $H_2O$  molecules, which hold the  $H_2O$  molecules till 72 °C as confirmed by VT-SCXRD. However, in case of Ca-BTC-DMF, the lattice  $H_2O$  molecules are arranged as discrete hydrogen bonded cluster, which hold the  $H_2O$  molecules till 40 °C. Ca-BTC-DMA and Ca-BTC does not contain any such continuous hydrogen bonded network

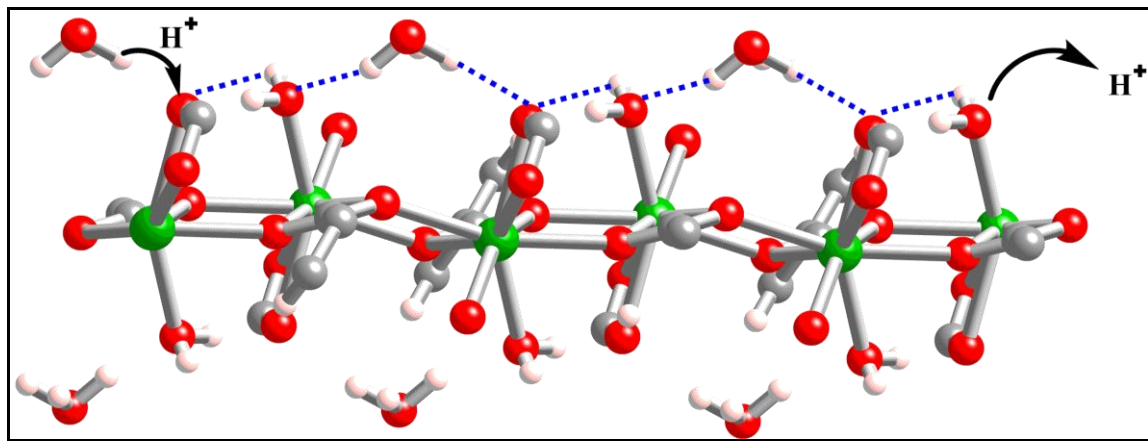


**Figure 3.8:** a) Arrhenius plots of Ca-BTC-H<sub>2</sub>O, Ca-BTC-DMF and Ca-BTC-DMA. The activation energy has been calculated from the slope of the Arrhenius plots. b) The barchart representation of proton conductivity values with respect to different Ca-BTC-MOFs.

within the framework. Hence, we believe that strong hydrogen bonding between coordinated and non-coordinated H<sub>2</sub>O molecules plays a key role in high temperature proton conduction in Ca-BTC-H<sub>2</sub>O.

### 3.2.3.3 Proton conduction mechanism:

The activation energy calculation suggest that proton conductivity in Ca-BTC-MOFs follows the Grotthuss proton hopping pathway [3.8]. On the basis of crystal structures and supporting experimental data, we have proposed a possible mechanism for the proton transport inside the frameworks. In case of Ca-BTC-H<sub>2</sub>O, there is continuous hydrogen bonding through the channel along *a* axis which favours the proton conduction. Also, in



**Figure 3.9:** Possible scheme of Grotthuss proton hopping mechanism of In and Cd-5TIA.

humidified condition the incoming water molecules adsorb inside the channel and easily form hydrogen bonding with the coordinated water molecules and carboxylate oxygen atoms (**Figure 3.9**). Since Ca-BTC-DMF and Ca-BTC-DMA don't have continuous hydrogen bonding channel, only the absorbed water molecules are responsible for proton conduction through the channel.

### 3.3 Conclusions:

In conclusion, we have studied the crystal structure and the proton conductivity of five Ca-based MOFs at variable temperature and relative humidity. The Ca-BTC-H<sub>2</sub>O MOF having 1.00 water content per Ca units, shows high conductivity  $1.2 \times 10^{-4} \text{ Scm}^{-1}$  and exhibit low activation energy of 0.18 eV. Whereas, the Ca-BTC-DMF and Ca-BTC-DMA having 0.66 and 0.50 water content per Ca unit show proton conductivity of  $4.8 \times 10^{-5} \text{ Scm}^{-1}$  and  $1.46 \times 10^{-5} \text{ Scm}^{-1}$  and activation energy of 0.32 and 0.40 eV, respectively. As expected, Ca-BTC doesn't show any proton conductivity due to the absence of water content. Hence, we believe that the extent of water content per metal unit plays a key role in high proton conduction in humidified condition. We hope that these kinds of materials will provide a roadmap towards synthesis of controllable proton conducting materials by varying water content per metal centre.

### 3.4 Experimental procedures:

#### 3.4.1 Materials:

1,3,5-benzenetricarboxylic acid was purchased from the Aldrich Chemicals. The Ca(OAc)<sub>2</sub>, Ca(NO<sub>3</sub>)<sub>2</sub>·4H<sub>2</sub>O, CaCl<sub>2</sub>, N,N'-dimethylformamide (DMF), N,N'-dimethylacetamide (DMA), N,N'-dimethylsulfoxide (DMSO) and other solvents were purchased from Rankem chemicals.

#### 3.4.2 Synthesis of all Ca-BTC based MOFs:

**Ca-BTC-H<sub>2</sub>O:** A mixture of 1,3,5-benzenetricarboxylic acid (C<sub>9</sub>H<sub>6</sub>O<sub>6</sub>, H<sub>3</sub>, BTC, 0.042 g, 0.2 mmol), Ca(OAc)<sub>2</sub> (0.0316 g, 0.2 mmol), H<sub>2</sub>O (3.0 mL), and Ethanol (EtOH, 1.0 mL) was stirred for 20 min at room temperature in a 15 mL vial to form a homogeneous solution. The vial was capped and kept in oven at 90 °C for 24 h. After this time, colourless needle like crystals were obtained, which were filtered off using Whatmann filter paper and washed thoroughly with 99.9% as received EtOH. The so-obtained MOF

[Ca<sub>2</sub>(BTC)(H<sub>2</sub>O)·H<sub>2</sub>O] (41.8 mg, 81% yield) was dried at RT under air atmosphere (60 min).

**FT-IR (4000-600 cm<sup>-1</sup>):** 3216 (m, br), 1670 (m), 1616 (m), 1550 (s), 1450 (m), 1381 (s), 1297 (w), 1244 (m), 1170 (w), 1085 (m), 1043 (w), 900 (w), 773 (m), 740 (m), 683 (m).

**Elemental analysis (for activated sample):** *calc.* (%) (C<sub>9</sub>H<sub>9</sub>O<sub>8</sub>Ca): C, 25.24; H, 3.16;

*Found* (%): C, 24.79; H, 3.29.

**Ca-BTC-DMF:** A mixture of 1,3,5-benzenetricarboxylic acid (C<sub>9</sub>H<sub>6</sub>O<sub>6</sub>, H<sub>3</sub>, BTC, 0.021 g, 0.1 mmol), Ca(NO<sub>3</sub>)<sub>2</sub>·4H<sub>2</sub>O (0.0708 g, 0.3 mmol), DMF (5.0 mL), and water (H<sub>2</sub>O, 1.0 mL) was stirred for 20 min at room temperature in a 15 mL vial to form a homogeneous solution. The vial was capped and kept in oven at 85 °C for 48 h. After this time, colourless plate like crystals were obtained, which were filtered off using filter paper and washed thoroughly with 99.9% as received EtOH. The so-obtained MOF [Ca(BTC)<sub>2</sub>(DMF)<sub>2</sub>(H<sub>2</sub>O)<sub>2</sub>·3H<sub>2</sub>O] (67.55 mg, 57% yield) was dried at RT under air atmosphere (60 min).

**FT-IR (4000-600 cm<sup>-1</sup>):** 3304 (m, br), 2305 (w), 1608 (s), 1548 (s), 1421 (s), 1356 (s), 1200 (w), 1100 (m), 932 (w), 758 (m), 711 (s).

**Elemental analysis (for activated sample):** *calc.* (%) (C<sub>10</sub>H<sub>4</sub>N<sub>3</sub>O<sub>5</sub>Ca): C, 40.24; H, 1.96; N, 21.82; *Found* (%): C, 39.20; H, 1.99; N, 22.24.

**Ca-BTC-DMA:** A mixture of 1,3,5-benzenetricarboxylic acid (C<sub>9</sub>H<sub>6</sub>O<sub>6</sub>, H<sub>3</sub>, BTC, 0.063 g, 0.3 mmol), Ca(OAc)<sub>2</sub> (0.0158 g, 0.1 mmol), DMA (2.0 mL), and water (H<sub>2</sub>O, 0.5 mL) was stirred for 10 min at room temperature in a 5 mL vial to form a homogeneous solution. The vial was capped and kept in oven at 90 °C for 24 h. After this time, colourless plate like crystals were obtained, which were filtered off using filter paper and washed thoroughly with 99.9% as received EtOH. The so-obtained MOF [Ca<sub>2</sub>(BTC)(DMA)(H<sub>2</sub>O)] (18.85 mg, 76% yield) was dried at RT under air atmosphere (60 min).

**FT-IR (4000-600 cm<sup>-1</sup>):** 3425 (m, br), 1615 (s), 1555 (s), 1434 (s), 1681 (s), 1247 (w), 1106 (m), 1026 (m), 938 (w), 824 (w), 764 (s), 725 (s).

**Elemental analysis (for activated sample):** *calc.* (%) (C<sub>26</sub> H<sub>28</sub> N<sub>2</sub> O<sub>16</sub> Ca<sub>3</sub>): C, 41.89; H, 3.75; N, 3.76; *Found* (%): C, 41.91; H, 3.58; N, 3.57.

**Ca-BTC-DMSO:** A mixture of 1,3,5-benzenetricarboxylic acid ( $C_9H_6O_6, H_3$ , BTC, 0.063 g, 0.3 mmol),  $Ca(OAc)_2$  (0.0158 g, 0.1 mmol), DMSO (2.0 mL), and water ( $H_2O$ , 0.5 mL) was stirred for 10 min at room temperature in a 5 mL vial to form a homogeneous solution. The vial was capped and kept in oven at 90 °C for 24 h. After this time, colourless plate like crystals were obtained, which were filtered off using filter paper and washed thoroughly with 99.9% as received EtOH. The so-obtained MOF [ $Ca_2(BTC)(H_2O)(DMSO) \cdot DMSO$ ] (22.07 mg, 75% yield) was dried at RT under air atmosphere (60 min).

**FT-IR (4000-600  $cm^{-1}$ ):** 3424 (m, br), 1615 (s), 1555 (s), 1428 (s), 1368 (s), 1207 (w), 1100 (m), 1006 (s), 946 (s), 772 (s), 718 (s), 628 (w).

**Elemental analysis (for activated sample):** *calc.* (%) ( $C_{10}H_4N_3O_5Ca$ ): C, 35.60; H, 3.82; S, 10.82; *Found* (%): C, 35.43; H, 3.75; S, 9.53.

**Ca-BTC:** A mixture of 1,3,5-benzenetricarboxylic acid ( $C_9H_6O_6, H_3$ , BTC, 0.063 g, 0.3 mmol),  $CaCl_2$  (0.0111 g, 0.1 mmol), DMF (2.0 mL) was stirred for 10 min at room temperature in a 5 mL vial to form a homogeneous solution. The vial was capped and kept in oven at 90 °C for 24 h. After this time, colourless polyhedral crystals were obtained, which were filtered off using filter paper and washed thoroughly with 99.9% as received EtOH. The so-obtained MOF [ $Ca(BTC)$ ] (16.15 mg, 70% yield) was dried at RT under air atmosphere (60 min).

**FT-IR (4000-600  $cm^{-1}$ ):** 1616 (s), 1553 (s), 1435 (s), 1680 (s), 1250 (w), 1107 (m), 1016 (m), 941 (w), 820 (w), 764 (s), 725 (s).

**Elemental analysis (for activated sample):** *calc.* (%) ( $C_6 H_2 Ca O_4$ ): C, 40.39; H, 1.25; *Found* (%): C, 40.04; H, 1.18.

### 3.4.3 General methods for characterization:

All reagents were commercially available and used as received. Leica M-80 optical microscope was used for collecting photographs.

**Powder X-Ray Diffraction (PXRD):** The PXRD patterns were collected on a Phillips PANalytical diffractometer on a  $Cu K\alpha$  radiation ( $\lambda = 1.5406 \text{ \AA}$ ), with a scan speed of  $2^\circ \text{ min}^{-1}$ . The tube voltage and amperage were set at 40 kV and 50 mA respectively. Each

sample was scanned between 5 and 50° 2 $\theta$  with a step size of 0.02°. The instrument was previously calibrated using a silicon standard.

**Thermogravimetric Analysis (TGA):** TGA was performed on a SDT Q600 TG-DTA analyzer instrument. Approximately 5 mg of the sample was added to a platinum crucible and heated from 25 to 800 °C under N<sub>2</sub> atmosphere at a heating rate of 10 °C min<sup>-1</sup>.

**IR Spectroscopy:** The Fourier transform (FT) infrared spectra of the MOFs were taken on a *PERKIN ELMER FT-IR SPECTRUM* (Nicolet) spectrometer. KBr samples (2 mg in 20 mg of KBr) were prepared and 10 scans were collected at 4 cm<sup>-1</sup> resolution for each sample. The spectra were measured over the range of 4000-400 cm<sup>-1</sup>.

**Proton Conductivity:** Proton conductivity data were measured in a quasi-two-probe method, with a Solartron 1287 Electrochemical Interface with frequency response analyzer.

**Water Adsorption Analyses:** All low-pressure water adsorption experiments (up to 1 bar) were performed on a BELSORP-max volumetric instrument. Approximately 50 mg of the sample was activated after solvent exchange by the use of activation chamber. The activated sample was loaded inside the glass bulb of water adsorption instrument and measured the capacity.

### 3.4.4 X-ray crystallography:

#### 3.4.4.1 General data collection and refinement procedures:

Datas were collected on a Super Nova Dual source X-ray Diffractometer system (Agilent Technologies) equipped with a CCD area detector and operated at 250 W (50 kV, 0.8 mA) to generate Mo K $\alpha$  radiation ( $\lambda = 0.71073 \text{ \AA}$ ) and Cu K $\alpha$  radiation ( $\lambda = 1.54178 \text{ \AA}$ ). The crystal reported in this chapter was mounted on Nylon CryoLoops (Hampton Research) with Paraton-N (Hampton Research). Initial scans of each specimen were performed to obtain preliminary unit cell parameters and to assess the mosaicity (breadth of spots between frames) of the crystal to select the required frame width for data collection. CrysAlis<sup>Pro</sup> [3.9] program software suite to carry out was used overlapping  $\phi$  and  $\omega$  scans at detector (2 $\theta$  settings (2 $\theta = 28$ ). Following data collection, reflections were sampled from all regions of the Ewald sphere to redetermine unit cell parameters for data

integration. In no data collection was evidence for crystal decay encountered. Following exhaustive review of collected frames the resolution of the dataset was judged. Data were integrated using CrysAlis<sup>Pro</sup> software with a narrow frame algorithm. Data were subsequently corrected for absorption by the program SCALE3 ABSPACK [3.9] scaling algorithm.

These structures were solved by direct method and refined using the SHELXTL 97 [2.23] software suite. Atoms were located from iterative examination of difference F-maps following least squares refinements of the earlier models. Final model was refined anisotropically (if the number of data permitted) until full convergence was achieved. Hydrogen atoms were placed in calculated positions (C-H = 0.93 Å) and included as riding atoms with isotropic displacement parameters 1.2-1.5 times  $U_{eq}$  of the attached C atoms. Data were collected at 100(2) K for the MOF presented in this chapter. This lower temperature was considered to be optimal for obtaining the best data. The structure was examined using the *Addsym* subroutine of PLATON [2.25] to assure that no additional symmetry could be applied to the models. The ellipsoids in ORTEP diagrams are displayed at the 50% probability level unless noted otherwise. For all structures we note that elevated R-values are commonly encountered in MOF crystallography for the reasons expressed above by us and by other research groups [2.26-2.35]. Crystallographic data (excluding structure factors) for the structures are reported in this chapter have been deposited in CCDC as deposition No. CCDC 885042 - 885046. Copies of the data can be obtained, free of charge, on application to the CCDC, 12 Union Road, Cambridge CB2 1EZ, U.K. [fax: þ 44 (1223) 336 033; e-mail: deposit@ccdc.cam.ac.uk].

#### 3.4.4.2 Experimental and refinement details for Ca-BTC-DMA:

A white block like crystal ( $0.25 \times 0.19 \times 0.15 \text{ mm}^3$ ) of **Ca-BTC-DMA** was placed in 0.7 mm diameter nylon CryoLoops (Hampton Research) with Paraton-N (Hampton Research). The loop was mounted on a Super Nova Dual source X-ray Diffractometer system (Agilent Technologies) equipped with a CCD area detector and operated at 250 W power (50 kV, 0.8 mA) to generate Mo  $K\alpha$  radiation ( $\lambda = 0.71073 \text{ \AA}$ ) and Cu  $K\alpha$  radiation ( $\lambda = 1.54178 \text{ \AA}$ ) at 190(2) K in a liquid N<sub>2</sub> cooled stream of nitrogen. A total of 3737 reflections were collected of which 3207 were unique. The range of  $\theta$  was from



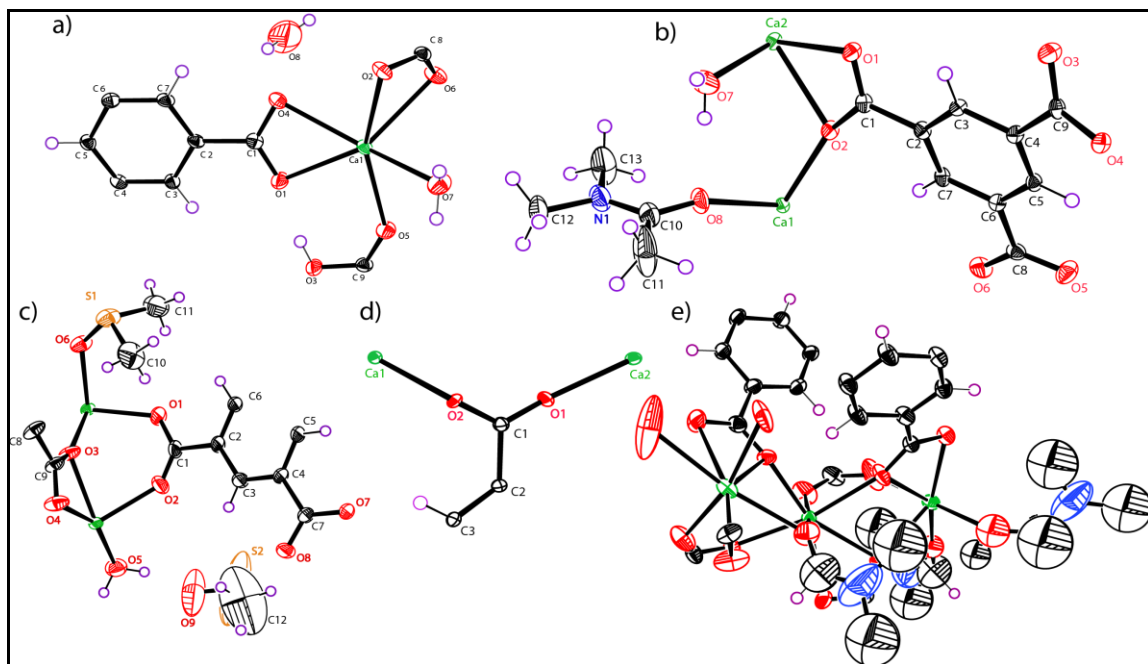
1.85 to 28.92. Analysis of the data showed negligible decay during collection. The structure was solved in the monoclinic  $C 2/c$  space group, with  $Z = 4$ , using direct methods. All non-hydrogen atoms were refined anisotropically with hydrogen atoms generated as spheres riding the coordinates of their parent atoms (**Figure 3.10**). Final full matrix least-squares refinement on  $F^2$  converged to  $R_1 = 0.0742$  ( $F > 2\sigma F$ ) and  $wR_2 = 0.1651$  (all data) with GOF = 1.597 (**Table 3.1**).

#### 3.4.4.3 Experimental and refinement details for Ca-BTC-DMSO:

A white block like crystal ( $0.31 \times 0.23 \times 0.14 \text{ mm}^3$ ) of **Ca-BTC-DMSO** was placed in 0.7 mm diameter nylon CryoLoops (Hampton Research) with Paraton-N (Hampton Research). The loop was mounted on a Super Nova Dual source X-ray Diffractometer system (Agilent Technologies) equipped with a CCD area detector and operated at 250 W power (50 kV, 0.8 mA) to generate Mo  $K\alpha$  radiation ( $\lambda = 0.71073 \text{ \AA}$ ) and Cu  $K\alpha$  radiation ( $\lambda = 1.54178 \text{ \AA}$ ) at 190(2) K in a liquid  $N_2$  cooled stream of nitrogen. A total of 5252 reflections were collected of which 3542 were unique. The range of  $\theta$  was from 1.85 to 29.07. Analysis of the data showed negligible decay during collection. The structure was solved in the monoclinic  $C 2/c$  space group, with  $Z = 4$ , using direct methods. All non-hydrogen atoms were refined anisotropically with hydrogen atoms generated as spheres riding the coordinates of their parent atoms (**Figure 3.10**). Final full matrix least-squares refinement on  $F^2$  converged to  $R_1 = 0.0809$  ( $F > 2\sigma F$ ) and  $wR_2 = 0.2522$  (all data) with GOF = 1.139 (**Table 3.1**).

#### 3.4.4.4 Experimental and Refinement Details for Ca-BTC:

A white block like crystal ( $0.21 \times 0.19 \times 0.15 \text{ mm}^3$ ) of **Ca-BTC** was placed in 0.7 mm diameter nylon CryoLoops (Hampton Research) with Paraton-N (Hampton Research). The loop was mounted on a Super Nova Dual source X-ray Diffractometer system (Agilent Technologies) equipped with a CCD area detector and operated at 250 W power (50 kV, 0.8 mA) to generate Mo  $K\alpha$  radiation ( $\lambda = 0.71073 \text{ \AA}$ ) and Cu  $K\alpha$  radiation ( $\lambda = 1.54178 \text{ \AA}$ ) at 190(2) K in a liquid  $N_2$  cooled stream of nitrogen. A total of 795 reflections were collected of which 580 were unique. The range of  $\theta$  was from 1.85 to 28.92. Analysis of the data showed negligible decay during collection. The structure was solved in the trigonal  $R \bar{3}$  space group, with  $Z = 9$ , using direct methods. All non-hydrogen atoms were refined anisotropically with hydrogen atoms generated as spheres riding the



**Figure 3.10:** Ortep Drawing of the asymmetric unit of a) *Ca-BTC-H<sub>2</sub>O* b) *Ca-BTC-DMA*, c) *Ca-BTC-DMSO*, d) *Ca-BTC*, e) *Ca-BTC-DMF*. Thermal ellipsoids set to 50% probability level.

coordinates of their parent atoms (**Figure 3.10**). Final full matrix least-squares refinement on  $F^2$  converged to  $R_1 = 0.0375$  ( $F > 2\sigma F$ ) and  $wR_2 = 0.0874$  (all data) with GOF = 1.139 (**Table 3.1**).

#### 3.4.4.5 Experimental and refinement details for *Ca-BTC-H<sub>2</sub>O*:

A white block like crystal ( $0.31 \times 0.25 \times 0.14$  mm<sup>3</sup>) of **Ca-BTC-H<sub>2</sub>O** was placed in 0.7 mm diameter nylon CryoLoops (Hampton Research) with Paraton-N (Hampton Research). The loop was mounted on a Super Nova Dual source X-ray Diffractometer system (Agilent Technologies) equipped with a CCD area detector and operated at 250 W power (50 kV, 0.8 mA) to generate Mo K $\alpha$  radiation ( $\lambda = 0.71073$  Å) and Cu K $\alpha$  radiation ( $\lambda = 1.54178$  Å) at 348(2) K in a liquid N<sub>2</sub> cooled stream of nitrogen. A total of 2980 reflections were collected of which 2100 were unique. The range of  $\theta$  was from 1.85 to 29.24. Analysis of the data showed negligible decay during collection. The structure was solved in the triclinic *P*-1 space group, with  $Z = 2$ , using direct methods. All non-hydrogen atoms were refined anisotropically with hydrogen atoms generated as spheres riding the coordinates of their parent atoms (**Figure 3.10**). Final full matrix least-squares refinement on  $F^2$  converged to  $R_1 = 0.0410$  ( $F > 2\sigma F$ ) and  $wR_2 = 0.1072$  (all data) with GOF = 1.079 (**Table 3.1**).

**3.4.4.6 Experimental and refinement details for Ca-BTC-DMF:**

A white block like crystal ( $0.32 \times 0.25 \times 0.18 \text{ mm}^3$ ) of **Ca-BTC-DMF** was placed in 0.7 mm diameter nylon CryoLoops (Hampton Research) with Paraton-N (Hampton Research). The loop was mounted on a Super Nova Dual source X-ray Diffractometer system (Agilent Technologies) equipped with a CCD area detector and operated at 250 W power (50 kV, 0.8 mA) to generate Mo  $K\alpha$  radiation ( $\lambda = 0.71073 \text{ \AA}$ ) and Cu  $K\alpha$  radiation ( $\lambda = 1.54178 \text{ \AA}$ ) at 348(2) K in a liquid  $N_2$  cooled stream of nitrogen. A total of 8481 reflections were collected of which 5946 were unique. The range of  $\theta$  was from 1.85 to 8.08. Analysis of the data showed negligible decay during collection. The structure was solved in the triclinic  $P-1$  space group, with  $Z = 4$ , using direct methods. All non-hydrogen atoms were refined anisotropically with hydrogen atoms generated as spheres riding the coordinates of their parent atoms (**Figure 3.10**). Final full matrix least-squares refinement on  $F^2$  converged to  $R_1 = 0.0610$  ( $F > 2\sigma F$ ) and  $wR_2 = 0.1728$  (all data) with GOF = 1.062 (**Table 3.1**).

**Table 3.1.** Crystal data and structure refinement for Ca-BTC-MOFs.

MOFs	Ca-BTC-DMA	Ca-BTC-DMSO	Ca-BTC	Ca-BTC-H <sub>2</sub> O	Ca-BTC-DMF
<b>Empirical formula</b>	C <sub>26</sub> H <sub>28</sub> Ca <sub>3</sub> N <sub>2</sub> O <sub>16</sub>	C <sub>24</sub> H <sub>28</sub> Ca <sub>3</sub> O <sub>18</sub> S <sub>4</sub>	C <sub>6</sub> H <sub>2</sub> CaO <sub>4</sub>	C <sub>9</sub> H <sub>6</sub> CaO <sub>7</sub>	C <sub>54</sub> H <sub>30</sub> Ca <sub>6</sub> N <sub>6</sub> O <sub>31</sub>
<b>Formula wt.</b>	744.74	852.98	178.16	266.22	1499.32
<b>Temperature</b>	190(2) K	190(2) K	190(2) K	348(2) K	313(2) K
<b>Wavelength</b>	0.71073 Å	0.71073 Å	0.71073 Å	0.71073 Å	0.71073 Å
<b>Cryst. system</b>	Monoclinic	Monoclinic	Trigonal	Triclinic	Monoclinic
<b>Space group</b>	<i>C2/c</i>	<i>C2/c</i>	<i>R -3</i>	<i>P -1</i>	<i>C 2</i>
<b>Unit cell dimensions</b>	<i>a</i> = 16.552(7) Å <i>α</i> = 90° <i>b</i> = 13.6128(19) Å <i>β</i> = 101.88(2)° <i>c</i> = 18.691(11) Å, <i>γ</i> = 90°	<i>a</i> = 15.547(3) Å, <i>α</i> = 90° <i>b</i> = 21.58(2) Å, <i>β</i> = 90° <i>c</i> = 18.981(4) Å, <i>γ</i> = 90°	<i>a</i> = 8.9636(3) Å <i>α</i> = 90° <i>b</i> = 8.9636(3) Å <i>β</i> = 90° <i>c</i> = 19.283(11) Å <i>γ</i> = 120°	<i>a</i> = 6.865(11) Å <i>α</i> = 101° <i>b</i> = 9.128(16) Å <i>β</i> = 99.683(12)° <i>c</i> = 9.920(14) Å <i>γ</i> = 111.950(16)°	<i>a</i> = 16.281(3) Å <i>α</i> = 90° <i>b</i> = 13.514(3) Å <i>β</i> = 93.254(18)° <i>c</i> = 15.759(3) Å <i>γ</i> = 90°
<b>Volume</b>	3155(3)	3931.0(12)	1341.76(10)	545.11(18)	3461.92(12)
<b>Z</b>	4	4	9	2	4
<b>Density (calculated)</b>	1.568	1.441	1.984	1.622	1.438
<b>Absorption coefficient</b>	0.602	0.700	1.000	0.596	0.549
<b>Goodness-of-fit on F<sup>2</sup></b>	1.597	1.139	1.139	1.079	1.062
<b>Final R indices [I &gt; 2σ(I)]</b>	<i>R</i> <sub>1</sub> = 0.0742, <i>wR</i> <sub>2</sub> = 0.1613	<i>R</i> <sub>1</sub> = 0.0809, <i>wR</i> <sub>2</sub> = 0.2320	<i>R</i> <sub>1</sub> = 0.0375, <i>wR</i> <sub>2</sub> = 0.0874	<i>R</i> <sub>1</sub> = 0.0410, <i>wR</i> <sub>2</sub> = 0.0983	<i>R</i> <sub>1</sub> = 0.0610, <i>wR</i> <sub>2</sub> = 0.1671
<b>R indices (all data)</b>	<i>R</i> <sub>1</sub> = 0.0869, <i>wR</i> <sub>2</sub> = 0.1651	<i>R</i> <sub>1</sub> = 0.0976, <i>wR</i> <sub>2</sub> = 0.2522	<i>R</i> <sub>1</sub> = 0.0468, <i>wR</i> <sub>2</sub> = 0.0953	<i>R</i> <sub>1</sub> = 0.0502, <i>wR</i> <sub>2</sub> = 0.1072	<i>R</i> <sub>1</sub> = 0.0647, <i>wR</i> <sub>2</sub> = 0.1728

**NOTE:** The results of this chapter have already been published in *Chem. Commun.*, **2012**, **48**, **8829-8831**, with the title: “*Correlation between Coordinated Water Content and Proton Conductivity in Ca-BTC-based Metal-Organic Frameworks.*” These publications were the results from the group of Dr. Rahul Banerjee and his students Arijit Mallick and Tanay Kundu from CSIR National Chemical Laboratory, Pune, India. Major works are contributed by Arijit Mallick with the help of the instrumental facilities of CSIR National Chemical Laboratory.

Tanay Kundu was involved in proton conductivity measurement studies. Finally figure preparation and draft writing was carried out by Arijit Mallick under the guidance of Dr. Rahul Banerjee.

## Solvatochromic and Photochromic Metal-Organic Framework Containing Naphthalenediimide (NDI) based Linker for Solid State Organic Amine Sensing

**Abstract:** In this chapter a new Mg(II) based photochromic porous metal-organic framework (MOF) has been synthesized bearing naphthalenediimide (NDI) chromophoric unit. This MOF (Mg-NDI) shows



instant and reversible solvatochromic behavior in presence of solvents with different polarity. Mg-NDI also exhibits fast and reversible photochromism via radical formation. Due to the presence of electron deficient NDI moiety, this MOF exhibits selective organic amine (electron rich) sensing in solid state. The organic amine detection has been confirmed by photoluminescence quenching experiment and visual color change.

#### 4.1 Introduction:

For over two decades researchers have paid huge attention on transformation of the chemical information stored in a molecule into an analyzable signal [4.1]. A chemical sensor can detect an analyte through different ways like change in color, luminescence, conductivity, etc [4.2]. However, analytes like explosives, hazardous chemicals, or gases, harmful radiations and bioactive reagents need to be detected in very low concentrations in order to avoid the danger inherent in them. In this regard, porous crystalline chemical sensors are quite interesting because of their quick, reversible and recyclable sensing ability [4.3]. As we discussed earlier [4.4] MOFs can be synthesized from metal ions and linkers, where properties of the MOFs can be tuned by changing the functionality of the organic linkers and different metal ions. It is possible to make chemo sensor MOFs using luminescent linkers or metal ions. In recent years researchers, began to explore the potential of MOFs as chemical sensors. MOFs could be better candidate than other chemo sensors due to its robustness, possibilities of properties modification by changing organic linkers, high crystallinity and geometrically well define structure. In literature mainly four types of MOF sensors has been reported: i) *Ligand based luminescence, which includes, a) ligand localized emission, b) ligand to metal charge transfer (LMCT) emission, c) metal to ligand charge transfer (MLCT) emission* [4.5]. ii) *Metal ion based emission* [4.6]. iii) *Antennae effect* [4.7]. iv) *Guest induced effect* [4.8].

MOFs can absorb the analyte molecules into the definite pores, which allows the species to immobilized in close proximity to the luminescent centers. The incorporation of the analytes in the MOF pores, leads to the change in luminescent properties by means of shift in wavelength, change in intensity or new emission peak formation.

In this thesis, a porous solvatochromic MOF (Mg-NDI), constructed from the environmentally friendly element Mg(II) and naphthalenediimide (NDI) based fluorescent linker has been reported. The Mg-NDI has capability of sensing a diverse range of solvents in less than 60 seconds and having ability to detect the new incoming solvent during fast analyte–solvent exchange. Chemical entities such as organic amines have enormous importance in polymer, dye and pharmaceutical industries [4.9]. However, most of these amines are colorless, making their differentiation via visual

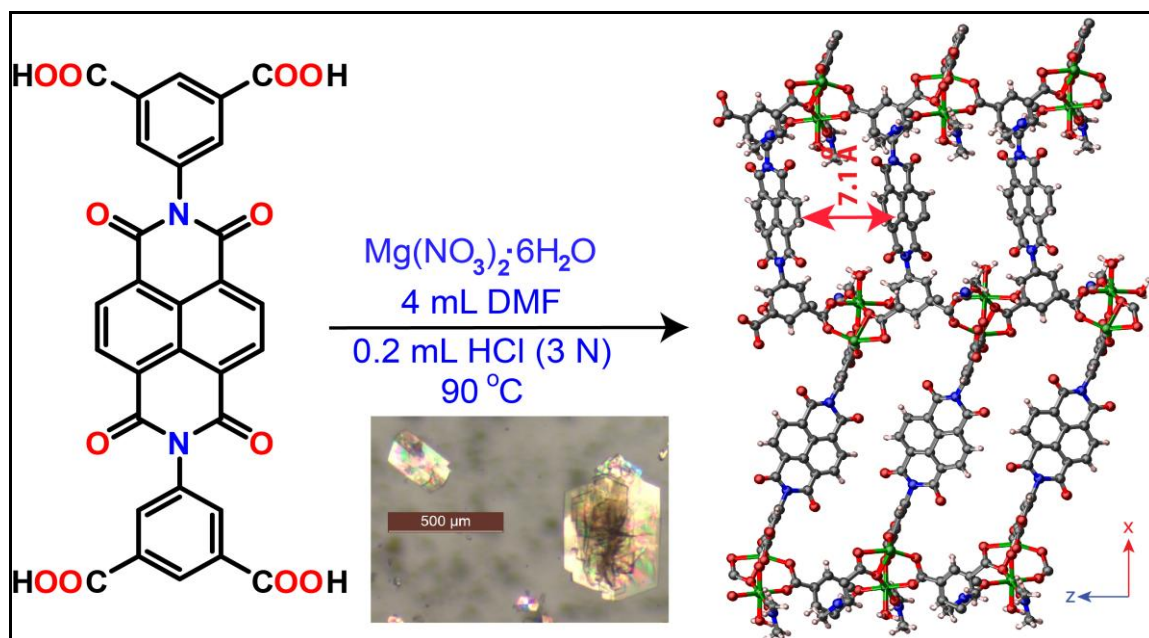
inspection chemical entities such as solvent molecules, organic amines are small in size and have intense importance in polymer, dye and pharmaceutical industries [4.9]. Most of these liquids are colorless and similar looking, making their differentiation via visual inspection difficult. These chemicals are mostly hazardous to environment, and hence spillage of these materials into the nature should be difficult. These amines are also hazardous to the environment, and hence spillage of these materials should be sensed efficiently in order to prevent any probable harm. Traditional chemical sensors generally dissolve or decompose in presence of such analytes [4.10]. Porous MOFs, on the other hand, bear an advantage over these traditional chemical sensors because of their heterogeneous nature and ability to be used over multiple cycles. However, solvatochromic MOFs reported in the literature, have sluggish reversibility and require long detection time and /or sophisticated instrumental fabrication [4.11]. Hence, it is still quite challenging to make a porous MOF which capable of sensing an analyte quickly and reliably. This Mg-NDI MOF, reported in this paper, is able to sense small sized amines by visual color change as well as photoluminescence quenching, making it a dual sensor of solvents and amines. Apart from these chemical entities, Mg-NDI is also able to detect the presence of radiations by showing reversible colour change. This photochromism adds as another sensing property for Mg-NDI. To the best of our knowledge, this is the first report of a MOF where both solvatochromism and photochromism could be observed in one system. This type of dual sensing property is possible because of the presence of chromophoric unit forming the porous structure.

## 4.2 Result and discussion:

### 4.2.1 Structural analysis of Mg-NDI:

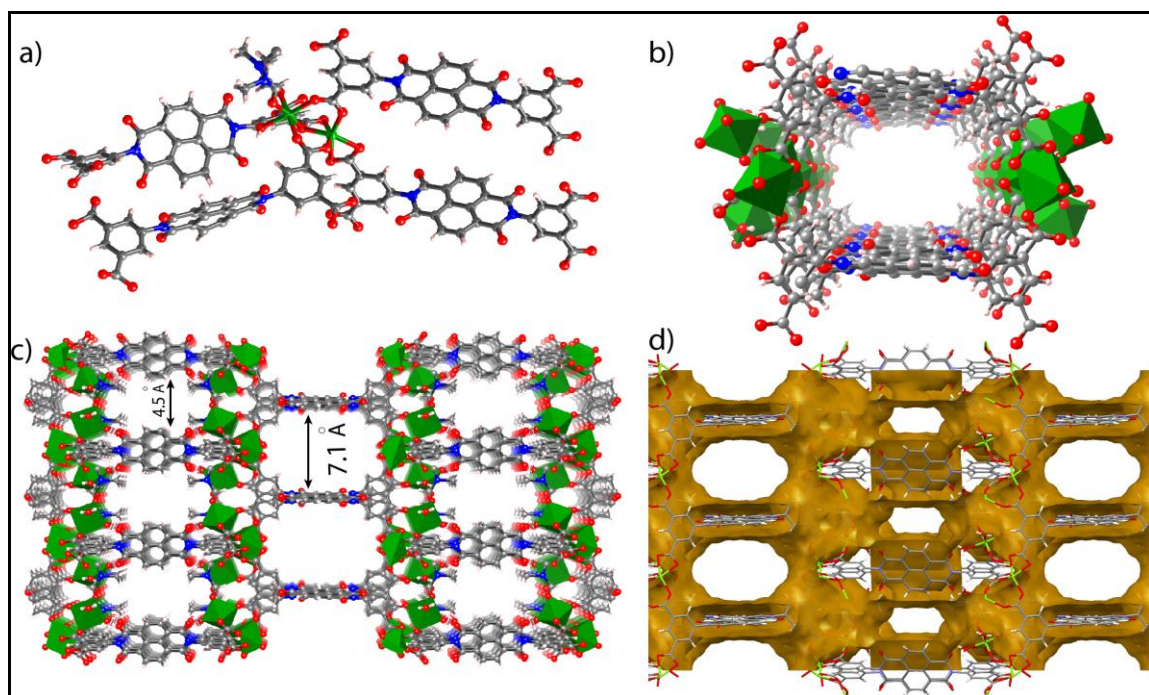
Here  $\text{Mg}(\text{NO}_3)_2 \cdot 6\text{H}_2\text{O}$  has been used as Mg(II) metal source for MOF synthesis. There is few advantage of selecting Mg(II) as metal centres: a) The electronic configuration of Mg(II) is  $1S^2, 2S^2, 2P^6$ . So there are no unpaired *d* electrons (i.e. paramagnetic character) which can quench the luminescent properties of the organic linkers. b) The abundance of Mg present in upper layer of earth crust is 23300 ppm, which is one of the top 10 abundance elements present in earth crust. So the Mg based materials would be low cost and nontoxic products. The organic linker used here is *N,N'*-





**Figure 4.1:** Scheme represents the synthesis of Mg-NDI. Color code: Mg-green, O-red, C-black, N-blue and H-redish white.

bis(5-isophthalic acid)naphthalenediimide ( $H_4BINDI$ ).  $H_4BINDI$  has naphthalenediimide (NDI) chromophoric unit which induced luminescent property in Mg-NDI. This solvatochromic MOF (Mg-NDI) was synthesized from the solvothermal reaction of  $Mg(NO_3)_2 \cdot 6H_2O$  (24 mg, 0.093 mmol) and  $N,N'$ -bis(5-isophthalic acid)naphthalenediimide ( $H_4BINDI$ , 21 mg, 0.035 mmol) in a mixture of DMF (4 mL) and 3 N HCl (0.2 mL) at 90 °C. Mg-NDI MOF crystallized in  $P2/c$  space group and the secondary building unit (SBU) contains two different hexacoordinated Mg(II) metal centers, two BINDI ligands, two coordinated DMF and one water molecule. The first Mg(II) center is coordinated to the six carboxylate oxygen atoms of isophthalate moieties present in BINDI ligand while the second Mg(II) center is coordinated to three BINDI carboxylate oxygen atoms, two DMF and one water molecules. Each BINDI ligands also binds with six Mg(II) centers to form a 3D networks. The crystal structure of Mg-NDI shows, along  $a$  axis, there is no porosity and along  $b$  axis around 4 Å pore aperture is present, but through  $c$  axis, two types of channels are present (pore aperture: 4.3 and 7.1 Å respectively). The most interesting part of the structure is that, all NDI linkers are pull apart from each other by coordination with metals. As a result there is no  $\pi$ - $\pi$  interaction between each ligands which helps the NDI linkers behave like a individual chromophore.



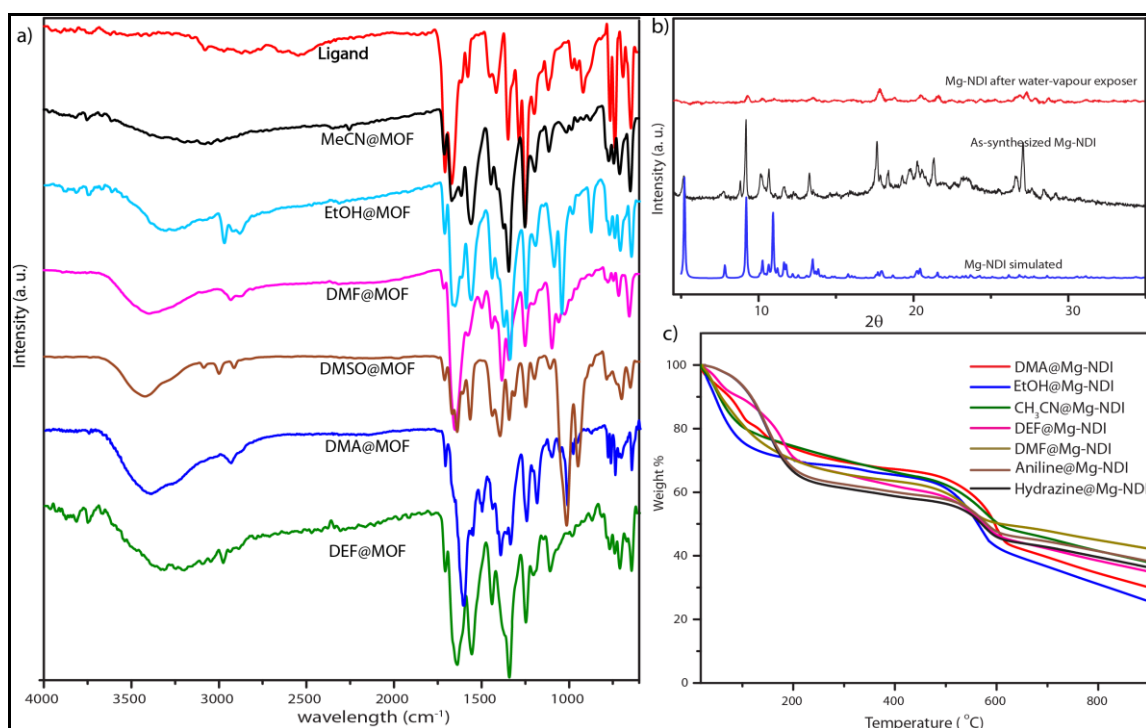
**Figure 4.2:** a) The SBU of Mg-NDI shows coordination geometry of the metal centers and the binding fashion of the ligands. b) The perspective view of 1D channel in Mg-NDI present along *c* axis. c) Packing diagrams showing the 3D arrangement along crystallographic *c* axis. d) Solvent accessible void present in Mg-NDI. **Color code:** Ca-green, O-red, C-grey, N-blue, S-yellow and H-redish white.

#### 4.2.2 FT-IR, thermal properties and X-ray powder diffraction analysis:

The PXRD pattern of the as-synthesized material matched well with the simulated pattern, except for the additional small peak at  $2\theta = 8.8^\circ$ , possibly originated from the disordered solvent molecules present in the framework (**Figure 3.4b** and **Figure 4.4d**). Mg-NDI retained its PXRD patterns after addition of analyte molecules (such as various solvents and amines), indicating the retention of crystallinity after incorporation of guest molecules in the framework. Generation of no additional peak in the PXRD pattern suggests that the solvent molecules are not coordinated to the metal ions; rather they are situated within the pores and weakly interacting with the pore walls to generate the necessary analyte response.

FT-IR analysis of the vacuum dried MOF (**Figure 4.3a**) shows sharp peaks at 1656 and 1550  $\text{cm}^{-1}$  due to the presence of amide and carboxylate carbonyl

functionalities, respectively. In comparison to the free ligand, this amide carbonyl stretching frequency ( $1708\text{ cm}^{-1}$ ) got shifted by  $52\text{ cm}^{-1}$ , possibly due to the change in



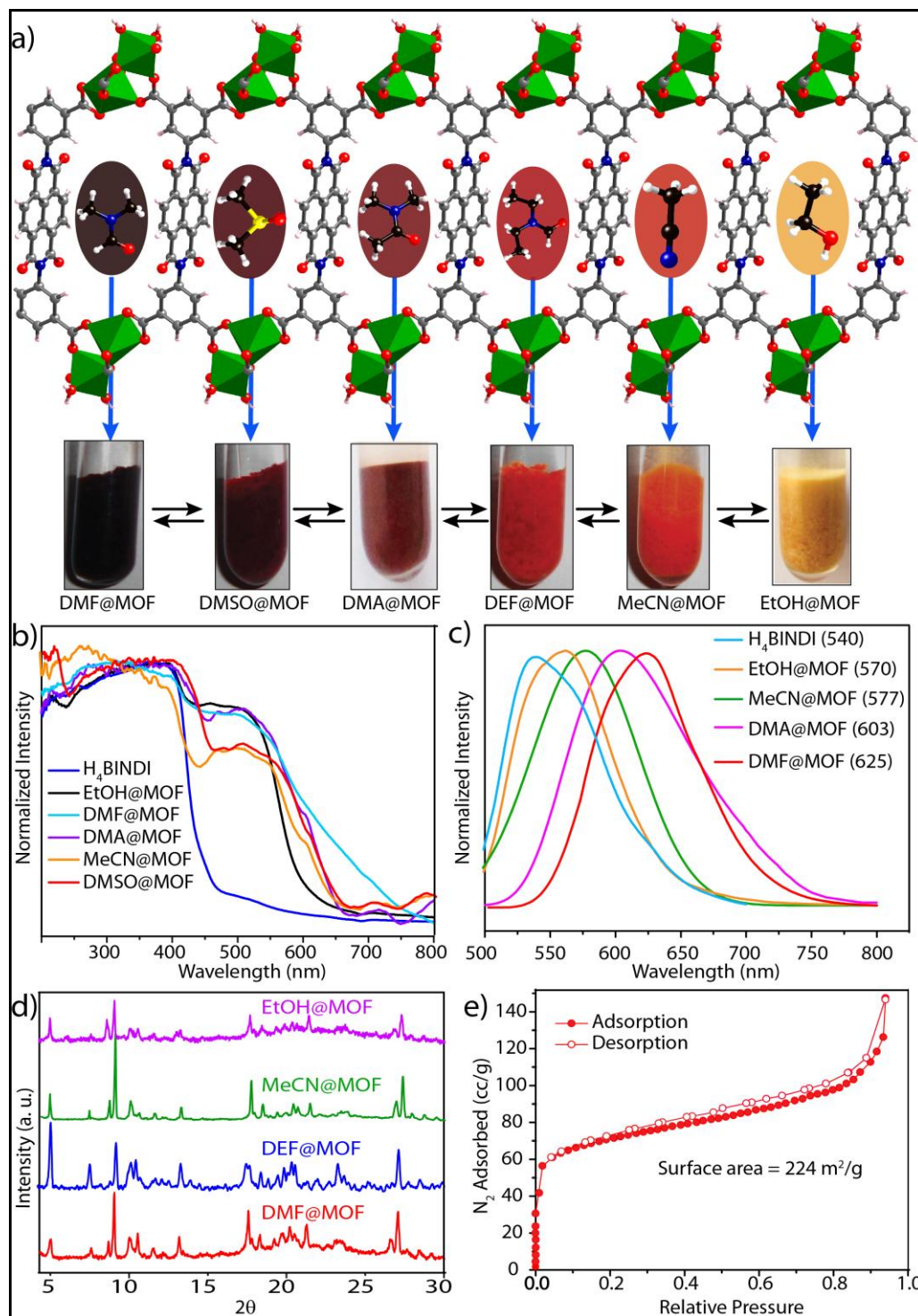
**Figure 4.3:** a) FT-IR spectra of  $H_4\text{BINDI}$  and solvent incorporated Mg-NDI. b) PXRD pattern of water vapor treated Mg-NDI compared with the simulated and as-synthesized pattern of Mg-NDI. c) TGA plots of Mg-NDI and different analyte incorporated MOFs.

dihedral angle from  $128$  to  $103^{\circ}$  in the crystal lattice (**Figure 4.14c**). Generation of additional broad peak at  $3305$  and sharp peaks at  $2971$  and  $1044\text{ cm}^{-1}$  account for the O–H, C–H and C–O stretching frequencies for the EtOH present in EtOH@Mg–NDI. Such characteristic peaks (**Figure 4.3a**) were also observed for DMF, DEF, DMA incorporated MOFs ( $1649$ ,  $1642$ ,  $1607\text{ cm}^{-1}$ , respectively for carbonyl stretching), DMSO@Mg–NDI ( $1015\text{ cm}^{-1}$  for S=O stretching) and MeCN@Mg–NDI ( $2253\text{ cm}^{-1}$  for C–N stretching). These weakly interacting solvent molecules do not affect the thermal stability of the MOF and are released from the framework between  $80$ – $150^{\circ}\text{C}$  during TGA which causes  $\sim 15\%$  weight loss of the material (**Figure 4.3c**). Mg–NDI framework is stable up to  $300^{\circ}\text{C}$  under  $\text{N}_2$  atmosphere.

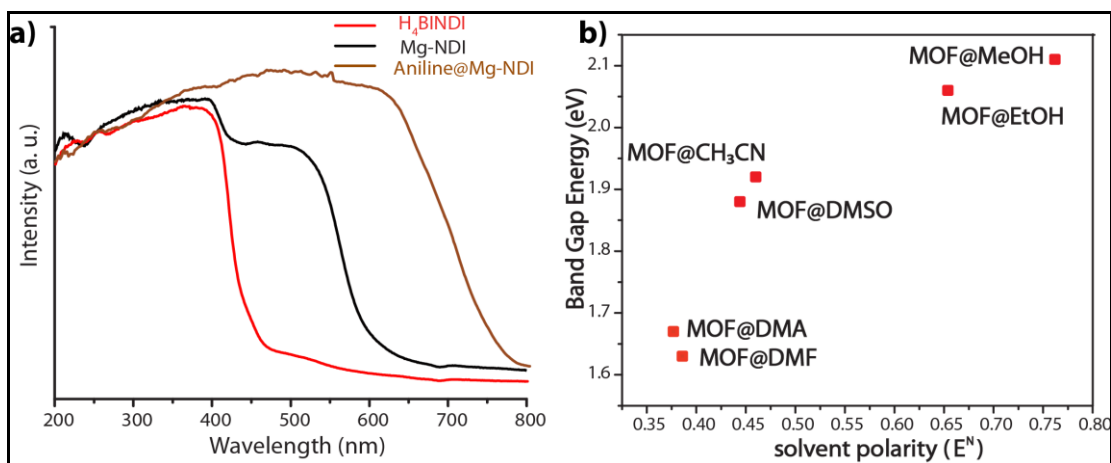
#### 4.2.3 Solvatochromism in Mg-NDI:

In the crystal structure of free H<sub>4</sub>BINDI ligand, the chromophoric naphthalenediimide (NDI) moieties are  $\pi$ -stacked and separated by a distance of 3.3 Å (**Figure 4.15a**). However, within the MOF lattice, the moieties are separated by a longer distance of 7.1 Å (**Figure 4.2c**), preventing them from forming any  $\pi$ -stacked assembly. This spacing allows the NDI moieties to behave as discrete fragments, unlike H<sub>4</sub>BINDI ligand where the smaller spacing and existing  $\pi$ -interaction prohibit the analyte molecules from interacting with the chromophore. Analyte molecules can pass through the pores of Mg-NDI MOF, creating a definite interaction with the pore walls constructed by the BINDI linkers. N<sub>2</sub> adsorption analysis also indicated the presence of 224 m<sup>2</sup>g<sup>-1</sup> available surface area within this MOF (**Figure 4.4e**). When the dark-brown colored as-synthesized MOF was placed in ethanol, the color of the resulting compound (EtOH@Mg-NDI) changed to bright-yellow. Similar solvent exchange with other solvents like DMSO, DEF, DMA, MeCN, generates different colors (brown, dark red, red, orange, respectively; **Figure 4.4a**) for the MOF depending on the polarity of the solvent. This color change is instant and reversible, i.e. after placing the MOF into the solvent; it converted into the corresponding distinct colored MOF in less than 60 seconds. This fact indicated that the interaction of the incorporated solvent and framework is short ranged and weak, allowing the external bulk solvents to easily replace the core solvent already present inside the porous framework.

Solid state UV-vis spectra revealed that the solvent incorporated Mg-NDI samples showed absorption in the visible range and absorption maxima are consistent with the solvent polarity. The UV-vis spectrum of both Mg-NDI and free H<sub>4</sub>BINDI ligand showed a strong absorption band at 370 nm (**Figure 4.4b**), which corresponds to the n- $\pi^*$  and  $\pi$ - $\pi^*$  transition of the aromatic carboxylate ligands [4.12]. In addition, a shoulder peak around 515 nm can also be observed in Mg-NDI, which could be attributed to an intermolecular electron-transfer transition. The UV-vis spectra of solvent@Mg-NDI (**Figure 4.4b**) displayed a gradual broadening of absorption band in the region 515–680 nm with respect to different solvent polarity, which may arise from the intermolecular electron-transfer transition from solvent to BINDI linker within the MOF framework. The band gap energies of these solvent incorporated MOFs were



**Figure 4.4:** a) Schematic representation of Mg-NDI crystals showing different color in different solvents; b) solid state UV-vis spectra; c) solid state photoluminescence of Mg-NDI crystals soaked in different solvents; d) PXRD patterns of solvent@Mg-NDI materials and e) N<sub>2</sub> adsorption isotherm for Mg-NDI.

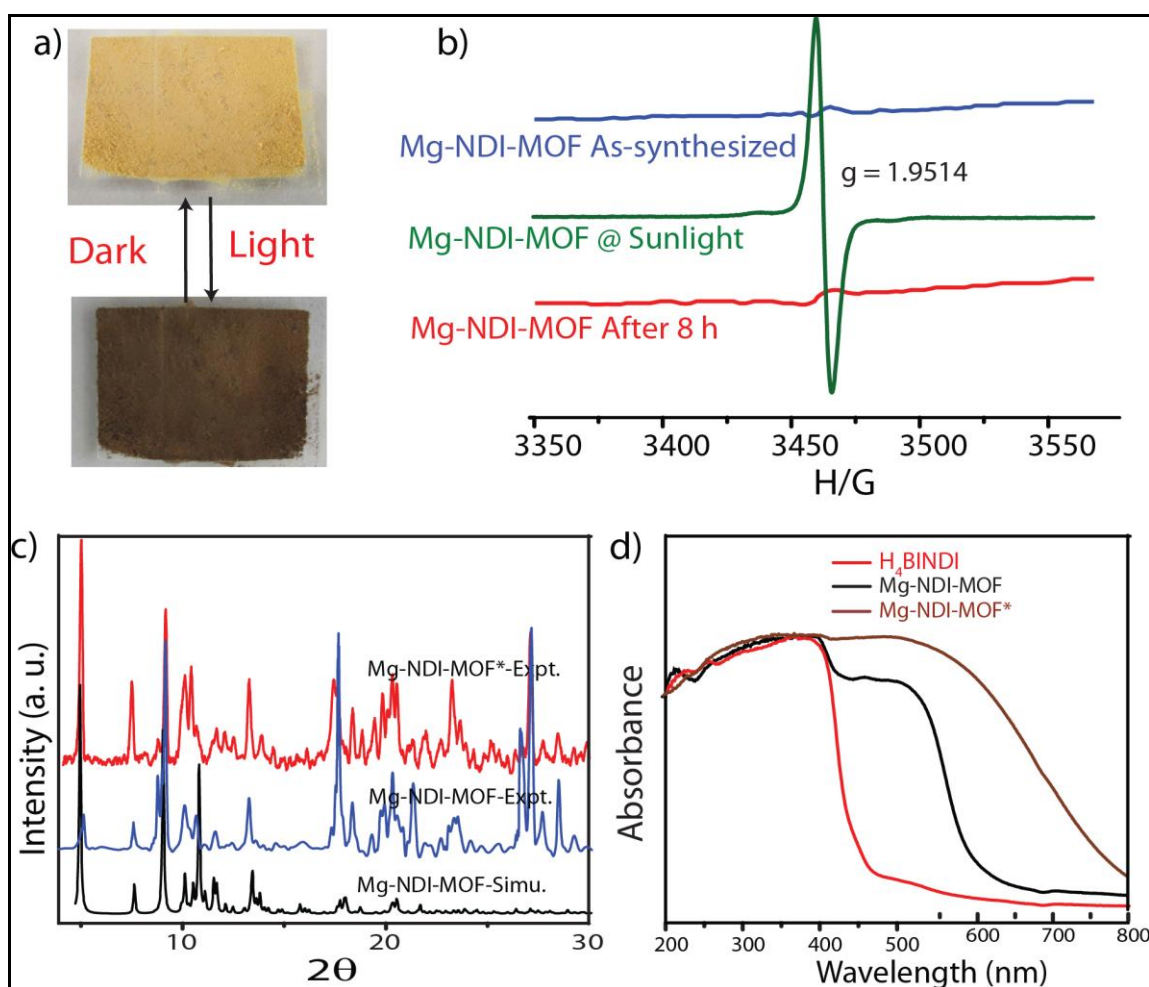


**Figure 4.5:** a) Solid state UV-vis spectra of H<sub>4</sub>BINDI (red), Mg-NDI (black) and aniline@Mg-NDI (brown). b) Band gap value vs. polarity has been plotted, which shows the band gap value increases with increasing polarity.

calculated from UV-vis data which show that band gap energy of DMF@Mg-NDI and EtOH@Mg-NDI are 1.63 eV and 2.06 eV, respectively and are extreme values for all the tested solvents. The band gap energies of other solvent incorporated MOFs were found to increase with the increment of the solvent polarity (1.87, 1.88, 1.91, and 1.92 eV for DMA, DMSO, DEF, and MeCN, respectively; (**Figure 4.5b**)). Mg-NDI also exhibited solvent-dependent photoluminescence (PL). The PL spectrum of EtOH@Mg-NDI shows an emission at 570 nm and DMF@Mg-NDI shows an emission at 625 nm upon excitation at 515 nm, i.e. a 55 nm shift of  $\lambda_{em}$  was observed upon changing the solvent from EtOH to DMF. With increasing solvent polarity [DMF < DMSO < DEF < MeCN < EtOH] a gradual blue shift of  $\lambda_{em}$  was observed which correlates with the band gap energies of the solvent@Mg-NDI MOFs, showing that Mg-NDI MOF has a negative solvatochromic effect. The solid H<sub>4</sub>BINDI ligand showed the photoluminescence emission maxima at 540 nm upon excitation at 370 nm (**Figure 4.4c**). Whereas, the PL spectra of the dry Mg-NDI MOF showed strong emission bands centered at  $\lambda_{em}$  = 570 nm upon excitation at 515 nm. The probable reason behind the strong red shift of emission maxima is the coupling interaction between the neighboring ligands through Mg(II) inside the framework. Thus, the solvatochromism of Mg-NDI MOF is much better than that of the H<sub>4</sub>BINDI ligand itself.

#### 4.2.4 Photochromism in Mg-NDI:

It is noteworthy that Mg-NDI also shows sensitivity towards sunlight irradiation. The yellow colored crystals of Mg-NDI undergo photochromic transition and become black within five minutes. The black crystals then regain their yellow color when kept in dark for 8 hours at ambient condition (**Figure 4.6a**). PXRD data of Mg-NDI collected before and after the photochromic transition are exactly identical (**Figure 4.6c**) which proves that no structural change is caused because of the irradiation. However, the UV-vis spectra show an abrupt change in absorption band (**Figure 4.6d**) which reveals that reversible photochromism may be resulted from an electron-transfer chemical process



**Figure 4.6:** a) photograph representing the reversible photochromic behavior of Mg-NDI MOF crystal in sunlight and dark; b) ESR spectra of Mg-NDI crystals before and after irradiation of sunlight; c) PXRD patterns of Mg-NDI crystals before and after irradiation of sunlight; d) solid state UV-vis spectra of  $H_4$ BINDI (red), Mg-NDI (black) and Mg-NDI\* (brown).

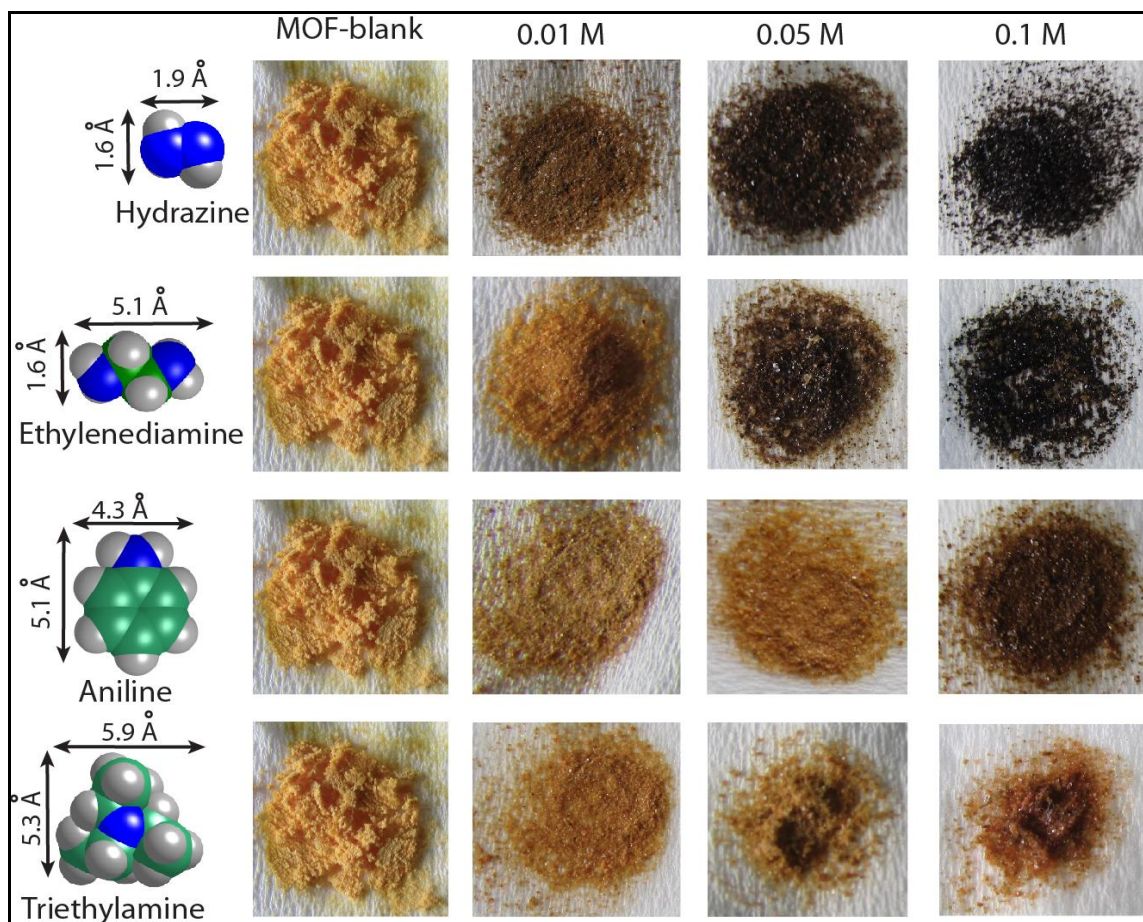
inside the structure, and not from a structural transformation. The UV-vis spectrum of the irradiated Mg-NDI (Mg-NDI<sup>\*</sup>) displays a transformation of the tiny shoulder peak at 515 nm for Mg-NDI, into a broad band in the region 515–700 nm (**Figure 4.6d**). This broadening is arising from the photo-induced electron-transfer transition in Mg-NDI<sup>\*</sup>. NDI moiety is known to be redox-active and can generate radicals upon light irradiation [4.12]. Therefore, besides  $\pi$ - $\pi$  electron-transfer, this photochromic process may also arise from the photo-induced radical generation of organic ligand. This radical generation has been confirmed by ESR spectra. Mg-NDI exhibits no ESR signal, but Mg-NDI<sup>\*</sup> shows a single-peak radical signal with a *g* value of 1.9514 (**Figure 4.6b**).

#### 4.2.5 Solid state amine sensing in Mg-NDI:

As the Mg-NDI framework is electron deficient in nature due to the presence of NDI chromophore, we decided to check its ability to sense electron rich chemical species. Among several electron rich chemical species, this MOF can selectively sense small sized organic amines by visual color change as well as quenching of its fluorescence efficiency. Electron rich organic amines can form charge transfer complex with the NDI moieties within the framework, resulting a change in color as well as photoluminescence property. Treatment of Mg-NDI with various organic amines like aniline, hydrazine, ethylene diamine, triethylamine, dimethylamine, 1,3-propanediamine, ethylamine, methylamine showed a distinct color change (to black) over other functionalized analytes like chlorobenzene, toluene, benzene, phenol, 4-nitrophenol, nitrobenzene, 4-bromotoluene, etc (**Figure 4.9a**). This color change is extremely rapid and very prominent and can be easily detected from naked eye inspection. Mg-NDI is able to detect the presence of amine from a very low concentration ( $10^{-5}$  M) in the solid state. Chemical sensing using as-synthesized solid MOF samples is rarely reported in the literature. In all the previous reports [4.13], analyte sensing has been done with a suspension of the sensor MOF, or by making a thin film probably due to their poor efficiency.

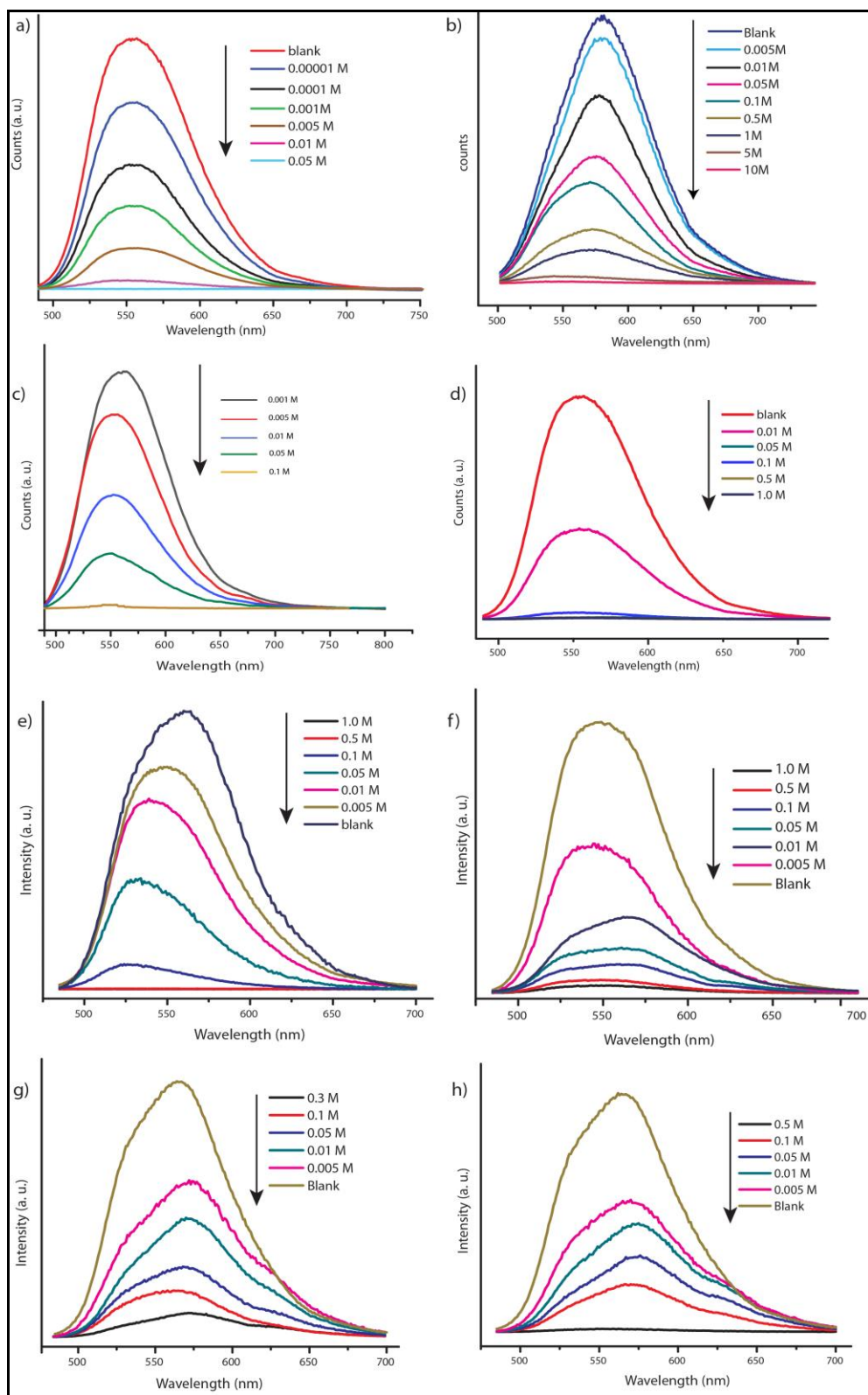
Presence of the chromophoric NDI moiety has made Mg-NDI capable to sense organic amines in solid state. To explore the ability of Mg-NDI to sense a trace quantity of amine, fluorescence quenching experiment were performed with addition of analytes,



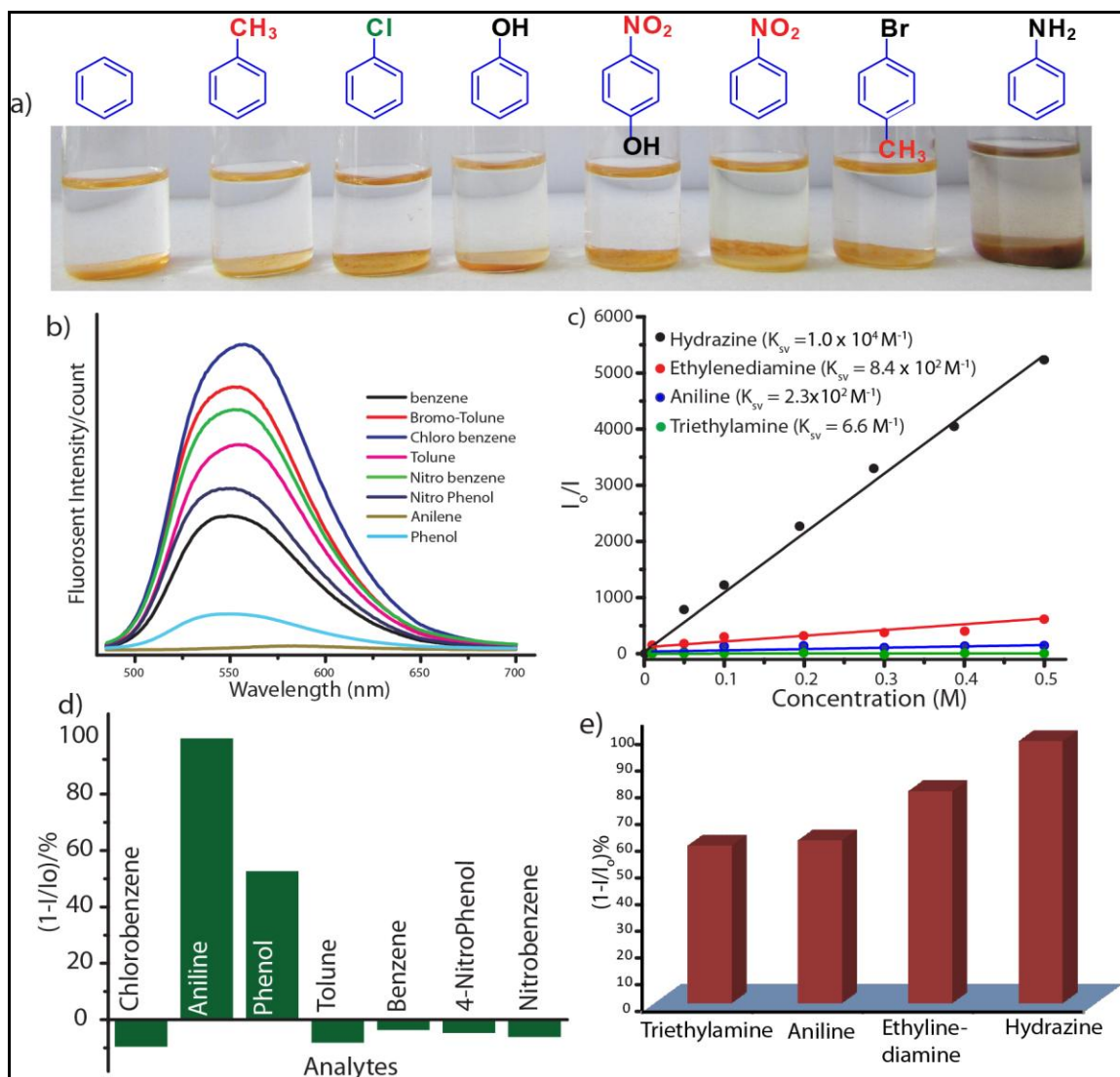


**Figure 4.7:** Optical images representing the color change of Mg-NDI in presence of different amines at different concentrations.

with increasing concentration to the fixed amount Mg-NDI. Rapid and strong fluorescence quenching was observed upon increasing the concentration of amine solution. The MOF was tested for its sensing ability against a wide range of amines like aniline, ethylenediamine, triethylamine, hydrazine, etc. where an instant color change of the solid material was observed for the case of hydrazine, methylamine, ethylamine, dimethylamine and ethylenediamine [Figure 4.7]. In the cases of aniline and triethylamine, the rate of color change was found to be relatively slow because of their bulky size. The PL spectra revealed that the tested amines showed prominent PL quenching response over other analytes [Figure 4.8] which can also be detected by visual color change to black. The fluorescence quenching can be attributed to the donor-acceptor electron transfer between amines and MOF. To understand the electron transfer process, the HOMO and LUMO energy of Mg-NDI was determined by cyclic



**Figure 4.8:** PL quenching spectra of Mg-NDI in presence of different concentration of a) Hydrazine, b) aniline, c) ethylenediamine, d) triethylamine, e) Diethylamine, b) 1,3-propanediamine, c) Ethylamine, d) Methylamine.



**Figure 4.9:** a) Photograph representing the selective color change in case of aniline with respect to other aromatic functional molecules; b) Solid state PL spectra of Mg-NDI in different aromatic functional molecules; c) Bar chart representation for quenching efficiency of Mg-NDI in presence of different amines (0.01 M) in EtOH d) bar chart representation for quenching efficiency of Mg-NDI in presence of different analytes (0.01 M in EtOH); (e) Stern-Volmer plot for Mg-NDI with different amines.

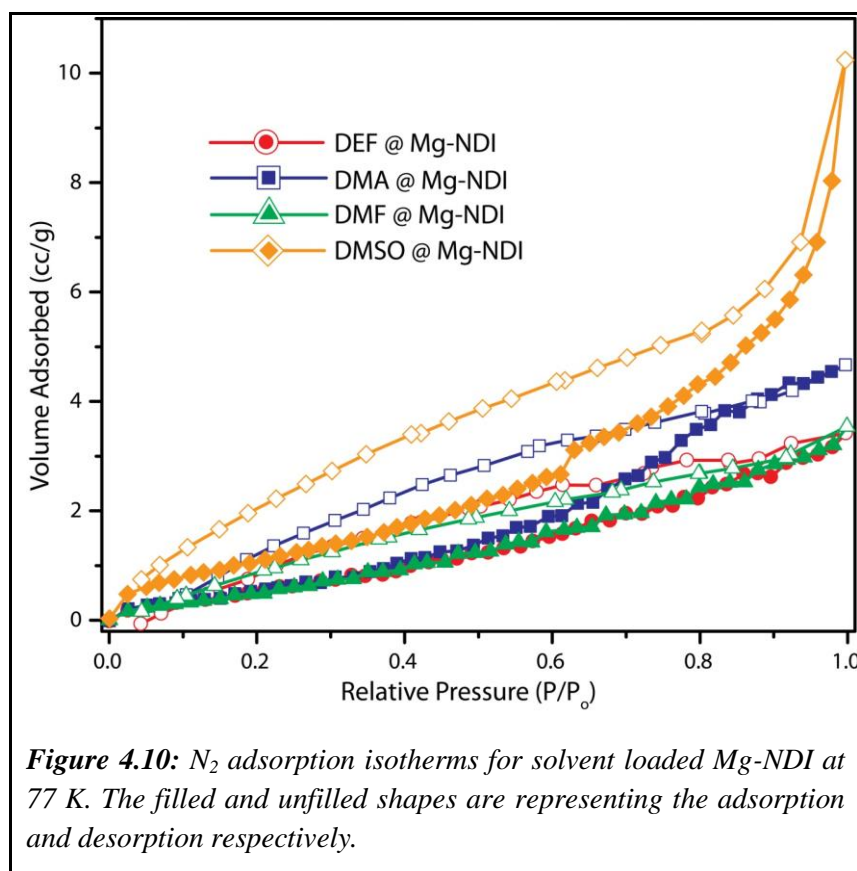
voltammetry measurement (**Figure 4.11**). The electron transfer happens because the HOMO energy (−6.02 eV) of Mg-NDI is lower than that of amine analytes [hydrazine: −5.47 eV, ethylenediamine: −5.60 eV, aniline: −5.63 eV and triethylamine: −5.76 eV]. The electron transfer from hydrazine to Mg-NDI is faster than other amines because of higher energy difference as compare to other amines (**Figure 4.12a**). In case of phenol the PL quenching is also observed due to the presence of electron rich phenolic hydroxy groups,

but no color change has been observed in visible light. Few experiments have been designed to check vapor phase sensing ability of Mg-NDI. In a typical experiment, the vacuum dried Mg-NDI was exposed to the vapor of the amines (obtained from the evaporation of the pure liquid amines) for a period of ~30 min and then measured their photoluminescence property. It was observed that because of the exposure to the amine vapor, photoluminescence property of Mg-NDI has been completely quenched, as that for amines from solution. Thus, Mg-NDI is also able to show vapor phase sensing for amines.

#### 4.2.6 $N_2$ adsorption analysis:

In order to understand the interaction of the analyte molecules with the pore walls for showing the solvatochromic property the  $N_2$  adsorption isotherms have been checked of the solvent molecule incorporated Mg-NDI MOF materials. Thus, if there are any solvent molecules trapped inside the MOF pores, the change in  $N_2$  adsorption of the

materials can be observed. For this, the assynthesized Mg-NDI crystals were soaked in the respective solvent(s) for a prolonged time [2 h] and then dried the material under vacuum for 6 h to remove the loosely bound solvent molecules on the crystal surface and in between the crystallites.  $N_2$



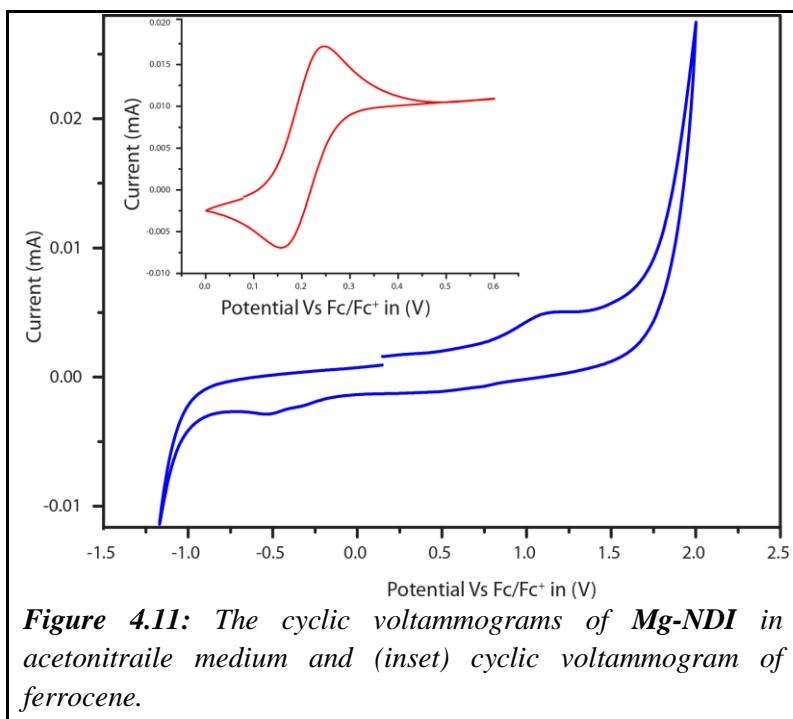
adsorption of these dried materials revealed their non-porous nature and the BET surface area was drastically decreased because of the presence of solvent molecules. The

following N<sub>2</sub> adsorption isotherms indicate that the respective materials do not contain any pore surfaces accessible for the incoming N<sub>2</sub> molecules. Thus, it can be concluded that this decrease in surface area for the solvent loaded materials compared to the completely evacuated materials is because of the trapped solvent molecules present inside the MOF pores. It is noteworthy that the MOF crystals were vacuum dried with a degasser prior to this study, thus chances of pore blockage by the solvent molecules adsorbed on surface of in the inter-crystallite spaces has been diminished. Therefore, this non porous nature of the solvent incorporated materials concluded that the solvatochromic behavior of Mg-NDI is because of the solvent molecules present and interacting inside the pores of the framework.

#### 4.2.7 Electrochemical measurements:

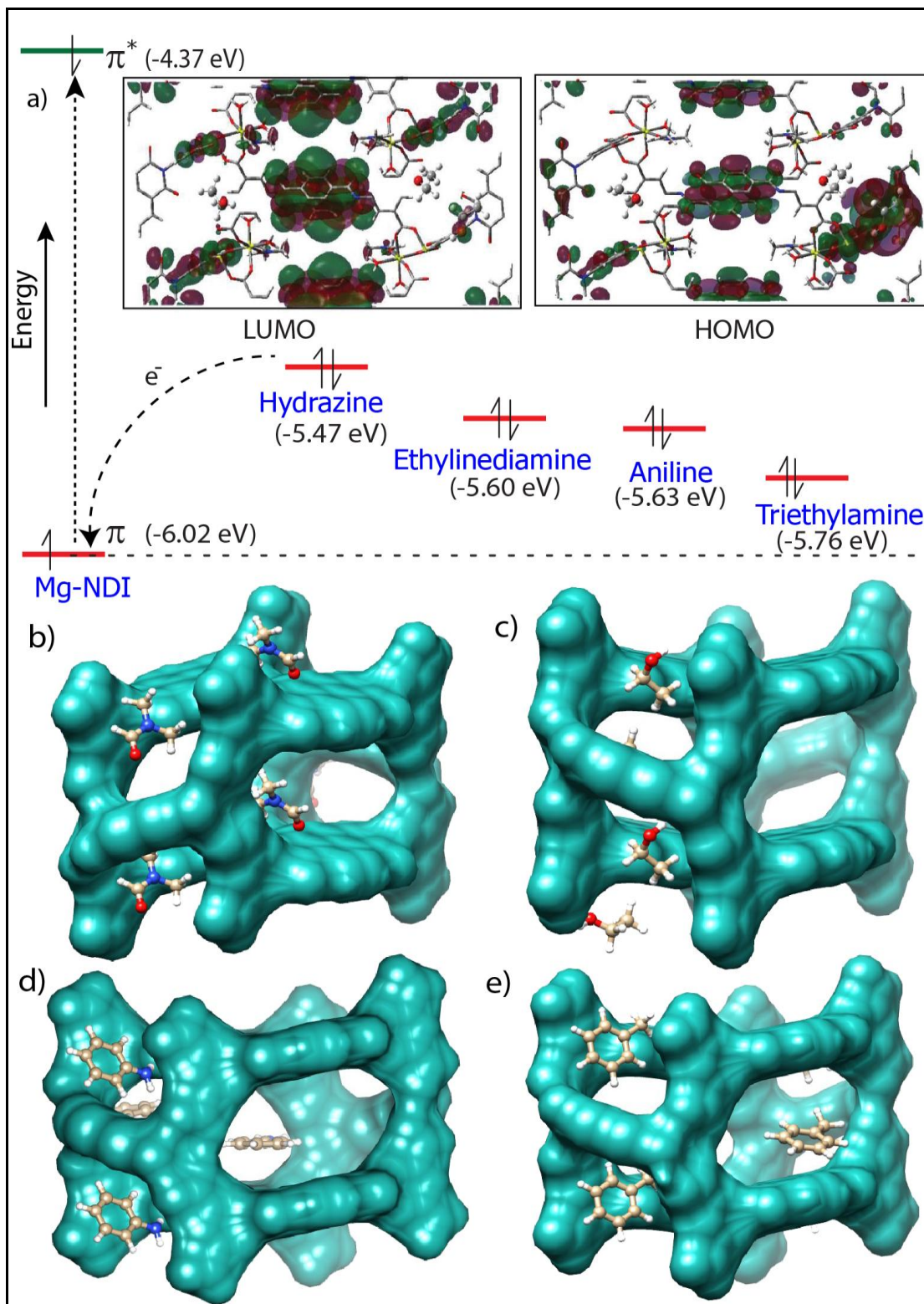
The reduction potentials of the Mg-NDI were measured using a three-electrode cell at room temperature. A platinum electrode was used as the working electrode, platinum wire as the counter-electrode, and a reference using ferrocene coupled (Fc/Fc<sup>+</sup>).

Electrochemical measurements of the analytes were carried out



**Figure 4.11:** The cyclic voltammograms of Mg-NDI in acetonitrile medium and (inset) cyclic voltammogram of ferrocene.

using 0.01 mmol solutions of tetrabutylammonium hexafluoro phosphate solution in acetonitrile. For the MOFs, the powdered materials were coated on 3 mm wide platinum electrode. The reduction potentials of the compounds were obtained from the cyclic voltammograms and corrected with respect to the Fc/Fc<sup>+</sup> internal standard.



**Figure 4.12:** a) HOMO ( $\pi$ ) and LUMO ( $\pi^*$ ) energy levels of Mg-NDI and different amines. The inset shows contour plots of the HOMO and LUMO for Mg-NDI. Energy optimized structures of b) DMF, c) EtOH, d) Aniline and e) Toluene incorporated Mg-NDI has been represented.

#### 4.2.8 DFT calculation for Mg-NDI:

In order to get better understanding of the solvatochromic behavior and the corresponding PL quenching of Mg-NDI, DFT calculations were performed for bare and analyte incorporated MOFs. Optimized structures of the solvent incorporated MOFs (**Figure 4.12b, 4.12c**) suggest that the solvent molecules have a weak dipolar interaction with the pore walls. Band gap energy for DMF@Mg-NDI and EtOH@Mg-NDI were found to be 1.32 and 1.41 eV, respectively. The calculated band gap values, calculated while keeping all framework atoms fixed in their crystallographic positions, are in accordance with the corresponding experimental band-gap values. For each solvent@MOF combination, 100 initial geometries were generated using the Kick [4.14] stochastic structure generator [4.15]. Positions of the solvent molecules were optimised using DFTB [4.16], keeping the framework fixed at the experimental geometry. The optimised structures were ranked in terms of energy and the energy levels of the HOMO and LUMO were extracted for the lowest energy structure of each solvent@MOF system. To generate cube files for the frontier orbitals, single point calculations of the DFTB optimized geometry in periodic boundary conditions were performed at DFT level. Density functional theory (DFT) was applied within the generalized gradient approximation, using the PBE XC functional [4.17]. The Gaussian and Plane-Wave method, as it is implemented in CP2K package, [4.18] with DZVP-MOLOPT-GTH basis set and Goedecker-Teter-Hutter pseudopotentials [4.19] was applied for all atoms. The charge density cutoff of the finest grid level is equal to 400 Ry. The number of used multigrids is 5.

#### 4.3 Conclusions

In conclusion, a new metal organic framework (Mg-NDI) has been synthesized using a NDI-based chromophoric linker. Presence of the NDI moiety inside the framework made Mg-NDI capable of showing photochromic as well as solvatochromic property. Mg-NDI is able to demonstrate a quick (within 60 seconds) and reversible solvatochromic behavior in presence of solvents having different polarities. The photoluminescence emission maximum shows hypsochromic shift according to the increase in solvent polarity. Interestingly, the band gap of the solvent incorporated material was found to show a linear relationship with the solvent polarity. Mg-NDI is also exhibit

photochromism via electron transfer pathway because of the presence of the redox active organic linker. Mg–NDI also exhibits colorimetric and fluorescence sensor of small sized amine molecules. Mg–NDI is able to selectively sense amine molecules, from a series of similar sized analytes, through prominent color change. Sensing of the mixed solvents and vapor phase amine detection are underway in our laboratory.

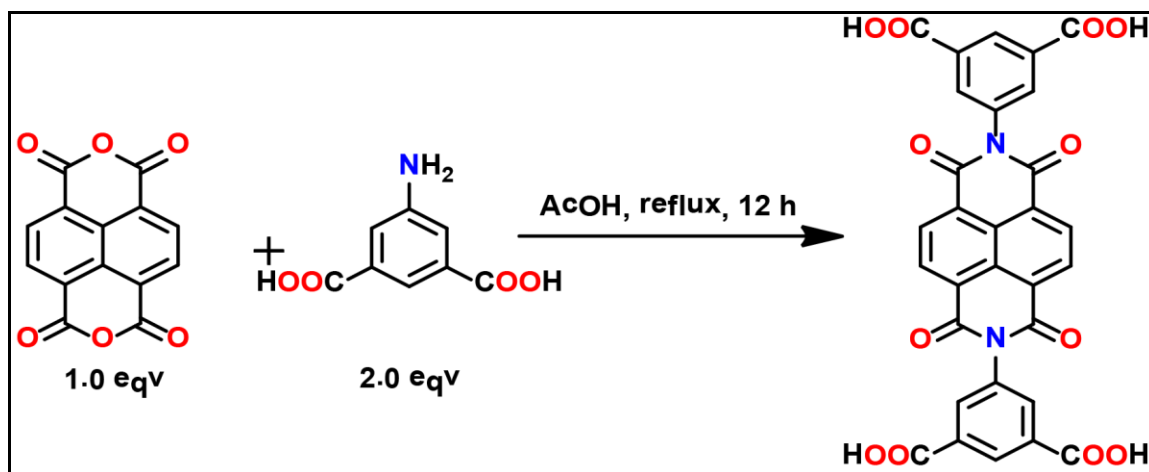
#### 4.4 Experimental procedures:

##### 4.4.1 Materials:

The starting materials for synthesis of H<sub>4</sub>BINDI were purchased from the Aldrich Chemicals. Mg(NO<sub>3</sub>)<sub>2</sub>·6H<sub>2</sub>O, *N,N'*-dimethylformamide (DMF), *N,N'*-dimethylacetamide (DMA), *N,N'*-dimethylsulfoxide (DMSO), *N,N'*-diethylformamide (DEF), Acetonitrile (CH<sub>3</sub>CN), Ethanol (EtOH) and other solvents were purchased from Rankem chemicals.

##### 4.4.2 Synthesis of H<sub>4</sub>BINDI and Mg-NDI:

*N,N'*-bis(5-isophthalic acid)naphthalenediimide (H<sub>4</sub>BINDI) was synthesized according to a previously reported procedure<sup>1</sup>. 1,4,5,8-tetracarboxydianhydride (1.34 g, 5.0 mmol) was taken into a 250 mL round bottomed flask and suspended in 25 mL acetic acid. The mixture was stirred for 10 min. To this solution, 5-aminoisophthalic acid (1.81 g, 10.0 mmol) was added and the solution allowed reflux for 12 h. The reaction was allowed to



**Figure 4.13:** Scheme for synthesis of H<sub>4</sub>BINDI.

cool to room temperature and water (20 mL) was added to precipitate the product. The product was collected by filtration washed with ethanol and dried in vacuum to yield 2.4



g of off-white solid (isolated yield = 2.4 g, 77%). The compound was recrystallized from DMF as an off-yellow materials (isolated yield = 2.1 g, 67%).

**Synthesis of Mg-NDI:** The plate-like crystals of Mg-NDI MOF was synthesized by reacting *N,N'*-bis(5-isophthalic acid)naphthalenediimide (H<sub>4</sub>BINDI) (21 mg, 0.035 mmol) with Mg(NO<sub>3</sub>)<sub>2</sub>.6H<sub>2</sub>O (24 mg, 0.093 mmol) in 4 mL DMF and 0.2 mL HCl (3 N) at 90 °C for 24 h. Orange color crystals were separated after the reaction and preserved in dry DMF/DEF for further applications/characterizations.

#### 4.4.3 General methods for characterization:

All reagents were commercially available and used as received. All gas adsorption experiments (up to 1 bar) were performed on a *Quantachrome Autosorb* automatic volumetric instrument. UV-vis absorbance studies were carried out with Varian Carry 50 instrument equipped with a single beam facility (with a spectral resolution of 0.5 nm). Horiba Jobin Yvon Fluorolog 3 spectrophotometer having 450 W Xenon lamp was used for steady state fluorescence studies.

**Powder X-Ray diffraction (PXRD).** Powder X-ray diffraction (PXRD) patterns were recorded on a Rigaku Smartlab diffractometer for Cu K<sub>α</sub> radiation ( $\lambda = 1.5406 \text{ \AA}$ ), with a scan speed of  $2^\circ \text{ min}^{-1}$ . The tube voltage and amperage were set at 40 kV and 50 mA respectively. Each sample was scanned between 5 and  $50^\circ 2\theta$  with a step size of  $0.02^\circ$ . The instrument was previously calibrated using a silicon standard.

**Thermogravimetric analysis (TGA).** TGA was performed on a SDT Q600 TG-DTA analyzer instrument. Approximately 5 mg of the sample was added to a platinum crucible and heated from 25 to 800 °C under N<sub>2</sub> atmosphere at a heating rate of  $10^\circ \text{ C min}^{-1}$ .

**IR spectroscopy.** Fourier transform infrared (FT-IR) spectra were taken on a Bruker Optics ALPHA-E spectrometer with a universal Zn-Se ATR (attenuated total reflection) accessory in the  $600\text{-}4000 \text{ cm}^{-1}$  region or using a Diamond ATR (Golden Gate). 24 scans were collected at  $4 \text{ cm}^{-1}$  resolution for each sample.

#### 4.4.4 X-ray crystallography:

##### 3.4.4.1 General data collection and refinement procedures:

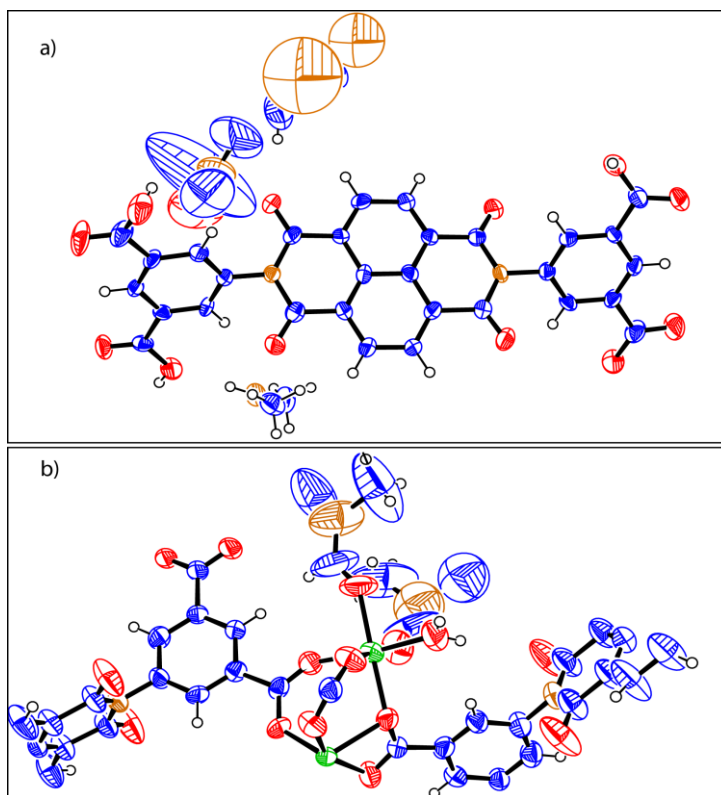
As synthesized crystals of **Mg-NDI** and **H<sub>4</sub>BINDI** were coated with paratone-N and placed on top of a nylon cryoloop (Hampton research) and then mounted in the diffractometer. The data collection was done at 150 and 293 K, respectively. The crystals were mounted on a Super Nova Dual source X-ray Diffractometer system (Agilent Technologies) equipped with a CCD area detector and operated at 250 W power (50 kV, 0.8 mA) to generate Mo K $\alpha$  radiation ( $\lambda = 0.71073 \text{ \AA}$ ) and Cu K $\alpha$  radiation ( $\lambda = 1.54178 \text{ \AA}$ ) at 298(2) K. Initial scans of each specimen were performed to obtain preliminary unit cell parameters and to assess the mosaicity (breadth of spots between frames) of the crystal to select the required frame width for data collection. CrysAlis<sup>Pro</sup> program software [3.9] was used suite to carry out overlapping  $\varphi$  and  $\omega$  scans at detector ( $2\theta$ ) settings ( $2\theta = 28$ ). Following data collection, reflections were sampled from all regions of the Ewald sphere to redetermine unit cell parameters for data integration. In no data collection was evidence for crystal decay encountered. Following exhaustive review of collected frames the resolution of the data set was judged. Data were integrated using CrysAlis<sup>Pro</sup> software with a narrow frame algorithm. Data were subsequently corrected for absorption by the program SCALE3 ABSPACK scaling algorithm.

These structures were solved by direct method and refined using the SHELXTL 97 [2.23] software suite. Atoms were located from iterative examination of difference F-maps following least squares refinements of the earlier models. Final model was refined anisotropically (if the number of data permitted) until full convergence was achieved. Hydrogen atoms were placed in calculated positions (C-H = 0.93  $\text{\AA}$ ) and included as riding atoms with isotropic displacement parameters 1.2-1.5 times  $U_{eq}$  of the attached C atoms. In some cases modeling of electron density within the voids of the frameworks did not lead to identification of recognizable solvent molecules in these structures, probably due to the highly disordered contents of the large pores in the frameworks. Highly porous crystals that contain solvent-filled pores often yield raw data where observed strong (high intensity) scattering becomes limited to  $\sim 1.0 \text{ \AA}$  at best, with higher resolution data present at low intensity. A common strategy for improving X-ray data, increasing the exposure time of the crystal to X-rays, did not improve the quality of the high angle data in this case, as the intensity from low angle data saturated the detector and minimal improvement in the high angle data was achieved. Additionally, diffused scattering from

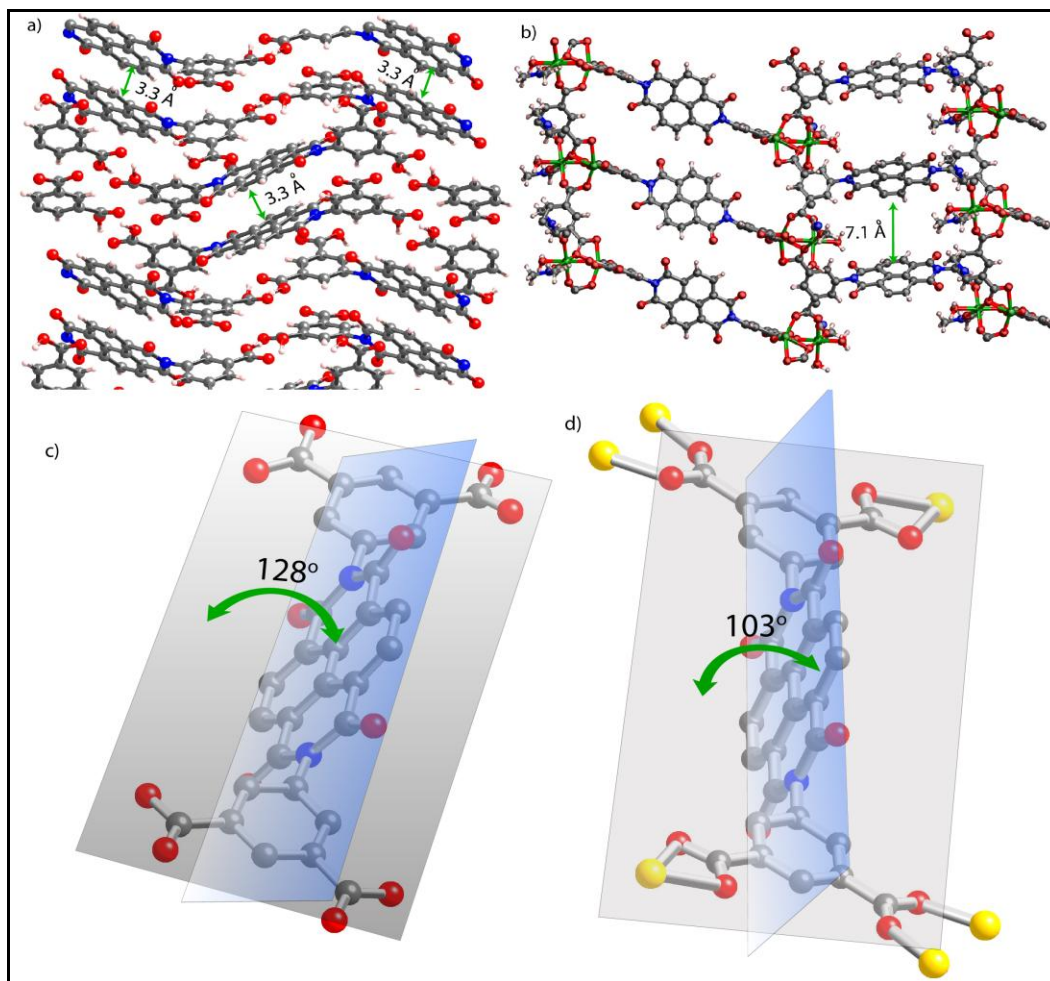
the highly disordered solvent within the void spaces of the framework and from the capillary to mount the crystal contributes to the background and the ‘washing out’ of the weaker data. Electron density within void spaces has not been assigned to any guest entity but has been modeled as isolated oxygen and/or carbon atoms. The foremost errors in all the models are thought to lie in the assignment of guest electron density. The structure was examined using the *ADSYM* subroutine of PLATON [2.25] to assure that no additional symmetry could be applied to the models. The ellipsoids in ORTEP diagrams are displayed at the 50% probability level unless noted otherwise. For all structures we note that elevated R-values are commonly encountered in MOP crystallography for the reasons expressed above by us and by other research groups [2.26-2.35]. CCDC 1024270 and CCDC 1024271 contain the crystallographic data for **H<sub>4</sub>BINDI** and **Mg-NDI** respectively.

#### 4.4.4.2 Experimental and refinement details for H<sub>4</sub>BINDI:

A white block like crystal ( $0.41 \times 0.40 \times 0.10 \text{ mm}^3$ ) of **H<sub>4</sub>BINDI** was placed in 0.7 mm diameter nylon CryoLoops (Hampton Research) with Paraton-N (Hampton Research). The loop was mounted on a Super Nova Dual source X-ray diffractometer system (Agilent Technologies) equipped with a CCD area detector and operated at 250 W power (50 kV, 0.8 mA) to generate Mo K $\alpha$  radiation ( $\lambda = 0.71073 \text{ \AA}$ ) and Cu K $\alpha$  radiation ( $\lambda = 1.54178 \text{ \AA}$ ) at 293(2) K in a liquid N<sub>2</sub> cooled stream of nitrogen. A total of 7311 reflections were collected of which 4775 were



**Figure 4.14:** Ortep Drawing of the asymmetric unit of a) **H<sub>4</sub>BINDI** b) **Mg-NDI**. Thermal ellipsoids set to 50% probability level.



**Figure 4.15:** Single crystal structure and packing diagram of a)  $H_4$ BINDI showing the  $\pi$ - $\pi$  interaction between NDI moieties (3.3 Å) and b) Mg-NDI showing the absence of  $\pi$ - $\pi$  interaction between NDI moieties (7.1 Å). The dihedral angle between naphthalene ring and isophthalic acid moiety in c)  $H_4$ BINDI and d) Mg-NDI framework was presented.

unique. The range of  $\theta$  was from 3.08 to 29.20. Analysis of the data showed negligible decay during collection. The structure was solved in the monoclinic  $C 2/c$  space group, with  $Z = 1$ , using direct methods. All non-hydrogen atoms were refined anisotropically with hydrogen atoms generated as spheres riding the coordinates of their parent atoms. Final full matrix least-squares refinement on  $F^2$  converged to  $R_1 = 0.1780$  ( $F > 2\sigma F$ ) and  $wR_2 = 0.2988$  (all data) with GOF = 1.113 (Table 4.1).

#### 4.4.4.3 Experimental and refinement details for Mg-NDI:

A white block like crystal ( $0.40 \times 0.20 \times 0.20$  mm<sup>3</sup>) of Mg-NDI was placed in 0.7 mm diameter nylon CryoLoops (Hampton Research) with Paratone-N (Hampton Research).

The loop was mounted on a Super Nova Dual source X-ray Diffractometer (Agilent Technologies) equipped with a CCD area detector and operated at 250 W power (50 kV, 0.8 mA) to generate Mo K $\alpha$  radiation ( $\lambda = 0.71073 \text{ \AA}$ ) at 150(2) K in a liquid N<sub>2</sub> cooled stream of nitrogen. A total of 14116 reflections were collected of which 5643 were unique. The range of  $\theta$  was from 2.98 to 29.19. Analysis of the data showed negligible decay during collection. The structure was solved in the monoclinic  $P 2/c$  space group, with  $Z = 2$ , using direct methods. All non-hydrogen atoms were refined anisotropically with hydrogen atoms generated as spheres riding the coordinates of their parent atoms. Final full matrix least-squares refinement on  $F^2$  converged to  $R_1 = 0.1637$  ( $F > 2\sigma F$ ) and  $wR_2 = 0.2975$  (all data) with GOF = 0.7929 (**Table 4.1**).

**Table 4.1** Crystal data and structure refinement for **H<sub>4</sub>BINDI** and **Mg-NDI**.

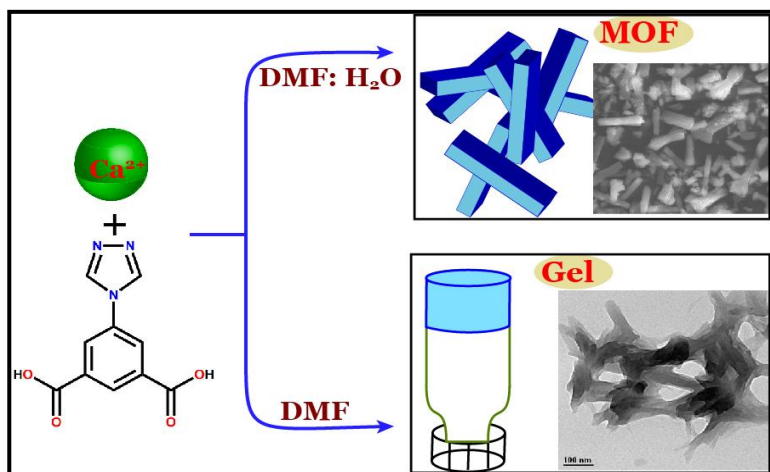
MOFs	<b>H<sub>4</sub>BINDI</b>	<b>Mg-NDI</b>
<b>Empirical formula</b>	C <sub>279.28</sub> H <sub>164</sub> N <sub>37</sub> O <sub>100</sub>	C <sub>69</sub> H <sub>35</sub> Mg <sub>4</sub> N <sub>7</sub> O <sub>30</sub>
<b>Formula wt.</b>	5637.84	1539.28
<b>Temperature</b>	293(2) K	150(2) K
<b>Wavelength</b>	0.71073 Å	0.71073 Å
<b>Cryst. system</b>	Monoclinic	Monoclinic
<b>Space group</b>	<i>C2/c</i>	<i>P2/c</i>
<b>Unit cell dimensions</b>	$a = 33.067(4) \text{ \AA}$ $\alpha = 90^\circ$ $b = 14.8252(15) \text{ \AA}$ $\beta = 121.19(10)^\circ$ $c = 17.1809(12) \text{ \AA}$ $\gamma = 90^\circ$	$a = 34.3413(18) \text{ \AA}$ , $\alpha = 90^\circ$ $b = 10.0447(7) \text{ \AA}$ , $\beta = 96.234(6)^\circ$ $c = 17.7382(17) \text{ \AA}$ , $\gamma = 90^\circ$
<b>Volume</b>	7205.1(12)	6082.6(8)
<b>Z</b>	1	2
<b>Density (calculated)</b>	1.401	0.8404
<b>Absorption coefficient</b>	0.101	0.085
<b>Goodness-of-fit on F<sup>2</sup></b>	1.113	0.7929
<b>Final R indices [I &gt; 2σ(I)]</b>	$R_1 = 0.1429$ , $wR_2 = 0.2897$	$R_1 = 0.1057$ , $wR_2 = 0.2679$
<b>R indices (all data)</b>	$R_1 = 0.1780$ , $wR_2 = 0.2988$	$R_1 = 0.1637$ , $wR_2 = 0.2975$

**NOTE:** The results of this chapter have already been published in *Chem. Sci.*, 2015, 6, 1420 - 1425, with the title: “Solid State Organic Amine Detection in a Photochromic Porous Metal Organic Framework.” These publications were the results from the group of Dr. Rahul Banerjee and his students Arijit Mallick and Bikas Garai from CSIR-National Chemical Laboratory, Pune, India. Prof. Dr. Thomas Heine with his student Matthew A. Addicoat and Petko St. Petkov have actively contributed to the publication by performing computational studies on MOFs. Major works are contributed by Arijit Mallick with the help of the instrumental facilities of CSIR National Chemical Laboratory.

## CHAPTER 5

### Ca(II) based Metal-Organic Framework and Metal-Organic Gel for Hydrosilylation Catalysis: Tuning between Gelation and Crystallisation

**Abstract:** A porous, crystalline metal-organic framework (Ca-5TIA-MOF), as well as stable viscoelastic metallogel (Ca-5TIA-Gel) is represented in this chapter. Presence of water in the solvent system favors the



formation of crystalline MOF, whereas pure organic solvent induces gelation. this chapter describes unprecedented Ca-based low molecular weight-metallogels, as well as the first porous Ca-based MOF, which shows adsorption capacity for CO<sub>2</sub> at 1 atm pressure. Interestingly, Ca-5TIA-Xergel shows 20% higher CO<sub>2</sub>-uptake than the crystalline Ca-5TIA-MOF at 1 atm and 298 K. Both Ca-5TIA-MOF and Ca-5TIA-Gel displayed a modest catalytic activity towards the hydrosilylation of benzaldehyde, Meanwhile gel showed better performance over the MOF in the aforementioned catalysis.

## 5.1 Introduction:

Metal-organic frameworks (MOFs) are porous, crystalline materials in which metal ions are linked together by multidentate, low-molecular-weight (LMW) organic ligands resulting in supramolecular coordination polymers of different topologies [5.1]. Over the past few years, research on MOFs has rapidly drawn considerable attention due to their promising applications in gas storage adsorption [5.1a, 5.2], separations [5.2t, 5.3], heterogeneous catalysis [5.4], drug delivery [5.5] and sensors [5.6]. The practical advantages of MOFs mainly relies on their uniform channels, high porosities, excellent thermal stability and chemical tailorability [5.7]. However, the brittle nature of these crystalline materials can challenge their industrial processing and combination with other functional materials without pore blocking and/or decrease in their inner surface area [5.8]. It is worthy to mention that viscoelastic metallogels [5.9] could overcome, this limitation partially [5.10] for high-tech applications in a number of fields such as catalysis [5.4g, 5.11], photo physics [5.12], sensing [5.13], magnetic materials [5.14], redox responsiveness [5.15], and electron emission [5.16]. In particular, the catalytic potential of wide-ranging metallogel-based materials [5.9k, 5.17] relies on two major aspects; i) two-phase nature, which may facilitate recovering and recycling; and ii) a much higher accessibility of small reagents towards highly solvated 3D porous network in comparison to other standard heterogeneous catalysts.

Metallogels can perform catalytic activity in three ways; i) metal centers based catalysis, ii) organic ligand based catalysis and iii) guest (trapped in gel matrix) induced catalysis. In this chapter the metal center based catalysis has been discussed briefly. Despite a substantial volume of literature on MOFs and metallogels, reports on Ca-based porous 3D MOFs are rather limited when we critically compare with other metals [5.18]. Among the most recent examples, catalytically active Ca-based MOFs have been prepared using 4,4'-(hexafluoroisopropylidene)bis(benzoic acid) [5.18k] or anthraquinone-2,6-disulfonate [5.18k] as ligands. On the other hand Lin and co-workers [5.18n] have also demonstrated a series of new 3D MOFs made from aromatic carboxylic acids and Ca(II) ions under different conditions, which can undergo remarkable destruction/construction structural transformations involving a break and reformation of the Ca-O bond. From the sustainable point of view, calcium is non-toxic and highly



abundant in nature (3.4% of Earth's crust), which converts it in one of the cheapest commercially available metals without environmental hazards [5.19]. Here we demonstrated the synthesis, characterization, gas uptake and catalytic properties of a new self-assembled porous Ca-based 3D MOF (Ca-5TIA-MOF) and stable Ca-based metallogels (Ca-5TIA-Gel), synthesized from 5-(1,2,4-triazole) isophthalic acid (5TIA) as LMW organic ligand.

## 5.2 Result and discussion:

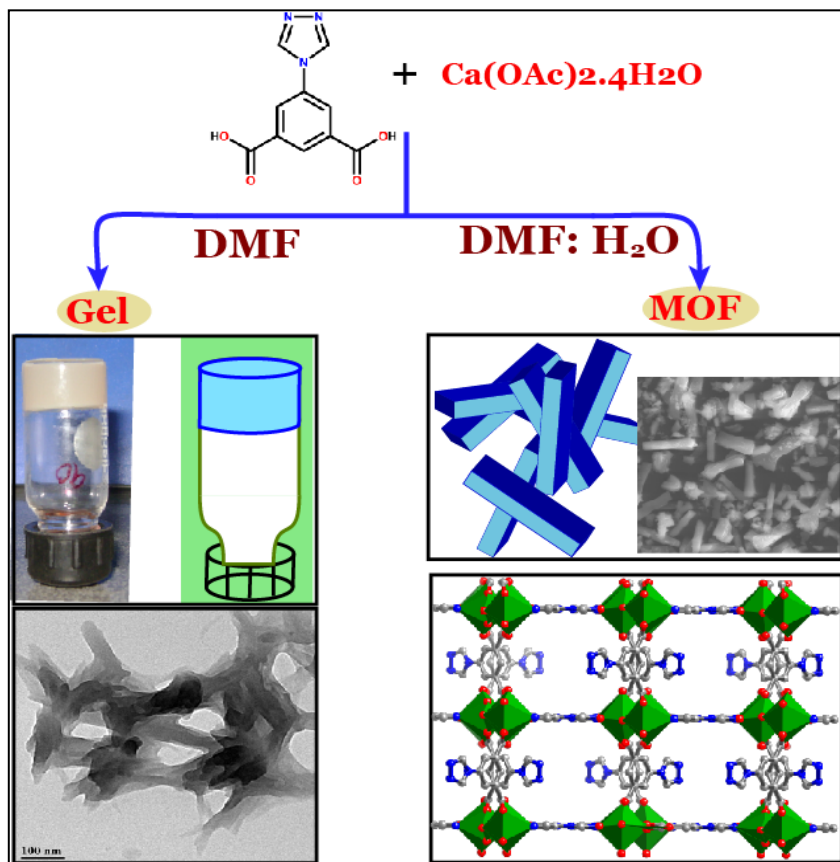
### 5.2.1 Synthesis of Ca-5TIA-MOF and Gel:

In general, the synthesis of MOFs involves the combination of metal ions (connectors) and organic polyanions (linkers) with strong coordination ability toward metals (*e.g.* carboxylates, phosphonates, sulfonates). Among these linkers, aromatic carboxylates constitute useful building blocks for the synthesis of stable MOFs due to the considerable rigidity imparted by the organic ligand. It is well established that cooperative stabilization provided by a combination of hydrogen bonding,  $\pi$ - $\pi$  and metal-ligand interactions is a powerful approach for the synthesis of gel-phase materials [5.20]. In this sense, we recently focused our attention in a 1,2,4-triazole-containing ligand (5TIA) [5.21a] for the construction of new Mn-MOFs showing template-based structural conversions [5.21b]. The versatile coordination modes of this *N*-heterocyclic carboxylic acid ligand is governed by the presence of both nitrogen and oxygen donor atoms in the structure. This favours the coordination with soft- and hard-metals respectively [5.22] allowing the preparation of a number of functional heterometallic coordination polymers [5.23]. Use of soft metals like calcium in combination with 5TIA allow the formation of either MOF (Ca-5TIA-MOF) or metallogels (Ca-5TIA-Gel), where the solvent composition plays a pivotal role.

The synthesis of plate-like colourless crystals of Ca-5TIA-MOF was carried out using Ca(OAc)<sub>2</sub> and 5TIA as ligand in a DMF:H<sub>2</sub>O (v/v 1:1) mixture at 90 °C. In contrast, when pure DMF was used as liquid phase a fast and complete gelation was observed (**Figure 5.1**). The gelation time upon sonication at RT was established in 30 ± 5 min for a gelator system of concentration 0.2 M. The material was stable (*viz.* did not flow) by the “test-tube inversion” method [5.24] and the gel nature was further confirmed

by dynamic rheological measurements. It is widely accepted that the solvent molecules in gel materials are immobilized by capillaries and other related forces in the 3D network structures [5.9].

As 5TIA alone is unable to produce gel in DMF, its rapid coordination with Ca(II) plays a key role in the gelation phenomenon, leading to the growth of coordination polymeric species. This coordination polymeric species then undergo further entanglement in order to develop the 3D gel network. The as formed material was characterized by single crystal X-ray



**Figure 5.1:** Schematic diagram showing the synthesis of Ca-5TIA-MOF and Ca-5TIA-Gel under different conditions. TEM image of Ca-5TIA-Gel (scale bar = 100 nm) and SEM image of Ca-5TIA-MOF (scale bar = 100  $\mu\text{m}$ ).

diffraction. The experimental PXRD peaks of both Ca-5TIA-Xerogel and Ca-5TIA-MOF matched with simulated PXRD pattern as well. This suggests the presence of, at least, some common structural elements in the 3D networks of both xerogel and crystalline Ca-5TIA-MOF phases.

Stable non-thermoreversible Ca-5TIA-Gel could also be obtained at different temperatures ranging from room temperature (RT) to 150  $^{\circ}\text{C}$  (**Figure 5.2**). A pH range between 6–8 was found to be optimum for the gel formation. Interestingly, both optical and microstructure of the materials were found to be influenced by the processing temperature. For instance, bright pinkish gels were usually obtained at RT (**Figure 5.2b**),

whereas yellowish materials are obtained at 120 °C (**Figure 5.2e**). Regardless of the processing temperature, ultrasonic pre-treatment of the mixture [Ca(OAc)<sub>2</sub> + 5TIA] in the appropriate solvent usually provided more homogeneous gel samples. The minimum gelation concentration (MGC) for the equimolar mixture [Ca(OAc)<sub>2</sub> + 5TIA] in DMF was established as 0.1 M. This result indicates that up to *ca.* 258 molecules of solvent are immobilized per molecule of ligand. To check the effect of water in gel formation, we varied the volume of water from 0.1 mL to 2.0 mL. A ratio H<sub>2</sub>O:DMF 1:20 (v/v) was established as the limit, above which no gelation but crystallization took place (**Table 5.2**). This result also confirmed the so-called “delicate balance” existing between these two phenomena [5.25].

### 5.2.2 Solubility and gelation properties:

The gelation ability of the gelator system [Ca(OAc)<sub>2</sub> + 5TIA] was evaluated for various solvents upon sonication at RT for 15 min at concentrations of the gelator system ranging between 0.1 to 0.5 M. We found that stable gels could be prepared in at least five solvents such as DMF, DMSO, DMA, quinoline and DEF (entries 2–5, 10) (**Figure 5.2f**). Water (entry 1) afforded a clear solution of both the ligand and the metal salt, whereas the gelator system was found insoluble in the rest of tested solvents. It was established that Kamlet-Taft parameters [5.26] accounts for specific interactions between solvent and gelator molecules [5.27]. The  $\alpha$  parameter defines the hydrogen bond donor ability of the solvent, which is of special importance in 3D networks built by hydrogen bonding. The  $\beta$  parameter represents the hydrogen bond acceptor ability and can be associated to the thermal stability of the gel, whereas the  $\pi^*$  parameter accounts for the polarisability and plays a vital role on solvation processes during the gelation phenomenon. In our particular case, and from the results of Table 1, it is obvious that those solvents with very low  $\alpha$  values and high  $\beta$  and  $\pi^*$  values simultaneously provided an optimal environment for the gelation process leading to highly thermally stable gels. Thus, solvents that can not (or have a very low tendency) donate hydrogen bonds to the gelator and have low or moderate hydrogen bond acceptor ability and/or polarisability (entries 11–22) results in incompatible phases. On the other hand, solvents with high  $\alpha$  values dissolve the gelator system (entry 1) or have a considerable tendency to dissolve it (entries 7–9) regardless






the  $\beta$  and  $\pi^*$  parameters. An exception to the rule was found with an ionic liquid (entry 6), which afforded partial gelation in spite of its moderate  $\alpha$  value and low  $\beta$  value. Ca-5TIA-Gel was found to be stable on standing at RT under dark conditions at least for 1.5 months. With the idea in

**Table 5.1:** Gelation ability in various solvents for the system [Ca(OAc)<sub>2</sub> (0.1 mmol) + 5TIA (0.1 mmol)].<sup>[a]</sup>

Entry	Solvent	Result <sup>[b]</sup>	Conc. <sup>[c]</sup>	Time <sup>[d]</sup>	Gel-phase colour	Kamlet-Taft parameters		
						$\alpha$	$\beta$	$\pi^*$
1	H <sub>2</sub> O	S	0.2-0.5	-	-	1.17	0.47	1.09
2	DMF	G	0.2	30 ± 5 min	light pinkish	0.00	0.69	0.88
3	DMSO	G	0.4	10 ± 5 <sup>[e]</sup> min	light brownish	0.00	0.76	1.00
4	DMA	G	0.67	24 -48 <sup>[f]</sup> h	light pinkish	0.00	0.76	0.88
5	Quinoline	G	0.5	10 ± 5 <sup>[e]</sup> min	brownish	0.00	0.64	0.92
6	[BMIM][PF <sub>6</sub> ]	G + P	0.2-0.5	-	white	0.63	0.21	1.03
7	MeOH	I <sup>[g]</sup>	0.2-0.5	-	-	0.98	0.66	0.60
8	EtOH	I <sup>[g]</sup>	0.2-0.5	-	-	0.86	0.75	0.54
9	<i>i</i> -PrOH	I <sup>[g]</sup>	0.2-0.5	-	-	0.76	0.84	0.48
10	DEF	G	0.5	90 ± 5 min	-	<sub>[h]</sub>	<sub>[h]</sub>	<sub>[h]</sub>
11	Acetone	I	0.2-0.5	-	-	0.08	0.43	0.71
12	THF	I	0.2-0.5	-	-	0.00	0.55	0.58
13	<i>n</i> -Hexane	I	0.2-0.5	-	-	0.00	0.00	-0.04
14	Et <sub>2</sub> O	I	0.2-0.5	-	-	0.00	0.47	0.27
15	1,4-Dioxane	I	0.2-0.5	-	-	0.00	0.37	0.55
16	Cyclohexane	I	0.2-0.5	-	-	0.00	0.00	0.00
17	EtOAc	I	0.2-0.5	-	-	0.00	0.45	0.55
18	CH <sub>2</sub> Cl <sub>2</sub>	I	0.2-0.5	-	-	0.13	0.10	0.82
19	CHCl <sub>3</sub>	I	0.2-0.5	-	-	0.20	0.10	0.58
20	Benzene	I	0.2-0.5	-	-	0.00	0.10	0.59
21	Toluene	I	0.2-0.5	-	-	0.00	0.11	0.54
22	CH <sub>3</sub> CN	I	0.2-0.5	-	-	0.19	0.40	0.75

[a] Upon sonication at RT for 15 min. After this time, the temperature of the bath was  $27 \pm 1$  °C. Additional heating with a “heat gun” was necessary only to prepared the isotropic solution of the IL. [b] Abbreviations: S = solution; G = gel; I = insoluble (upon sonication with or without further heating with “heat gun”); P = precipitate. [c] Molar concentration (or range of concentrations in the cases where no stable gels were obtained) of the mixture [5TIA + Ca(OAc)<sub>2</sub>] employed for the gelation tests (unit mol/L). [d] Time required for complete gelation at given concentration. [e] Gelation occurred during sonication. [f] Sonication was applied for 30 min at 50 °C. [g] A white viscous blend was obtained. [h] Unknow value.

**Table 5.2:** Controlling of gelation and crystallisation by addition of water for the system [Ca(OAc)<sub>2</sub> (0.2 mmol) + 5TIA (0.2 mmol) + 2mL DMF].

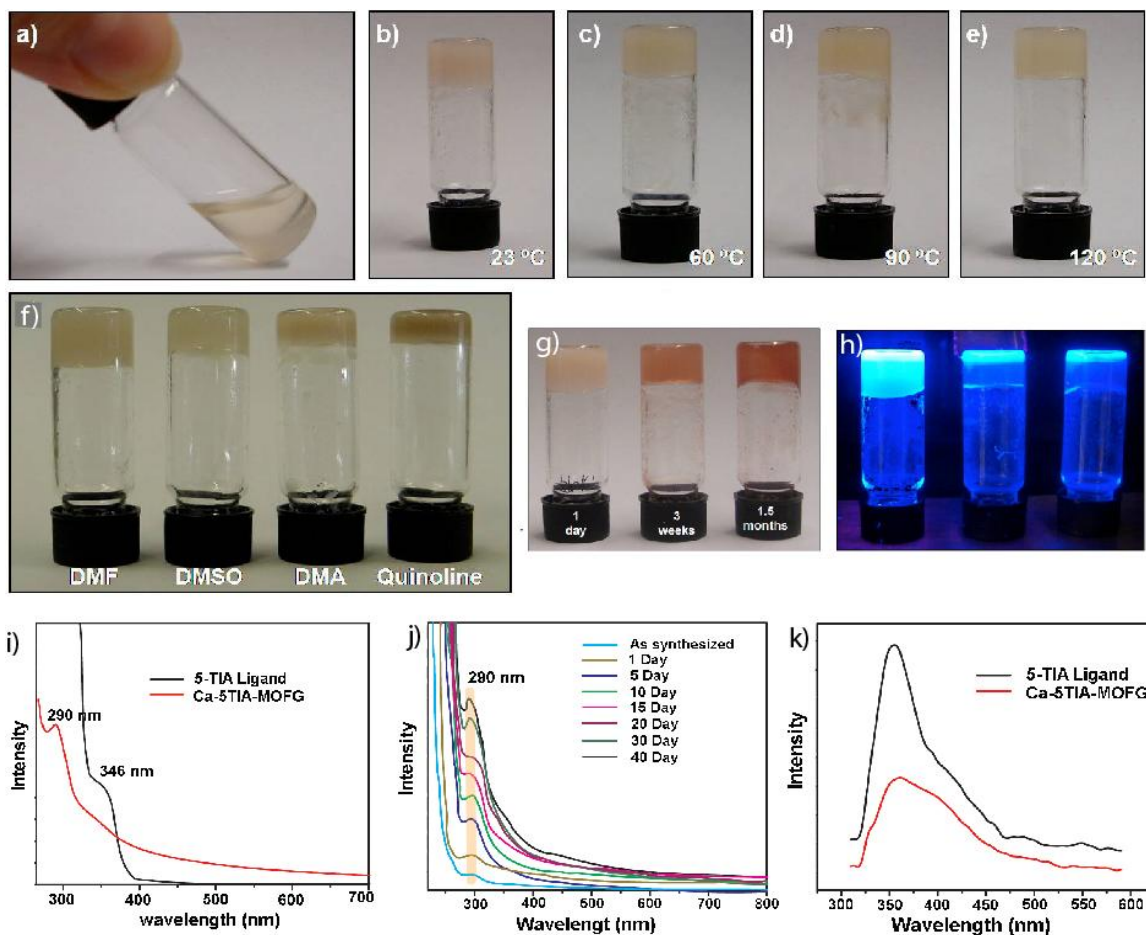
Name	Metal salt conc.	Conc. of 5TIA ligand	Volume of DMF	Volume of H <sub>2</sub> O	Picture	Remarks
1	0.2 mmol	0.2 mmol	2.0 mL	0.1 mL		Gel
2	0.2 mmol	0.2 mmol	2.0 mL	0.2 mL		Precipitate
3	0.2 mmol	0.2 mmol	2.0 mL	0.5 mL		Precipitate
4	0.2 mmol	0.2 mmol	2.0 mL	0.7 mL		Precipitate
5	0.2 mmol	0.2 mmol	2.0 mL	1.0 mL		Precipitate
6	0.2 mmol	0.2 mmol	2.0 mL	1.5 mL		Precipitate
7	0.2 mmol	0.2 mmol	2.0 mL	2.0 mL		Precipitate
8	0.2 mmol	0.2 mmol	2.0 mL	2.5 mL		Crystals

mind of further testing the potential catalytic activity of Ca-5TIA-Gel, its stability over time (up to 5 days) in the presence of other solvents was qualitatively evaluated for the gel prepared in DMF at RT upon sonication. Small pieces of the gel were placed in glass vials and covered with different solvents. In general, the gel suffered fragmentation if shaken vigorously in the presence of other solvents, suggesting a rigid rather than a

flexible supramolecular network. The results indicate that only external water can dissolve the gel, whereas strong acidic (1.0 M HCl) or basic (1.0 M NaOH) solutions caused precipitation after 24 h. Partial fragmentation of the gel body into smaller pieces was observed on standing in most of organic solvents after 1 h in the following order: MeOH ~ THF ~ CH<sub>2</sub>Cl<sub>2</sub> ~ toluene ~ acetone > 1,4-Dioxane ~ CH<sub>3</sub>CN ~ EtOAc ~ DMF ~ Et<sub>3</sub>N. In CHCl<sub>3</sub>, the gel was stable up to 3 h. In contrast, the bulk gel was found to be fairly stable at least up to 5 days in the presence of DMSO, toluene, cyclohexane, *n*-hexane and Et<sub>2</sub>O, which points out that some of these solvents could be a good choice for catalytic experiments. Among these solvents, the gel embedded in DMSO clearly exhibited the highest resistance to mechanical stirring. Moreover, resolute change in the refraction index of the material occurs in the presence of Et<sub>2</sub>O (the gel body become more white-opaque), which is not observed with the other solvents. The light pinkish opaque Ca-5TIA-Gels remained stable to the “test-tube inversion” method but experienced a clear colour intensification over time when exposed to visible light (**Figure 5.2g**). This change in the optical properties can be inhibited under dark conditions, which suggested intra-ligand or ligand-metal charge transfer episodes during light exposure. To gain additional insight into this process, UV-vis and fluorescence spectra of Ca-5TIA-Gel was measured at RT and different ageing time. The UV-vis spectrum of the ligand in DMF displayed only a broad absorption at 346 nm, which may be assigned to an intraligand orbital transition from *n* to  $\pi^*$  and  $\pi$  to  $\pi^*$  (**Figure 5.2i**). In contrast, Ca-5TIA-Gel showed the major phenyl ring absorption peak at 290 nm and a minor hump at 346 nm probably due to unreacted ligand (**Figure 5.2k**). A remarkable decrease in intensity of the peak at 290 nm with increasing time exposure to light points out the blockade of  $\pi$  to  $\pi^*$  or *n* to  $\pi^*$  transitions between the aromatic moiety conjugated with the lone-pair electrons of the triazole unit or the unsaturated bonds of the carbonyl groups (-COOH). On the other hand, the intense fluorescence emission concentrated at 356 nm was most likely due to a product of intraligand fluorescent emission as it was also observed for the free ligand (**Figure 5.2k**). The signal intensity pattern signified that the fluorescence emission of the system is quenched due to metal coordination.

Moreover, a series of studies were carried out to determine the influence of the metal counter anion on the gelation phenomenon. Interestingly, we found that the acetate

anions could be efficiently exchanged by hydroxides and oxides (i.e. using  $\text{Ca}(\text{OH})_2$  and  $\text{CaO}$  instead of  $\text{Ca}(\text{OAc})_2$ ) in the gel formulation). In contrast, the use of other hard anions like chloride, carbonate, sulfate or nitrate led to the formation of either clear solutions or amorphous precipitates upon sonication at room temperature [5.28]. These results indicate that the counter anion plays an important role in the supramolecular


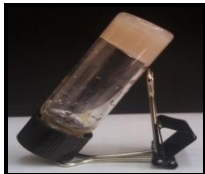



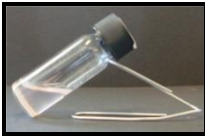



**Figure 5.2:** a) Digital photograph of the milky solution obtained by mixing 0.1 mmol  $\text{Ca}(\text{OAc})_2$  and 0.1 mmol 5TIA in 1 mL DMF upon sonication at RT for 15 min. Gel formation after b) standing at RT or heating at c) 60 °C, d) 90 °C, e) 120 °C in an oil bath for 2 h. f) Gels prepared in DMF, DMSO, DMA and Quinoline at 0.5 M concentration in the gelator system. g) Digital photograph of the Ca-5TIA-Gel made in DMF after 1 day, 3 weeks and 1.5 months; h) digital photograph of the same gels under UV irradiation. i) UV-Vis spectra for 5TIA ligand (black) and Ca-5TIA-Gel (red). j) Time dependent UV-Vis spectra for Ca-5TIA-Gel. k) Fluorescence emission spectra for 5TIA ligand (black) and Ca-5TIA-Gel (red).

assembly of the Ca-5TIA complex in solution as it has been observed for other metallogels [5.23a, 5.29]. We observed that experimental PXRD peaks of both Ca-5TIA-

Xerogel and Ca-5TIA-MOF matched reasonably well with simulated PXRD pattern of Ca-5TIA-MOF, suggesting the presence of, some common structural elements in the 3D networks of both xerogel and crystalline phases. However, the PXRD peaks of the xerogels obtained from  $\text{Ca(OH)}_2$  and  $\text{CaO}$  did not match with the simulated PXRD patterns of Ca-5TIA-MOF, albeit it was noteworthy that the PXRD of the  $\text{Ca(OH)}_2$ - and  $\text{CaO}$ -based xerogels matched well each other, which indicating some structural similarities of these two gel materials (*Figure 5.5d*).

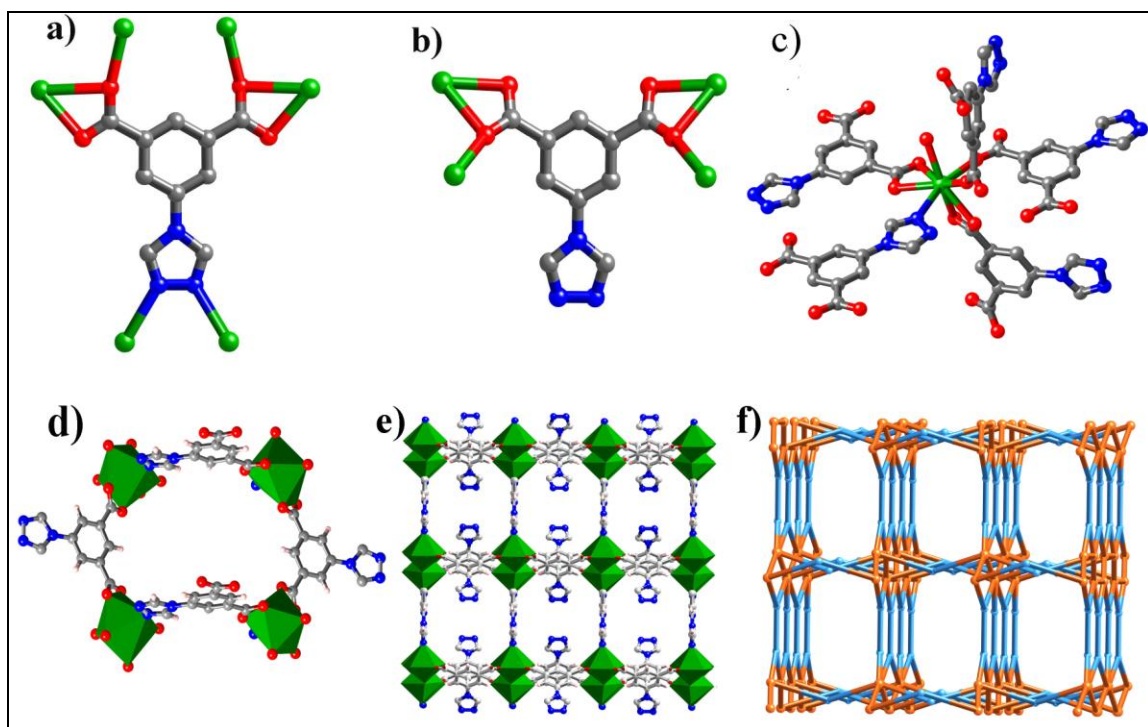
**Table 5.3:** Gelation ability of the system [Ca-salt (0.1 mmol) + 5TIA (0.1 mmol)] in DMF (1.0 mL) using different metal counteranions.

Metal salts	Conc. of metal salts	Conc. of 5TIA ligand	Volume of DMF added	Pictures	Description of the obtained material
$\text{Ca(OH)}_2$	0.1 mmol (7.4 mg)	0.1 mmol (22.3 mg)	1.0 mL		Gel (white opaque)
$\text{CaO}$	0.1 mmol (6.5 mg)	0.1 mmol (22.3 mg)	1.0 mL		Gel (brownish)
$\text{Ca(OAc)}_2$	0.1 mmol (15.8 mg)	0.1 mmol (22.3 mg)	1.0 mL		Gel (white opaque)
$\text{CaSO}_4$	0.1 mmol (13.6 mg)	0.1 mmol (22.3 mg)	1.0 mL		Pinkish solution and solid material at the bottom of the vial
$\text{CaCl}_2$	0.1 mmol (11.1 mg)	0.1 mmol (22.3 mg)	1.0 mL		Clear solution
$\text{CaCO}_3$	0.1 mmol (10.0 mg)	0.1 mmol (22.3 mg)	1.0 mL		Pinkish solution and solid material at the bottom of the vial
$\text{Ca(NO}_3)_2$	0.1 mmol (7.4 mg)	0.1 mmol (22.3 mg)	1.0 mL		Clear yellowish solution



### 5.2.3 Structural analysis of Ca-5TIA:

The Ca-5TIA-MOF crystallizes in space group  $Cmca$  and structural determination by X-ray single crystal diffraction revealed a well-defined 3D network of Ca(II) linked by 5TIA ligands. The asymmetric unit of Ca-5TIA-MOF consisted of only one crystallographically independent Ca(II) ion having eight coordination sites. Within the framework, each Ca(II) was surrounded by one nitrogen atom (from the triazole-N functionality) and six oxygen atoms (O1, O2, O3, O4, O1A and O4A) from four carboxylate groups of 5TIA ligands and one coordinated water molecule. 5TIA ligand adopted two types of binding modes in Ca-5TIA-MOF. In the first case, 5TIA was hexadentate and all its carboxylate and triazole functionalities were coordinated with metal centers (**Figure 5.3a**). In the second type of binding, 5TIA was found to be tetradentate and only carboxylate groups of 5TIA were coordinated to the metal centers (**Figure 5.3b**). In the crystal structure the Ca–O bond distances ranged from 2.425(3)



**Figure 5.3:** a) Coordination sites of 5TIA along  $c$  axis. b) Coordination sites of 5TIA along  $a$  axis. c) Coordination environment around Ca(II) centre. d) The SBU in the crystal structure of Ca-5TIA-MOF showing the arrangement of 5TIA. e) Packing diagram showing formation of one dimensional pores through  $c$  axis for Ca-5TIA-MOF. f) Topological simplification of Ca-5TIA-MOF through  $c$  axis, by joining only Ca(II) centres (orange) with 5TIA ligand (blue).

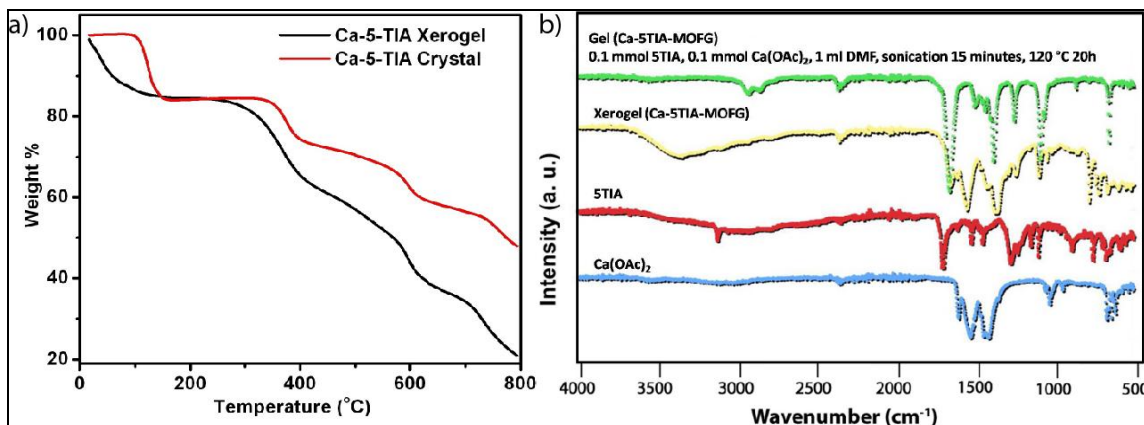
to 2.660(3) Å. The Ca–O<sub>water</sub> and Ca–N<sub>triazole</sub> bond distances were 2.428(3) and 2.544(3) Å respectively. Eight coordination sites of Ca(II) ions were fulfilled by five 5TIA ligands and one water molecule (**Figure 5.3c**). Ca-5TIA-MOF contained 1D channel along the crystallographic *c* axis and the free triazole rings were facing towards the channel (**Figure 5.3e**). Solvent accessible void of Ca-5TIA-MOF was calculated using *PLATON* [2.25] and which suggested a 21.1% void volume relative to the total crystal volume. However, this was increased to 38.5% after removal of the solvent molecules residing inside the pores. The pore diameter of the channel was found to be 33.6 Å (this value was calculated by considering the Van der Waals radii of the constituent atoms).

#### 5.2.4 Thermal properties and FT-IR analysis:

The Ca-5TIA-MOF was prepared at the gram scale to allow detailed investigation of the aforementioned 3D structure and to examine the stability (chemical, thermal and mechanical), gas affinity and catalytic properties. Thermal gravimetric analysis (TGA) performed on as-synthesized Ca-5TIA-MOF revealed that these compounds were thermally stable (**Figure 5.4a**). The TGA curve for Ca-5TIA-MOF showed a sharp weight-loss step of 15% (90–160 °C), corresponding to evaporation of water and organic molecules (DMF) absorbed on the surface and trapped inside the pores. This was followed by a weight-loss of 27 % (330–400 °C) assigned to the collapse of the framework, which was also observed for Ca-5TIA-Xerogel (38 % weight loss). Common weight-losses up to 800 °C were attributed to further decomposition of the organic ligand in both systems. As for other Ca-MOF, the final residual was attributed to calcium oxide. From the TGA traces it was observed that solvent removal at Ca-5TIA-Gel happens over a broader temperature range (gradual weight-loss of 15% between 30–160 °C) because solvent molecules are loosely bound in the gel state. Meanwhile in crystalline Ca-5TIA-MOF, the solvent entrapped inside the pores left the framework over much narrow temperature range.

Fourier transform infrared (FT-IR) spectroscopy of the Ca-5TIA-Gel, Ca-5TIA-Xerogel and Ca-5TIA-MOF appeared to be virtually identical (**Figure 5.4b**). This suggested that the internal structure of the Ca-5TIA-Gel was preserved during the preparation of its Ca-5TIA-Xerogel, and resemblanced with the crystalline Ca-5TIA-

MOF. FT-IR spectra confirmed the presence of carboxylate groups in the coordination sphere of the metal and suggested that at least > 95% of the carboxylic groups of 5TIA are deprotonated in the MOFs materials. In this regard, 5TIA ligand showed the C=O stretching frequency of free aromatic carboxylic acid at *ca.* 1699  $\text{cm}^{-1}$ .



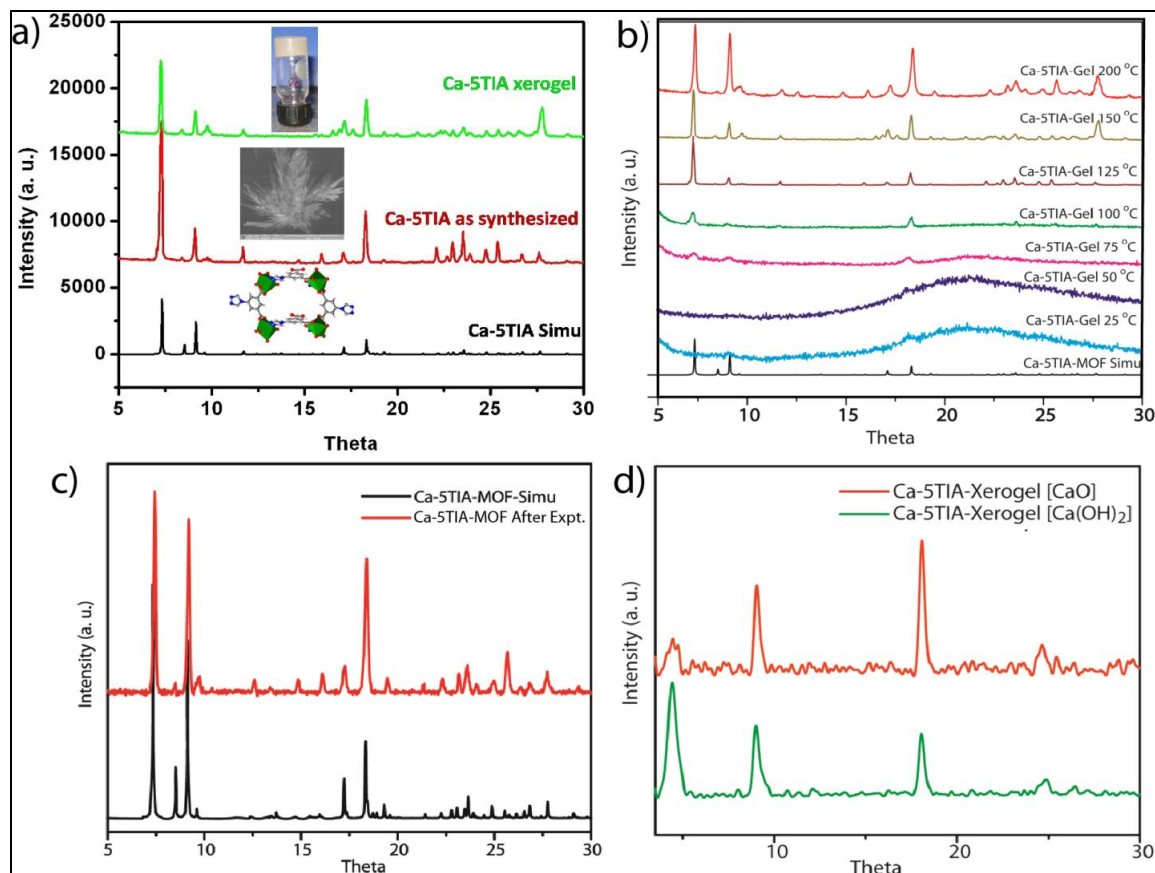
**Figure 5.4:** a) TGA traces of Ca-5TIA-Xerogel (black) and Ca-5TIA-MOF (red). b) FTIR spectra patterns of Ca(OAc)<sub>2</sub> (blue), 5TIA ligand (red) Ca-5TIA-Xerogel (yellow) and Ca-5TIA-Gel (green).

When the carboxylic acid coordinates to the metal atoms, C=O stretching frequency was shifted to lower frequencies (*ca.* 1550  $\text{cm}^{-1}$ ). This phenomenon was clearly observed in Ca-5TIA-Gel, Ca-5TIA-Xerogel and Ca-5TIA-MOF. However the C=O stretching frequency and the coordinated triazole stretching frequency were overlapped in the range of 1540–1550  $\text{cm}^{-1}$ .

### 5.2.5 X-ray powder diffraction analysis:

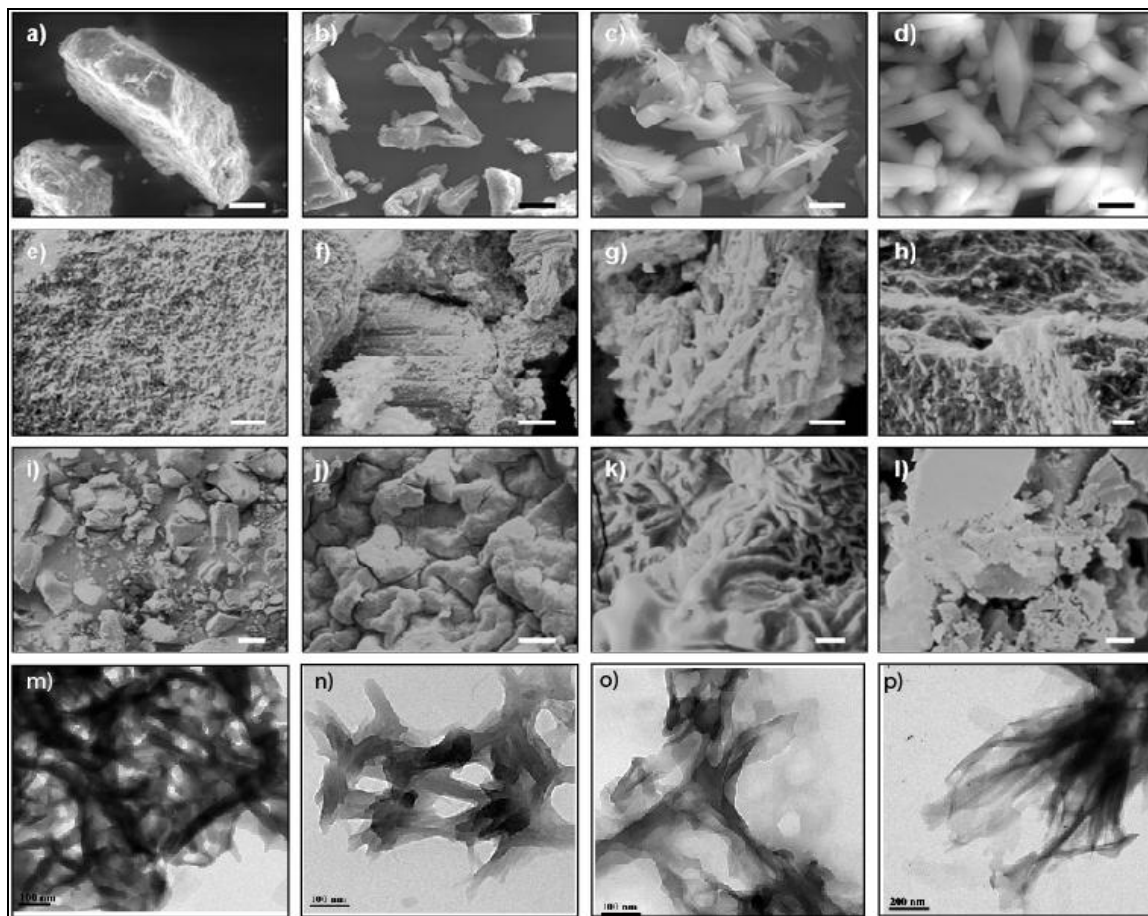
In order to confirm the phase purity of the bulk materials, powder X-ray diffraction (PXRD) experiments were carried out (**Figure 5.5a**). All major peaks of experimental PXRD of Ca-5TIA-Xerogel and Ca-5TIA-MOF matched well with simulated PXRD of Ca-5TIA-MOF, indicating reasonably crystalline phase purity [5.30]. There were some low intensity peaks that were observed in Ca-5TIA-Xerogel which might be due to the unreacted starting materials trapped inside the gel network. Despite these similarities, it seems unlikely that the MOF structure is fully retained in the gel materials. In fact, the absence of additional water during gelation, as well as the influence of the counter anion in the stabilization of the gel materials point out a gelation mechanism in which the gelator agent is not the intact self-assembled 3D porous MOF. In this sense, no gels could

be formed upon sonication of the MOF material in DMF, whereas the in-situ coordination of the metal with the ligand and the solvation of the solvent molecules cannot be reproduced exactly from the xerogel (i.e. up to one week is necessary to obtain a partial gel from the corresponding xerogel material) either because of some structural change (not observable



**Figure 5.5:** a) Comparison of PXRD patterns of the Ca-5TIA-Xerogel (green) and Ca-5TIA-MOF (red) with the simulated pattern from the single-crystal structure (black). b) VT-PXRD patterns of the Ca-5TIA-Gel in the temperature range of 25–200 °C. c) Comparison of PXRD patterns of the Ca-5TIA-MOF after catalysis experiment (red) with the simulated pattern from the single-crystal structure of Ca-5TIA-MOF (black). d) Comparison of PXRD patterns of the Ca-5TIA-Xerogel [CaO] (red) and Ca-5TIA-Xerogel [Ca(OH)<sub>2</sub>] (green).

by PXRD) that occurs during the evaporation of the solvent or because the insoluble nature of the metal-complex system, which prevents the right accommodation of the solvent molecules which is necessary for the gelation phenomena. Moreover, in situ variable temperature PXRD (VT-PXRD) was performed on Ca-5TIA-Gel in order to understand the phase changes that might take place with increasing temperature (**Figure**



**Figure 5.6:** SEM images of Ca-5TIA-Gels prepared in 1 mL DMF under different conditions: a) 0.2 mmol  $\text{Ca}(\text{OAc})_2$  + 0.2 mmol 5TIA sonication at RT for 15 min, then standing at 30 °C → peach coloured gel (scale bar = 50  $\mu\text{m}$ ); b) 0.2 mmol  $\text{Ca}(\text{OAc})_2$  + 0.2 mmol 5TIA sonication at RT for 15 min, then standing at 60 °C inside the oven → peach coloured gel (scale bar = 30  $\mu\text{m}$ ); c) 0.2 mmol  $\text{Ca}(\text{OAc})_2$  + 0.2 mmol 5TIA sonication at RT for 15 min, then standing at 90 °C inside the oven → peach coloured gel (scale bar = 5  $\mu\text{m}$ ); d) 0.2 mmol  $\text{Ca}(\text{OAc})_2$  + 0.2 mmol 5TIA sonication at RT for 15 min, then standing at 120 °C inside the oven → bright yellow coloured gel (scale bar = 10  $\mu\text{m}$ ); e) 0.1 mmol  $\text{Ca}(\text{OAc})_2$  + 0.1 mmol 5TIA, sonication at RT for 15 min, then standing at RT → peach coloured gel (scale bar = 2  $\mu\text{m}$ ); f-g) 0.1 mmol  $\text{Ca}(\text{OAc})_2$  + 0.1 mmol 5TIA, sonication at RT for 15 min, then heating at 120 °C in an oil bath for 2 h (scale bars = 5 and 2  $\mu\text{m}$ , respectively); h) 0.1 mmol  $\text{Ca}(\text{OAc})_2$  + 0.1 mmol 5TIA, sonication at RT for 15 min, then heating at 120 °C in an oil bath for 20 h → yellow coloured gel (scale bar = 2  $\mu\text{m}$ ); i) 0.1 mmol  $\text{Ca}(\text{OAc})_2$  + 0.1 mmol 5TIA, sonication at RT for 15 min, then standing at 4 °C (scale bar = 100  $\mu\text{m}$ ); j-k) 0.1 mmol  $\text{Ca}(\text{OAc})_2$  + 0.075 mmol 5TIA, sonication at RT for 15 min, then heating at 120 °C in an oil bath for 3 h → bright yellow coloured gel (scale bars = 20 and 1  $\mu\text{m}$ , respectively); l) 0.1 mmol  $\text{Ca}(\text{OAc})_2$  + 0.075 mmol 5TIA, sonication at RT for 15 min, then heating at 60 °C in an oil bath for 2.5 h → bright peach coloured gel (scale bar = 5  $\mu\text{m}$ ).

**5.5b**). In situ VT-PXRD patterns of Ca-5TIA-Gel collected at different temperatures (25 °C to 200 °C with a periodic interval of 25 °C) showed that the amorphous gel phase starts converting to a crystalline xerogel phase at around 100 °C. This suggested that Ca-acetate-5TIA induced gelation (amorphous phase) was irreversible, upon removal of solvent it was converted into a crystalline xerogel phase. Small differences in the intensities of the reflections were observed at higher temperatures because of the removal of residual solvent molecules. These results support also the premise that both the Ca-5TIA 3D MOF and the xerogel systems possess, at least, some common structural elements.

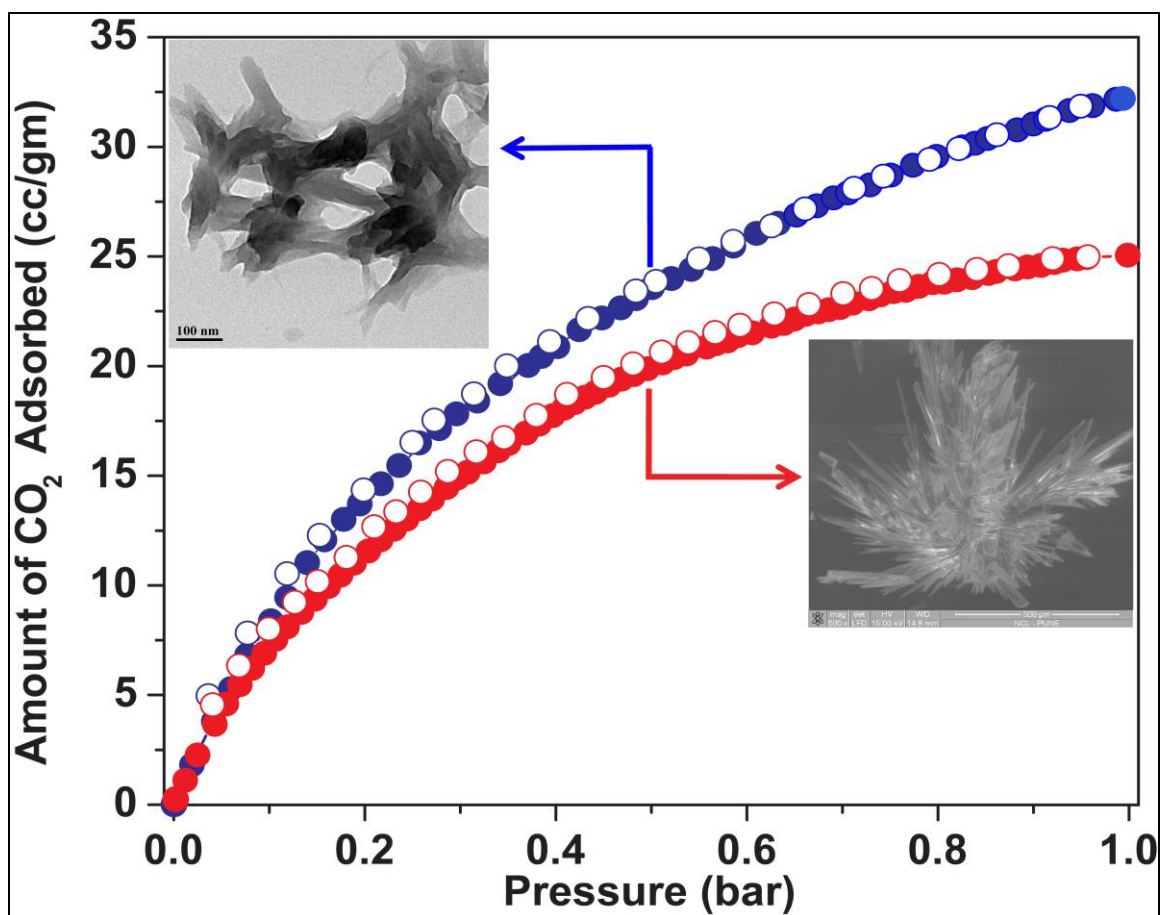
### **5.2.6 Morphological characterization:**

Scanning electron microscopy (SEM) and transmission electron microscope (TEM) images of Ca-5TIA-MOF and Ca-5TIA-Gel were recorded in order to gain insights about the microstructure of the materials. Gel formation usually comprises the formation of 1D aggregates, which further undergo entanglement to form the 3D-network. In the case of Ca-5TIA-Gels, the experimental protocol was used to prepare the organogels which showed a remarkable influence on the morphology of the 3D microfiber like-networks. For example, the use of sonication in order to disperse the gelator system seems to promote the formation of fibrillar networks of much higher homogeneity and high aspect ratio regardless of processing temperature (**Figure 5.6a-d vs. 5.6e-i**). Interestingly, the use of 25% less ligand concentration with respect to Ca(OAc)<sub>2</sub> induced the formation of much denser and highly entangled rope-like structures, specially at high processing temperatures, with fiber diameters ranging between 0.5–10 μm (**Figure 5.6j-l**). In the other hand, extended periods of heating results in the evolution of well-defined fibrillar clusters towards a more compact material without visible bundles (**Figure 5.6f-g vs. h**). The fibrillar evolution of the gel microstructure with increasing temperature was also confirmed when the samples were allowed to stand at 4 °C upon initial sonication, leading to a cobbled paving rather than a developed fibrillar surface (**Figure 5.6i**).

### **5.2.7 Gas adsorption analysis:**

The architectural rigidity and consequently the permanent porosity of evacuated Ca-5TIA-MOF and Ca-5TIA-Gel were unequivocally proven by gas-sorption analysis. Ca-

5TIA-MOF resulted non-porous to nitrogen ( $N_2$ ) because its aperture size ( $3.6 \text{ \AA}$ ) was almost equivalent to the kinetic diameter of  $N_2$  ( $3.6 \text{ \AA}$ ). However, it was responsive towards hydrogen ( $H_2$ ) and carbon dioxide ( $CO_2$ ) uptake. The kinetic diameter of  $N_2$  ( $3.65 \text{ \AA}$ ) is not only higher than pore size of Ca-5TIA-MOF ( $3.6 \text{ \AA}$ ), but also  $N_2$  molecules have low kinetic energy at 77 K. As a result  $N_2$  molecules are unable to enter through the small pores of Ca-5TIA-MOF. However, Ca-5TIA-MOF was able to take up  $CO_2$  ( $3.4 \text{ \AA}$ ) as it has the less kinetic diameter than the MOF aperture size. The  $CO_2$



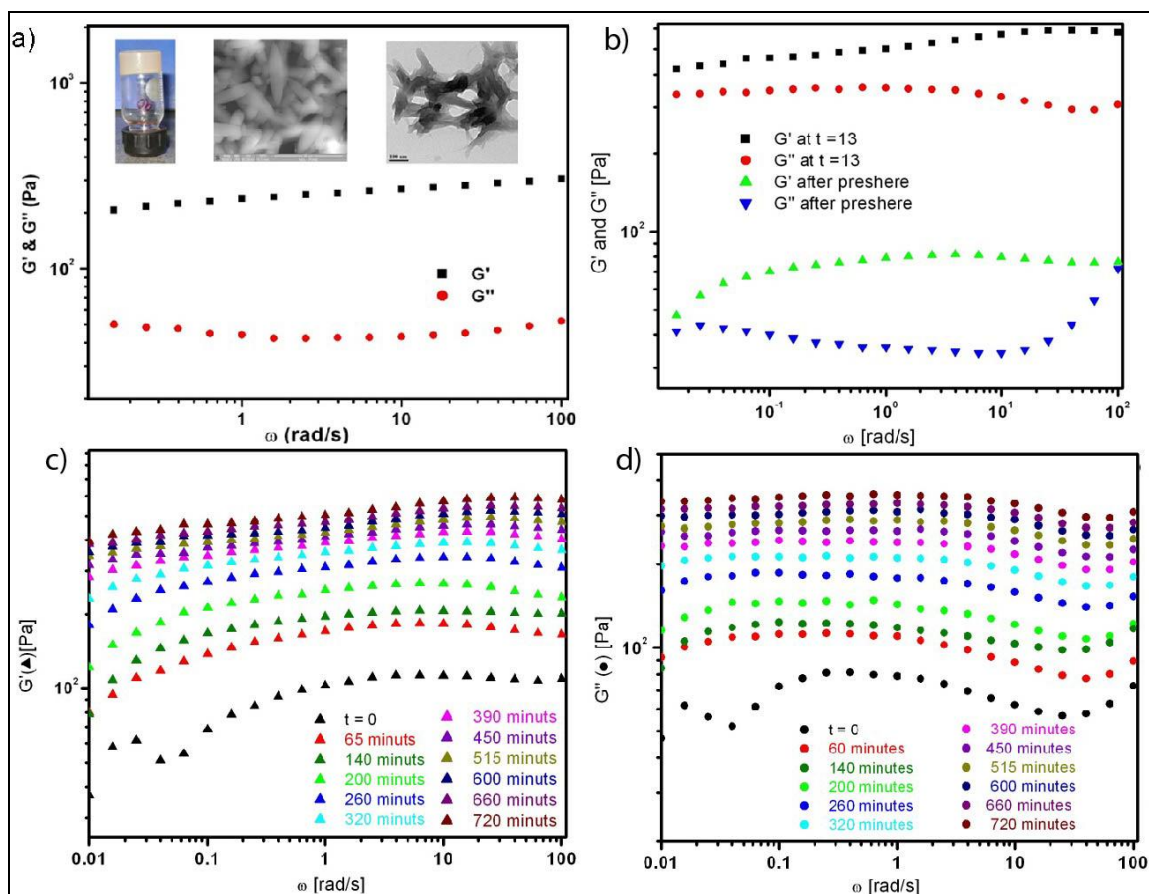
**Figure 5.7:**  $CO_2$  adsorption isotherms below 1.0 bar for Ca-5TIA-Xerogel (blue) and Ca-5TIA-MOF (red) at 298 K. Filled and open circles represent adsorption and desorption data, respectively.

adsorption properties of Ca-5TIA-MOF and Ca-5TIA-Gel are shown in Figure 5.7. Ca-5TIA-MOF and Ca-5TIA-Xerogel both showed reversible type-I  $CO_2$  adsorption isotherms at 298 K. Ca-5TIA-MOF and Ca-5TIA-Xerogel adsorbs 1.12 and 1.45 mmol/g of  $CO_2$  at 298 K and 1 atm pressure. It is noteworthy that Ca-5TIA-Xerogel showed 20% increase in  $CO_2$  adsorption in comparison to crystalline Ca-5TIA-MOF. This result

remained persistent after repeated experiments, although the reason behind such anomalies are still unresolved.

### 5.2.8 Rheological and SAXS measurements:

We used rheology and small angle X-ray scattering to probe *in-situ* both the nature and change in the gel structure during ageing. Our rheological measurements were performed after intense pre-shearing to prepare a well-defined initial state for the sample. We observed that, even immediately after pre-shear (viz. at  $t = 0$ ), the solid modulus,  $G'$ , had



**Figure 5.8:** Rheology studies: a) A plot of the solid modulus ( $G'$ ) and loss modulus ( $G''$ ) as a function of frequency ( $\omega$ ) for Ca-5TIA-Gel; b) A plot of the solid modulus ( $G'$ ) and loss modulus ( $G''$ ) as a function of frequency ( $\omega$ ) at final holding time (720 minutes) and after preshearing with strain ( $\gamma$ ) of 1% and frequency ( $\omega$ ) from 0.1 to 100  $\text{rad}\cdot\text{s}^{-1}$  using Couette geometry for Ca-5TIA-Gel. c) plot of the solid modulus ( $G'$ ) as a function of frequency ( $\omega$ ) with ageing time at RT using Couette geometry for Ca-5TIA-Gel. d) Plot of the loss modulus ( $G''$ ) as a function of frequency ( $\omega$ ) with ageing time at RT using Couette geometry for Ca-5TIA-Gel.

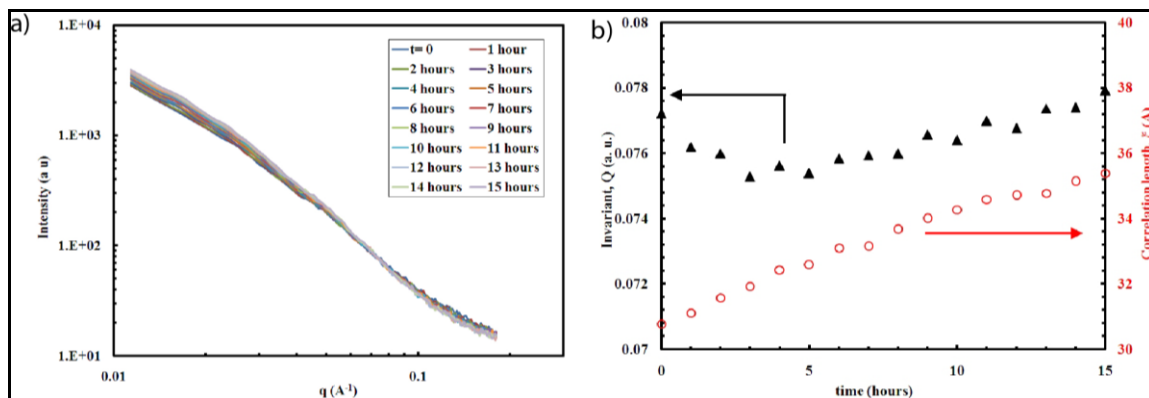
a very weak frequency dependence (**Figure 5.8c**). With ageing time, the solid modulus increased, but still maintained a very weak frequency dependence ( $G' \sim \omega^{0.045}$ ) over the



entire 4-decades of frequency probed. The loss modulus ( $G''$ ) was lower than the solid modulus, and has a minimum at high frequencies ( $\omega$  between 10 and 100 rad s<sup>-1</sup>, **Figure 5.8c**). This indicated that the material had a network like structure, viz. it could be defined as a gel. However, the mechanical response was not dominated by the solid-like behaviour and there was significant dissipation (viz.  $G''$  is not significantly lower than  $G'$ , **Figures 5.8c, 5.8d**). It was possible that the solid-like response was characteristic of the network structure formed by gelation of the particles of the Ca-5TIA, while the dissipation was resulted from the associated solvent phase [5.31]. We can use the relation between the crosslink density and modulus for elastic networks,  $G' = \rho k_B T$ , (where  $\rho$  is the number density of network junctions,  $k_B$  is Boltzmann constant and  $T$  is the temperature), to estimate the spacing between “network junctions” as *ca.* 2–3 nm.

Interestingly, the solid modulus showed a slow, logarithmic thixotropic growth with ageing time, increasing about four-fold over 11 h (**Figure 5.8c**). This indicated the slow kinetics of the ageing process (**Figure 5.8c**). At the end of the experiment, viz. after about 11 h of ageing, the solid modulus of the gel was about 400 to 500 Pa. At the end of the ageing experiment, the gel was again subjected to intense steady shear at 10 rad s<sup>-1</sup>, and a decrease in the gel modulus was observed indicating a break-down of the network structure. The material was transformed to gel again on standing, suggesting that a weak attraction between the Ca-5TIA particles were responsible for the thixotropic behaviour. The thixotropic response of the Ca-5TIA-Gels was qualitatively independent of the processing temperature, which could make them attractive for potential biomedical applications.

In agreement with the gradual increase in the modulus, the gel microstructure was evolved gradually with ageing time as revealed, from small angle X-ray scattering (**Figure 5.9a**). The scattering invariant was used to characterize a two-phase structure in a model-independent manner. As we did not have scattering data over the entire  $q$  range, we approximated the invariant,  $Q$  as  $\int q^2 I(q) dq$  from the experimental  $q_{\min}$  to  $q_{\max}$ . The scattering invariant did not show any significant systematic change with time (**Figure**



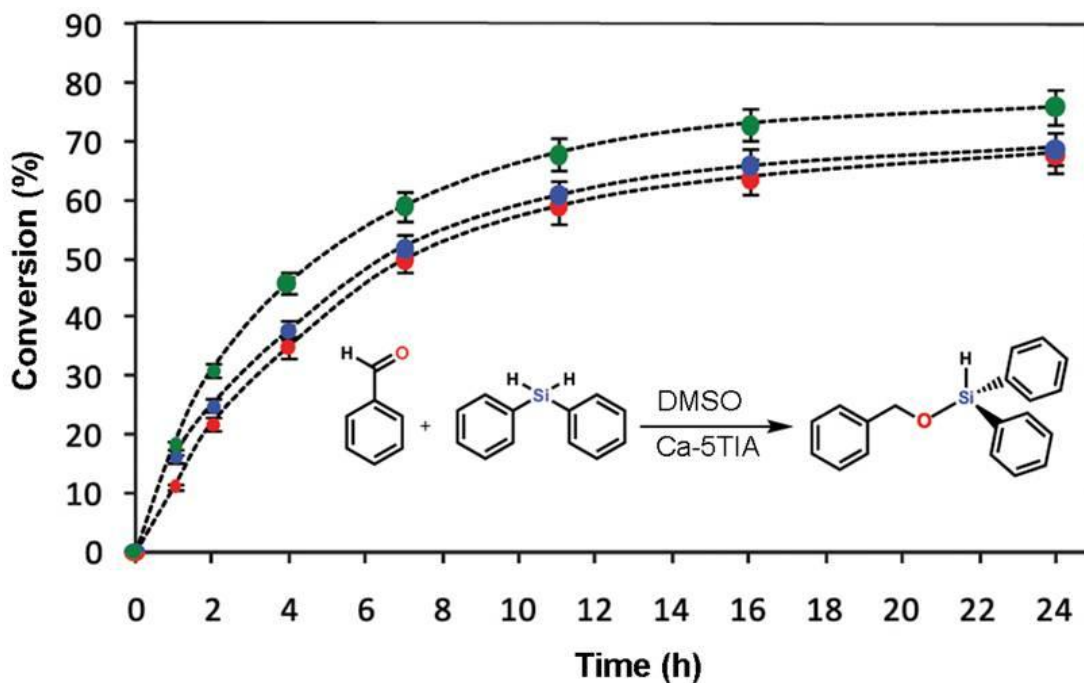
**Figure 5.9:** a) SAXS plot of  $q$  ( $\text{\AA}^{-1}$ ) as a function of scattering intensity (a.u.) with varying time. b) SAXS plot of time (hours) as a function of correlation length (right-red) and Invariant (left-black) plots for Ca-5TIA-Gel at 60 °C.

**5.9b).** Therefore the invariant could be written as,  $Q = 2\pi^2x(1-x)\Delta\rho^2$ , where  $x$  is the fraction of the Ca-TIA particle,  $(1-x)$  is the solvent fraction and  $\Delta\rho$  is the difference in electron density between the Ca-5TIA and the solvent. Thus, this result indicated that there was no significant change with ageing time of  $\Delta\rho$ , viz. the particles did not appear to densify with ageing. Based on the structure observed from TEM (**Figure 5.6m-5.6p**) [5.22], the small angle X-ray scattering data was used to model arising from a random two phase structure. Further this was fitted with Debye-Bueche model, as follows:  $I = I_0/(1 + q^2\xi^2)^2 + I_B$ . [ $\xi$  is a correlation length that characterizes the structure, and  $I_0$  and  $I_B$  are fitting constants where  $I_B$  represents a  $q$ -independent background]. The fitted data was reasonable, except at very low  $q$  and indicated that the correlation length,  $\xi$ , increases gradually from about 31 to 36 Å over an ageing time of 15 h (**Figure 5.9b**). These values of  $\xi$  showed reasonable correlation with the distance between network points estimated from the rheology data, and with the dimensions of the void space between the Ca-5TIA particles from TEM.

### 5.2.9 Catalytic performance:

Finally, the performance of both Ca-5TIA-MOF and Ca-5TIA-Gel as heterogeneous catalysts was also tested for the atom-efficient hydrosilylation of benzaldehyde with diphenylsilanes Lewis-acid catalyzed model reaction was define as:  $[\text{PhCHO} + \text{Ph}_2\text{SiH}_2 \rightarrow \text{PhCH}_2\text{OSiHPh}_2]$ . The reactions were carried out in DMSO based on the above-mentioned stability of the Ca-5TIA-Gel. The key factors responsible for the catalytic

conversion of small molecules using Ca-based MOFs [5.18k,m] are (1) a low restriction in mass transport due to macroporosity of the catalyst, (2) the Lewis acid character of the calcium and (3) the presence of coordinated solvent molecules (*e.g.* DMF) in the structure of the catalyst, which offsets the acidity of the Ca(II) center and favours the exchange of coordinated water molecules by other hard bases like carbonyl oxygens. In agreement with recent observations albeit with somewhat lower efficiency [5.18k,m] Ca-5TIA-MOF (10 mol%) catalyzed the hydrosilylation of benzaldehyde affording the expected silylated product up to 70% within 24 h (**Figure 5.10**). In spite of the modest catalytic activity, the gel phase exhibited moderately higher activity than the corresponding MOF and xerogel samples under comparable conditions ( $\text{TOFs}_{1/2} (\text{h}^{-1}) = 1.09$  (Ca-5TIA-Gel), 0.74 (Ca-5TIA-Xerogel), 0.71 (MOF)). Such enhanced performance for the gel phase in comparison to the solid or crystalline phase was also observed in other metallogels [5.4g, 5.9k].



**Figure 5.10:** Kinetic profile for the hydrosilylation of benzaldehyde catalyzed by Ca-5TIA-MOF (red), Ca-5TIA-Xerogel (blue) and Ca-5TIA-Gel (green) (catalyst loading = 10 mol%).

The absence of catalytic active species in solution, generated by potential leaching from the catalytic systems, was unequivocally confirmed by a series of control experiments in which the reactions conditions (*i.e.* amount of catalyst, solvent,

temperature and time) were simulated in the absence of reactants or in the presence of only one of the two reactants. After heating the padlocked catalyst in DMSO at  $65 \pm 5$  °C for 1 h, the liquid phase was separated and used as reaction medium for the hydrosilylation reaction of benzaldehyde with diphenylsilane under homogeneous conditions. No reaction was observed during the control experiments for both Ca-5TIA-MOF and Ca-5TIA-Gel, which ruled out leaching of active species, at least, above the minimum catalytic concentration. Moreover, no further conversion was observed when the catalysts were removed from the reactor after 1 h. Considering the estimated experimental error (*ca.*  $\pm 5\%$ ) only a minor detriment in the reaction conversion ( $\Delta < 10\%$ ) was observed after the third run of the recycling experiments. The integrity of the catalysts was further confirmed by comparison of the PXRD patterns before and after the reaction.

### 5.3 Conclusions:

In conclusion, 5TIA has been demonstrated a versatile ligand for the construction of new 3D Ca-based MOFs and stable metallogels. To the best of our knowledge Ca-based metallogels and 3D MOF synthesized from the same organic and metal components has been represented for the first time. This is also the first porous Ca-based MOF, which shows adsorption capacity for CO<sub>2</sub> at 1 atm pressure. Remarkably, Ca-5TIA-Xerogel presents, on a molar basis, 20% higher CO<sub>2</sub> uptake than the crystalline Ca-5TIA-MOF. These materials are highly stable and retain crystallinity until 400 °C as confirmed by TGA. Ca-5TIA-Gel also showed an interesting thixotropic behaviour and it is characterized by a dynamic gel microstructure, which evolves with ageing time as demonstrated by rheological and X-ray scattering measurements. Experimental PXRD peaks of both Ca-5TIA-Xerogel and Ca-5TIA-MOF matched reasonably well with simulated PXRD, suggesting the presence of, at least, some common structural elements in the 3D networks of both xerogel and crystalline phases, which was also supported by the similarities in FT-IR spectra. However, the absence of extra water during gelation, the influence of the counteranion in the stabilization of the gels, and the failure to form the gel materials using the crystalline Ca-5TIA-MOF directly as pure gelator agent, point out a somewhat modified internal structure of the gels compared to the MOF materials. In the other hand, the synthesized materials showed also a modest catalytic activity towards the

hydrosilylation of benzaldehyde with diphenylsilane, where improved catalytic performance was found to be observed for the gel phase in comparison to the crystalline or xerogel materials. The versatile ability of 5TIA to develop novel MOF, metallogel materials and including the corresponding MOF aerogels, by coordination with other metal ions could be promoted for designing of a wide variety of MOFs/gels with plethora of applications are envisioned.

## 5.4 Experimental procedures:

### 5.4.1 Materials:

Thionyl chloride, hydrazine hydrate, diethyl ether, benzene, and *N,N*-dimethylformamide (DMF), benzene were purchased from Rankem chemicals. 5-Amino isophthalic acid was purchased from the Aldrich Chemicals. All starting materials were used without further purification. All experimental operations were performed in air.

### 5.4.2 Synthesis of 5-triazole isophthalic acid:

#### 5.4.2.1 Synthesis of *N,N'*-dimethylformamide azine dihydrochloride (DMAz):

28.6 mL, 0.4 mol of Thionyl chloride ( $\text{SOCl}_2$ ) was added with stirring to DMF (150 mL) at 5 °C. After addition keep this mixture at 5 °C for 24h and then added slowly aqueous hydrazine hydrate (5 mL, 0.1 mol) in 20 mL DMF. After addition the mixture was stirred at room temperature for 48h and the white precipitate of *N,N'*-dimethylformamide azine dihydrochloride was collected by filtration and washed with DMF and diethyl ether: 19.1 g; mp 251 °C. **FT-IR:** (KBr 4000-600  $\text{cm}^{-1}$ ): 3473(s), 3223 (w), 2951(w), 2848(w), 2031(m), 1715(s), 1609(m), 1507(s), 1398(w), 1287(s), 1228(m), 1137(s), 1054(s), 1019(m), 877(m), 672(s), 654(m), 530(m), 496(m).

#### 5.4.2.1 Synthesis of 5-Triazole Isophthalic Acid:

Refluxing a mixture of *N,N'*-dimethylformamide azine dihydrochloride (4.0 g, 1.866 mmol) and 5-amino isophthalic acid (3.38 g, 1.866 mmol) in 50 mL benzene (Benzene is *carcinogenic*; reaction should be conducted in a fume hood) for 8h gave whitish solid. The solid was filtered and washed with ethanol ( $2 \times 15$  mL) and Diethyl ether ( $1 \times 17$  mL); yield: 2.38 g (68%). **FT-IR:** (KBr 4000-600  $\text{cm}^{-1}$ ): 3119(m), 2906 (w), 2552(w), 1699(s), 1519(s), 1448(m), 1268(m), 11224(m), 1143(m), 1095(s), 889(m), 755(s), 665(s).

### 5.4.3 Synthesis of Ca-5TIA-MOF and Ca-5TIA-Gel:

**5.4.3.1 [Ca-5TIA-MOF]  $\text{Ca}_2(\text{5TIA})_2(\text{H}_2\text{O})_2\text{-DMF}$ :** 0.2 mmol (0.0446 g) of 5TIA and 0.2 mmol (0.0316 g) of  $\text{Ca}(\text{OAc})_2$  was mixed in 3 mL of (1:1) DMF:H<sub>2</sub>O solution mixture in a 5 mL vial. The mixture solution was stirred for 30 minutes and was capped and heated to 85 °C for 48 h. Colorless plate like crystals were obtained, which were filtered off and washed with EtOH. Afterwards resulting MOF was dried in air (10 min). [Yield: 72 %, 0.0227 g depending on  $\text{Ca}(\text{OAc})_2$ ]. **FT-IR: (KBr 4000-600  $\text{cm}^{-1}$ ):** 3216 (m, br), 1669.83 (m), 1616.42 (m), 1549.79 (s), 1450.09 (m), 1380.82 (s), 1296.55 (w), 1244.21 (m), 1169.51 (w), 1084.79 (m), 1042.68 (w), 899.52 (w), 773.42 (m), 739.67 (m), 682.77 (m)  $\text{cm}^{-1}$ . **Elemental analysis:** Calc. (%) for activated sample ( $\text{C}_{10}\text{H}_4\text{N}_3\text{O}_5\text{Ca}$ ): C, 40.24; H, 1.96; N, 21.82; found: C, 39.20; H, 1.99; N, 22.24.

**5.4.3.2 [Ca-5TIA-Gel]:** 0.2 mmol (0.0316 g) of  $\text{Ca}(\text{OAc})_2$  and 0.2 mmol (0.0446 g) of 5-triazole isophthalic acid (5TIA) were added in a 5 mL vial. Then 2 mL of DMF was added to the mixture and sonicate the mixture solution (~15 min) till it become a homogeneous milk colored solution. Then the solution was kept in different temperature 30 °C, 60 °C, 90 °C and 120 °C for 2 days. In all cases white color gels are formed. **FT-IR: (KBr 4000-600  $\text{cm}^{-1}$ ):** 3348.58 (m, br), 1616.84 (m), 1550.28 (s), 1436.48 (m), 1386.03 (s), 1296.60 (w), 1248.48 (m), 1167.79 (w), 1095.51 (m), 1050.93 (w), 899.65 (w), 773.42 (m), 731.39 (m), 669.01(w)  $\text{cm}^{-1}$ .

### 5.4.4 General methods for characterization:

The Fourier transform (FT) IR spectra (KBr pellet) were taken on a *PERKIN ELMER FT-IR SPECTRUM* (Nicolet) spectrometer. Powder X-ray diffraction (PXRD) patterns were recorded on a Phillips PANalytical diffractometer for Cu K $\alpha$  radiation ( $\lambda = 1.5406 \text{ \AA}$ ), with a scan speed of  $2^\circ \text{ min}^{-1}$  and a step size of  $0.02^\circ$  in  $2\theta$ . Thermo-gravimetric experiments (TGA) were carried out in the temperature range of 25-800 °C on a SDT Q600 TG-DTA analyzer under N<sub>2</sub> atmosphere at a heating rate of  $10^\circ \text{ C min}^{-1}$ .

**Powder X-Ray diffraction (PXRD).** The PXRD patterns were collected on a Phillips PANalytical diffractometer on a Cu K $\alpha$  radiation ( $\lambda = 1.5406 \text{ \AA}$ ), with a scan speed of  $2^\circ \text{ min}^{-1}$ . The tube voltage and amperage were set at 40 kV and 50 mA respectively. Each sample was scanned between 5 and  $50^\circ 2\theta$  with a step size of  $0.02^\circ$ . The instrument was previously calibrated using a silicon standard.

**Thermogravimetric analysis (TGA).** TGA was performed on a SDT Q600 TG-DTA analyzer instrument. Approximately 5 mg of the sample was added to a platinum crucible and heated from 25 to 800 °C under N<sub>2</sub> atmosphere at a heating rate of 10 °C min<sup>-1</sup>.

**IR spectroscopy.** The Fourier transform (FT) infrared spectra of the MOFs were taken on a *PERKIN ELMER FT-IR SPECTRUM* (Nicolet) spectrometer. KBr samples (2 mg in 20 mg of KBr) were prepared and 10 scans were collected at 4 cm<sup>-1</sup> resolution for each sample. The spectra were measured over the range of 4000-400 cm<sup>-1</sup>.

**Gas adsorption.** All low-pressure CO<sub>2</sub> adsorption experiments (up to 1 bar) were performed on a Quantchome instrument. Approximately 50 mg of the sample was activated after solvent exchange by the use of activation chamber. The activated sample was loaded inside the glass bulb of water adsorption instrument and measured the capacity.

#### 5.4.5 X-ray crystallography:

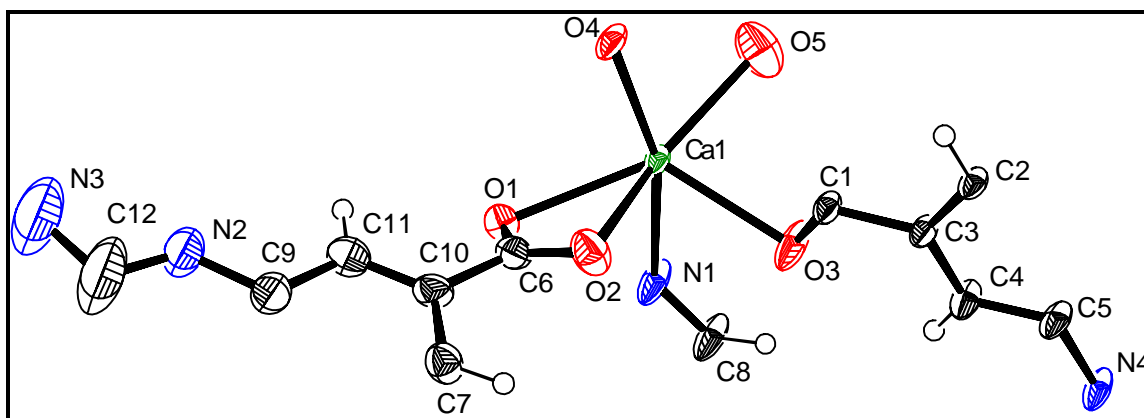
##### 5.4.5.1 General data collection and refinement procedures:

Single crystal data was collected on a Bruker *SMART APEX* three circle diffractometer equipped with a *CCD* area detector [2.29] and operated at 1500 W power (50 kV, 30 mA) to generate Mo K $\alpha$  radiation ( $\lambda = 0.71073 \text{ \AA}$ ). The incident X-ray beam was focused and monochromated using Bruker Excalibur Gobel mirror optics. A single crystal of the MOF was mounted on nylon CryoLoop (Hampton Research) with Paraton-N (Hampton Research). Data were integrated using Bruker *SAINTE* software [2.21] and subsequently corrected for absorption using the program *SADABS* [2.22]. Space group determinations and tests for merohedral twinning were carried out using *XPREP* [2.24]. In this case, the highest possible space group was chosen. The structure was solved by direct method and refined using the *SHELXTL 97* software suite [2.23]. Atoms were located from iterative examination of difference F-maps following least squares refinements of the earlier models. Hydrogen atoms were placed in calculated positions and included as riding atoms with isotropic displacement parameters 1.2–1.5 times  $U_{eq}$  of the attached C atoms. Data were collected at 298(2) K. The structure was examined using the *ADDSYM* subroutine of *PLATON* [2.25] to assure that no additional symmetry could be applied to

the models. Unless noted otherwise, all ellipsoids in *ORTEP* diagrams are displayed at the 50% probability level (see Supporting Information for crystallographic data table). CCDC 846548.

#### 5.4.5.2 Experimental and refinement details for Ca-5-TIA MOF (orthorhombic):

A colorless plate crystal ( $0.29 \times 0.21 \times 0.12 \text{ mm}^3$ ) of Ca-5-TIA MOF was mounted on 0.7 mm diameter nylon CryoLoops (Hampton Research) with Paraton-N (Hampton Research). The loop was mounted on a *SMART APEX* three circle diffractometer equipped with a CCD area detector (Bruker Systems Inc., 1999a)<sup>19</sup> and operated at 1500 W power (50 kV, 30 mA) to generate Mo  $K_{\alpha}$  radiation ( $\lambda = 0.71073 \text{ \AA}$ ). The incident X-ray beam was focused and monochromated using Bruker Excalibur Gobel mirror optics. A total of 31141 reflections were collected of which 3022 were unique and 2456 of these were greater than  $2\sigma(I)$ . The range of  $\theta$  was from 1.69 to 24.99°. Analysis of the data showed negligible decay during collection. The structure was solved in the orthorhombic *Cmca* space group, with  $Z = 16$ , using direct methods. All carbon, oxygen and nitrogen atoms were refined isotropically with hydrogen atoms generated as spheres riding the coordinates of their parent atoms. All Ca atoms were refined anisotropically. Modelling of electron density within the voids of the frameworks did not lead to identification of coordinated solvent molecules in all structures due to the lowered resolution of the data. The attempts made to model the coordinated solvent molecules did not lead to identification it in all structures due to the limited periodicity of the solvent molecules in the crystals. Since the solvent is bonded to the framework, this can be expected for the



**Figure 5.11.** *ORTEP* drawing of the asymmetric unit of Ca-5TIA-MOF.



MOF structures. Many atomic coordinates that have been attributed to solvent molecules lie on a special position. However, very high displacement parameters, high esd's and partial occupancy due to the disorder make it impossible to determine accurate positions for these solvent molecules. Thus, electron density within void spaces which could not be assigned to any definite guest entity was modeled as isolated carbon and oxygen atoms, and the foremost errors in all the models lies with assignment of guest electron density. To prove the correctness of the atomic positions in the framework the application of the SQUEEZE routine of A. Spek has been performed. Final full matrix least-squares refinement on  $F^2$  converged to  $R_1 = 0.0567$  ( $F > 2\sigma F$ ) and  $wR_2 = 0.1671$  (all data) with GOF = 1.083. Another possible structure solution was possible in *Cmca* space group for Ca-5TIA-MOF. It should be noted that other supporting characterization data are consistent with the crystal structure.

**Table 5.4:** Crystal data and structure refinement for Ca-5TIA-MOF.

<b>Empirical formula</b>	C <sub>10</sub> H <sub>4</sub> CaN <sub>3</sub> O <sub>5</sub>
<b>Formula weight</b>	286.24
<b>Temperature</b>	293(2) K
<b>Wavelength</b>	0.71073 Å
<b>Crystal system</b>	Orthorhombic
<b>Space group</b>	<i>C m c a</i>
<b>Unit cell dimensions</b>	$a = 19.346(2)\text{Å}$ $\alpha = 90^\circ$ $b = 24.081(3)\text{Å}$ $\beta = 90^\circ$ $c = 14.2543(15)\text{Å}$ $\gamma = 90^\circ$
<b>Volume</b>	6640.7(12)
<b>Z</b>	16
<b>Density (calculated)</b>	1.145
<b>Absorption coefficient</b>	0.392
<b>F(000)</b>	2320
<b>Crystal size</b>	0.29 × 0.21 × 0.12 mm <sup>3</sup>
<b>Theta range for data collection</b>	2.21– 27.52
<b>Index ranges</b>	-22 ≤ h ≤ 22, -28 ≤ k ≤ 28, -16 ≤ l ≤ 16
<b>Reflections collected</b>	31147
<b>Independent reflections</b>	7330
<b>Completeness to theta = 26.02°</b>	100 %
<b>Absorption correction</b>	Semi-empirical from equivalents
<b>Refinement method</b>	Full-matrix least-squares on F <sup>2</sup>
<b>Data / restraints / parameters</b>	3022 / 0 / 178
<b>Goodness-of-fit on F<sup>2</sup></b>	1.083
<b>Final R indices [I &gt; 2σ(I)]</b>	R <sub>1</sub> = 0.0567, wR <sub>2</sub> = 0.1671
<b>R indices (all data)</b>	R <sub>1</sub> = 0.0642, wR <sub>2</sub> = 0.1728
<b>Largest diff. peak and hole</b>	0.093 and -0.407 e.Å <sup>-3</sup>

**NOTE:**

The work presented in the chapter-5 was a collaborative work between the group of Dr. Rahul Banerjee from the Physical/Materials Chemistry Division at CSIR-National Chemical Laboratory in Pune, India and the group of Prof. Dr. David Díaz Díaz with his student Eva-Maria Schön from the Institut für Organische Chemie at Universität Regensburg, Germany. The experimental results depicted in this chapter have already been published in *J. Mater. Chem.* **2012, 22, 14951-14963**, with the title: “*Fine-tuning the balance between crystallization and gelation and enhancement of CO<sub>2</sub> uptake on functionalized calcium based MOFs and metallogels*”. The original idea and discovery was from Dr. Banerjee’s group and the major work has been contributed by Arijit Mallick. He was involved in synthesis of MOF and gel, characterisation of the materials by single crystal-XRD, PXRD, IR, TGA, UV, elemental analysis, photoluminescence measurement, rheology, SAXS, TEM imaging, gas adsorption studies. Eva-Maria Schön was involved in the gelation ability, stability study, SEM imaging, catalysis and digital imaging of the gel materials. Since this work was a collaboration work, the data were incorporated in both Arijit and Eva’s thesis.

---

**CHAPTER 6**

---

---

**Conclusions of all the chapters and future directive**

---

**6.1 Conclusion:**

In the first chapter of the thesis includes introduction of metal organic frameworks (MOFs), lightweight metal organic frameworks (LWMOFs) and their important applications. All the MOFs reported in this thesis are synthesized from lightweight metals Ca(II) and Mg(II) with different organic linkers. The advantages of using lightweight metals for MOF synthesis has been discussed briefly. The possible application of MOFs has also been highlighted with proper literature reports.

In chapter 2, we discussed the gas adsorption properties of Mg(II) based MOFs. Two Porous MOFs have been synthesized and H<sub>2</sub> and CO<sub>2</sub> adsorption studies were performed with these materials. The  $\gamma$ -Mg-formate has one-dimensional channels along the *a*-axis, and shows reversible hydrogen (~1.0 wt% at 77 K, 760 torr) and CO<sub>2</sub> uptake (2.1 mmol g<sup>-1</sup> at 298 K, 760 torr). The Mg-MOF-1 has one dimensional, hexagonal channel along *c* axis and it showed reversible hydrogen (~0.8 wt% at 77 K, 760 torr) and CO<sub>2</sub> uptake (14 cc g<sup>-1</sup> at 298 K, 760 torr). Also Grand Canonical Monte Carlo (GCMC) simulation has been performed to predict the initial positions of the hydrogen molecules in the framework. The positions of the each hydrogen molecules in the framework and their related adsorption energies were optimized using Density Functional Theory (DFT) and ab-initio Hartree-Fock (HF) method.

The chapter 3 includes the electrochemical behaviour of Ca-BTC (1,3,5-benzenetricarboxylic acid) based MOFs. Proton conductivity of five Ca-based MOFs has been demonstrated, which depends on the amount of water molecules coordinated to the Ca-centers. Ca-BTC-H<sub>2</sub>O, which has the highest amount of water content per Ca unit (1.00/Ca unit), shows high conductivity  $1.2 \times 10^{-4} \text{ Scm}^{-1}$  and exhibit low activation energy of 0.18 eV. Ca-BTC-DMF and Ca-BTC-DMA have water content per Ca unit as 0.66 and 0.50 respectively, and show lower proton conductivity ( $4.8 \times 10^{-5} \text{ Scm}^{-1}$  and  $2.0$

$\times 10^{-5} \text{ Scm}^{-1}$ ) as well as higher activation energy (0.32 and 0.40 eV). So we can conclude that MOFs having high amount of water content per asymmetric unit, should have high proton conduction values.

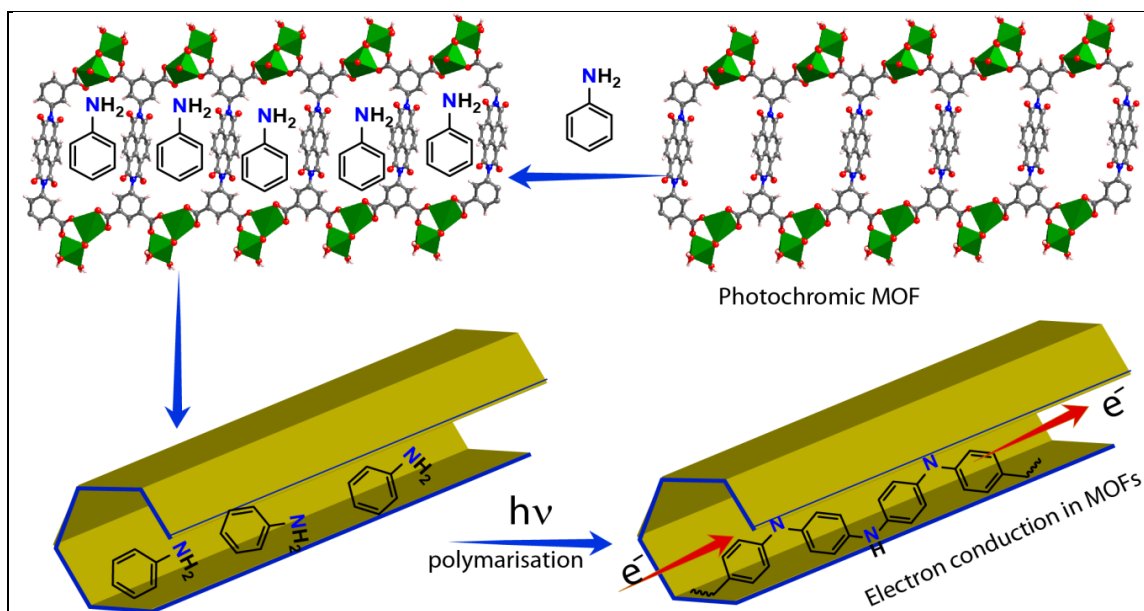
In chapter 4, a new Mg(II) based photochromic porous metal–organic framework (MOF) has been synthesized bearing naphthalenediimide (NDI) chromophoric unit. This MOF (Mg–NDI) shows instant and reversible solvatochromic behavior in presence of solvents with different polarity. Mg–NDI also exhibits fast and reversible photochromism via radical formation. Due to the presence of electron deficient NDI moiety, this MOF exhibits selective organic amine (electron rich) sensing in solid state. The organic amine detection has been confirmed by photoluminescence quenching experiment and visual color change.

In chapter 5, Ca-based metallogels and 3D MOF synthesized from the same organic and metal components has been represented. This porous Ca-based MOF shows adsorption capacity for CO<sub>2</sub> at 1 atm pressure, where as the Ca-5TIA-Xerogel presents 20% higher (on a molar basis) CO<sub>2</sub> uptake than the crystalline Ca-5TIA-MOF. Ca-5TIA-Gel also showed an interesting thixotropic. Both Ca-5TIA-Xerogel and Ca-5TIA-MOF matched reasonably well with simulated PXRD, suggesting the presence of, at least, some common structural elements in the 3D networks of both xerogel and crystalline phases. However, the absence of extra water during gelation, the influence of the counteranion in the stabilization of the gels, and the failure to form the gel materials using the crystalline Ca-5TI. In the other hand, the synthesized materials showed also a modest catalytic activity towards the hydrosilylation of benzaldehyde with diphenylsilane, where improved catalytic performance was found to observed for the gel phase in comparison to the crystalline or xerogel materials.

## 6.2 Future directive:

### Design and synthesis of photochromic porous MOFs for electron conduction application.

The aim of this future plan is to synthesize electrically conducting MOFs from a photochromic MOFs. In our previous work, presented in chapter 4, a photochromic MOF has been synthesized for sensing application. Photochromic MOFs contain redox active chromophoric linkers, which in presence of particular wavelength light generates radicals. The idea behind this proposed work is to use these radicals for initiating radical polymerisation reaction [6.1]. Since MOFs are porous enough to accommodate small molecules [6.2], it is possible to absorb aniline in MOF pores. This aniline loaded MOFs have to place under light for the synthesis of polyaniline in MOF pores. The polymerisation will be initiated by photo generated radicals from photochromic MOFs.



**Figure 6.1:** Scheme for synthesis of electron conducting MOFs using a photochromic MOF.

The next step is to check the electron conduction properties of this polyaniline loaded MOFs. Polyaniline have extended  $\pi$  conjugated system and it has been used as an important electron conducting polymer in some electronic devices [6.3]. So these polyaniline channels inside the MOF pore will provide electron conduction pathway (Figure 6.1) and the nonconducting MOF will be converted to conducting MOF.

---

**REFERENCES****CHAPTER 1**

- [1.1] (a) M. E. Davis, *Nature* 2002, **417**, 813. (b) Y. Ma, W. Tong, H. Zhou, S. L. Suib, *Micropor Mesopor Mat* 2000, **37**, 243.
- [1.2] (a) A. Corma, *Chem. Rev.* 1997, **97**, 2373. (b) F. Schüth and W. Schmidt, *Adv. Mater.* 2002, **9**, 629.
- [1.3] (a) M. Eddaoudi, D. B. Moler, H. Li, B. Chen, T. M. Reinecke, M. O’Keeffe, O. M. Yaghi, *Acc. Chem. Res.* 2001, **34**, 319. (b) C. Janiak, *Angew. Chem., Int. Ed. Engl.*, 1997, **36**, 1431. (c) A. J. Blake, N. R. Champness, P. Hubberstey, W.-S. Li, M. A. Withersby, M. Schroder, *Coord. Chem. Rev.*, 1999, **183**, 117. (d) B. Kesanli, Y. Cui, M. Smith, E. Bittner, B. Bockrath, W. Lin, *Angew. Chem., Int. Ed.*, 2005, **44**, 72. (e) S. Kitagawa, R. Kitaura, S. -I. Noro, *Angew. Chem., Int. Ed.*, 2004, **43**, 2334. (f) G. Férey, *Chem. Soc. Rev.* 2008, **37**, 191. (g) B. Chen, S. Xiang, G. Qian, *Acc. Chem. Res.*, 2010, **43**, 1115. (h) L. Ma, C. Abney, W. Lin, *Chem. Soc. Rev.*, 2009, **38**, 124. (i) Z. G. Gu, Y. P. Cai, H. C. Fang, Z. Y. Zhou, P. K. Thallapally, J. A. Tian, J. Liu, G. J. Exarhos, *Chem. Commun.*, 2010, **46**, 5373. (j) B. Chen, M. Eddaoudi, S. T. Hyde, M. O’Keeffe, O. M. Yaghi, *Science*, 2001, **291**, 1021. (k) P. Pachfule, Y. Chen, J. Jiang, R. Banerjee *J. Mater. Chem.*, 2011, **21**, 17737. (l) J. W. Yoon, S. H. Jhung, Y. K. Hwang, S. M. Humphrey, P. T. Wood, J. -S. Chang, *Adv. Mater.* 2007, **19**, 1830. (m) K. L. Mulfort, O. K. Farha, C. D. Malliakas, M. G. Kanatzidis and J. T. Hupp, *Chem. Eur. J.*, 2010, **16**, 276. (n) H. -S. Choi, M. P. Suh, *Angew. Chem.* 2009, **121**, 6997. (o) X. Gu, Z.-H. Lu, Q. Xu, *Chem. Commun* 2010, **46**, 7400. (p) S. -T. Zheng, J. T. Bu, Y. Li, T. Wu, F. Zuo, P. Feng, X. Bu. *J. Am. Chem. Soc.* 2010, **132**, 17062. (q) J. An, N. L. Roci, *J. Am. Chem. Soc.* 2010, **132**, 5578. (r) A. G. Wong-Foy, O. Lebel, A. J. Matzger, *J. Am. Chem. Soc.* 2007, **129**, 15740. (s) H. Chun, D. N. Dybtsev, H. Kim, K. Kim, *Chem. Eur. J.* 2005, **11**, 3521. (t) J. Rowsell, A. Millward, K. Park, O. Yaghi *J. Am. Chem. Soc.* 2004, **126**, 5666.
- [1.4] (a) H. Furukawa, K. E. Cordova, M. O’Keeffe, O. M. Yaghi, *Science*, 2013, **341**, 6149; (b) R. J. Kuppler, D. J. Timmons, Q. -R. Fanga, J. -R. Lia, T. A. Makala,

- M. D. Younga, D. Yuana, D. Zhaoa, W. Zhuanga, H. -C. Zhou. *Coord. Chem. Rev.*, 2009, **253**, 3042; (c) A. Morozan, F. Jaouen, *Energy Environ. Sci.*, 2012, **5**, 9269. (d) A. U. Czaja, N. Trukhan, U. Müller, *Chem. Soc. Rev.*, 2009, **38**, 1284. (e) U. Mueller, M. Schubert, F. Teich, H. Puetter, K. Schierle-Arndt and J. Pastré *J. Mater. Chem.*, 2006, **16**, 626.
- [1.5] (a) N. Stock, S. Biswas *Chem. Rev.* 2012, **112**, 933. (b) C. Dey, T. Kundu, B. P. Biswal, A. Mallick and R. Banerjee, *Acta Cryst.*, 2014, **B70**, 3.
- [1.6] (a) N. Stock, S. Biswas, *Chem. Rev.*, 2012, **112**, 933. (b) J.-S. Chang, Y. K. Hwang, S. H. Jung, Patent **WO2008/066293 A1**. (c) Q. M. Wang, D. Shen, M. Bülow, M. L. Lau, S. Deng, F. R. Fitch, N. O. Lemcoff, J. Semancin, *Microporous Mesoporous Mater.* 2002, **55**, 217. (d) M. Díaz-García, Á. Mayoral, I. Díaz, M. Sánchez-Sánchez, *Crystal Growth & Design*, 2014, **14**, 2479. (e) T. Ahnfeldt, J. Moellmer, V. Guillerme, R. Staudt, C. Serre, N. Stock, *Chem.—Eur. J.*, 2011, **23**, 6462. (f) T. Friscic, D. G. Reid, I. Halasz, R. S. Stein, R. E. Dinnebier, M. J. Duer, *Angew. Chem., Int. Ed.* 2010, **49**, 712. (g) U. Mueller, H. Puetter, M. Hesse, H. Wesssi, **WO 2005/049892**.
- [1.7] (a) M. Schröder, *Functional Metal-Organic Frameworks: Gas Storage, Separation and Catalysis*; (2010), Springer Berlin Heidelberg. (b) L. R. McGillivray, *Metal-Organic Frameworks: Design and Application*; (2010), Wiley-Blackwell.
- [1.8] (a) L. J. Murray, M. Dincă, J. R. Long, *Chem. Soc. Rev.*, 2009, **38**, 1294 (b) Y. Tao, H. Kanoh, L. Abrams, K. Kaneko, *Chem. Rev.* 2006, **106**, 896.
- [1.9] (a) M. P. Suh, H. J. Park, T. K. Prasad, D. -W. Lim, *Chem. Rev.*, 2012, **1128**, 782. (b) D. J. Collinsa, H. -C. Zhou, *J. Mater. Chem.*, 2007, **17**, 3154.
- [1.10] M. P. Suh, H. J. Park, T. K. Prasad, D.-W. Lim, *Chem. Rev.*, 2012, **112**, 782.
- [1.11] (a) N.L. Rosi, J. Eckert, M. Eddaoudi, D.T. Vodak, J. Kim, M. O’Keeffe, O.M. Yaghi, *Science* 2003, **300**, 1127. (b) Y. Yan, X. Lin, S. Yang, A. J. Blake, A. Dailly, N. R. Champness, P. Hubberstey and M. Schröder *Chem. Commun.*, 2009, 1025. (c) O. K. Farha, A. O. Yazaydin, I. Eryazici, C. D. Malliakas, B. G. Hauser, M. G. Kanatzidis, S. T. Nguyen, R. Q. Snurr, J. T. Hupp, *Nat. Chem.* 2010, **2**, 944. (d) H. Furukawa, N. Ko, Y. B. Go, N. Aratani, S. B. Choi, E. Choi, A. O.



- Yazaydin, R. Q. Snurr, M. O’Keeffe, J. Kim, O. M. Yaghi, *Science* 2010, **329**, 424.
- [1.12] B. Kesanli, Y. Cui, M. R. Smith, E. W. Bittner, B. C. Bockrath, W. Lin, *Angew. Chem., Int. Ed.*, 2005, **44**, 72.
- [1.13] H. Chun, D. N. Dybtsev, H. Kim, K. Kim, *Chem. Eur. J.* 2005, **11**, 3521.
- [1.14] (a) K. W. Chapman, P. J. Chupas, E. R. Maxey, J. W. Richardson, *Chem. Commun.*, 2006, 4013. (b) H. Frost, T. Duren, R. Q. Snurr, *J. Phys. Chem. B*, 2006, **110**, 9565. (c) P. Ryan, L. J. Broadbelt, R. Q. Snurr, *Chem. Commun.*, 2008, 4132.
- [1.15] (a) A. Corma, H. Garcia, *Chem. Soc. Rev.*, 2008, **37**, 2096. (b) J. C. Fierro-Gonzalez, B. C. Gates, *Chem. Soc. Rev.*, 2008, **37**, 2127.
- [1.16] (a) H. S. Cheng, L. Chen, A. C. Cooper, X. W. Sha, G. P. Pez, *Energy Environ. Sci.*, 2008, **1**, 338. (b) L. F. Wang, R. T. Yang, *Energy Environ. Sci.*, 2008, **1**, 268. (c) M. Suri, M. Dornfeld, E. Ganz, *J. Chem. Phys.*, 2009, **131**, 174703. (d) B. D. Adams, C. K. Ostrom, S. Chen, A. Chen, *J. Phys. Chem. C*, 2010, **114**, 19875.
- [1.17] (a) O. K. Farha, A. O. Yazaydin, I. Eryazici, C. D. Malliakas, B. G. Hauser, M. G. Kanatzidis, S. T. Nguyen, R. Q. Snurr, J. T. Hupp, *Nat. Chem.* 2010, **2**, 944. (b) Y. Yan, X. Lin, S. Yang, A. J. Blake, A. Dailly, N. R. Champness, P. Hubbersteya, M. Schroder, *Chem. Commun.*, 2009, 1025. (c) D. Yuan, D. Zhao, D. Sun, Hong-Cai Zhou, *Angew. Chem. Int. Ed.* 2010, **49**, 5357. (d) M. Dinca, A. Dailly, Y. Liu, C. M. Brown, D. A. Neumann, J. R. Long, *J. Am. Chem. Soc.* 2006, **128**, 16876. (e) X. Lin, J. Jia, X. Zhao, K. M. Thomas, A. J. Blake, G. S. Walker, N. R. Champness, P. Hubberstey, M. Schroder, *Angew. Chem.* 2006, **118**, 7518. (f) O. K. Farha, K. L. Mulfort, J. T. Hupp, *Inorg. Chem.*, 2008, **47**, 10223. (g) O. K. Farha, A. M. Spokoyny, K. L. Mulfort, M. F. Hawthorne, C. A. Mirkin, J. T. Hupp, *J. Am. Chem. Soc.*, 2007, **129**, 12680. (h) D. F. Sava, V.C. Kravtsov, J. Eckert, J. F. Eubank, F. Nouar, M. Eddaoudi, *J. Am. Chem. Soc.*, 2009, **131**, 10394. (i) A. G. Wong-Foy, O. Lebel, A. J. Matzger *J. Am. Chem. Soc.* 2007, **129**, 15740. (j) S. R. Caskey, A. G. Wong-Foy, A. J. Matzger, *J. Am. Chem. Soc.* 2008, **130**, 10870. (k) H. Chun, D. N. Dybtsev, H. Kim, K. Kim, *Chem. Eur. J.* 2005, **11**, 3521.

- [1.18] (a) X. B. Zhao, B. Xiao, A. J. Fletcher, K. M. Thomas, D. Bradshaw, M. J. Rosseinsky, *Science* 2004, **306**, 1012. (b) D. Sun, S. Ma, Y. Ke, D. J. Collins, H. C. Zhou, *J. Am. Chem. Soc.* 2006, **128**, 3896. (c) Y. Yan, I. Telepeni, S. Yang, X. Lin, W. Kockelmann, A. Dailly, A. J. Blake, W. Lewis, G. S. Walker, D. R. Allan, S. A. Barnett, N. R. Champness, M. Schroder, *J. Am. Chem. Soc.* 2010, **132**, 4092. (d) S.-T. Zheng, J. T. Bu, Y. Li, T. Wu, F. Zuo, P. Feng, X. Bu, *J. Am. Chem. Soc.* 2010, **132**, 17062. (e) F. Debatin, A. Thomas, A. Kelling, N. Hedin, Z. Bacsik, I. Senkovska, S. Kaskel, M. Junginger, H. Muller, U. Schilde, C. Jager, A. Friedrich, H. J. Holdt, *Angew. Chem. Int. Ed.* 2010, **49**, 1258. (f) R. Vaidhyanathan, S. S. Iremonger, K. W. Dawson, G. K. H. Shimizu, *Chem. Commun.*, 2009, 5230. (g) O. K. Farha, A. M. Spokoyny, K. L. Mulfort, S. Galli, J. T. Hupp, C. A. Mirkin, *small*, 2009, **5**, 1727. (h) T. Panda, P. Pachfule, Y. Chen, J. Jiang, R. Banerjee *Chem. Commun.*, 2011, 2011. (i) J. W. Yoon, S. H. Jhung, Y. K. Hwang, S. M. Humphrey, P. T. Wood, J. S. Chang, *Adv. Mater.* 2007, **19**, 1830. (j) A. Demessence, D. M. D'Alessandro, M. L. Foo, J. R. Long, *J. Am. Chem. Soc.* 2009, **131**, 8784. (k) J. An, S. J. Geib, N. L. Rosi *J. Am. Chem. Soc.* 2010, **132**, 38. (l) K. S. Park, Z. Ni, A. P. Cote, J. Y. Choi, R. D. Huang, F. J. Uribe-Romo, H. K. Chae, M. O'Keeffe, O. M. Yaghi, *Proc. Natl. Acad. Sci. U. S. A.*, 2006, **103**, 10186. (m) J. L. C. Rowsell, A. R. Millward, K. S. Park, O. M. Yaghi, *J. Am. Chem. Soc.* 2004, **126**, 5666. (n) P. Pachfule, Y. Chen, J. Jiang, R. Banerjee, *J. Mater. Chem.*, 2011, **21**, 17737.
- [1.19] (a) X. -S. Wang, S. Ma, P. M. Forster, D. Yuan, J. Eckert, J. J. Lopez, B. J. Murphy, J. B. Parise, H. -C. Zhou *Angew. Chem. Int. Ed.* 2008, **47**, 7263. (b) Z. Guo, H. Wu, G. Srinivas, Y. Zhou, S. Xiang, Z. Chen, Y. Yang, W. Zhou, M. O'Keeffe, B. Chen, *Angew. Chem. Int. Ed.* 2011, **50**, 3178. (c) S. Ma, D. Sun, J. M. Simmons, C. D. Collier, D. Yuan, H.-C. Zhou, *J. Am. Chem. Soc.*, 2008, **130**, 1012. (d) X. Lin, I. Telepen, A. J. Blake, A. Dailly, C. M. Brown, J. M. Simmons, M. Zoppi, G. S. Walker, K. M. Thomas, T. J. Mays, P. Hubberstey, N. R. Champness, M. Schroder, *J. Am. Chem. Soc.*, 2009, **131**, 2159. (e) X. S. Wang, S. Ma, K. Rauch, J. M. Simmons, D. Yuan, X. Wang, T. Yildirim, W. C. Cole, J. J. Lspez, A. de Meijere, H. C. Zhou, *Chem. Mater.*, 2008, **20**, 3145. (f) X. Lin, J. H.

- Jia, X. B. Zhao, K. M. Thomas, A. J. Blake, G. S. Walker, N. R. Champness, P. Hubberstey, M. Schroder, *Angew. Chem., Int. Ed.*, 2006, **45**, 7358. (g) C. Tan, S. Yang, N. R. Champness, X. Lin, A. J. Blake, W. Lewis, M. Schroder, *Chem. Commun.*, 2011, 4487. (h) B. Chen, N. W. Ockwig, A. R. Millward, D. S. Contreras, O. M. Yaghi, *Angew. Chem. Int. Ed.* 2005, **44**, 4745. (i) M. Dinca, W. S. Han, Y. Liu, A. Dailly, C. M. Brown, J. R. Long, *Angew. Chem., Int. Ed.*, 2007, **46**, 1419. (j) F. Nouar, J. F. Eubank, T. Bousquet, L. Wojtas, M. J. Zaworotko, M. Eddaoudi, *J. Am. Chem. Soc.*, 2008, **130**, 1833. (k) X. Gu, Z. -H. Lu, Q. Xu, *Chem. Commun.*, 2010, **46**, 7400.
- [1.20] (a) J. Grigg, *Arch Dis Child*, 2002, **86**, 79. (b) D. Lüthi, M. Le Floch, B. Bereiter, T. Blunier, J. M. Barnola, U. Siegenthaler, D. Raynaud, J. Jouzel, H. Fischer, K. Kawamura, T. F. Stocker, *Nature*, 2008, **453**, 379. (c) Health Effects of Climate Change in the UK (2008), UK Department of Health.
- [1.21] (a) F. Barzagli, F. Mani, M. Peruzzini, *Energy Environ. Sci.* 2010, **3**, 772. (b) C.-H. Yu, C.-H. Huang, C.-S. Tan, *Aerosol Air Qual. Res.* 2012, **12**, 745. (c) W. M. Budzianowski, Value-added carbon management technologies for low CO<sub>2</sub> intensive carbon based energy vectors, *Energy*, 2012, 37.
- [1.22] (a) A.-H. Lu, G.-P. Hao, *Annu. Rep. Prog. Chem., Sect. A: Inorg. Chem.*, 2013, **109**, 484. (b) A.-H. Lu, S. Dai, Porous Materials for Carbon Dioxide Capture, Springer-Verlag Berlin Heidelberg, 2014.
- [1.23] (a) K. Sumida, D. L. Rogow, J. A. Mason, T. M. McDonald, E. D. Bloch, Z. R. Herm, T.-H. Bae, J. R. Long, *Chem. Rev.*, 2012, **112**, 724. (b) Y. Liu, U. Z. Wang, H.-C. Zhou, *Greenhouse Gases: Sci. Technol.* 2012, **2**, 239. (c) J. Liu, P. K. Thallapally, B. P. McGrail, D. R. Brown, J. Liu, *Chem. Soc. Rev.*, 2012, **41**, 2308. (d) Z. Zhang, Y. Zhao, Q. Gong, Z. Li, J. Li, *Chem. Commun.*, 2013, **49**, 653.
- [1.24] (a) A. R. Millward, O.M. Yaghi, *J. Am. Chem. Soc.*, 2005, **127**, 17998. (b) P. D. C. Dietzel, R. E. Johnsen, H. Fjellvag, S. Bordiga, E. Groppo, S. Chavan, R. Blom, *Chem. Commun.* 2008, 5125. (c) T. M. McDonald, D. M. D'Alessandro, R. Krishna, J. R. Long, *Chem. Sci.* 2011, **2**, 2022. (d) S. S.-Y. Chui, S. M.-F. Lo, J. Charmant, A. G. Orpen, I. D. Williams, *Science*, 1999, **283**, 1148. (e) D. Britt, H.

- Furukawa, B. Wang, T. G. Glover, O. M. Yaghi, *Proc. Natl. Acad. Sci. U. S. A.*, 2009, **106**, 20637. (f) P. Nugent, Y. Belmabkhout, S. D. Burd, A.J. Cairns, R. Luebke, K. Forrest, T. Pham, S. Ma, B. Space, L. Wojtas, M. Eddaoudi, M. J. Zaworotko, *Nature*, 2013, **495**, 80.
- [1.25] (a) O. K. Farha, C. D. Malliakas, M. G. Kanatzidis, J. T. Hupp, *J. Am. Chem. Soc.* 2010, **132**, 950. (b) Y.-S. Bae, O. K. Farha, J. T. Hupp, R. Q. Snurr, *J. Mater. Chem.*, 2009, **19**, 213. (c) Y. S. Bae, O. K. Farha, A. M. Spokoyny, C. A. Mirkin, J. T. Hupp, R. Q. Snurr, *Chem. Commun.*, 2008, 4135. (d) K. L. Mulfort, O. K. Farha, C. D. Malliakas, M. G. Kanatzidis, J. T. Hupp, *Chem. Eur. J.* 2010, **16**, 276. (e) H. S. Choi, M. P. Suh, *Angew. Chem.* 2009, **121**, 6997. (f) J. An, N. L. Rosi, *J. Am. Chem. Soc.* 2010, **132**, 5578. (g) R. Banerjee, H. Furukawa, D. Britt, C. Knobler, M. O’Keeffe, O. M. Yaghi, *J. Am. Chem. Soc.* 2009, **131**, 3875. (h) W. Morris, B. Leung, H. Furukawa, O. K. Yaghi, N. He, H. Hayashi, Y. Houndonougbo, M. Asta, B. B. Laird, O. M. Yaghi, *J. Am. Chem. Soc.* 2010, **132**, 11006.
- [1.26] U.S. Department of Energy, U.S. Energy Information Administration: International Energy Outlook 2013 (Report: DOE/EIA-0484(2013)), 2013.
- [1.27] (a) Boyle, Godfrey. *Renewable energy*. OXFORD university press, 2004. (b) Johansson, Thomas B., and Laurie Burnham, eds. *Renewable energy: sources for fuels and electricity*. Island Press, 1993.
- [1.28] (a) G. K. H. Shimizu, J. M. Taylor, S. Kim, *Science*, 2013, **341**, 354. (b) S. Horike, D. Umeyama, S. Kitagawa, *Acc. Chem. Res.* 2013, **46**, 2376. (c) N. Agmon *Chem. Phys. Lett.* 1995, **5**, 456. (d) H. Arribart, Y. Piffard, *Solid State Commun.*, 1983, **45**, 571. (e) K. D. Kreuer, A. Rabenau, W. Weppner, *Angew. Chem., Int. Ed.* 1982, **21**, 208.
- [1.29] (a) A. Shigematsu, T. Yamada, H. Kitagawa, *J. Am. Chem. Soc.* 2011, **133**, 2034. (b) J. M. Taylor, R. K. Mah, I. L. Moudrakovski, C. I. Ratcliffe, R. Vaidhyanathan, G. K. H. Shimizu, *J. Am. Chem. Soc.* 2010, **132**, 14055. (c) T. Yamada, M. Sadakiyo, H. Kitagawa, *J. Am. Chem. Soc.* 2009, **131**, 3144. (d) M. Yoon, K. Suh, H. Kim, Y. Kim, N. Selvapalam, K. Kim, *Angew. Chem. Int. Ed.* 2011, **50**, 7870. (e) M. Sadakiyo, T. Yamada, H. Kitagawa, *J. Am. Chem. Soc.*

- 2009, **131**, 9906. (f) V. G. Ponomareva, K. A. Kovalenko, A. P. Chupakhin, D. N. Dybtsev, E. S. Shutova, V. P. Fedin, *J. Am. Chem. Soc.* 2012, **134**, 15640. (g) S. Kanda, K. Yamashita, K. Ohkawa, *Bull. Chem. Soc. Jpn.* 1979, **52**, 3296. (h) T. Yamada, S. Morikawa, H. Kitagawa, *Bull. Chem. Soc. Jpn.* 2010, **83**, 42. (i) S. Kim, K. W. Dawson, B. S. Gelfand, J. M. Taylor, G. K. H. Shimizu, *J. Am. Chem. Soc.* 2013, **135**, 963. (j) S. C. Sahoo, T. Kundu, R. Banerjee. *J. Am. Chem. Soc.* 2011, **133**, 17950. (k) S. Sen, N. N. Nair, T. Yamada, H. Kitagawa, P. K. Bharadwaj, *J. Am. Chem. Soc.* 2012, **134**, 19432. (l) C. Dey, T. Kundu, R. Banerjee. *Chem. Commun.*, 2012, **48**, 266. (m) H. Okawa, A. Shigematsu, M. Sadakiyo, T. Miyagawa, K. Yoneda, M. Ohba, H. Kitagawa, *J. Am. Chem. Soc.* 2009, **131**, 13516. (n) E. Pardo, C. Train, G. Gontard, K. Boubekeur, O. Fabelo, H. Liu, B. Dkhil, F. Lloret, K. Nakagawa, H. Tokoro, S. Ohkoshi, M. Verdagner, *J. Am. Chem. Soc.* 2011, **133**, 15328. (o) B. M. Wiers, M. -L. Foo, N. P. Balsara, J. R. Long, *J. Am. Chem. Soc.* 2011, **133**, 14522. (p) M. Sadakiyo, H. Okawa, A. Shigematsu, M. Ohba, T. Yamada, H. Kitagawa, *J. Am. Chem. Soc.* 2012, **134**, 5472. (q) C. Serre, F. Millange, C. Thouvenot, M. Nogus, G. Marsolier, D. Lour, G. Frey, *J. Am. Chem. Soc.* 2002, **124**, 13519. (r) A. Shigematsu, T. Yamada, H. Kitagawa, *J. Am. Chem. Soc.* 2011, **133**, 2034. (s) T. Kundu, S. C. Sahoo, R. Banerjee. *Chem. Commun.*, 2012, **48**, 4998. (t) V. G. Ponomareva, K. A. Kovalenko, A. P. Chupakhin, D. N. Dybtsev, E. S. Shutova, V. P. Fedin, *J. Am. Chem. Soc.* 2012, **134**, 15640.
- [1.30] (a) S. Bureekaew, S. Horike, M. Higuchi, M. Mizuno, T. Kawamura, D. Tanaka, N. Yanai, S. Kitagawa, *Nat. Mater.* 2009, **8**, 831. (b) J. A. Hurd, R. Vaidhyanathan, V. Thangadurai, C. I. Ratcliffe, I. L. Moudrakovski, G. K. Shimizu, *Nat. Chem.* 2009, **1**, 705. (c) D. Umeyama, S. Horike, M. Inukai, Y. Hijikata, S. Kitagawa, *Angew. Chem., Int. Ed.* 2011, **50**, 11706. (d) S. Horike, D. Umeyama, M. Inukai, T. Itakura, S. Kitagawa, *J. Am. Chem. Soc.* 2012, **134**, 7612. (e) D. Umeyama, S. Horike, M. Inukai, T. Itakura, S. Kitagawa, *J. Am. Chem. Soc.* 2012, **134**, 12780.

- [1.31] (a) M. D. Allendorf, C. A. Bauer, R. K. Bhakta, R. J. T. Houk, *Chem. Soc. Rev.* 2009, **38**, 1330. (b) J. Rocha, L. D. Carlos, F. A. A. Paz, D. Ananias, *Chem. Soc. Rev.* 2011, **40**, 926.
- [1.32] Z.-Z. Lu, R. Zhang, Y.-Z. Li, Z.-J. Guo, H.-G. Zheng, *J. Am. Chem. Soc.* 2011, **133**, 4172.
- [1.33] (a) L. G. Beauvais, M. P. Shores, J. R. Long, *J. Am. Chem. Soc.* 2000, **122**, 2763. (b) H. Lee, S. H. Jung, W. S. Han, J. H. Moon, S. Kang, J. Y. Lee, J. H. Jung, S. Shinkai, *Chem.-Eur. J.* 2011, **17**, 2823.
- [1.34] Y. Takashima, V. M. Martinez, S. Furukawa, M. Kondo, S. Shimomura, H. Uehara, M. Nakahama, K. Sugimoto, S. Kitagawa, *Nat. Commun.* 2011, **2**, 168.
- [1.35] S. Achmann, G. Hagen, J. Kita, I. M. Malkowsky, C. Kiener, R. Moos, *Sensors*, 2009, **9**, 1574.
- [1.36] K. A. Willets, R. P. Van Duyne, *Annu. Rev. Phys. Chem.* 2007, **58**, 267.
- [1.37] L. Han, L. Qin, L. Xu, Y. Zhou, J. Sun and X. Zou *Chem. Commun.*, 2013, **49**, 406.
- [1.38] Y.-N. Gong, T.-B. Lu, *Chem. Commun.*, 2013, **49**, 7711.
- [1.39] (a) J. Y. Lee, O. K. Farha, J. Roberts, K. A. Scheidt, S. T. Nguyen, J. T. Hupp, *Chem. Soc. Rev.*, 2009, **38**, 1450. (b) M. Zhao, S. Ou, C. -D. Wu *Acc. Chem. Res.*, 2014, **47**, 1199. (c) J. Gascon, A. Corma, F. Kapteijn, F. X. L. Xamena, *ACS Catal.*, 2014, **4**, 361.
- [1.40] M. Fujita, Y. J. Kwon, S. Washizu, K. Ogura *J. Am. Chem. Soc.* 1994, **116**, 1151.
- [1.41] J. S. Seo, D. Whang, H. Lee, S. I. Jun, J. Oh, Y. J. Jeon, K. Kim, *Nature* 2000, **404**, 982.
- [1.42] S. Horike, N. Dinca, K. Tamaki, J. R. Long, *J. Am. Chem. Soc.* 2008, **130**, 5854.
- [1.43] D. J. Lun, G. I. N. Waterhouse, S. G. Telfer, *J. Am. Chem. Soc.* 2011, **133**, 5806.
- [1.44] (a) F. Song, C. Wang, W. Lin, *Chem. Commun.* 2011, **47**, 8256. b) F. Song, T. Zhang, C. Wang, W. Lin, *Proc. R. Soc. A.* 2012, **468**, 2035.
- [1.45] C. Liu, Y. Y. Fan, M. Liu, H. T. Cong, H. M. Cheng, M. S. Dresselhaus, *Science*, 1999, **286**, 1127.
- [1.46] (a) S. Bureekaew, S. Horike, M. Higuchi, M. Mizuno, T. Kawamura, D. Tanaka, N. Yanai, S. Kitagawa, *Nat. Mater.*, 2009, **8**, 831. (b) J. A. Hurd, R.

- Vaidhyanathan, V. Thangadurai, C. I. Ratcliffe, I. L. Moudrakovski, G. K. Shimizu, *Nat. Chem.*, 2009, **1**, 705. (c) D. Umeyama, S. Horike, M. Inukai, Y. Hijikata, S. Kitagawa, *Angew. Chem., Int. Ed.*, 2011, **50**, 11706. (d) S. Horike, D. Umeyama, M. Inukai, T. Itakura, S. Kitagawa, *J. Am. Chem. Soc.*, 2012, **134**, 7612. (e) D. Umeyama, S. Horike, M. Inukai, T. Itakura, S. Kitagawa, *J. Am. Chem. Soc.*, 2012, **134**, 12780.
- [1.47] <http://hyperphysics.phy-astr.gsu.edu/hbase/tables/elabund.html>;
- [1.48] Lee, J. D. Concise Inorganic Chemistry; Chapman & Hall: New York, 1991.
- [1.49] D. Banerjee, J. B. Parise, *Cryst. Growth Des.* 2011, **11**, 4704.
- [1.50] G. Férey, C. Mellot-Draznieks, C. Serre, F. Millange, J. Dutour, S. Surblé, I. Margiolaki, *Science*, 2005, **309**, 2040.
- [1.51] D. Britt, H. Furukawa, B. Wang, T. G. Glover, O. M. Yaghi, *Proc. Nati. Acad. Sci. USA*, 2009, **106**, 20637
- [1.52] A. E. P. Prats, V. A. de la Peña-O'Shea, M. Iglesias, N. Snejko, Á. Monge, E. Gutiérrez-Puebla, *ChemCatChem*, 2010, **2**, 147.
- [1.53] N. B. Shustova, A. F. Cozzolino, S. Reineke, M. Baldo, M. Dincă, *J. Am. Chem. Soc.*, 2013, **135**, 13326.
- [1.54] J. J. Gassensmith, J. Yoon Kim, J. M. Holcroft, O. K. Farha, J. F. Stoddart, J. T. Hupp, N. C. Jeong, *J. Am. Chem. Soc.*, 2014, **136**, 8277.
- [1.55] P. Horcajada, C. Serre, M. Vallet-Regi, M. Sebban, F. Taulelle, G. Férey, *Angew. Chem., Int. Ed.* 2006, **45**, 5974.
- [1.56] H. Deng, S. Grunder, K. E. Cordova, C. Valente, H. Furukawa, M. Hmadeh, F. Gándara, A. C. Whalley, Z. Liu, S. Asahina, H. Kazumori, M. O'Keeffe, O. Terasaki, J. F. Stoddart, O. M. Yaghi, *Science*, 2012, **336**, 1018.

## CHAPTER 2

- [2.1] (a) M. D. Allendorf, C. A. Bauer, R. K. Bhakta, R. J. T. Houk, *Chem. Soc. Rev.* 2009, **38**, 1330. (b) B. Chen, S. Xiang, G. Qian, *Acc. Chem. Res.* 2010, **43**, 1115.

- (c) A. U. Czaja, N. Trukhan, U. Muller, *Chem. Soc. Rev.* 2009, **38**, 1284. (d) M. Eddaoudi, D. B. Moler, H. Li, B. Chen, T. M. Reineke, M. O'Keeffe, O. M. Yaghi, *Acc. Chem. Res.* 2001, **34**, 319. (e) O. R. Evans, W. Lin, *Acc. Chem. Res.* 2002, **35**, 511. (f) O. K. Farha, J. T. Hupp, *Acc. Chem. Res.* 2010, **43**, 1166. (g) G. Ferey, C. Serre, *Chem. Soc. Rev.* 2009, **38**, 1380. (h) R. J. Hill, D.-L. Long, N. R. Champness, P. Hubberstey, M. Schröder, *Acc. Chem. Res.* 2005, **38**, 335. (i) J. J. P. Iv, J. A. Perman, M. J. Zaworotko, *Chem. Soc. Rev.* 2009, **38**, 1400. (j) M. Kurmoo, *Chem. Soc. Rev.* 2009, **38**, 1353. (k) J. Lee, O. K. Farha, J. Roberts, K. A. Scheidt, S. T. Nguyen, J. T. Hupp, *Chem. Soc. Rev.* 2009, **38**, 1450. (l) L. R. MacGillivray, G. S. Papaefstathiou, T. Frišćić, T. D. Hamilton, D.-K. Bučar, Q. Chu, D. B. Varshney, I. G. Georgiev, *Acc. Chem. Res.* 2008, **41**, 280. (m) L. J. Murray, M. Dinca, J. R. Long, *Chem. Soc. Rev.* 2009, **38**, 1294. (n) N. W. Ockwig, O. Delgado-Friedrichs, M. O'Keeffe, O. M. Yaghi, *Acc. Chem. Res.* 2005, **38**, 176. (o) E. R. Parnham, R. E. Morris, *Acc. Chem. Res.* 2007, **40**, 1005. (p) A. Phan, C. J. Doonan, F. J. Uribe-Romo, C. B. Knobler, M. O'Keeffe, O. M. Yaghi, *Acc. Chem. Res.* 2009, **43**, 58. (q) D. J. Tranchemontagne, J. L. Mendoza-Cortes, M. O'Keeffe, O. M. Yaghi, *Chem. Soc. Rev.* 2009, **38**, 1257. (r) Z. Wang, S. M. Cohen, *Chem. Soc. Rev.* 2009, **38**, 1315. (s) O. M. Yaghi, H. Li, C. Davis, D. Richardson, T. L. Groy, *Acc. Chem. Res.* 1998, **31**, 474. (t) J. Yu, R. Xu, *Acc. Chem. Res.* 2010, **43**, 1195. (u) D. Zacher, O. Shekhah, C. Woll, R. A. Fischer, *Chem. Soc. Rev.* 2009, **38**, 1418.
- [2.3] O. D.-Friedrichs, M. D. Foster, M. O'Keeffe, D. M. Proserpio, M. Treacy, O. M. Yaghi, *J. Solid State Chem.*, 2005, **178**, 2533.
- [2.4] Diamond has also been described as the underlying topology of a MOF structure that actually has low crystallographic symmetry (reference 1.7a)
- [2.5] M. O'Keeffe, B. G. Hyde, *Crystal Structures I. Patterns and Symmetry* Mineralogical Society of America: Washington, DC, 1996.
- [2.6] (a) G. R. Desiraju, *Chem. Commun.*, 2005, **24**, 2995. (b) G. R. Desiraju, *Acc. Chem. Res.*, 2002, **35**, 565. (c) J. Elguero, *Angew. Chem. Int. Ed.* 2001, **40**, 799.



- [2.7] (a) A. Sayari, Y. Belmabkhout, *J. Am. Chem. Soc.*, 2010, **132**, 6312 (b) W. Morris, B. Leung, H. Furukawa, O. K. Yaghi, N. He, H. Hayashi, Y. Houndonougbo, M. Asta, B. B. Laird, O. M. Yaghi, *J. Am. Chem. Soc.*, 2010, **132**, 11006;
- [2.8] A. Samanta, T. Furuta, J. Li, *J. Chem. Phys.*, 2006, **125**
- [2.9] O. S. Smart, J. G. Neduvélil, X. Wang, B. A. Wallace, M. S. P. Sansom, *J. Mol. Graphics Model.* 1996, **14**, 354.
- [2.10] Materials Studio, v., Accelrys: San Diego, 2007.
- [2.11] A. Hirotsu, K. Mizukami, R. Miura, H. Takaba, T. Miya, A. Fahmi, A. Stirling, M. Kubo, A. Miyamoto, *Appl. Surf. Sci.* 1997, **120**, 81.
- [2.12] A. K. Rappe, C. J. Casewit, K. S. Colwell, W. A. Goddard, W. M. Skiff, *J. Am. Chem. Soc.* 1992, **114**, 10024.
- [2.13] G. Garberoglio, A. I. Skoulidas, J. K. Johnson, *J. Phys. Chem. B.* 2005, **109**, 13094.
- [2.14] A. I. Skoulidas, D. S. Sholl, *J. Phys. Chem. B.* 2005, **109**, 15760.
- [2.15] R. Babarao, Z. Q. Hu, J. W. Jiang, S. Chempath, S. I. Sandler, *Langmuir*, 2007, **23**, 659.
- [2.16] R. Babarao, J. W. Jiang, *Langmuir*, 2008, **24**, 6270.
- [2.17] S. F. Boys and F. Bernardi, *Mol. Phys.* 1970, **19**, 553.
- [2.18] M. J. Frisch, G. W. Trucks, H. B. Schlegel, G. E. Scuseria, M. A. Robb, J. R. Cheeseman, V. G. Zakrzewski, J. A. Montgomery, R. E. Stratmann, J. C. Burant, S. Dapprich, J. M. Millam, A. D. Daniels, K. N. Kudin, M. C. Strain, O. Farkas, J. Tomasi, V. Barone, M. Cossi, R. Cammi, B. Mennucci, C. Pomelli, C. Adamo, S. Clifford, J. Ochterski, G. A. Petersson, P. Y. Ayala, Q. Cui, K. Morokuma, D. K. Malick, A.D. Rabuck, K. Raghavachari, J. B. Foresman, J. Cioslowski, J. V. Ortiz, B. B. Stefanov, G. Liu, A. Liashenko, P. Piskorz, I. Komaromi, R. Gomperts, R. L. Martin, D. J. Fox, T. Keith, M. A. Al-Laham, C. Y. Peng, A. Nanayakkara, C. Gonzalez, M. Challacombe, P. M. W. Gill, B. G. Johnson, W. Chen, M. W. Wong, J. L. Andres, M. Head-Gordon, E. S. Replogle and J. A. Pople, *Gaussian 09*, Revision D.01 ed. Gaussian Inc., Wallingford CT, 2009.
- [2.19] Bruker (2005). *APEX2*. Version 5.053. Bruker AXS Inc., Madison, Wisconsin, USA.

- [2.20] Sheldrick, G. M. (2004). *CELL\_NOW*. University of Göttingen, Germany. Steiner, Th. (1998). *Acta Cryst.* B54, 456–463.
- [2.21] Bruker (2004). *SAINT-Plus* (Version 7.03). Bruker AXS Inc., Madison, Wisconsin, USA.
- [2.22] Sheldrick, G. M. (2002). *SADABS* (Version 2.03) and *TWINABS* (Version 1.02). University of Göttingen, Germany.
- [2.23] Sheldrick, G. M. (1997). *SHELXS '97* and *SHELXL '97*. University of Göttingen, Germany.
- [2.24] WINGX version 1.80.04. Louis Farrugia, University of Glasgow.
- [2.25] A. L. Spek (2005) PLATON, *A Multipurpose Crystallographic Tool*, Utrecht University, Utrecht, The Netherlands.
- [2.26] L. A. Dakin, P. C. Ong, J. S. Panek, R. J. Staples, and P. Stavropoulos, *Organometallics*, 2000, **19**, 2896.
- [2.27] S. Noro, R. Kitaura, M. Kondo, S. Kitagawa, T. Ishii, H. Matsuzaka, and M. Yamashita, *J. Am. Chem. Soc.* 2002, **124**, 2568.
- [2.28] M. Eddaoudi, J. Kim, D. Vodak, A. Sudik, J. Wachter, M. O’Keeffe, and O. M. Yaghi, *Proc. Natl. Acad. Sci. USA*, 2002, **99**, 4900.
- [2.29] R. A. Heintz, H. Zhao, X. Ouyang, G. Grandinetti, J. Cowen, and K. R. Dunbar, *Inorg. Chem.* 1999, **38**, 144.
- [2.30] K. Biradha, Y. Hongo, and M. Fujita, *Angew. Chem. Int. Ed.* 2000, **39**, 3843.
- [2.31] P. Grosshans, A. Jouaiti, M. W. Hosseini, and N. Kyritsakas, *New J. Chem*, (Nouv. J. Chim,) 2003, **27**, 793.
- [2.32] N. Takeda, K. Umemoto, K. Yamaguchi, and M. Fujita, *Nature (London)* 1999, **398**, 794.
- [2.33] M. Eddaoudi, J. Kim, N. Rosi, D. Vodak, J. Wachter, M. O’Keeffe, and O. M. Yaghi, *Science*, 2002, **295**, 469.
- [2.34] B. Kesanli, Y. Cui, M. R. Smith, E. W. Bittner, B. C. Bockrath, and W. Lin, *Angew. Chem. Int. Ed.* 2005, **44**, 72.
- [2.35] F. A. Cotton, C. Lin, and C. A. Murillo, *Inorg. Chem.* 2001, **40**, 478.

---

**CHAPTER 3**

- [3.1] K. D. Kreuer, *Chem. Mater.* 1996, **8**, 610.
- [3.2] K. A. Mauritz, R. B. Moore, *Chem. Rev.* 2004, **104**, 4535.
- [3.3] (a) S. Bureekaew, S. Horike, M. Higuchi, M. Mizuno, T. Kawamura, D. Tanaka, N. Yanai, S. Kitagawa, *Nat. Mater.* 2009, **8**, 831. (b) J. A. Hurd, R. Vaidhyanathan, V. Thangadurai, C. I. Ratcliffe, I. M. Moudrakovski, G. K. H. Shimizu, *Nat. Chem.* 2009, **1**, 705. (c) A. Shigematsu, T. Yamada, H. Kitagawa, *J. Am. Chem. Soc.* 2011, **133**, 2034. (d) M. Yoon, K. Suh, H. Kim, Y. Kim, N. Selvapalam, K. Kim, *Angew. Chem. Int. Ed.* 2011, **50**, 7870. (e) S. C. Sahoo, T. Kundu, R. Banerjee, *J. Am. Chem. Soc.* 2011, **133**, 17950. (f) M. Sadakiyo, H. Okawa, A. Shigematsu, M. Ohba, T. Yamada, H. Kitagawa, *J. Am. Chem. Soc.* 2012, **134**, 5472. (g) J. M. Taylor, R. K. Mah, I. L. Moudrakovski, C. I. Ratcliffe, R. Vaidhyanathan, G. K. H. Shimizu, *J. Am. Chem. Soc.* 2010, **132**, 14055. (h) T. Kundu, S. C. Sahoo, R. Banerjee, *Chem. Commun.* 2012, **48**, 4998. (i) T. Yamada, M. Sadakiyo, H. Kitagawa, *J. Am. Chem. Soc.* 2009, **131**, 3144. (j) T. Panda, T. Kundu, R. Banerjee, *Chem. Commun.* 2012, **48**, 5464. (k) C. Dey, T. Kundu, R. Banerjee, *Chem. Commun.* 2012, **48**, 266.
- [3.4] (a) G. K. H. Shimizu, J. M. Taylor, S. Kim, *Science*, 2013, **341**, 354. (b) S. Horike, D. Umeyama, S. Kitagawa, *Acc. Chem. Res.*, 2013, **46**, 2376. (c) N. Agmon *Chem. Phys. Lett.* 1995, **5**, 456. (d) H. Arribart, Y. Piffard, *Solid State Commun*, 1983, **45**, 571. (e) K. D. Kreuer, A. Rabenau, W. Weppner, *Angew. Chem., Int. Ed.* 1982, **21**, 208.
- [3.5] (a) A. L. Garay, A. Pichon, S.L. James, *Chemical Society Reviews* 2007, **36**, 846. (b) T. Liu, Y. J. Zhang, Z. M. Wang, S. Gao, *J. Am. Chem. Soc.* 2008, **130**, 10500. (c) A. D. Burrows, C. G. Frost, M. F. Mahon, C. Richardson, *Angew. Chem. Int. Ed.* 2008, **47**, 8482. (d) X. S. Wang, L. Meng, Q. Cheng, C. Kim, L. Wojtas, M. Chrzanowski, Y. S. Chen, X. P. Zhang, S. Ma, *J. Am. Chem. Soc.* 2011, **133**, 16322. (e) A. D. Burrows, *CrystEngCom.* 2011, **13**, 3623.

- [3.6] (a) M. J. Platers, R. A. Howie, A. J. Roberts, *Chem. Commun.* 1997, 893. (b) P. C. Liang, H. K. Liu, C. T. Yeh, C.H. Lin, V. Zima, *Cryst. Growth Des.* 2011, **11**, 699. (c) B. M. Borah, S. K. Dey, G. Das, *Cryst. Growth Des.* 2011, **11**, 2773. (d) A. M. Plonka, D. Banerjee, J. B. Parise, *Cryst. Growth Des.* 2012, **12**, 2460. (e) C. A. Williams, A. J. Blake, C. Wilson, P. Hubberstey, M. Schröder, *Cryst. Growth Des.* 2008, **8**, 911.
- [3.7] G. R. Desiraju and T. Steiner, *The Weak Hydrogen Bond: In Structural Chemistry and Biology*, Oxford University Press, Oxford, 1999.
- [3.8] (a) S. I. Cukierman, *Biochim. Biophys. Acta, Bioenerg.* 2006, **1757**, 876. (b) “Proton Conductors: Solids, Membranes and Gels-Materials and Devices”: P. Colomban in *Chemistry of Solid State Materials, Vol. 2*, Cambridge University Press, Cambridge, U.K., 1992.
- [3.9] CrysAlisPro, Version 1.171.33.66; Oxford Diffraction Ltd.: Abingdon, U.K., 2010.
- [3.10] (a) M. Eddaoudi, H. Li, O. M. Yaghi, *J. Am. Chem. Soc.*, 2000, **122**, 1391. (b) K. E. deKrafft, Z. Xie, G. Cao, S. Tran, L. Ma, O. Z. Zhou, W. Lin, *Angew. Chem. Int. Ed.*, 2009, **48**, 9901.
- [3.11] (a) F. Nouar, J. F. Eubank, T. Bousquet, L. Wojtas, M. J. Zaworotko, M. Eddaoudi, *J. Am. Chem. Soc.* 2008, **130**, 1833. (b) S. Xiang, W. Zhou, J. M. Gallegos, Y. Liu, B. Chen, *J. Am. Chem. Soc.* 2009, **131**, 12415. (c) D. J. Tranchemontagne, J. L. Mendoza-Cortes, M. O’Keefe, O. M. Yaghi, *Chem. Soc. Rev.*, 2009, **38**, 1257. (d) M. O’Keefe, M. Eddaoudi, H. Li, T. M. Reineke, O. M. Yaghi, *J. Solid State Chem.*, 2000, **152**, 3. (e) M. O’Keefe, B. G. Hyde, *Crystal Structures I. Patterns and Symmetry*; Mineralogical Society of America: Washington, DC, 1996.
- [3.12] A. W. Addison, T. N. Rao, J. Reedijk, J. V. Rijn and G. C. Verschoor, *J. Chem. Soc., Dalton Trans.*, 1984, 1349.

**CHAPTER 4**

- [4.1] (a) G. Lu, J. T. Hupp, *J. Am. Chem. Soc.* 2010, **132**, 7832. (b) J. J. Gassensmith, H. Furukawa, R. A. Smaldone, R. S. Forgan, Y. Y. Botros, O. M. Yaghi, J. F. Stoddart, *J. Am. Chem. Soc.* 2011, **133**, 15312. (c) M. D. Allendorf, R. J. T. Houk, L. Andruszkiewicz, A. A. Talin, J. Pikarsky, A. Choudhury, K. A. Gall, P. J. Hesketh, *J. Am. Chem. Soc.* 2008, **130**, 14404. (d) L. E. Kreno, K. Leong, O. K. Farha, M. Allendorf, R. P. V. Duyne, J. T. Hupp, *Chem. Rev.* 2012, **112**, 1105. (e) Z. Hu, B. J. Deibert, Li, *J. Chem. Soc. Rev.* 2014, **43**, 5815. (f) Y. Cui, Y. Yue, G. Qian, B. Chen, *Chem. Rev.* 2012, **112**, 1126.
- [4.2] (a) A. Hulanicki, S. Geab, F. Ingman, *Pure & App. Chem.* 1991, **63**, 1247. (b) J. R. Stetter, W. R. Penrose, S. Yao, *J. Electrochem. Soc.* 2003, **150**, S11.
- [4.3] (a) M. E. Davis, *Nature*, 2002, **417**, 813. (b) Z. Xie, L. Ma, K. E. deKrafft, A. Jin, W. Lin, *J. Am. Chem. Soc.* 2010, **132**, 922. (c) J. Zhang, X. Liu, S. Wu, M. Xu, X. Guo, S. Wang, *J. Mater. Chem.* 2010, **20**, 6453.
- [4.4] (a) H. Li, M. Eddaoudi, M. O’Keffee, O. M. Yaghi, *Nature*, 1999, **402**, 276. (b) A. Mallik, S. Saha, P. Pachfule, S. Roy, R. Banerjee, *J. Mater. Chem.* 2010, **20**, 9073. (c) H. Deng, S. Grunder, K. E. Cordova, C. Valente, H. Furukawa, M. Hmadeh, F. Gándara, A. C. Whalley, Z. Liu, S. Asahina, H. Kazumori, M. O’Keeffe, O. Terasaki, J. F. Stoddart, O. M. Yaghi, *Science* 2012, **336**, 1018. (d) F. Hinterholzinger, B. Rühle, S. Wuttke, K. Karaghiosoff, T. Bein, *Sci. Rep.* 2013, **3**, 2562. (e) R. Grünker, V. Bon, P. Muller, U. Stoeck, S. Krause, U. Müller, I. Senkovska, S. Kaskel, *Chem. Commun.* 2014, **50**, 3450. (f) D. J. Xiao, E. D. Bloch, J. A. Mason, W. L. Queen, M. R. Hudson, N. Planas, J. Borycz, A. L. Dzubak, P. Verma, K. Lee, F. Bonino, V. Crocella, J. Yano, S. Bordiga, D. G. Truhlar, L. Gagliardi, C. M. Brown, J. R. Long, *Nat. Chem.* 2014, **6**, 590. (g) W. M. Bloch, A. Burgun, C. J. Coghlan, R. Lee, M. L. Coote, C. J. Doonan, C. J. Sumby, *Nat. Chem.* 2014, **6**, 906. (h) J. F. Van Humbeck, T. M. McDonald, X. Jing, B. M. Wiers, G. Zhu, J. R. Long, *J. Am. Chem. Soc.* 2014, **136**, 2432. (i) P. Deria, W. Bury, J. T. Hupp, O. K. Farha, *Chem. Commun.* 2014, **50**, 1965. (j) J. A.; Veenstra, M.; Long, J. R. *Chem. Sci.* 2014, **5**, 32.

- [4.5] (a) R. –B. Lin, F. Li, S. –Y. Liu, J. –P. Zhang, X. –M. Chen, *Angew. Chem. Int. Ed.* 2013, **52**, 13429. (b) Z. Xie, L. Ma, K. E. deKrafft, A. Jin, W. Lin, *J. Am. Chem. Soc.* 2010, **132**, 922. (c) Y. Takashima, V. M. Martínez, S. Furukawa, M. Kondo, S. Shimomura, H. Uehara, M. Nakahama, K. Sugimoto, S. Kitagawa, *Nat. Commun.* 2011, **2**, 1. (d) M. M. Wanderley, C. Wang, C. –D. Wu, W. Lin, *J. Am. Chem. Soc.* 2012, **134**, 9050. (e) A. Lan, K. Li, H. Wu, D. H. Olson, T. J. Emge, W. Ki, M. Hong, J. Li, *Angew. Chem. Int. Ed.* 2009, **48**, 2334.
- [4.6] (a) B. Chen, L. Wang, F. Zapata, G. Qian, E. B. Lobkovsky, *J. Am. Chem. Soc.* 2008, **130**, 6718. (b) Y. Li, S. Zhang, D. Song, *Angew. Chem. Int. Ed.* 2013, **52**, 710. (c) B. Chen, L. Wang, Y. Xiao, F. R. Fronczek, M. Xue, Y. Cui, G. Qian, *Angew. Chem. Int. Ed.* 2009, **48**, 500. (d) B. Zhao, X. –Y. Chen, P. Cheng, D. –Z. Liao, S. –P. Yan, Z. –H. Jiang, *J. Am. Chem. Soc.* 2004, **126**, 15394. (e) J. Rocha, L. D. Carlos, F. A. A. Paz, D. Ananias, *Chem. Soc. Rev.* 2011, **40**, 926.
- [4.7] (a) N. Sabbatini, M. Guardigli, J.-M. Lehn, *Coord. Chem. Rev.*, 1993, **123**, 201. (b) F. S. Richardson, *Chem. Rev.*, 1982, **82**, 541. (c) B. D. Chandler, D. T. Cramb, G. K. H. Shimizu, *J. Am. Chem. Soc.*, 2006, **32**, 10403.
- [4.8] (a) Y. –Q. Lan, H. –L. Jiang, S. –L. Li, Q. Xu, *Adv. Mater.* 2011, **23**, 5015. (b) J. An, C. M. Shade, D. A. Chengelis–Czegan, S. Petoud, N. L. Rosi, *J. Am. Chem. Soc.* 2011, **133**, 1220. (c) H. Li, X. Feng, Y. Guo, D. Chen, R. Li, X. Ren, X. Jiang, Y. Dong, B. Wang, *Sci. Rep.* 2014, **4**, 4366.
- [4.9] (a) B. Lee, R. Scopelliti, K. Severin, *Chem. Commun.* 2011, **47**, 9639. (b) J. M. Landete, B. d. I. Rivas, A. Marcobal, R. Muñoz, *Int. J. Food Microbiol.* 2007, **117**, 258.
- [4.10] (a) V. P. Aneja, P. A. Roelle, G. C. Murray, J. Schuthirland, J. W. Erisman, D. Faler, W. A. H. Asman, N. Patni, *Atoms. Environ.* 2001, **35**, 1903. (b) X. Zhang, X. Liu, R. Lu, H. Zhang, P. Gong, *J. Mater. Chem.* 2012, **22**, 1167. (c) Y. Che, X. Yang, S. Loser, L. Zang, *Nano. Lett.* 2008, **8**, 2219. (d) J. H. Bang, S. H. Lim, E. Park, K. S. Suslick, *Langmuir*, 2008, **24**, 13168.
- [4.11] (a) Z. –Z. Lu, R. Zhang, Y. –Z. Li, Z. –J. Guo, H. –G. Zheng, *J. Am. Chem. Soc.* 2011, **133**, 4172. (b) C. –Y. Sun, X. –L. Wang, C. Qin, J. –L. Jin, Z. –M. Su, P. Huang, K. –Z. Shao, *Chem. Eur. J.* 2013, **19**, 3639. (c) R. Grüner, V. Bon, A.

- Heerwig, N. Klein, P. Müller, U. Stoeck, I. A. Baburin, U. Mueller, I. Senkovaska, S. Kaskel, *Chem. Eur. J.* 2012, **18**, 13299. (d) J. Cui, Y. Li, Z. Guo, H. Zheng, *Chem. Commun.* 2013, **49**, 555.
- [4.12] L. Han, L. Qin, L. Xu, Y. Zhou, J. Sun and X. Zou, *Chem. Commun.*, 2013, **49**, 406.
- [4.13] (a) B. –P. Jiang, D. –S. Guo, Y. Liu, *J. Org. Chem.* 2010, **75**, 7258. (b) L. Shi, C. He, D. Zhu, Q. He, Y. Li, Y. Chen, Y. Sun, Y. Fu, D. Wen, H. Cao, J. Cheng, *J. Mater. Chem.* 2012, **22**, 11629. (c) X. Liu, X. Zhang, R. Lu, P. Xue, D. Xu, H. Zhou, *J. Mater. Chem.* 2011, **21**, 8756.
- [4.14] M. Wahiduzzaman, A. F. Oliveira, P. Philipsen, L. Zhechkov, E. van Lenthe, H. A. Witek, T. Heine, *J. Chem. Theory Comput.* 2013, **9**, 4006.
- [4.15] M. A. Addicoat, S. Fukuoka, A. J. Page, S. Irle, *J. Comput. Chem.*, 2013, **30**, 2591.
- [4.16] (a) B. Aradi, B. Hourahine, T. Frauenheim, *J. Phys. Chem. A* 2007, **111**, 5678. (b) M. Wahiduzzaman, A. F. Oliveira, P. Philipsen, L. Zhechkov, E. van Lenthe, H. A. Witek, T. Heine, *J. Chem. Theory Comput.*, 2013, **9**, 4006.
- [4.17] J. P. Perdew, K. Burke, M. Ernzerhof, *Phys. Rev. Lett.* 1996, **77**, 3865.
- [4.18] (a) J. VandeVondele, M. Krack, F. Mohamed, M. Parrinello, T. Chassaing, J. Hutter, *Comput. Phys. Commun.* 2005, **167**, 103. (b) The CP2K developers group, <http://www.cp2k.org/> 2012.
- [4.19] (a) S. Goedecker, M. Teter, J. Hutter, *Phys. Rev.*, 1996, **B54**, 1703. (b) C. Hartwigsen, S. Goedecker, J. Hutter, *Phys. Rev.*, 1998, **B58**, 3641.

## CHAPTER 5

- [5.1] (a) G. Férey, *Chem. Soc. Rev.*, 2008, **37**, 191. (b) A. U. Czaja, N. Trukhan, U. Müller, *Chem. Soc. Rev.*, 2009, **38**, 1284. (c) D. J. Tranchemontagne, J. L. Mendoza-Cortes, M. O’Keeffe, O. M. Yaghi, *Chem. Soc. Rev.*, 2009, **38**, 1257.
- [5.2] (a) H. L. Li, M. Eddaoudi, M. O’Keeffe, O. M. Yaghi, *Nature*, 1999, **402**, 276. (b) M. Eddaoudi, J. Kim, N. Rosi, D. Vodak, J. Wachter, M. O’Keeffe, O. M. Yaghi, *Science*, 2002, **295**, 469. (c) O. M. Yaghi, M. O’Keeffe, N. W. Ockwig, H. K. Chae, M. Eddaoudi, J. Kim, *Nature*, 2003, **423**, 705. (d) S. Kitagawa, R. Kitaura, S.-I. Noro, *Angew. Chem., Int. Ed.*, 2004, **43**, 2334. (e) R. Matsuda, R. Kitaura, S.

- Kitagawa, Y. Kubota, R. V. Belosludov, T. C. Kobayashi, H. Sakamoto, T. Chiba, M. Takata, Y. Kawazoe, Y. Mita, *Nature*, 2005, **436**, 238. (f) J. L. C. Rowsell, E. C. Spencer, J. Eckert, J. A. K. Howard, O. M. Yaghi, *Science*, 2005, **309**, 1350. (g) A. R. Millward, O. M. Yaghi, *J. Am. Chem. Soc.*, 2005, **127**, 17998. (h) D. Sun, S. Ma, Y. Ke, D. J. Collins, H.-C. Zhou, *J. Am. Chem. Soc.*, 2006, **128**, 3896. (i) H. Frost, T. Dulren, R. Q. Snurr, *J. Phys. Chem. B*, 2006, **110**, 9565. (j) J. L. C. Rowsell, O. M. Yaghi, *J. Am. Chem. Soc.*, 2006, **128**, 1304. (k) H. Furukawa, M. A. Miller, O. M. Yaghi, *J. Mater. Chem.*, 2007, **17**, 3197. (l) H. Noguchi, A. Kondo, Y. Hattori, H. Kajiro, H. Kanoh, K. Kaneko, *J. Phys. Chem. C*, 2007, **111**, 248. (m) T. K. Maji, S. Kitagawa, *Pure Appl. Chem.*, 2007, **79**, 2155. (n) R. E. Morris, P. S. Wheatley, *Angew. Chem., Int. Ed.*, 2008, **47**, 4966. (o) T. K. Trung, P. Trens, N. Tanchoux, S. Bourrelly, P. L. Llewellyn, S. Loera-Serna, C. Serre, T. Loiseau, F. Fajula, G. Férey, *J. Am. Chem. Soc.*, 2008, **130**, 16926. (p) H. Wang, J. Getzschmann, I. Senkowska, S. Kaskel, *Micropor. Mesopor. Mater.* 2008, **116**, 653. (q) D. Britt, D. Tranchemontagne, O. M. Yaghi, *Proc. Natl. Acad. Sci. U. S. A.*, 2008, **105**, 11623. (r) P. L. Llewellyn, S. Bourrelly, C. Serre, A. Vimont, M. Daturi, L. Hamon, G. De Weireld, J.-S. Chang, D.-Y. Hong, Y. K. Hwang, S. H. Jhung, G. Férey, *Langmuir*, 2008, **24**, 7245. (s) L. J. Murray, M. Dinca, J. R. Long, *Chem. Soc. Rev.* 2009, **38**, 1294. (t) B. Chen, S. Xiang, G. Qian, *Acc. Chem. Res.*, 2010, **43**, 1115.
- [5.3] (a) J. A. R. Navarro, E. Barea, J. M. Salas, N. Masciocchi, , S. GalliSironi, A. Ania, C. O.; Parra, J. B. *Inorg. Chem.*, 2006, **45**, 2397. (b) P. K. Thallapally, J. Tian, M. R. Kishan, C. A. Fernandez, S. J. Dalgarno, P. B. McGrail, J. E. Warren, J. L. Atwood, *J. Am. Chem. Soc.*, 2008, **130**, 16842. (c) L. Alaerts, M. Maes, L. Giebeler, P. A. Jacobs, J. A. Martens, J. F. M. Denayer, C. E. A. Kirschhock, D. E. De Vos, *J. Am. Chem. Soc.*, 2008, **130**, 14170. (d) Y. S. Bae, K. L. Mulfort, H. Frost, P. Ryan, S. Punnathanam, L. J. Broadbelt, J. T. Hupp, R. Q. Snurr, *Langmuir*, 2008, **24**, 8592. (e) M. Hartmann, S. Kunz, D. Himsl, O. Tangermann, S. Ernst, A. Wagener, *Langmuir*, 2008, **24**, 8634. (f) J.-P. Zhang, X.-M. Chen, *J. Am. Chem. Soc.*, 2008, **130**, 6010. (g) J.-R. Li, R. J. Kuppler, H.-C. Zhou, *Chem.*



- Soc. Rev.*, 2009, **38**, 1477. (h) Y. S. Bae, O. K. Farha, J. T. Hupp, R. Q. Snurr, *J. Mater. Chem.*, 2009, **19**, 2131.
- [5.4] (a) K. Schlichte, T. Kratzke, S. Kaskel, *Micropor. Mesopor. Mater.*, 2004, **73**, 81. (b) B. Gómez-Lor, E. Gutiérrez-Puebla, M. Iglesias, M. A. Monge, C. Ruiz-Valero, N. Snejko, *Chem. Mater.*, 2005, **17**, 2568. (c) A. Henschel, K. Gedrich, R. Kraehnert, S. Kaskel, *Chem. Commun.*, 2008, 4192. (d) F. Gándara, B. Gómez-Lor, E. Gutiérrez-Puebla, M. Iglesias, M. A. Monge, D. M. Proserpio, N. Snejko, *Chem. Mater.*, 2008, **20**, 72. (e) J. Y. Lee, O. K. Farha, J. Roberts, K. A. Scheidt, S. B. T. Nguyen, J. T. Hupp, *Chem. Soc. Rev.*, 2009, **38**, 1450. (f) L. Ma, C. Abney, W. Lin, *Chem. Soc. Rev.*, 2009, **38**, 1248. (g) J. Zhang, X. Wang, L. He, L. Chen, C.Y. Su, S. L. James, *New J. Chem.*, 2009, **33**, 1070.
- [5.5] (a) M. Vallet-Regí, F. Balas, D. Arcos, *Angew. Chem., Int. Ed.*, 2007, **46**, 7548. (b) A. Dupuis, N. Guo, Y. Gao, N. Godbout, S. Lacroix, C. Dubois, M. Skorobogatiy, *Opt. Lett.* 2007, **32**, 109. (c) P. Horcajada, C. Serre, G. Maurin, N. A. Ramsahye, F. Balas, M. Vallet-Regí, M. Sebban, F. Taulelle, G. Férey, *J. Am. Chem. Soc.*, 2008, **130**, 6774. (d) W. Lin, W. Rieter, K. Taylor, *Angew. Chem., Int. Ed.*, 2009, **48**, 650. (e) O. Shekhah, H. Wang, M. Paradinas, C. Ocal, B. Schupbach, A. Terfort, D. Zacher, R. A. Fischer, C. Woll, *Nature Mater.* 2009, **8**, 481. (f) K. M. L. Taylor-Pashow, J. D. Rocca, Z. Xie, S. Tran, W. Lin, *J. Am. Chem. Soc.*, 2009, **131**, 14261. (g) N. J. Hinks, A. C. McKinlay, B. Xiao, P. S. Wheatley, R. E. Morris, *Micropor. Mesopor. Mat.*, 2010, **129**, 330.
- [5.6] (a) B. L. Chen, L. B. Wang, F. Zapata, G. D. Qian, E. B. Lobkovsky, *J. Am. Chem. Soc.*, 2008, **130**, 6718. (b) B. L. Chen, L. B. Wang, Y. Q. Xiao, F. R. Fronczek, M. Xue, Y. J. Cui, G. D. Qian, *Angew. Chem., Int. Ed.*, 2009, **48**, 500. (c) J. R. Long, O. M. Yaghi, *Chem. Soc. Rev.*, 2009, **38**, 1213. (d) Z. Xie, L. Ma, K. E. deKrafft, A. Jin, W. Lin, *J. Am. Chem. Soc.*, 2010, **132**, 922.
- [5.7] K. S. Park, Z. Ni, A. P. Côté, J. Y. Choi, R. D. Huang, F. J. Uribe-Romo, H. K. Chae, M. O'Keeffe, O. M. Yaghi, *Proc. Natl. Acad. Sci. USA*, 2006, **103**, 10186.
- [5.8] S. Han, Y. Wei, C. Valente, R. S. Forgan, J. J. Gassensmith, R. A. Smaldone, H. Nakanishi, A. Coskun, J. F. Stoddart, B. A. Grzybowski, *Angew. Chem., Int. Ed.*, 2011, **50**, 276.

- [5.9] (a) D. J. Abdallah, R. G. Weiss, *Adv. Mater.*, 2000, **12**, 1237. (b) L. A. Estroff, A. D. Hamilton, *Chem. Rev.*, 2004, **104**, 1201. (c) N. M. Sangeetha, U. Maitra, *Chem. Soc. Rev.*, 2005, **34**, 821. (d) M. George, R. G. Weiss, *Acc. Chem. Res.*, 2006, **39**, 489. (e) S. Ray, A. K. Das, A. Banerjee, *Chem. Mater.*, 2007, **19**, 1633. (f) P. Dastidar, *Chem. Soc. Rev.*, 2008, **37**, 2699. (g) A. Ajayaghosh, V. K. Praveen, C. Vijayakumar, *Chem. Soc. Rev.*, 2008, **37**, 109. (h) A. R. Hirst, B. Escuder, J. F. Miravet, D. K. Smith, *Angew. Chem., Int. Ed.*, 2008, **47**, 8002. (i) A. Pal, H. Basit, S. Sen, V. K. Aswal, S. Bhattacharya, *J. Mater. Chem.*, 2009, **19**, 4325. (j) S. Samai, J. Dey, K. Biradha, *Soft Matter*, 2011, **7**, 2121. (k) D. D. Díaz, D. Kühbeck, R. J. Koopmans, *Chem. Soc. Rev.*, 2011, **40**, 427.
- [5.10] B. Xing, M.-F. Choi, B. Xu, *Chem. Commun.*, 2002, 362.
- [5.11] (a) S. J. Novick, J. S. Dordick, *Chem. Mater.*, 1998, **10**, 955. (b) B. G. Xing, M. F. Choi, B. Xu, *Chem. Eur. J.*, 2002, **8**, 5028. (c) J. F. Miravet, B. Escuder, *Chem. Commun.*, 2005, 5796. (d) Q. G. Wang, Z. M. Yang, X. Q. Zhang, X. D. Xiao, C. K. Chang, B. Xu, *Angew. Chem., Int. Ed.*, 2007, **46**, 4285. (e) T. Tu, W. Assenmacher, H. Peterlik, R. Weisbarth, M. Nieger, K. H. Dötz, *Angew. Chem., Int. Ed.*, 2007, **46**, 6368. (f) Q. G. Wang, Z. M. Yang, Y. Gao, W. W. Ge, L. Wang, B. Xu, *Soft Matter*, 2008, **4**, 550. (g) J. Zhang, X. Wang, L. He, L. Chen, C.Y. Su, S. L. James, *New J. Chem.*, 2009, **33**, 1070.
- [5.12] (a) M. Shirakawa, N. Fujita, T. Tani, K. Kanekob, S. Shinkai, *Chem. Commun.*, 2005, 4149. (b) S.; Kume, K. Kuroiwa, N. Kimizuka, *Chem. Commun.* 2006, 2442. (c) W. L. Leong, S. K. Batabyal, S. Kasapis, J. J. Vittal *Chem. Eur. J.*, 2008, **14**, 8822. (d) A. Saha, S. Manna, A. K. Nandi *Chem. Commun.*, 2008, 3732. (e) S. K. Batabyal, W. L. Leong, J. J. Vittal, *Langmuir*, 2010, **26**, 7464.
- [5.13] (a) H. Z. Bu, A. M. English, S. R. Mikkelsen, *Anal. Chem.*, 1996, **68**, 3951. (b) L. Yang, S. S. Saavedra, N. R. Armstrong, *Anal. Chem.*, 1996, **68**, 1834. (c) H. Suzuki, A. Kumagai, *Biomacromolecules*, 2004, **5**, 486. (d) C. D. Geary, I. Zudans, A. V. Goponenko, S. A. Asher, S. G. Weber, *Anal. Chem.*, 2005, **77**, 185. (e) M. Honda, K. Kataoka, T. Seki, Y. Takeoka *Langmuir*, 2009, **25**, 8349.
- [5.14] (a) O. Roubeau, A. Colin, V. Schmitt, R. Clérac, *Angew. Chem., Int. Ed.*, 2004, **43**, 3283. (b) M. R. Lohe, M. Rose, S. Kaskel, *Chem. Commun.*, 2009, 6056. (c) P. J.

- Bracher, M. Gupta, E. T. Mack, G. M. Whitesides, *ACS Appl. Mater. Interfaces*, 2009, **1**, 1807. (d) Y. Liao, L. He, J. Huang, J. Zhang, L. Zhuang, H. Shen, C. Y. Su, *ACS Appl. Mater. Interfaces*, 2010, **2**, 2333.
- [5.15] (a) K. Tsuchiya, Y. Orihara, Y. Kondo, N. Yoshino, T. Ohkubo, H. Sakai, M. Abe, *J. Am. Chem. Soc.*, 2004, **126**, 12282. (b) S. Kawano, N. Fujita, S. Shinkai, *J. Am. Chem. Soc.*, 2004, **126**, 8592.
- [5.16] (a) M. Shirakawa, N. Fujita, T. Tani, K. Kaneko, M. Ojima, A. Fujii, M. Ozaki, S. Shinkai, *Chem. Eur. J.*, 2007, **13**, 4155. (b) S. K. Batabyal, A. M. P. Peedikakkal, S. Ramakrishna, C. H. Sow, J. J. Vittal, *Macromol. Rapid Commun.*, 2009, **15**, 1356.
- [5.17] D. S. Tsekova, V. B. Stoyanova, *Bulg. Chem. Commun.*, 2009, **41**, 149.
- [5.18] (a) M. J. Platers, R. A. Howie, A. Roberts, *J. Chem. Commun.*, 1997, 893. (b) L. Pan, T. Frydel, M. B. Sander, X. Huang, J. Li, *Inorg. Chem.*, 2001, **40**, 1271. (c) R. K. B. Nielsen, K. O. Kongshaug, H. Fjellvag, *Solid State Sci.*, 2006, **8**, 1237. (d) Z. Fei, T. J. Geldbach, R. Scopelliti, P. J. Dyson, *Inorg. Chem.*, 2006, **45**, 6331. (e) Y. Yang, G. Jiang, Y.-Z. Li, J. Bai, Y. Pan, X.-Z. You, *Inorg. Chim. Acta*, 2006, **359**, 3257. (f) C. Volkringer, T. Loiseau, G. Férey, J. E. Warren, D. S. Wragg, R. E. Morris, *Solid State Sci.*, 2007, **9**, 455. (g) Q. Shuai, S. Chen, S. Gao, *Inorg. Chim. Acta*, 2007, **360**, 1381. (h) K. Aliouane, N. Rahahlia, A. Guehria-Laidoudi, S. Dahaoui, C. Lecomte, *Acta Crystallogr., Sect. E*, 2007, **63**, m1834. (i) C. Volkringer, J. Marrot, G. Férey, T. Loiseau, *Cryst. Growth Des.*, 2008, **8**, 685. (j) C. A. Williams, A. J. Blake, C. Wilson, P. Hubberstey, M. Schröder, *Cryst. Growth Des.*, 2008, **8**, 911. (k) P. D. C. Dietzel, R. Blom, H. Z. Fjellvag, *Anorg. Allg. Chem.*, 2009, **635**, 1953. (l) A. E. Platero-Prats, V. A. de la Peña-O'Shea, M. Iglesias, N. Snejko, A. Monge, E. Gutiérrez-Puebla, *ChemCatChem*, 2010, **2**, 147. (m) A. E. Platero-Prats, V. A. de la Peña-O'Shea, N. Snejko, A. Monge, E. Gutiérrez-Puebla, *Chem. Eur. J.*, 2010, **16**, 11632. (n) A. E. Platero-Prats, M. Iglesias, N. Snejko, A. Monge, E. Gutiérrez-Puebla, *Cryst. Growth Des.*, 2011, **11**, 1750. (o) P.-C. Liang, H.-K. Liu, C.-T. Yeh, C.-H. Lin, V. Zima, *Cryst. Growth Des.*, 2011, **11**, 699.
- [5.19] S. Harder, *Chem. Rev.*, 2010, **110**, 3853.

- [5.20] (a) F. Fages, *Angew. Chem., Int. Ed.*, 2006, **45**, 1680. (b) M. M. Pires, J. Chmielewski, *J. Am. Chem. Soc.*, 2009, **131**, 2706.
- [5.21] (a) D. Lässig, J. Lincke, H. Krautscheid, *Tetrahedron Lett.*, 2010, **51**, 653. (b) T. Panda, P. Pachfule, R. Banerjee, *Chem. Commun.*, 2011, **47**, 7674.
- [5.22] (a) E. Neofotistou, C. D. Malliakas, P. N. Trikalitis, *CrystEngComm*, 2010, **12**, 1034. (b) P. Thuéry, B. Masci, *CrystEngComm*, 2010, **12**, 2982. (c) Z. P. Deng, L. H. Huo, H. Y. Wang, S. Gao, H. Zhao, *CrystEngComm*, 2010, **12**, 1526.
- [5.23] (a) S. Kume, K. Kuroiwa, N. Kimizuka, *Chem. Commun.*, 2006, 2442. (b) M. Chen, S.-S. Chen, T.-a. Okamura, Z. Su, M.-S. Chen, Y. Zhao, W.-Y. Sun, N. Ueyama, *Cryst. Growth Des.*, 2011, **11**, 1901. (c) M. Chen, M.-S. Chen, T.-a. Okamura, M.-F. Lv, W.-Y. Sun, N. Ueyama, *CrystEngComm*, 2011, **13**, 3801. (d) J. F. Eubank, L. Wojtas, M. R. Hight, T. Bousquet, V. C. Kravtsov, M. Eddaoudi, *J. Am. Chem. Soc.*, 2011, **133**, 17532.
- [5.24] M. Takeuchi, S. Kageyama, *Colloid Polym. Sci.*, 2003, **281**, 1178.
- [5.25] D. J. Adams, K. Morris, L. Chen, L. C. Serpell, J. Bacsá, G. M. Day, *Soft Matter*, 2010, **6**, 4144.
- [5.26] (a) M. J. Kamlet, J. L. M. Abbout, M. H. Abraham, R. W. Taft, *J. Org. Chem.*, 1983, **48**, 2877. (b) R. M. C. Goncalves, A. M. N. Simoes, L. M. P. C. Albuquerque, M. Roses, C. Rafols, E. Bosch, *J. Chem. Res. (M)*, 1993, 1380. (c) M. El-Sayed, H. Müller, G. Rheinwald, H. Lang, S. Spange, *Monatsh. Chem.*, 2003, **134**, 361. (d) A. Natrajan, D. Wen, *Green Chem.*, 2011, **13**, 913.
- [5.27] W. Edwards, C. A. Lagadec, D. K. Smith, *Soft Matter*, 2011, **7**, 110.
- [5.28] A. Y.Y. Tam, K. M. C. Wong, V. W. W. Yam, *Chem. Eur. J.*, 2009, **15**, 4775.
- [5.29] (a) M. Ma, D. Zacher, X. Zhang, R. A. Fischer, N. M. Nolte, *Cryst. Growth Des.*, 2011, **11**, 185. (b) Q. Zhang, J. Zhang, Q. Y. Yu, M. Pan, C. Y. Su, *Cryst. Growth Des.*, 2010, **10**, 4076. (c) C. S. Carr, D. F. Shantz, *Chem. Mater.*, 2005, **17**, 6192.
- [5.30] V. Trappe, D. A. Weitz, *Phys. Rev. Lett.*, 2000, **85**, 449.
- [5.31] (a) M. R. Lohe, M. Rose, S. Kaskel, *Chem. Commun.*, 2009, 6056. (b) A. P. Nelson, O. K. Farha, K. L. Mulfort, J. T. Hupp, *J. Am. Chem. Soc.*, 2009, **131**, 458.

## CHAPTER 6

- [6.1] (a) J.-S. Wang, K. Matyjaszewski, *J. Am. Chem. Soc.* 1995, **117**, 5614. (b) J. Chiefari, Y. K. (Bill) Chong, F. Ercole, J. Krstina, J. Jeffery, T. P. T. Le, R. T. A. Mayadunne, G. F. Meijs, C. L. Moad, G. Moad, E. Rizzardo, S. H. Thang, *Macromolecules*, 1998, **31**, 5559. (c) M. K. George, R. P. N. Veregin, P. M. Kazmaier, G K. Hamer, *Macromolecules*, 1993, **26**, 2987.
- [6.2] (a) O. M. Yaghi, G. Li, H. Li, *Nature*, **378**, 703. (b) Q.-K. Liu, J.-P. Ma, Y.-B. Dong, *J. Am. Chem. Soc.*, 2010, **132**, 7005. (c) S. Mukherjee, B. Joarder, B. Manna, A. V. Desai, A. K. Chaudhari, S. K. Ghosh, *Scientific Reports*, 2014, **4**, 5761.
- [6.3] (a) W. W. Focke, G. E. Wnek, Y. Wei, *J. Phys. Chem.*, 1987, **91**, 5814. (b) J. Stejskal, A. Riede, D. Hlavatá, J. Prokeš, M. Helmstedt, P. Holler, *Synthetic Metals*, 1998, **96**, 55.

## ABOUT THE AUTHOR

Arijit Mallick, son of Ashoke Mallick and Arati Mallick, was born in Satjelia village of South 24 Parganas district, West Bengal, India, in 1987. He received his secondary education from Satjelia Natabar Vidyayatan and higher secondary education from Rangabelia High School, Gosaba. He completed his B.Sc. from University of Calcutta (Dinabandhu Anderws Collage), Kolkata in 2007. After the completion of his B.Sc. he joined Department of Chemistry, Indian Institute of Technology Roorkee, Uttarakhand, to pursue his M.Sc. He joined Department of Physical chemistry, NCL, Pune to pursue his Ph.D. degree in July 2009 under the guidance of Dr. Rahul Banerjee. He was awarded research fellowship by Council of Scientific and Industrial Research (JRF and SRF) for 2009-2014.

## List of Publications

1. **Arijit Mallick**, Bikash Garai, Matthew Addicoat, Petko St. Petkov, Thomas Heine and Rahul Banerjee\* "Solid State Organic Amine Detection in a Photochromic Porous Metal Organic Framework" *Chem. Sci.*, 2015, **6**, 1420 – 1425.
2. Valmik S. Shinde, Manoj V. Mane, Kumar Vanka, **Arijit Mallick** and Nitin T. Patil\* "Gold(I)/Chiral Brønsted Acid Catalyzed Enantioselective Hydroamination–Hydroarylation of Alkynes: The Effect of a Remote Hydroxyl Group on the Reactivity and Enantioselectivity" *Chem. Euro. J.*, 2015, **21**, 975–979.
3. Chandan Dey, Tanay Kundu, Bishnu P. Biswal, **Arijit Mallick\*** and Rahul Banerjee\*" *Crystalline Metal Organic Frameworks (MOFs): Synthesis, Structure and Function* "Acta Cryst. B70, 2014, 3-10. [Published in the Special issue on Crystal engineering]
4. **Arijit Mallick**, Bikash Garai, David Díaz Díaz and Rahul Banerjee\* "Hydrolytic Conversion of a Metal-Organic Polyhedron into a Metal-Organic Framework" *Angew. Chem. Int. Ed.*, 2013, **52**, 13755–13759.
5. Bappaditya Gole, Arun Kumar Bar, **Arijit Mallick**, Rahul Banerjee and Partha Sarathi Mukherjee\* " Electron rich porous extended framework as heterogeneous catalyst for Diels-Alder reaction " *Chem. Commun.*, 2013, **49**, 7439-7441.
6. Soham Maity, Srimanta Manna, Sujoy Rana, Togati Naveen, **Arijit Mallick**, and Debabrata Maiti\* "Efficient and Stereoselective Nitration of Mono- and Disubstituted Olefins with AgNO<sub>2</sub> and TEMPO" *J. Am. Chem. Soc.*, 2013, **135**, 3355–3358.
7. Vadapalli Chandrasekhar,\* Chandrajeet Mohapatra, Rahul Banerjee\* and **Arijit Mallick** "Synthesis, Structure, and H<sub>2</sub>/CO<sub>2</sub> Adsorption in a Three-Dimensional 4-Connected Triorganotin Coordination Polymer with a sqc Topology" *Inorg. Chem.*, 2013, **52**, 3579–3581.

8. Mala Nath,\* Asheesh Kumar, **Arijit Mallick** “Microporous Carbonaceous Materials Incorporated with Metal (Ti, V and Zn) for Hydrogen Storage” *Materials Science Forum*, 2013, **755**, 111-117.
9. **Arijit Mallick**, Tanay Kundu, Rahul Banerjee\* “Correlation between Coordinated Water Content and Proton Conductivity in Ca-BTC-based Metal-Organic Frameworks” *Chem. Commun.*, 2012, **48**, 8829-8831.
10. Sharath Kandambeth, **Arijit Mallick**, Binit Lukose, Manoj V. Mane, Thomas Heine, and Rahul Banerjee\* "Construction of Crystalline 2D Covalent Organic Frameworks with Remarkable Chemical (Acid/Base) Stability via a Combined Reversible and Irreversible Route" *J. Am. Chem. Soc.*, 2012, **134**, 19524–19527.
11. Munmun Ghosh, **Arijit Mallick** and David Díaz Díaz\* " Crystal structure of 2-benzyl 1-tert-butyl (2*S*,4*R*)-4-(*p*-tolylsulfonyloxy)pyrrolidine-1,2-dicarboxylate, C<sub>24</sub>H<sub>29</sub>NO<sub>7</sub>S" *Z. Kristallogr. NCS*, 2012, **227**, 361-362.
12. **Arijit Mallick**, Eva-Maria Schön, Tamas Panda, K. Sreenivas, David Díaz Díaz and Rahul Banerjee\* "Fine-Tuning the Balance between Crystallization and Gelation and Enhancement of CO<sub>2</sub> Uptake on Functionalized Calcium Based MOFs and Metallogels” *J. Mater. Chem.*, 2012, **22**, 14951-14963.
13. **Arijit Mallick**, Subhadeep Saha, Pradip Pachfule, Sudip Roy, and Rahul Banerjee\* “Structure and Gas Sorption Behavior of a New Three Dimensional Porous Magnesium Formate” *Inorg. Chem.* 2011, **50**, 1392–1401. [[Among Top 10 most-accessed articles published in Inorganic Chemistry during the First quarter of 2011](#)]
14. **Arijit Mallick**, Subhadeep Saha, Pradip Pachfule, Sudip Roy and Rahul Banerjee\* “Selective CO<sub>2</sub> and H<sub>2</sub> Adsorption in a Chiral Magnesium based Metal Organic Framework (Mg-MOF) with Open Metal Sites” *J. Mater. Chem.*, 2010, **20**, 9073–9080.